frontiers | Research Topics

New telescope advances with novel techniques

Edited by
Hairen Wang, Shengfeng Yang and Jianhua Guo

Published in
Frontiers in Astronomy and Space Sciences

ISSN 1664-8714
ISBN 978-2-8325-6946-7
DOI 10.3389/978-2-8325-6946-7

Generative AI statement
Any alternative text (Alt text) provided alongside figures in the articles in this ebook has been generated by Frontiers with the support of artificial intelligence and reasonable efforts have been made to ensure accuracy, including review by the authors wherever possible. If you identify any issues, please contact us.

About Frontiers

Frontiers is more than just an open access publisher of scholarly articles: it is a pioneering approach to the world of academia, radically improving the way scholarly research is managed. The grand vision of Frontiers is a world where all people have an equal opportunity to seek, share and generate knowledge. Frontiers provides immediate and permanent online open access to all its publications, but this alone is not enough to realize our grand goals.

Frontiers journal series

The Frontiers journal series is a multi-tier and interdisciplinary set of open-access, online journals, promising a paradigm shift from the current review, selection and dissemination processes in academic publishing. All Frontiers journals are driven by researchers for researchers; therefore, they constitute a service to the scholarly community. At the same time, the *Frontiers journal series* operates on a revolutionary invention, the tiered publishing system, initially addressing specific communities of scholars, and gradually climbing up to broader public understanding, thus serving the interests of the lay society, too.

Dedication to quality

Each Frontiers article is a landmark of the highest quality, thanks to genuinely collaborative interactions between authors and review editors, who include some of the world's best academicians. Research must be certified by peers before entering a stream of knowledge that may eventually reach the public - and shape society; therefore, Frontiers only applies the most rigorous and unbiased reviews. Frontiers revolutionizes research publishing by freely delivering the most outstanding research, evaluated with no bias from both the academic and social point of view. By applying the most advanced information technologies, Frontiers is catapulting scholarly publishing into a new generation.

What are Frontiers Research Topics?

Frontiers Research Topics are very popular trademarks of the *Frontiers journals series*: they are collections of at least ten articles, all centered on a particular subject. With their unique mix of varied contributions from Original Research to Review Articles, Frontiers Research Topics unify the most influential researchers, the latest key findings and historical advances in a hot research area.

Find out more on how to host your own Frontiers Research Topic or contribute to one as an author by contacting the Frontiers editorial office: frontiersin.org/about/contact

New telescope advances with novel techniques

Topic editors

Hairen Wang — Purple Mountain Observatory, Chinese Academy of Sciences (CAS), China

Shengfeng Yang — Indiana University, Purdue University Indianapolis, United States

Jianhua Guo — Purple Mountain Observatory, Chinese Academy of Sciences (CAS), China

Citation

Wang, H., Yang, S., Guo, J., eds. (2025). *New telescope advances with novel techniques*. Lausanne: Frontiers Media SA. doi: 10.3389/978-2-8325-6946-7

Table of contents

frontiers | Frontiers in Astronomy and Space Sciences

TYPE Methods
PUBLISHED 15 December 2023
DOI 10.3389/fspas.2023.1311323

OPEN ACCESS

EDITED BY
Hairen Wang,
Chinese Academy of Sciences (CAS), China

REVIEWED BY
Jianqiang Ma,
Ningbo University, China
Donglin Ma,
Huazhong University of Science and Technology, China

*CORRESPONDENCE
Yang Fei,
yangflying@163.com

RECEIVED 09 October 2023
ACCEPTED 21 November 2023
PUBLISHED 15 December 2023

CITATION
Yuan-Guo L, Fei Y, Jia-Kang Z and Yin-Long H (2023), Jitter error evaluation in large-aperture optical telescopes based on normalized point source sensitivity.
Front. Astron. Space Sci. 10:1311323.
doi: 10.3389/fspas.2023.1311323

Jitter error evaluation in large-aperture optical telescopes based on normalized point source sensitivity

Liu Yuan-Guo[1,2], Yang Fei[1]*, Zhu Jia-Kang[1,2] and Huo Yin-Long[1,2]

[1]Changchun Institute of Optics, Chinese Academy of Sciences, Changchun, China, [2]University of Chinese Academy of Sciences, Beijing, China

To comprehensively analyze the jitter error in large-aperture optical telescopes, this paper introduces normalized point source sensitivity (PSSn) to evaluate the telescope system. First, the concept and basic properties of PSSn were introduced, and then the jitter error under expected random loads and the contribution percentage of each mode to the total jitter were analyzed through a model. The PSSn of the system under the influence of different error sources was studied, and its variation trend was estimated. A comparison of evaluation methods, such as the Strehl ratio, and the proposed method reflects the characteristics of more accurate data and a more concise calculation. The jitter error evaluation method proposed in this article, combined with PSSn, provides practical and beneficial guidance for the design and detection of large-aperture optical telescope systems.

KEYWORDS

large-aperture telescope, normalized point source sensitivity, integrated modeling, mode contribution, jitter evaluation

1 Introduction

In order to conduct more in-depth and detailed exploration of the universe, telescope technology, as one of the main exploration methods, is increasingly being valued by scientists from various countries. Furthermore, with the ongoing improvement of performance requirements for target observation, the scale of large-aperture optical telescopes is also increasing. In order to achieve better optical imaging quality, the requirements for system jitter errors are becoming increasingly strict. The system contains numerous error sources, such as mechanical vibration, noise, and external environmental interference, which have different frequency domain characteristics and more complex statistical correlations. Jitter not only affects the stability of the system structure but also leads to a decrease in the quality of the imaging system. In this context, traditional analysis methods such as root mean square have become difficult to adapt to the system error analysis of large-aperture optical telescopes.

The spot diagram represents the imaging of multiple light rays from a single point source after passing through an optical system. Due to the presence of aberrations in the optical system, the imaged image no longer converges to a single point but presents a dispersed form. In many cases, it cannot accurately evaluate image quality, so it cannot reflect the actual situation. The resolution method refers to the minimum distance that can distinguish two object points or images, reflecting the ability of optical systems to distinguish object details. Like the spot diagram method, it is mainly applicable to small aberration systems. Rayleigh

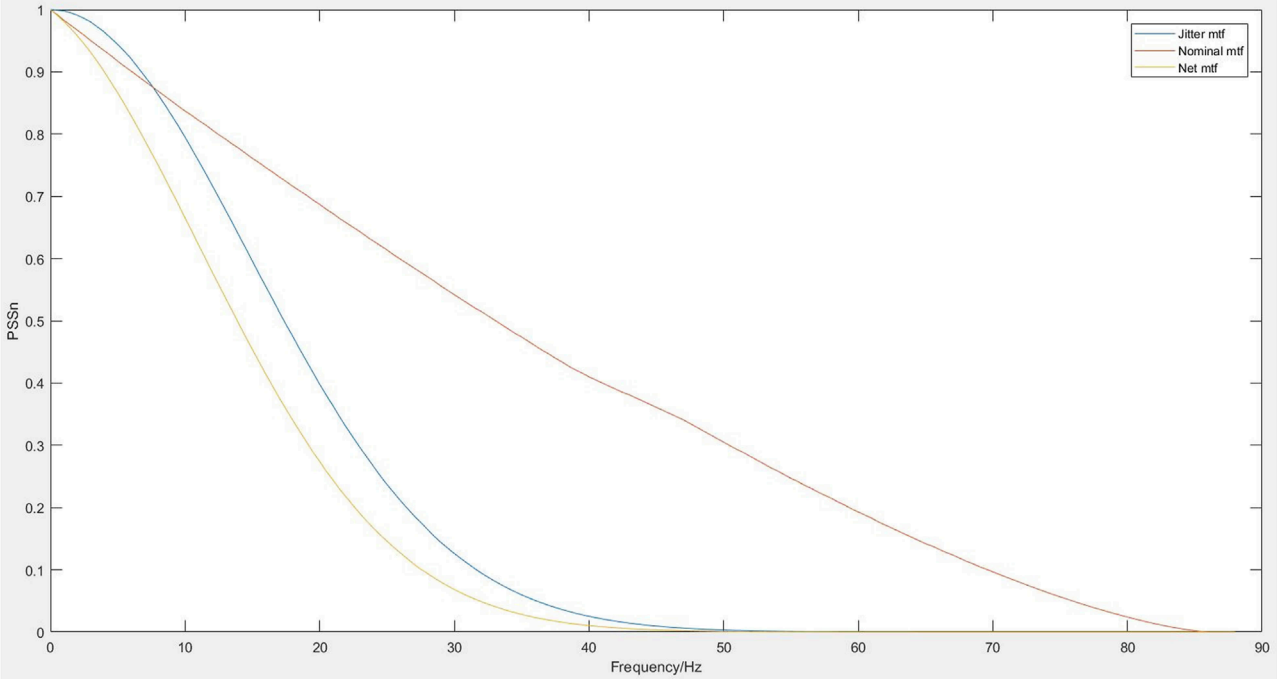

FIGURE 1
Curve plot of the jitter impact factor.

judgment is based on the principle that the maximum wave aberration between the actual wavefront and the reference spherical wave does not exceed λ/4 to judge whether the image quality is perfect. However, in some cases, the Rayleigh judgment may not be comprehensive enough, as it only considers the maximum value of wavefront aberration and does not fully consider the proportion of defects on the wavefront in the entire wavefront.

The Strehl ratio, also known as center illuminance, represents the ratio of energy concentration of the point spread function (PSF) of the actual telescope to the point spread function at the diffraction limit of the telescope. This ratio can better reflect the optical performance of telescopes and systems processed by adaptive optics. Usually represented by SD, according to Strehl judgment, when SD ≥ 0.8, the optical system can be considered complete. However, its computational complexity is high and is often used to evaluate the imaging quality of small aberration optical systems; therefore, it is rarely used in practical applications. For systems far from the diffraction limit, the applicability of the Strehl ratio significantly decreases. More importantly, as the influence of atmospheric visibility on the performance of optical systems continues to increase, the Stellite ratio is no longer suitable as an evaluation indicator. In this case, the central intensity ratio (CIR) is widely adopted. Whether it is used to describe small aberrations in the Strehl ratio or CIR used in atmospheric visibility-dominated situations, they only consider the central frequency domain characteristics of the point spread function. If there is an evaluation index that comprehensively considers the characteristics of energy distribution throughout the frequency domain, it will better evaluate the imaging quality of the system (Barr et al., 1990; Miyashita et al., 2003; Angeli et al., 2011).

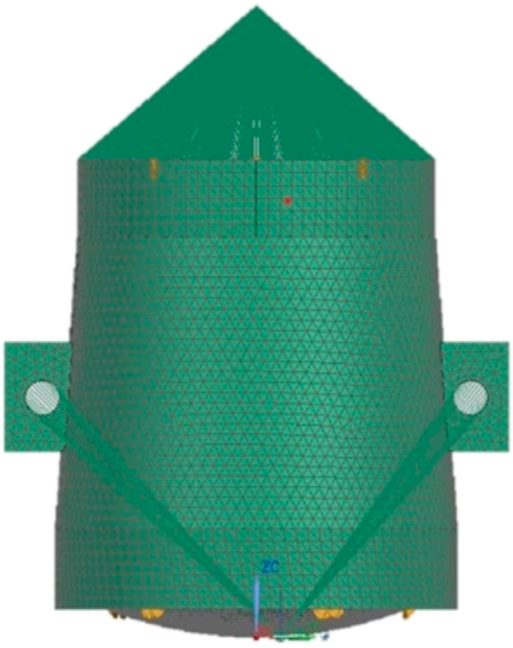

FIGURE 2
Optical–mechanical structure model.

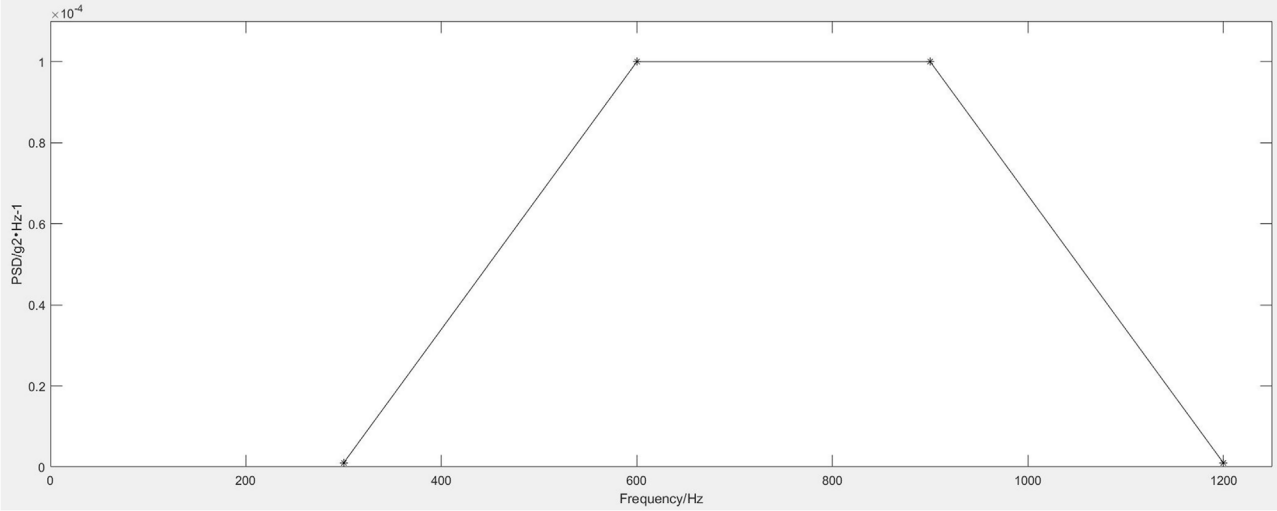

FIGURE 3
PSD input curve.

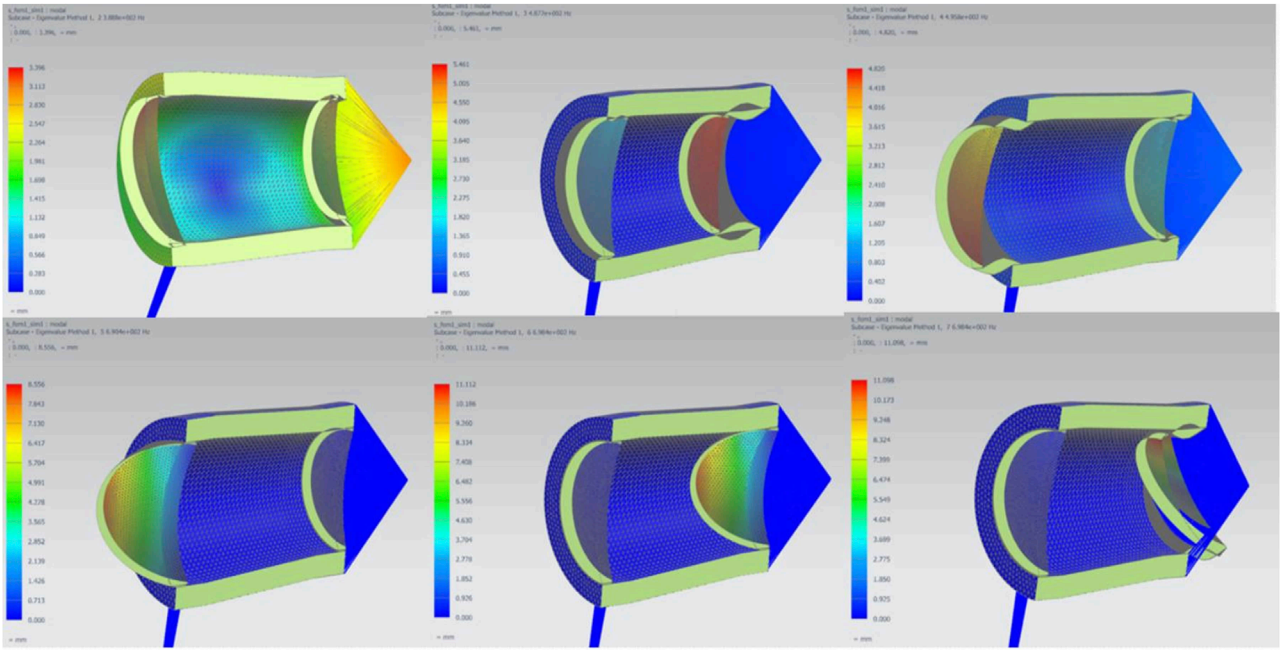

FIGURE 4
Sixth-order vibration diagram of the system.

The 30-m telescope (TMT) is an international collaborative project, with both the primary and secondary mirrors designed with double-curved surfaces, while the three-mirror system reflects light from the secondary mirror onto instruments used for scientific observation. Initiated by the United States, Canada, Japan, China, and India, it is currently one of the largest optical telescopes under construction. In this context, the US 30-m telescope team proposed using PSSn as the standard for error allocation in large-aperture telescopes. This article will study the jitter error evaluation method for large-aperture optical telescopes based on PSSn (Pazder et al., 2008; Vogiatzis and Angeli, 2008; Seo et al., 2009a).

2 PSSn and perturbation calculation

PSSn is the average of telescope errors in the background, fully utilizing the optical energy of the point spread function region, and, therefore, can comprehensively evaluate the imaging quality of the

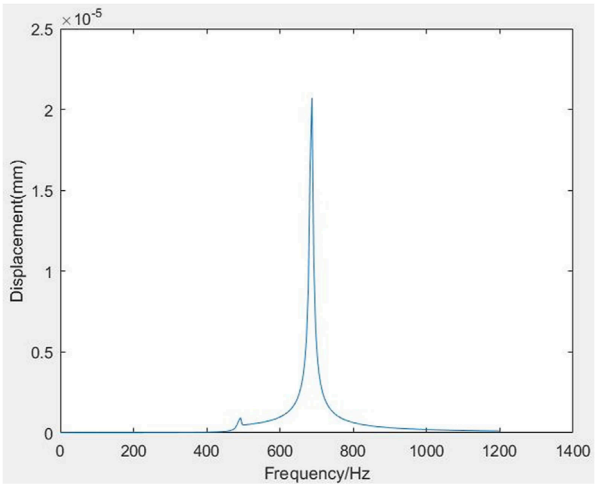

FIGURE 5
Sweep frequency analysis curve.

system (Cho et al., 2008). The basic definition is

$$PSSn = \frac{\int |PSF_{t+a+e}(\vec{\theta})|^2}{\int |PSF_{t+a}(\vec{\theta})|^2} = \frac{\int |OTF_{t+a+e}(\vec{\theta})|^2}{\int |OTF_{t+a}(\vec{\theta})|^2}. \quad (1)$$

Here, PSF_{t+a+e} and OTF_{t+a+e} are the point spread function and optical transfer function of the actual telescope in the atmosphere, while PSF_{t+a} and OTF_{t+a} are the point spread function and optical transfer function of the ideal telescope in the atmosphere, respectively. The subscripts t, a, and e represent the values due to telescope aperture, atmospheric, and telescope errors, respectively.

In order to utilize the synthetic properties of PSSn and simplify the expression, where f is the vector of the spatial frequency of the optical transfer function (OTF) (Sobek, 2005; Seo et al., 2009b),

$$OTF_{t+a+e}(\vec{f}) = OTF_{t+a}(\vec{f}) \cdot OTF_e(\vec{f}). \quad (2)$$

Use a symbol and a known operation expression to represent another operation, for simplicity, Sets the form of the operation, rather than defining the operator:

$$PSSn = <|OTF_e(\vec{f})|^2>, \quad (3)$$

$$< \cdot \geq \frac{\int |OTF_{t+a}(\vec{f})|^2 (\cdot) d\vec{f}}{\int |OTF_{t+a}(\vec{f})|^2 d\vec{f}}. \quad (4)$$

PSF is represented in the matrix form using Zemax ray tracing software, and the following formula is derived and applied:

$$PSSn = \iint |PSF(x,y)|^2 dxdy = \sum_{m,n} PSF^2(m,n) \times S_{m,n}. \quad (5)$$

Here, $S_{m,n}$ is the area of the rectangle in the mth row and nth column, and the ratio of the ideal and actual values is calculated (Chen and Hu, 2016). Due to the fact that OTF is the Fourier transform of PSF and the modulation transfer function (MTF) is the modulus of OTF, strict sampling of the data is required, and Fourier interpolation can be used to calculate the midpoint of the data. In practice, it is necessary to interpolate the regions that are meaningful for PSSn in the convolution between the reflector and the atmosphere, as Fourier interpolation is slower and MTF is windowed by the atmosphere. By calculating the denominator of PSSn, values with insignificant MTF errors can be found. Assuming a perfect MTF of 1, which is equivalent to an infinite aperture, then

$$PSSn = \frac{\triangle \sum (MTF_e MTF_a)^2}{\triangle \sum (MTF_p MTF_a)^2}. \quad (6)$$

Here, MTF_e, MTF_a, and MTF_p are the optical modulation functions of telescope error, atmosphere, and ideal value, respectively (An et al., 2016).

Finite element programs usually first calculate the natural frequency and mode shape. Modal analysis methods are then used to calculate the frequency response function (FRF). The forcing function and frequency response are input through power spectral density (PSD), allowing for the calculation of the PSD response function. Finally, the RMS response generated under the PSD response function is integrated. In modal response, by setting the expected PSD and subsequent integration analysis, PSD of the field-of-view response and the pointing error of each optical device can be obtained (YANGX et al., 2013). RMS of any response is the square root of the area under the PSD response function. The formulas are provided in Equations 7, 8. The transformation of the system's principal coordinates is completed based on the above characteristics.

$$PSD_{resp} = FRF_{resp}{}^2 PSD_{input}, \quad (7)$$

$$1\sigma_{resp} = RMS_{resp} = \sqrt{Area}. \quad (8)$$

Here, PSD_{resp} is the PSD response function of the optical system's visual axis, FRF_{resp} is the frequency response function, PSD_{input} is the PSD response function of the input, $1\sigma_{resp}$ is the standard deviation in a normal distribution, RMS_{resp} is the root mean square value of the random response, and $\sqrt{Area}$ is the square root of the surrounding area of the response function.

Multiplying the PSD response by the weighting function W, the line-of-sight error caused by jitter is divided into a drift term and a jitter term. Due to the significant impact of the jitter term on MTF compared to the drift term, the RMS value of the jitter term is mainly analyzed using the following equation:

$$\Delta_{rms} = \sqrt{\int_0^\infty W(f) \Delta_{PSD}(f) df}, \quad (9)$$

$$W = \frac{1 - 2(1 - cos(2\pi fT))}{(2\pi fT)^2}. \quad (10)$$

Here, W is used to divide the response, T is the sensor integration time, f is the response frequency, Δ_{rms} is the root mean square value of the jitter term, $W(f)$ is the jitter weighting function related to the frequency, and Δ_{PSD} is the PSD response to the line-of-sight error. The physical meaning of integrating the response power spectral

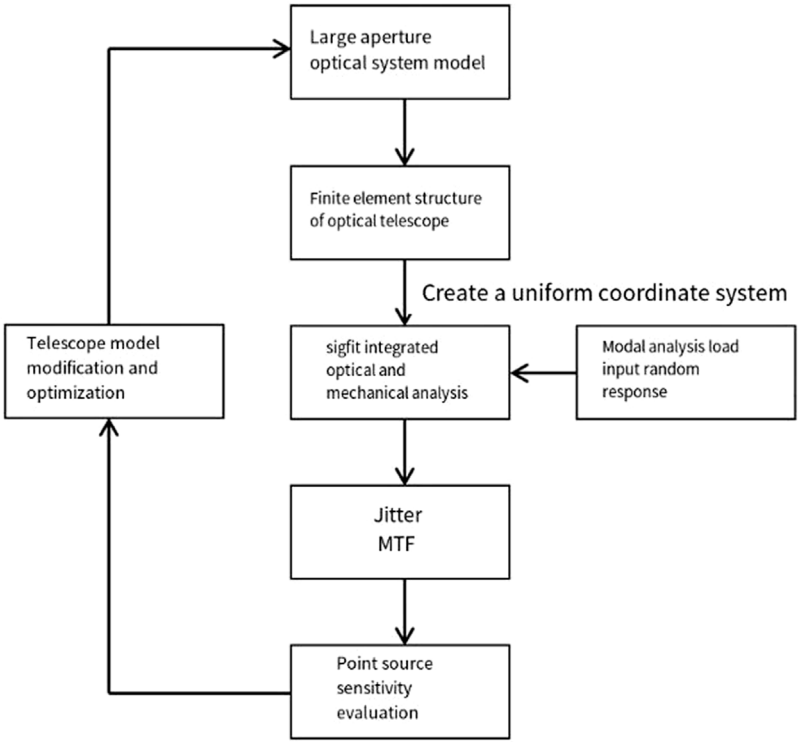

FIGURE 6
Flow chart of jitter error analysis of large-aperture optical telescopes.

density is to analyze the root mean square values of the system in different frequency bands.

MTF under jitter influence based on the RMS value is calculated as follows:

$$MTF_{Jitter}(f) = e^{-2\pi^2\Delta_{rms}^2 f^2}, \tag{11}$$

$$MTF_{Net} = MTF_{Nominal} \times MTF_{Jitter}. \tag{12}$$

Here, MTF_{Net} is MTF under the influence of jitter, $MTF_{Nominal}$ is the initial optical system MTF, and MTF_{Jitter} is the MTF influencing factor.

By modeling and setting disturbance factors, MTF and PSSn can be linked for disturbance calculation, as shown in Figure 1. The jitter curve is used to analyze and evaluate the impact factors.

By establishing the relationship between PSSn and MTF, perturbation factors and MTF are combined to make them interrelated. Subsequently, in the follow-up integration of optical–mechanical systems and the application of the large mass method, the recent research methods are extended to the field of jitter error evaluation and analysis so as to effectively meet the challenge of the detection and evaluation of jitter errors in large-aperture telescopes. In Figure 1, three curves are presented, namely, the MTF curve of the initial optical system, the MTF curve of the influence factor, and the MTF curve under the influence of jitter. For the modulation transfer function, which is affected by the jitter factor under the set power spectral density, the PSSn analysis method is applied to the optical integrated structure model; combined with the mode contribution ratio and the mode information in the frequency domain, it can help optimize the design of the system.

3 Modeling analysis

To address the degradation of imaging quality caused by jitter errors in optical telescope systems, an optical model and finite element system structure were established to unify their coordinate systems (McBride et al., 2016; Du et al., 2020). The frequency response function and root mean square were obtained using modal and power spectral density, and the effect of jitter was converted into a modulation transfer function through optical–mechanical integration. Then, the point source sensitivity function was used to analyze and evaluate the optical–mechanical system under the influence of jitter effects.

3.1 Optical–mechanical system

The opto-mechanical structure model of the primary and secondary mirrors is established, and the PSD input curve is set, as shown in Figure 2 and Figure 3, respectively.

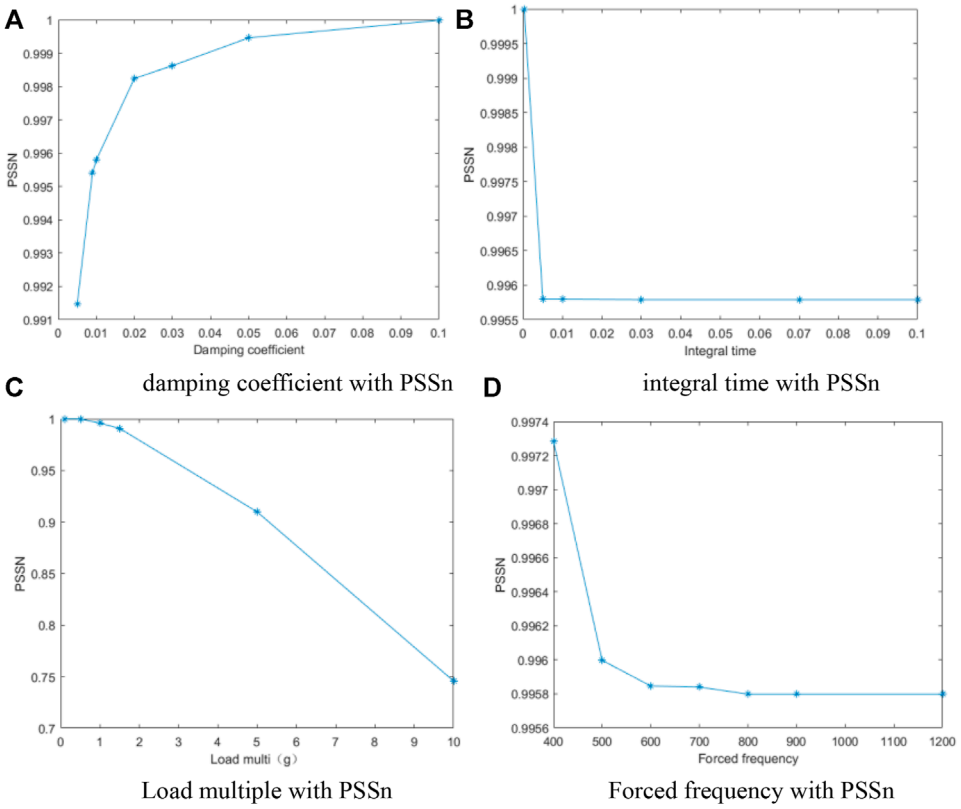

FIGURE 7
Relationship between various variable factors and PSSn. **(A)** Damping coefficient with PSSn. **(B)** Integral time with PSSn. **(C)** Load multiple with PSSn. **(D)** Forced frequency with PSSn.

3.2 Modal and sweep analysis

In modal response, PSD of the field-of-view response and the pointing error of each optical device can be calculated by setting the PSD input forcing function and the frequency response function of the field-of-view response. RMS of any response is the square root of the area under the PSD response function. Based on the above characteristics, the transformation of the system's principal coordinates can be completed, which is derived from the calculation of natural frequencies and vibration modes (Lee et al., 2012; Liu et al., 2021).

Modal analysis is one of the main methods for studying the dynamic characteristics of structures. Finite element modal analysis can be used to calibrate modes, improve model accuracy, and solve the natural frequencies and modes of the model, essentially solving eigenvalues and eigenvectors. View slicing is enabled, and the first six characteristic frequencies and corresponding vibration modes of the system are shown in Figure 4. Relevant data as shown in Table 1.

In order to conduct frequency sweep analysis under acceleration excitation, the large mass method is generally used, where the mass used is 10^6 times the model mass. The purpose is to determine the response of the structure under a simple harmonic load of a known frequency in order to find its resonant frequency and avoid structural damage due to resonance. The sweep frequency range is set from 2 to 1,202 Hz, with a step size of 5 and a frequency of 240, as shown in Figure 5. Different nodes in the structure are selected to draw a cloud chart. From the chart, it is found that under the same working conditions, the response of each node is slightly different, but the overall trend is roughly similar. The sweep frequency peaks are concentrated at 490 Hz and 687 Hz, which are close to the second- and fourth-order characteristic frequencies, respectively.

3.3 Integrated analysis

Based on the primary and secondary mirror and focal plane coordinate systems, the optical analysis model is connected in random response through polynomial fitting to obtain a linear optical model. The sensitivity coefficients of the optical response of each optical surface are used to establish equations for forced response analysis to obtain the dynamic response of optical performance (ZHAI et al., 2023). By applying the acceleration dynamic load and specifying nominal MTF through the interference module and disturbance range, a macro-file containing the system

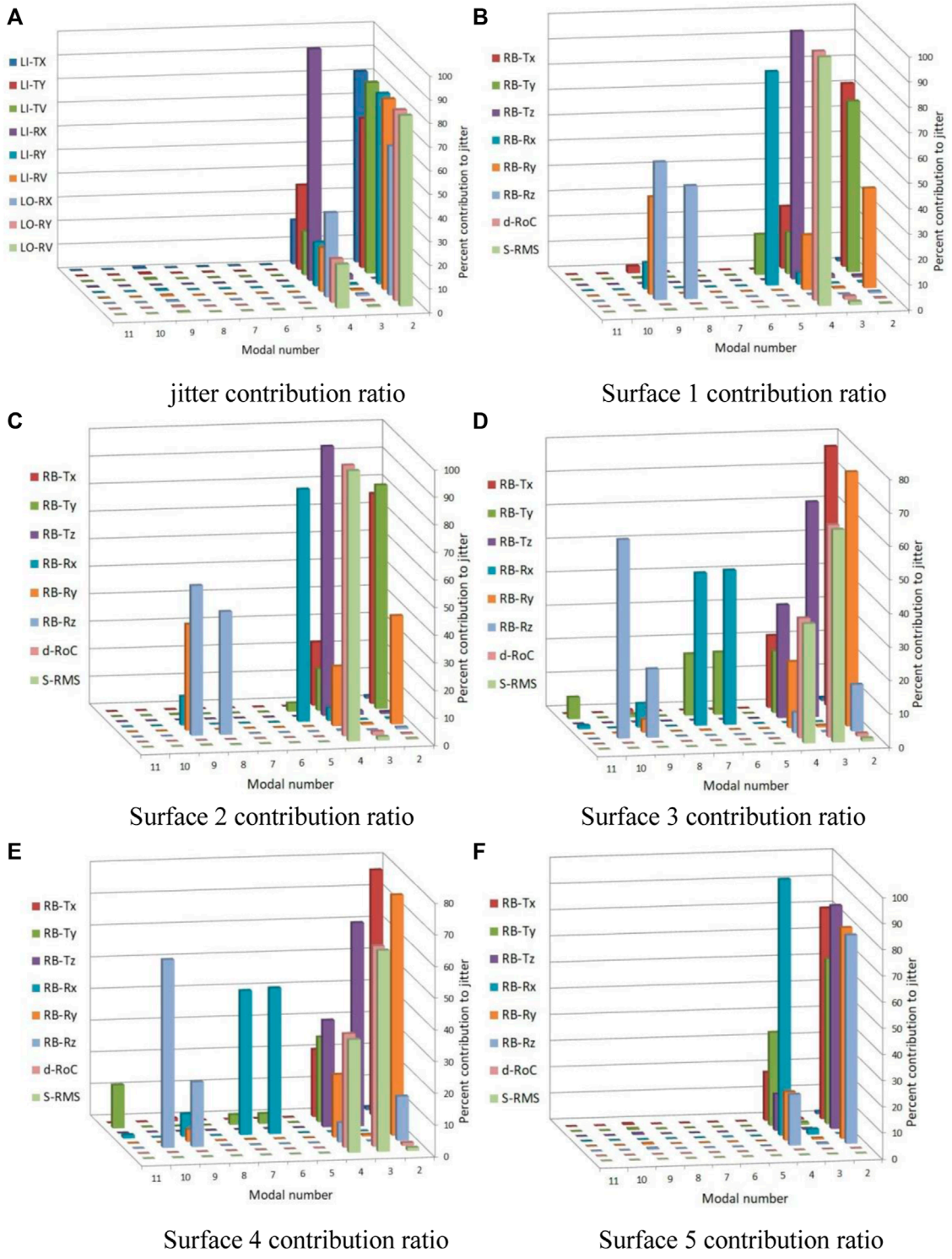

FIGURE 8
Modal contribution ratio. **(A)** Jitter contribution ratio. **(B)** Surface 1 contribution ratio. **(C)** Surface 2 contribution ratio. **(D)** Surface 3 contribution ratio. **(E)** Surface 4 contribution ratio. **(F)** Surface 5 contribution ratio.

surface error generated using SigFit is imported into the optical analysis based on the given forced frequency, random load, damping coefficient, and detector integration time. The jitter error is calculated using the ray tracing algorithm, and the subsequent results can be used to modify and optimize the model structure. The specific process is shown in Figure 6.

By integrating optical and mechanical models through SigFit, images of jitter MTF are obtained, the interference area of the

TABLE 1 Results of the first six modal analyses of the system.

Order	Characteristic frequency/Hz	Mode of vibration
1	388.7	The whole machine is rotated around the *Y*-axis
2	487.7	Primary and secondary mirror Z-opposite swing
3	495.8	Swing the primary and secondary mirror Z in the same direction
4	690.4	The primary mirror is rotated in the *X* direction
5	698.4	Secondary mirror *Y* turn
6	715.2	Secondary mirror *Y* swing

TABLE 2 Comparison between the Strehl ratio factor and PSSn under control variables of influencing factors.

Serial number	Strehl ratio factor	PSSn
1	9.9556E-01	9.9579E-01
2	9.9777E-01	9.9824E-01
3	9.9852E-01	9.9862E-01
4	9.9963E-01	9.9998E-01
5	9.9914E-01	9.9945E-01
6	9.9506E-01	9.9540E-01
7	9.9098E-01	9.9147E-01
8	9.9555E-01	9.9579E-01
9	7.2769E-01	7.4579E-01
10	9.0391E-01	9.0980E-01

telescope is determined, and subsequent design optimization is carried out to minimize the impact of jitter. At the same time, the point source sensitivity system is used to evaluate jitter errors.

The basic principle is to calculate the natural frequency and mode shape of the telescope using finite element and optical performance analysis tools and then decompose each optical surface of each mode into average rigid body motion and elastic deformation. The report provides the percentage contribution of each mode shape to the total field-of-view jitter, which helps accurately locate the area of the telescope structure for redesign. For the integration time of detector sensing, random errors are decomposed into drift and jitter components and converted into jitter MTF response functions. This function can generate optical system MTF in a random environment, providing data support for the application of PSSn. Figure 7 shows the relationship between various variable factors and PSSn. It can be seen that the damping coefficient is directly proportional to PSSn, as it is a random vibration. As the damping coefficient increases, the amplitude of structural vibration decreases, which means it tends to stabilize, and the factors affected by vibration decrease. When the integration time of the detector is not 0, the overall impact on PSSn tends to stabilize as the integration time increases. When only considering the load factor, the higher the load factor, the greater the system's bearing capacity and the greater the impact of vibration. In the forced frequency analysis, the starting frequency is 400 Hz, and as the ending frequency increases, PSSn gradually decreases. After 800 Hz, the change is not significant, and the two changes that are more obvious are related to the above swept-frequency peak.

SigFit is used to calculate the jitter component of the random response, as shown in Figure 8, where LI/LO represents the image space and object space, TX/TY represents the axial displacement of the *X*/*Y*-axis, LI-TV/LO-TV represents the linear displacement vector sum (mm) of the image space and object space on the *XY* plane, RX/RY represents the rotation around the *X*/*Y*-axis, and LI-RV/LO-RV represents the vector sum of the rotation between the image space and object space (rad), respectively. RB-TX/RB-TY/RB-TZ represents *X*/*Y* eccentricity and *Z* offset and RB-RX/RB-RY/RB-RZ represents *X*/*Y*/*Z* tilt, respectively. d-RoC represents the surface offset, and S-RMS represents the surface accuracy error. The first mode is essentially a free mode, where the key modes of the jitter component and the contribution percentage of each surface error in the system are concentrated in the second and fourth orders. Correspondingly, the peak frequencies of the above frequency sweep analysis indicate that the second and fourth orders are the main causes of errors. Taking the object space angular displacement LO-RV as an example, the contribution percentages of the second and fourth orders to LO-RV are 80.529% and 18.496%, respectively, while the contributions of other order modes are relatively small.

By obtaining the modal contribution ratio of each frequency order, the maximum value can be found and its vibration mode can be studied. Combined with the optical sensitivity coefficient, the optical element that is most affected by jitter can be obtained. Subsequently, its sensitivity characteristics can be used for optical and mechanical optimization or the pasting of monitoring sensors at corresponding positions.

Table 2 shows the data comparison between the Strehl ratio factor and PSSn under the control variables of various influencing factors. The calculation method of the Strehl ratio factor is the area under the MTF-Net curve divided by the area under the MTF-Nominal curve. It is used to multiply the nominal Strehl ratio of an unperturbed system and provides a single measure of system performance that can be applied to optimization techniques. When the sensor integration time is 0.03 s, that is, the serial number 8, the Strehl ratio factor is calculated to be 9.9555E-01, and jitter decreases with the decrease in detector integration time. In the case of 0.01 s, sequence number 1 increases the resulting Strehl ratio factor to 9.9556E-01. Alternatively, if the integration time is infinite, then all frequencies will cause jitter. Although the changing trend of the two datasets in the ten groups is the same under various influencing factors, the advantage of PSSn is that it makes full use of the optical energy in the point diffusion function region. The difference in the error margin between the two in serial number 9 is even 2%, and the PSSn is closer to 1 under the same conditions. Therefore, the data are more accurate and can be used to comprehensively evaluate the imaging quality of the system. Moreover, the processing and calculation processes are not as complicated as those for the Strehl

ratio. Subsequently, the system structure design can be improved according to the modal contribution ratio and the relationship between various variables and PSSn, and the overall performance of the system can be improved. Other evaluation methods, such as spot diagrams, resolution, and the Rayleigh criterion, have their own shortcomings compared with PSSn. For small-caliber components, RMS and PSSn analysis and evaluation are usually combined, which can accumulate the application experience of the PSSn evaluation method in practical engineering. However, in the application of large-aperture optical telescope systems, the use of RMS makes it difficult to fully reflect the influence of each error source on the performance of the integrated system. In view of the comprehensiveness of the PSSn evaluation method, if the error of different frequency band distributions is reasonably considered, the error limit range can be moderately increased. It can effectively reduce the overestimation in error analysis, and considering the error in different frequency bands conforms to both scientific and economic principles.

4 Conclusion

In this paper, the jitter error under a certain working condition is determined, and the proportion of influence of each order of frequency on jitter and the maximum contribution value is obtained. By introducing PSSn to evaluate the jitter error of a large-aperture telescope, the influence of jitter introduction is converted into a modulation transfer function, and the deformation results can be co-analyzed with the system, considering the overall and internal structural changes, efficiently and accurately reflecting the overall system performance. At the same time, the optical model and finite element analysis are used to link jitter with the optical performance analysis index. This approach helps understand the modes that have a greater impact on optical imaging under different working conditions, provides a reference for the design, helps in accurately predicting the working state of the optical telescope under the jitter environment, quantifies the system structure, and effectively improves the cost performance of the optical machine system. It is used to guide the structural design of large-aperture optical telescopes.

Data availability statement

The original contributions presented in the study are included in the article/Supplementary material; further inquiries can be directed to the corresponding author.

Author contributions

LY-G: writing–original draft and methodology. YF: writing–review and editing. ZJ-K: investigation and writing–review and editing. HY-L: supervision and writing–review and editing.

Funding

The author(s) declare that financial support was received for the research, authorship, and/or publication of this article. This research was supported by the Science and Technology Development Plan Project of Jilin Province (20230101008JC), Excellent Member of Youth Innovation Promotion Association CAS (Y202053), International Partnership Program of the Chinese Academy of Sciences (181722KYSB20200001), and National Natural Science Foundation of China (NSFC) (11973040).

Conflict of interest

The authors declare that the research was conducted in the absence of any commercial or financial relationships that could be construed as a potential conflict of interest.

Publisher's note

All claims expressed in this article are solely those of the authors and do not necessarily represent those of their affiliated organizations, or those of the publisher, the editors, and the reviewers. Any product that may be evaluated in this article, or claim that may be made by its manufacturer, is not guaranteed or endorsed by the publisher.

Supplementary material

The Supplementary Material for this article can be found online at: https://www.frontiersin.org/articles/10.3389/fspas.2023.1311323/full#supplementary-material

References

An, Q., Zhang Jingxu, 张., Yang Fei, 杨., Zhao Hongchao, 赵. (2016). Evaluation of the performance of large telescope based on normalized point source sensitivity. *Infrared Laser Eng.* 45, 1218001. doi:10.3788/irla20164512.1218001

Angeli, G. Z., Byoung-Joon, S., Carl, N., and Mitchell, T. (2011). A convenient telescope performance metric for imaging through turbulence. *Proc. SPIE - Int. Soc. Opt. Eng.* 8127. doi:10.1117/12.896919

Barr, L. D., Fox, J., Poczulp, G. A., and Roddier, C. A. (1990). Seeing studies on a 1.8-m mirror. *Adv. Technol. Opt. Telesc. IV* 1236. doi:10.1117/12.19220

Chen, L. S., and Hu, Z. W. (2016). The research on the application of normalized point source sensitivity in wide field optical spectrometer of the thirty meter telescope. *Acta Astron. Sin.* 57 (5), 585–596. doi:10.15940/j.cnki.0001-5245.2016.05.008

Cho, M., Corredor, A., Pootrakul, S., Vogiatzis, K., and Angeli, G. (2008). Thermal performance prediction of the TMT optics. *Model. Syst. Eng. Proj. Manag. Astronomy III* 7017, 369–381. SPIE. doi:10.1117/12.789212

Du, W., Liu, Y., Gao, W., and Hu, X. (2020). Analysis of passive athermalization structure design and integrated opto-mechanical-thermal of zoom lens of photoelectric

countermeasure platform. *Laser and Optoelectron. Prog.* 57 (13), 131204. doi:10.3788/lop57.131204

Lee, D.-O., Yoon, S.-H., and Han, J.-H. (2012). Integrated framework for jitter analysis combining disturbance, structure, vibration isolator and optical model. *Act. Passive Smart Struct. Integr. Syst.* 8341. SPIE. doi:10.1117/12.915428

Liu, R., Li, Z., Xu, W., Yang, X., Zhang, D., Yao, Z., et al. (2021). Dynamic analysis and experiment of a space mirror based on a linear state space expression. *Appl. Sci.* 11 (12), 5379. doi:10.3390/app11125379

McBride, I. I., William, R., Daniel, R., McBride, (2016). Using frequency response functions to manage image degradation from equipment vibration in the Daniel K. Inouye Solar Telescop. *Model. Syst. Eng. Proj. Manag. Astronomy VII* 9911. SPIE. doi:10.1117/12.2234316

Miyashita, A., Ogasawara, R., Takato, N., Kosugi, G., Takata, T., and Uraguchi, F. (2003). Temperature control for the primary mirror and seeing statistics of the Subaru Telescope. *Large Ground-based Telesc.* 4837. SPIE. doi:10.1117/12.458192

Pazder, J. S., Vogiatzis, K., and Angeli, G. Z. (2008). Dome and mirror seeing estimates for the thirty meter telescope. *Model. Syst. Eng. Proj. Manag. Astronomy III* 7017. SPIE. doi:10.1117/12.789636

Seo, B.-J., Nissly, C., Angeli, G., Ellerbroek, B., Nelson, J., Sigrist, N., et al. (2009a). Analysis of normalized point source sensitivity as a performance metric for large telescopes. *Appl. Opt.* 48 (31), 5997–6007. doi:10.1364/ao.48.005997

Seo, B.-J., Nissly, C., Angeli, G., MacMynowski, D., Sigrist, N., Troy, M., et al. (2009b). Investigation of primary mirror segment's residual errors for the Thirty Meter Telescope. *Opt. Model. Perform. Predict. IV* 7427. doi:10.1117/12.828046

Sobek, R. D. (2005). Mitigating wind induced telescope jitter. *Acquis. Track. Pointing XIX* 5810, 1–10. doi:10.1117/12.603963

Vogiatzis, K., and Angeli, G. Z. (2008). Monte Carlo simulation framework for TMT. *Model. Syst. Eng. Proj. Manag. Astronomy III* 7017. SPIE. doi:10.1117/12.787933

Yangx, X., Meng, H. R., Yin, Y. M., Wang, S., and Wu, Q. (2013). Jitter measurement for large opto-electronic telescope using accelerometers. *J. Electron. Meas. Instrum.* 27 (9), 823–830. doi:10.3724/sp.j.1187.2013.00823

Zhai, G., Yu, Q., Wang, Y., and Wei-jun, G. (2023). Real-time measurement for boresight vibration of dual line array surveying and mapping cameras. *Chin. Opt.* 16 (4), 878–888. doi:10.37188/co-2022-0175

frontiers | Frontiers in Astronomy and Space Sciences

TYPE Original Research
PUBLISHED 05 January 2024
DOI 10.3389/fspas.2023.1338284

OPEN ACCESS

EDITED BY
Hairen Wang,
Chinese Academy of Sciences (CAS), China

REVIEWED BY
Yuan Yu,
Huazhong University of Science and Technology, China
Lianbo Guo,
Huazhong University of Science and Technology, China

*CORRESPONDENCE
Bin Wang,
robin_hust@126.com
Ning Li,
ning-99@163.com

RECEIVED 14 November 2023
ACCEPTED 07 December 2023
PUBLISHED 05 January 2024

CITATION
Li F, Du J, Wang S, Yu R, Wang X, Zhang T, Chi Z, Wang B and Li N (2024), Ultra-broadband infrared metamaterial absorber based on MDMDM structure for optical sensing.
Front. Astron. Space Sci. 10:1338284.
doi: 10.3389/fspas.2023.1338284

Ultra-broadband infrared metamaterial absorber based on MDMDM structure for optical sensing

Fengjie Li[1], Jiansen Du[2], Shang Wang[3], Ruitao Yu[1], Xi Wang[4], Tiqiang Zhang[1], Zongtao Chi[1], Bin Wang[1]* and Ning Li[5]*

[1]College of Electronic Information, Micro-Nano Technology College, Qingdao University, Qingdao, China, [2]Qingdao International Travel Healthcare Center, Qingdao, China, [3]College of Science, North China Institute of Science and Technology, Yanjiao, China, [4]China Tobacco Shandong Qingdao Tobacco Co., Ltd., Logistics Center, Qingdao, China, [5]School of Basic Medicine, Qingdao University, Qingdao, China

Infrared observation is a crucial tool in the study of astronomical celestial bodies. Metamaterials have a vast prospect for applications in the field of optics due to their unique electromagnetic tunable characteristics. In order to obtain an ultra-broadband high absorption material in the infrared region, we proposed a metal-dielectric-metal-dielectric-metal (MDMDM) metamaterial absorber using a titanium (Ti) nano-cross layer based on surface plasmon polariton (SPP) resonance and magnetic resonance cavity principles. The geometrical parameters of each layer have been examined carefully. The influence of incident angle from 0° to 60° is investigated for transverse electric and transverse magnetic plane-waves. Near-perfect absorption performance is achieved from near-infrared to mid-infrared region. The average absorption reaches as high as 97.41% from 2.05 to 6.08 μm. The absorber exhibits polarization-sensitive characteristics. The absorption peaks are 99.50% and 99.80% at 2.55 and 5.24 μm, respectively. The proposed material has potential applications in astronomical imaging, volcano and fire detection, remote sensing, biological monitoring, and other optical devices.

KEYWORDS

metamaterials, broadband, absorber, infrared, imaging

1 Introduction

Metamaterial perfect absorbers (MPAs) are composite artificial structures with enhanced electromagnetic properties that are difficult to achieve with natural materials. Unlike traditional absorbers that rely on intrinsic absorption with low efficiency, MPAs exhibit broadband and high absorption characteristics that can be adjusted by changing the dimensions and shapes of the absorbers. Infrared observation is an essential method in astronomical research (Jakobsen et al., 2022). Astronomical observations play a crucial role in the study of celestial bodies (Gao et al., 2023). Infrared observations are crucial for studying low-temperature environments, such as star-forming regions with multiple dusty star clouds and the satellites and icy surfaces of planets within them. Changes in the star-forming regions enveloped by gases and dust can be detected by measuring the infrared wavelength,

TABLE 1 Comparison of published studies on near-infrared and mid-infrared light absorbers with this work.

References	Layers	Shape	Operating bandwidth	Absorption (%)
Li et al. (2022)	5	Nanorod	3.00–5.00 μm	86.00
Wu et al. (2023)	3	Embedded hemisphere	2.00–5.40 μm	93.50
Cao et al. (2021)	5	Spiral ITO structure	2.40–6.10 μm	85.00
			3.00–5.00 μm	96.00
This work	**5**	**Single cross**	**2.05–6.08 μm**	**97.41**
			3.00–5.00 μm	**97.54**

3–5 μm represents the entire mid-wave infrared.

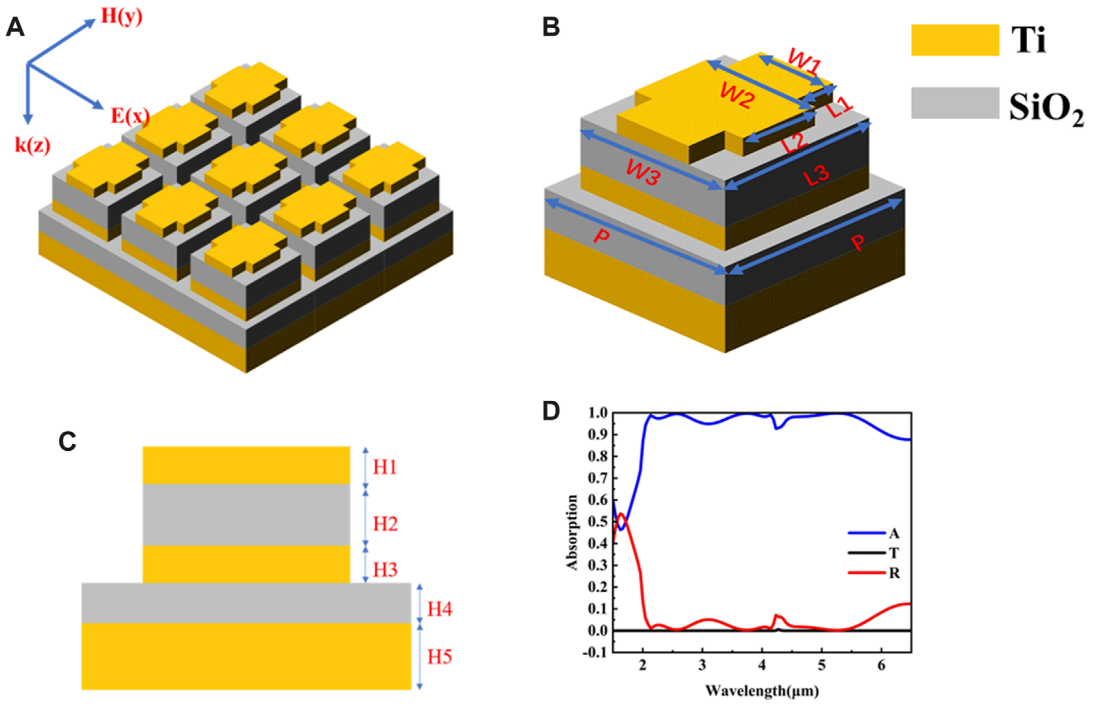

FIGURE 1
The structure and simulation results of proposed absorber. **(A)** The periodic array of the proposed absorber. **(B)** 3D view of the structural unit. **(C)** Side view of the structural unit. **(D)** The response of the proposed absorber with respect to absorption **(A)**, transmission (T) and reflection (R) for TE-polarized light.

providing insights into the ongoing processes (Hamilton et al., 2019). Utilizing the characteristics of metamaterials, broad-spectrum absorption in the infrared wavelength range can be achieved, holding significant importance for infrared astronomical observations.

MPAs have attracted significant attention due to their distinctive tunable properties. The development of nanotechnology has provided a greater range of metamaterial absorber applications. Landy et al. (2008) first proposed and implemented an experimental MPA in the microwave band. Subsequent research has resulted in the utilization of MPAs in various light wavebands: microwave (Zhang et al., 2019); ultraviolet (Zeng et al., 2021; Mehrabi et al., 2022; Takashima et al., 2022; Wang et al., 2022); visible (Yu et al, 2020a; Liu et al., 2020; Issah et al., 2021); infrared (Enoch et al., 2004; Wu et al, 2020a; Zhou et al., 2021; Shi et al., 2022; Wang et al., 2024); terahertz (Cong et al., 2015; Wang et al., 2019; Wu, 2020; Zheng et al., 2022). Due to the ultra-thin structure, broadband and high absorption capacities, MPAs have been widely used in imaging (Diem et al., 2009; Tittl et al., 2015; Zhang et al., 2024), sensing (Sabah et al., 2018), and solar energy collection (Yu et al, 2020b; Lin et al., 2020). Typical MPAs consist of a periodic array, a three-layer structure composed of metal-dielectric-metal (MDM). As a result of electromagnetic resonance, the high absorption shown by MDM occurs within a narrowband range (Cong et al., 2015). In recent years, researchers have been actively working to expand the bandwidth of absorbers. Arranging multi-shapes

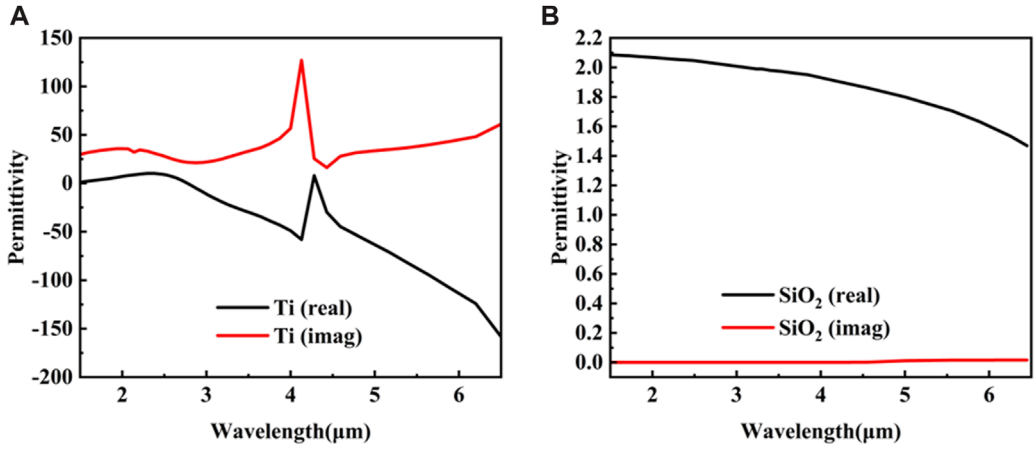

FIGURE 2
The permittivity values of materials **(A)** The permittivity values of Ti. **(B)** The permittivity values of SiO_2.

in the top layer represents a common approach to expanding bandwidth. Shobhit et al. proposed a metasurface solar absorber based on a $Ge_2Sb_2Te_5$ (GST) substrate (Patel et al., 2022). They adopted a square and a circle as the top-level periodic structure with a resultant absorption above 90% from ultraviolet to near-infrared band regions. Liang et al. (2022) designed a 4-layer ultra-broadband absorber with a second-order Peano fractal curve (PFC) metasurface; the average absorption reached 94.3%, with wavelengths ranging from 12.3 to 32 μm (Liang et al., 2022). Zheng et al. (2022) proposed a three-layer structure absorber with a VO_2 circular resonator, and explained the working principle in the basis of a distribution of the electric field. Following absorber optimization, the absorption was close to 100% at 3.7–9.7 THz. Due to resonance coupling of the horizontal plane, the bandwidth was greatly expanded. The design of a vertically-stacked resonator structure can enhance absorption. Wang et al. (2022) proposed an absorber integrated with metallic rings, where the associated average absorption exceeded 91% within the wavelength range 0.2–7 μm. Multilayer structures serve to expand the absorption bandwidth, as do the use of lumped-elements and plasmonic-nanocomposites.

The spectral band of the mentioned absorbers mainly focuses on terahertz, long-wave infrared, and visible light to near-infrared regions. There is currently limited reporting on wideband absorbers in the near-infrared to mid-infrared range. The near-infrared wideband absorption is not only applicable to environment detection (Wu et al, 2020b) but also can manage stray light and reduce interference. This is particularly crucial in optical communication systems, aiding in minimizing signal loss and maintaining signal integrity (Liu et al., 2022). The mid-infrared band is associated with thermal infrared remote sensing (Liu et al., 2021), infrared camouflage (Qin et al., 2022), and optical imaging (Zeng et al., 2018). The 2.50–5.00 μm range marks the beginning of the thermal infrared spectrum and is a crucial window for ground-based observations, encompassing the L and M bands. Multi-band infrared absorbers have a broader range of applications compared to single-band absorbers. However, achieving dual-band wideband high absorption poses a challenge due to the negative correlation between bandwidth and absorption rate. Li et al. (2022) designed a multi-layer nanorod structure to achieve full coverage absorption in the range of 3.00–5.00 μm. The absorption of their proposed absorber was only 86%. However, their research focuses only on the mid-infrared single band, and the absorption performance is relatively low. Wu et al. (2023) achieved an absorption efficiency of 93.5% in the 2.00–5.40 μm range by incorporating a metal (Ti) into the dielectric layer (Al_2O_3). The resultant absorber delivered excellent absorption performance from the near-infrared to the mid-infrared region, but the absorption rate still below 95%. In this study, we proposed an ultra-broadband metamaterial absorber consisting of a MDMDM (Ti-SiO_2-Ti-SiO_2-Ti) structure with a top-level periodic nano-cross shape. The absorption rate is 97.41% from 2.05 to 6.08 μm for light as a transverse electric (TE) plane-wave, with the wave perpendicular to the z direction and electrical field transmissions along the x direction. Moreover, Ti and SiO_2 are sufficiently abundant to facilitate widespread manufacturing. As shown in Table 1, in comparison to previous research on near-infrared and mid-infrared absorbers, our proposed absorber not only achieves dual-band infrared absorption in the near-infrared and mid-infrared regions but also demonstrates a significant improvement in bandwidth and absorption rate.

In Section 2, we introduced the detailed structure and materials of the proposed absorber. In Section 3, we analyzed the working principle of the absorber based on the impedance matching principle and surface plasmon resonance. The broadband absorption was analyzed by calculating the distribution of electromagnetic fields within the absorber. Multi-resonant coupling and multi-layer plasma resonance combine to extend bandwidth absorption. We investigated the impact of geometrical parameters on absorption performance. The polarization angle was studied. We also discussed the impact of various incident angles, from 0° to 60° for transverse electric (TE) polarized and transverse magnetic (TM) polarized light, on absorber performance. In Section 4, We made a conclusion.

TABLE 2 The parameter values of the absorber (μm).

W1	L1	W2	L2	W3 (L3)	P	H1	H2	H3	H4	H5
0.450	0.250	0.820	1.000	1.500	2.000	0.015	0.600	0.035	0.480	0.550

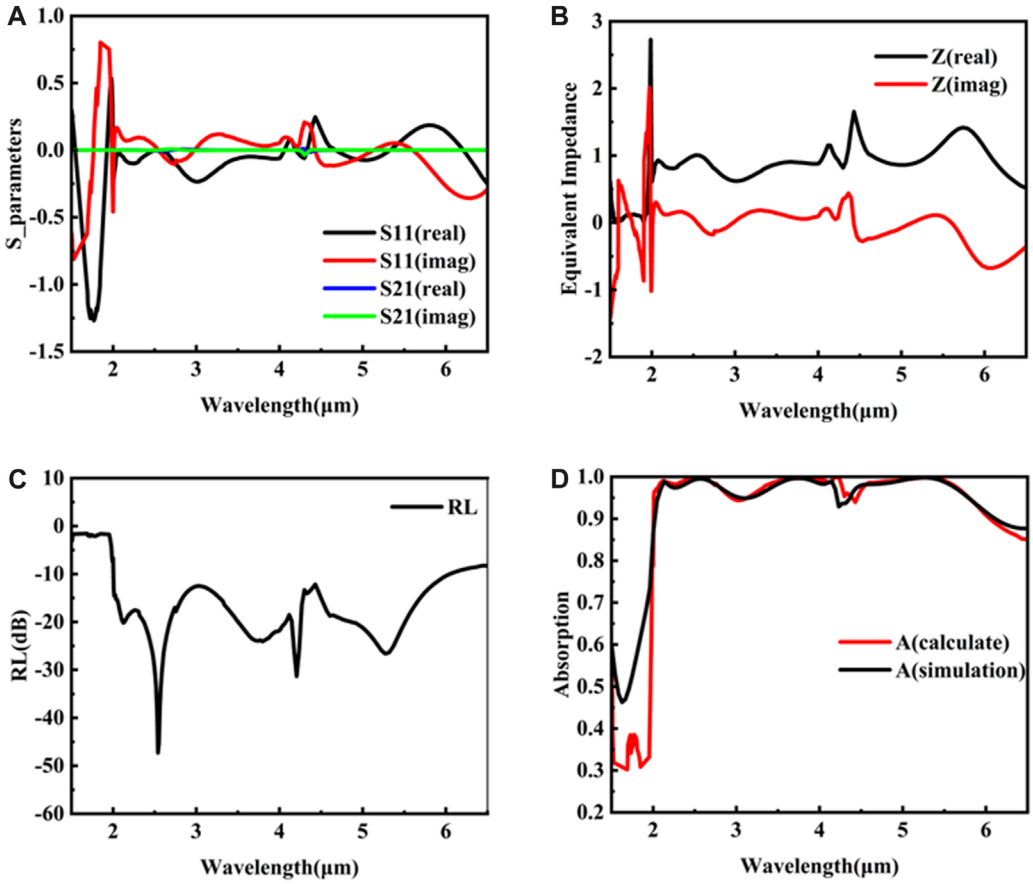

FIGURE 3
Numerical Calculation of Equivalent Impedance **(A)** the S parameter value of the proposed absorber. **(B)** Equivalent impedance value of the absorber. **(C)** Numerical calculation of the reflection loss of the absorber. **(D)**. Comparison of absorption between equivalent impedance calculation and simulation using the FDTD method.

2 Materials and methods

The structure of our proposed absorber is illustrated in Figure 1. The metamaterial absorber is composed of five layers. A Ti nano-cross structure appears on the top plane. The second layer is a SiO_2 square column (equal length and width). The third layer is a Ti square column, the fourth layer is a SiO_2 square column and the fifth layer is a Ti square column. Absorption can be represented by A = 1-T-R, where A, T, and R denote absorption, transmission, and reflection, respectively. The bottom metal layer is thick enough to prevent incident light from passing through the absorber. As the transmission is zero, absorption is given by A = 1−R.

In addition to the structure, the constituent materials also significantly impact the absorption. Ti is a metallic component, and SiO_2 serves as a dielectric material in our proposed absorber. In early research on the absorber, the metal layer employed high-Q factor noble metals (such as Ag and Au) resulting in excellent resonant selectivity within a specific wavelength range. The further development of absorber research incorporated other metals, including Ti, W, and Ni. In the near-infrared and mid-infrared regions, the imaginary permittivity of Ti contributes to broad absorption, improving absorptivity of the incident light and expanding the mid-infrared bandwidth. The incorporation of SiO_2 as the dielectric layer enhances the performance of the absorber. An ultrathin SiO_2 layer can realize broadband absorption at near-infrared and mid-infrared regions. Moreover, the permittivity of SiO_2 exerts an influence on intrinsic absorption which combines with plasmon resonance, and improves broadband absorption. The permittivity of both Ti and SiO_2 are taken from the handbook of Palik (Palik, 1997), as shown in Figure 2. The metamaterial absorber has been numerically simulated

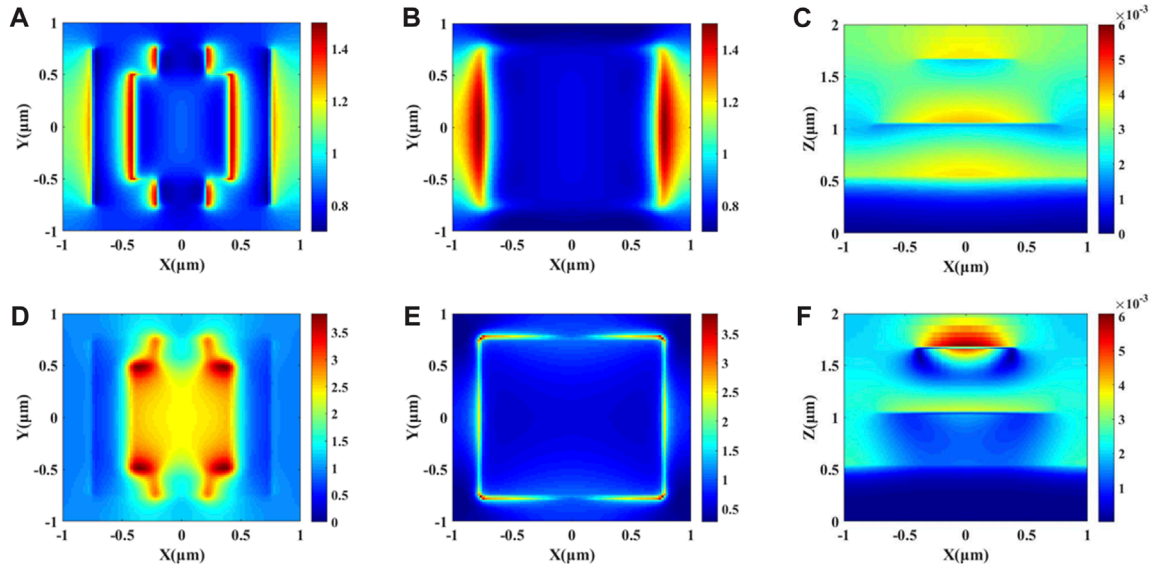

FIGURE 4
The electromagnetic field distribution at the absorption peaks. **(A–C)** the electromagnetic field distribution at 2.55 μm. **(A)** The electric-field distribution near the top-level nano-cross structure in the x-y plane. **(B)** The electric field distribution near the third Ti layer in the x-y plane. **(C)** The magnetic field distribution in the x-z plane. **(D–F)** The electromagnetic field distribution at 5.24 μm. **(D)** The electric field distribution near the top-level nano-cross structure in the x-y plane. **(E)** The electric field distribution near the third Ti layer in the x-y plane. **(F)** The magnetic field distribution in the x-z plane.

using the Finite-Difference Time-Domain (FDTD) method (Amedome Min-Dianey et al., 2019). In simulation calculations, the x-axis and y-axis boundaries were set periodically. Therefore, only a subunit calculation was required for photonic performance, which appreciably reduced the time and memory requirements. We used perfect-matched layers as a terminal condition for the z-axis which absorbed the incident electromagnetic field, equivalent to the field propagating unobstructed to infinity.

The absorber is illuminated perpendicularly by light with TE polarization, which simulates plane waves with oblique incidence using the Broadband Fixed Angle Source Technique (BFAST). We perform material data curve fitting on the data to ensure they converge with the actual situation. For the simulation conditions, we chose a 10 nm × 10 nm × 10 nm mesh size. In order to fulfill the future fabrication process, the brief preparation technique is proposed. First, the bottom Ti and SiO_2 films are deposited by physical vapor deposition (PVD) and plasma enhanced chemical vapor deposition (PECVD), respectively. Using the same PVD and PECVD deposition process, the middle Ti and SiO_2 patterns are developed by high resolution photolithography. In the last step, the cross Ti pattern is made with PVD and PECVD deposition and photolithography. This fabrication process is relatively simple.

3 Results and discussion

Figure 1D shows the result of absorption performance. The average absorption reaches as high as 97.41% from 2.05 to 6.08 μm. The Controlled Variables method is made to find out the optimized parameters after a lot of work. The parameters of our proposed absorber are shown in Table 2. The impedance matching principle can explain the absorption result. The equivalent impedance (Z) can be extracted using the S-parameter inversion technique (Smith et al., 2002); S11 represents the reflecting parameter in Eq. 1, S21 represents the transmitted parameter in Eq. 2, and Z is the equivalent impedance in Eq. 3. The S parameter for the proposed absorber is shown in Figure 3A. Figure 3B illustrates the equivalent impedance of the absorber in the wavelength range 2.05–6.08 μm, where the real part is close to 1 and the imaginary part is close to 0. In accordance with the principle of impedance matching (Mehrabi et al., 2022), it can be inferred that the incident light experiences minimal reflection back into free space within the 2.05–6.08 μm wavelength range. We also conduct numerical calculations to validate the accuracy of the results.

$$s_{11} = \frac{j}{2}\left(\frac{1}{z} - z\right)\sin(nkd) \tag{1}$$

$$s_{21} = \frac{1}{\cos(nkd) - \frac{j}{2}\left(z + \frac{1}{z}\right)\sin(nkd)} \tag{2}$$

$$z = \sqrt{\frac{(1+S_{11})^2 - S_{21}{}^2}{(1-S_{11})^2 - S_{21}{}^2}} \tag{3}$$

$$\Gamma = \frac{Z - Z_0}{Z + Z_0} \tag{4}$$

$$RL = 20\lg|\Gamma| \tag{5}$$

$$A = 1 - |\Gamma|^2 \tag{6}$$

Where Γ denotes the reflection coefficient in Eq. 4, Z_0 denotes the normalized value of the free-space impedance (Z_0 = 1), and

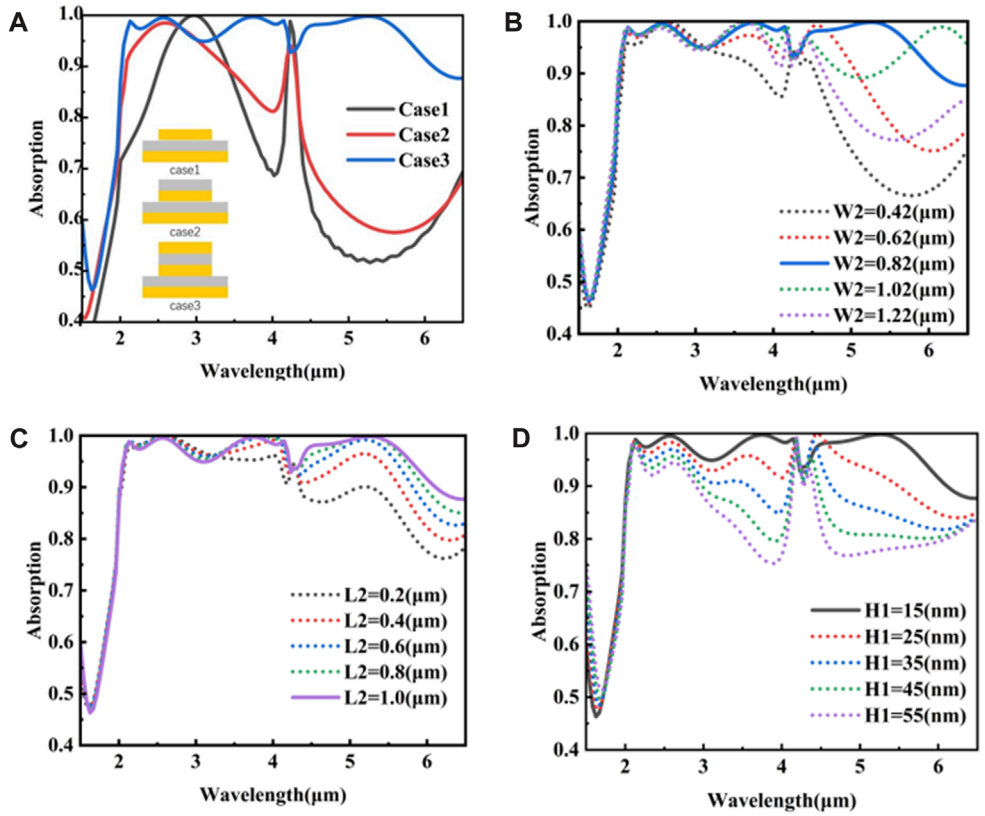

FIGURE 5
Influence of structure and parameters on absorption performance **(A)** absorption for the three structures. **(B)** Absorption where the width of the top Ti layer (W2) varies between 0.42 and 1.22 μm. **(C)** Absorption where the length of the top Ti layer (L2) varies between 0.2–1.0 μm. **(D)** Absorption where the height of the top Ti layer (H1) varies between 15 and 55 nm.

RL represents the reflection loss in Eq. 5. Absorption (A) can be determined from the equivalent impedance calculations in Eq. 6. As illustrated in Figure 3C, in the wavelength interval spanning 2.05 to 6.08 μm, RL falls below −10 dB, signifying an absorption exceeding 90%. In Figure 3D, the simulation results for absorbance closely align with those derived from the equivalent impedance computations. The equivalent impedance treats the absorber as a unified entity, disregarding the specific contributions of individual layers. Consequently, this approach can lead to deviations between calculated and simulated outcomes. However, the two curves representing equivalent impedance calculation and simulation fit very well. This level of agreement serves as verification for the high absorption characteristics obtained from simulation.

The performance of absorbers has a bearing on the electromagnetic field. There are many free electrons in the metal that participate in collective resonance under the influence of the light wave electromagnetic field when light impinges on the inner surface of the metal and dielectric. Surface plasmon polariton (SPP) resonance can be excited when the oscillation frequency of free electrons couples with the incident light. It contributes to a strong absorption performance, and exhibits an enhanced electric field. The metal layer generates ohmic loss, converting the energy of the incident light to thermal energy for electron motion, which augments absorption performance. The metal-dielectric-metal absorber can be regarded as a magnetic resonance cavity composed of a closed magnetic wall. The upper and lower metal layers serve as parallel mirrors. The incident light is reflected by the lower metal when the light enters the absorber from the upper metal and then passes through the middle dielectric layer. The incident light from the upper layer interferes with the reflected light from the lower layer, forming a closed magnetic resonance cavity within the middle dielectric layer.

In order to elucidate the spectral absorption process, we analyzed the electromagnetic field distribution within the absorber corresponding to two absorption peaks. The incident light is a TE wave perpendicular to the z-axis, where the electromagnetic field distribution demonstrates the absorption principle presented in Figure 4. As depicted in Figures 4A, B for 2.55 μm, the electric field is present in proximity to both the upper and third Ti layer. This indicates that SPP resonance occurs in the metal-dielectric inner surface. There is a strong electric field in the y direction, indicating that the y direction of the nano-cross structure exhibits multi-resonant coupling. Figure 4C reveals a magnetic field enhancement in the magnetic resonance cavity of the second layer. This suggests that the first metal layer, the second dielectric layer, and the third metal layer form a closed magnetic resonance cavity. Multiple reflections and interferences of the incident light occur within the magnetic resonance cavity. The electrical loss of SPP resonance

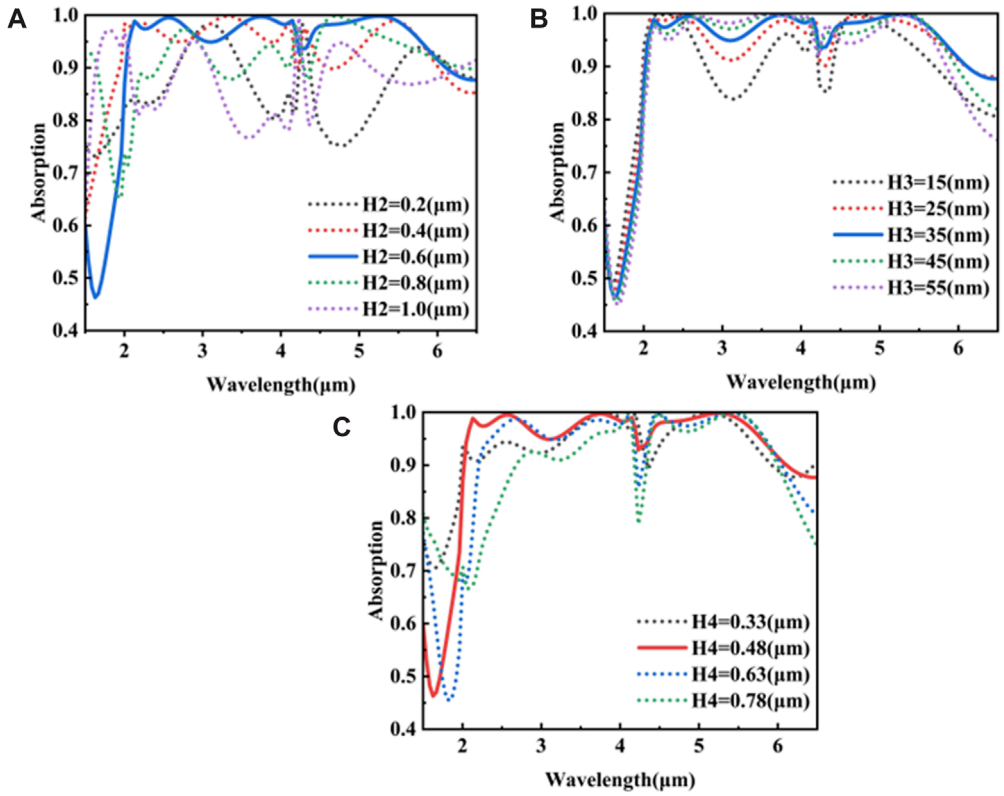

FIGURE 6
Impact of thickness on absorption performance **(A)** absorbance where the thickness of second SiO_2 layer (H2) changes from 0.2 to 1.0 μm. **(B)** Absorbance where the thickness of third Ti layer (H3) changes from 15 to 55 nm. **(C)** Absorbance where the thickness of fourth Ti layer (H4) changes from 0.33 to 0.78 μm.

and the magnetic loss of the magnetic resonance cavity jointly serve to enhance absorption. The distribution of the electric field enhancement near the top layer of the Ti nano-cross structure for a 5.24 μm wavelength is shown in Figures 4D, E. There is an electric field enhancement, indicating multi-resonant coupling in the first layer. An electric-field enhancement also occurs in the third Ti layer. As illustrated in Figure 4F, the magnetic field is primarily confined at the boundary between the uppermost layer and the airspace above it, as well as between the second SiO_2 dielectric layer and the third Ti layer. This suggests that the magnetic resonance cavity is no longer the primary contributor to absorption. At long wavelengths, local plasmon resonance caused by the top cross resonant structure contributes to absorption with an additional contribution due to the local plasmon resonance excited in the third layer.

We discussed the impact of the structure and parameters on the absorption performance. As shown in Figure 5A, Case 1 is a traditional metal-dielectric-metal (MDM) three-layer absorber, where the average absorption reaches 73.27% within the wavelength range of 2.05–6.08 μm. Case 2 adds a SiO_2 dielectric layer above the absorber, resulting in an average absorption of 78.67%. The added SiO_2 is a loss dielectric that can undergo intrinsic absorption with a resultant slightly higher absorption compared to Case 1. Case 3 represents our proposed 5-layer nano-cross structure that exhibited an absorption of 97.41% in the infrared band, representing a significant improvement. The top-level nano-cross pattern leads to the excitation of multiple resonators and the generation of a new MDM magnetic resonance cavity. The additional resonant cavity and multiple resonators at the top layer contribute to the enhanced performance. Focusing on the nano-cross top layer, we investigated the influence of essential size parameters on absorption. We considered an increase in W2 from 0.42 to 1.22 in incremental 0.2 μm intervals. As shown in Figure 5B, the absorption increases with an increase in W2 from 0.42 to 0.82 μm within the wavelength range of 2.05–6.08 μm. The absorption is found to decrease when the W2 value increases from 0.82 to 1.22 μm. It indicates that an excessively high or low values of W2 weaken the resonant coupling of the top nano-cross structure and the surface plasmon resonance, lowering absorption. As shown in Figure 5C, an increase in L2 from 0.20 to 1.00 μm (in steps of 0.2 μm) is accompanied by an average absorption increase from 91.97% to 97.41%. An electric field enhancement occurs in the y direction of the top nano-cross structure, where surface plasmon resonance and resonator coupling are the main factors determining broadband absorption. The increase in L2 contributes to an enhanced electric field, in tandem with surface plasmon resonance and resonator coupling, resulting in improved absorption in the infrared band. The results presented in Figure 5D indicate that an increase in H1 from 15

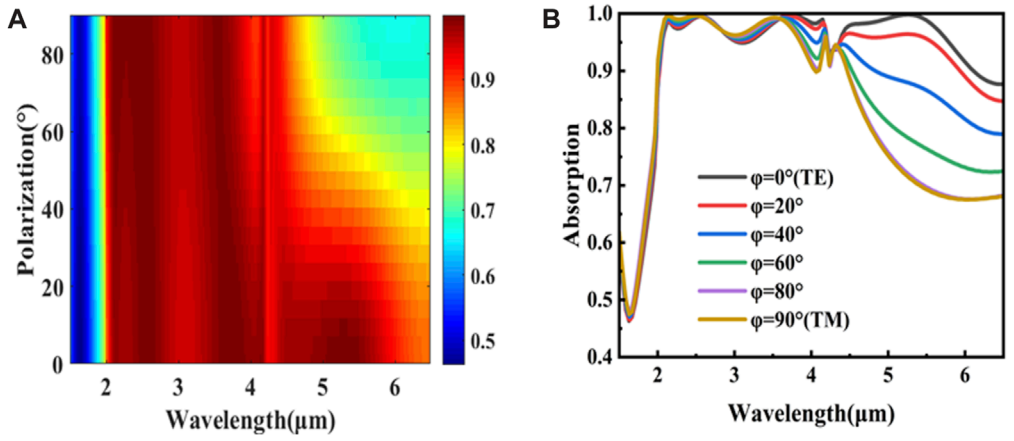

FIGURE 7
Influence of polarization angle on absorption performance **(A,B)** absorption at various polarization angles from 0° to 90°.

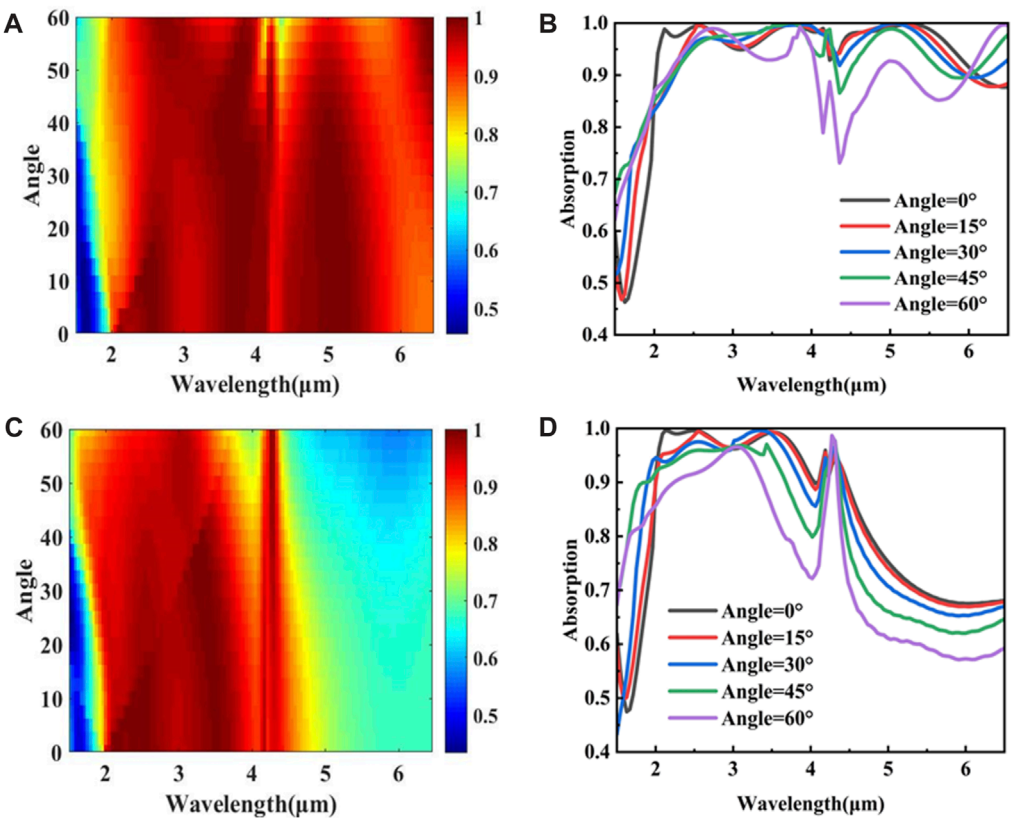

FIGURE 8
Impact of incidence angle on absorption performance **(A,B)** absorption at various angles for TE polarization modes. **(C,D)** Absorption at various angles for TM polarization modes.

to 55 nm (in steps of 10 nm) results in an average absorption decrease from 97.41% to 81.83%. Compared with L2 and W2, alterations in H1 exert a more substantial impact on absorption performance with a greater overall impact on the top-level nano-cross structure.

Other structural parameters also have a considerable effect on absorption. As shown in Figure 6A, an increase in H2 from 0.2 to 0.6 μm (in steps of 0.2 μm) serves to increase the average absorption from 87.05% to 97.41% within the wavelength range 2.05–6.08 μm. An additional rise from 0.6 to 1.0 μm results in a reduction in absorption to 85.61%. The change in H2 impacts on the phase of plane light entering the MDM resonant cavity, affecting the reflection interference. If H2 either is too large or too small, it weakens the effect of the resonant cavity, causing the

incident light to reflect off the absorber with a consequent reduction in absorption. The change in H2 has an appreciable influence on absorption performance in wavelength range 2.05–6.08 μm. As shown in Figure 6B, following a change in H3 from 15 to 55 nm (in steps of 10 nm) within the wavelength range of 2.05–4.00 μm there is no major difference in absorption performance. Moreover, changes in H3 result in a negligible effect on absorption at 4.0–6.08 μm. Considering the distribution of electromagnetic fields, the third Ti layer mainly exhibits electric field enhancement at short wavelengths. At longer wavelengths, the surface plasmon resonance of the top Ti layer principally improves absorption performance with a small contribution from Ti in the third layer. The results presented in Figure 6C illustrate that an increase in H4 from 0.33 to 0.78 μm (in steps of 0.15 μm) mainly affects absorption within the wavelength 2.05–4.00 μm. An enhanced magnetic field in the fourth layer (SiO_2) forms a magnetic resonance cavity but the enhancement gradually disappears with an increase in wavelength from 2.05 to 6.08 μm. The contribution of the fourth dielectric layer to absorption also gradually weakens. Through parameter analysis, we conclude that the resonator coupling of the top layer nano-cross structure contributes to absorption. The multi-layer structure generates multi-layer surface plasmon resonances and multiple magnetic resonance cavities that contribute to the broadband high absorption.

The absorption spectra where the polarization angle (φ) of the absorber is varied from 0° to 90° are presented in Figure 7. Absorption within the wavelength range 2.05–4.35 μm is minimally affected by variations in φ. The absorption spectrum is sensitive to φ in the range 4.30–6.08 μm. As the polarization angle increases from 0° to 90°, the average absorption within the infrared range decreases from 97.41% to 91.43%. This response that can be attributed to non-rotational symmetry, which impacts on the resonant coupling of the absorber. The wide-angle characteristic of absorbers is important in many practical applications. We have investigated the effect of angle on absorption in both TE and TM polarization modes. The absorption spectrum is presented in Figure 8 where the wavelengths ranged from 2.05 to 6.08 μm for TE and TM polarization with the incidence angle (θ) varying in 10° steps between 0° and 60°. As shown in Figures 8A, B, the average absorption decreases to 90.91% for a wavelength of 2.05–6.08 μm when θ is raised to 60° under TE polarization. The average absorption drops from 87.45% to 76.92% under TM polarization (Figures 8C, D) as θ is varied from 0° to 60° within the 2.05–6.08 μm wavelength band. The components of the electromagnetic field in various directions show significant changes due to the increase of incident angle. Enhancing the anisotropy of the incident light results in a more pronounced scattering of light (Mehrabi et al., 2022), which can account for the gradual decrease of absorption with an increase in θ. Our results demonstrate that the proposed absorber possesses wide-angle properties in the infrared region.

4 Conclusion

An ultra-broadband metamaterial absorber with a Ti nano-cross layer is proposed. Both the horizontal and vertical structural elements contribute to the enhanced absorption exhibited by the proposed absorber. The absorber generates multiple effects that contribute to enhancing the absorption of incident light. The absorption mechanism has been revealed through an analysis of the electromagnetic field distribution. The effects of SPP resonance and the magnetic resonance cavity contribute to an ultra-broadband absorption from 2.05 to 6.08 μm. We have demonstrated how the multi-layer structure affects absorption and have considered the role of geometrical parameters. The level of absorption decreases from 97.41% to 90.22% in the case of TE polarized incident light varying from 0° to 60° in the infrared region. The average absorption drops from 87.45% to 76.92% when varying θ from 0° to 60° at 2.05–6.08 μm under TM polarization. We have combined the advantages of horizontal multi-resonators and vertically stacked structures to broaden the absorption bandwidth. The proposed absorber possesses a simple nano-cross structure on the top layer and a total of only five layers. Our proposed absorber demonstrates remarkable absorption performance in the infrared region, making it applicable to various optical devices, including infrared imaging and celestial body observation in astronomy.

Data availability statement

The original contributions presented in the study are included in the article/Supplementary Material, further inquiries can be directed to the corresponding authors.

Author contributions

FL: Investigation, Writing–original draft, Writing–review and editing. JD: Software, Writing–review and editing. SW: Methodology, Writing–review and editing. RY: Data curation, Writing–review and editing. XW: Validation, Writing–review and editing. TZ: Writing–review and editing. ZC: Project administration, Writing–review and editing. BW: Visualization, Writing–original draft, Writing–review and editing. NL: Writing–review and editing.

Funding

The author(s) declare financial support was received for the research, authorship, and/or publication of this article. This work was supported by the Qingdao Postdoctoral Application Research Project, the Chinese Ministry of Education's Industry School Cooperation Collaborative Education project: 220606513074515, and the National Key Research and Development Program of China (2022YFC2302800).

Conflict of interest

Author XW was employed by China Tobacco Shandong Qingdao Tobacco Co., Ltd., Logistics Center.

The remaining authors declare that the research was conducted in the absence of any commercial or financial relationships that could be construed as a potential conflict of interest.

Publisher's note

All claims expressed in this article are solely those of the authors and do not necessarily represent those of their affiliated organizations, or those of the publisher, the editors and the reviewers. Any product that may be evaluated in this article, or claim that may be made by its manufacturer, is not guaranteed or endorsed by the publisher.

Supplementary material

The Supplementary Material for this article can be found online at: http://www.frontiersin.org/articles/10.3389/fspas.2023.1338284/full#supplementary-material

References

Amedome Min-Dianey, K. A., Sanogo, D., M'Bouana, N. L. P., and Zhang, H. C. (2019). Angular dependence in light propagation through silver material based ultra-compact photonic crystal. *Opt. Mater.* 91, 1–6. doi:10.1016/j.optmat.2019.03.002

Cao, B. W., Li, C., Shi, W. J., Han, C. Q., Wu, Y., and Yan, C. C. (2021). Large-area mid-infrared broadband absorbers based on spiral ITO resulting from the combination of two different broadening absorption methods. *Opt. Express* 29, 34427–34440. doi:10.1364/OE.440535

Cong, L., Tan, S., Yahiaoui, R., Yan, F., Zhang, W., and Singh, R. (2015). Experimental demonstration of ultrasensitive sensing with terahertz metamaterial absorbers: a comparison with the metasurfaces. *Appl. Phys. Lett.* 106. doi:10.1063/1.4906109

Diem, M., Koschny, T., and Soukoulis, C. M. (2009). Wide-angle perfect absorber/thermal emitter in the terahertz regime. *Phys. Rev. B* 79, 033101. doi:10.1103/PhysRevB.79.033101

Enoch, S., Quidant, R., and Badenes, G. (2004). Optical sensing based on plasmon coupling in nanoparticle arrays. *Opt. Express* 15, 3422–3427. doi:10.1364/OPEX.12.003422

Gao, J. J., Wang, H. R., Zuo, Y. X., Yang, J., Chen, X. P., Zhang, M. Z., et al. (2023). Modeling and analysis of the active surface system for the large single-dish sub-mm telescope. *IEEE Trans. Antennas Propag.* 71, 225–235. doi:10.1109/TAP.2022.3218746

Hamilton, V. E., Simon, A. A., Christensen, P. R., Reuter, D. C., Clark, B. E., Barucci, M. A., et al. (2019). Evidence for widespread hydrated minerals on asteroid. *Bennu* 4, 332–340. 101955. doi:10.1038/s41550-019-0722-2

Issah, I., Li, F., Baah, M., Otoo, I. A., Asilevi, L., Bawuah, P., et al. (2021). Passive tunable and polarization-insensitive fan-like metamaterial absorber in the visible spectrum. *J. Opt. Soc. Am. B* 38, C1. doi:10.1364/josab.426441

Jakobsen, P., Ferruit, P., Alves de Oliveira, C., Arribas, S., Bagnasco, G., Barho, R., et al. (2022). The near-infrared spectrograph (NIRSpec) on the james webb space telescope I. Overview of the instrument and its capabilities. *Astronomy Astrophysics* 661, A80. doi:10.1051/0004-6361/202142663

Landy, N. I., Sajuyigbe, S., Mock, J. J., Smith, D. R., and Padilla, W. J. (2008). Perfect metamaterial absorber. *Phys. Rev. Lett.* 100, 207402. doi:10.1103/PhysRevLett.100.207402

Li, L., Cui, Q., Zhang, Y. J., Wu, Y., Han, C. Q., and Yan, C. C. (2022). Visible transparent mid-infrared broadband absorbers based on gradient refractive indexes and multi-size cavity resonances. *Opt. Express* 30, 43078–43087. doi:10.1364/OE.473986

Liang, Y., Liu, X., Xin, J., Zhang, X., Wang, Y., and Song, Y. (2022). Ultra-broadband long-wave infrared metasurface absorber based on Peano fractal curve. *Results Phys.* 33, 105169. doi:10.1016/j.rinp.2021.105169

Lin, K. T., Lin, H., Yang, T., and Jia, B. (2020). Structured graphene metamaterial selective absorbers for high efficiency and omnidirectional solar thermal energy conversion. *Nat. Commun.* 11, 1389. doi:10.1038/s41467-020-15116-z

Liu, J., Ma, W. Z., Chen, W., Chen, Y. S., Deng, X. C., and Gu, Y. (2021). A metamaterial absorber based on particle swarm optimization suitable for earth's atmospheric transparency window. *IEEE Access* 9, 92941–92951. doi:10.1109/ACCESS.2021.3089895

Liu, J., Ma, W. Z., Chen, W., Yu, G. X., Chen, Y. S., Deng, X. C., et al. (2020). Numerical analysis of an ultra-wideband metamaterial absorber with high absorptivity from visible light to near-infrared. *Opt. Express* 28, 23748–23760. doi:10.1364/OE.399198

Liu, W. J., Xiong, X. L., Liu, M. L., Xing, X. W., Chen, H. L., Ye, H., et al. (2022). Bi4Br4-based saturable absorber with robustness at high power for ultrafast photonic device. *Appl. Phys. Lett.* 120, 5. doi:10.1063/5.0077148

Mehrabi, S., Bilal, R. M. H., Naveed, M. A., and Ali, M. M. (2022). Ultra-broadband nanostructured metamaterial absorber based on stacked square-layers of TiN/TiO_2. *Opt. Mater. Express* 12, 2199. doi:10.1364/ome.459766

Palik, E. D. (1997). *Handbook of optical constants of solids*. China: Academic Press.

Patel, S. K., Parmar, J., Katkar, V., Al-Zahrani, F. A., and Ahmed, K. (2022). Ultra-broadband and polarization-insensitive metasurface absorber with behavior prediction using machine learning. *Alexandria Eng. J.* 61, 10379–10393. doi:10.1016/j.aej.2022.03.080

Qin, Z., Zhang, C., Liang, Z. Z., Meng, D. J., Shi, X. Y., and Yang, F. M. (2022). Thin multispectral camouflage absorber based on metasurfaces with wide infrared radiative cooling window. *Adv. Photonics Res.* 3, 5. doi:10.1002/adpr.202100215

Sabah, C., Mulla, B., Altan, H., and Ozyuzer, L. (2018). Cross-like terahertz metamaterial absorber for sensing applications. *Pramana-Journal Phys.* 2, 17. doi:10.1007/s12043-018-1591-4

Shi, X., Hou, E., Liang, Z., Zhang, S., Dai, R., Xin, W., et al. (2022). Broadband metamaterial absorber based on hybrid multi-mode resonance in mid-wave and long-wave infrared region. *Results Phys.* 42, 105972. doi:10.1016/j.rinp.2022.105972

Smith, D. R., Schultz, S., Markoš, P., and Soukoulis, C. M. (2002). Determination of effective permittivity and permeability of metamaterials from reflection and transmission coefficients. *Phys. Rev. B* 65, 195104. doi:10.1103/PhysRevB.65.195104

Takashima, Y., Nagamatsu, K., Haraguchi, M., and Naoi, Y. (2022). Ultra-thin deep ultraviolet perfect absorber using an Al/TiO(2)/AlN system. *Opt. Express* 30, 44229–44239. doi:10.1364/OE.474847

Tittl, A., Michel, A. K., Schaferling, M., Yin, X., Gholipour, B., Cui, L., et al. (2015). A switchable mid-infrared plasmonic perfect absorber with multispectral thermal imaging capability. *Adv. Mater* 27, 4597–4603. doi:10.1002/adma.201502023

Wang, B., Ma, C., Yu, P., Govorov, A. O., Xu, H., Wang, W., et al. (2022). Ultra-broadband nanowire metamaterial absorber. *Photonics Res.* 10, 2718. doi:10.1364/prj.473332

Wang, B. X., Tang, C., Niu, Q., He, Y., and Chen, T. (2019). Design of narrow discrete distances of dual-/triple-band terahertz metamaterial absorbers. *Nanoscale Res. Lett.* 14, 64. doi:10.1186/s11671-019-2876-3

Wang, S., Du, J., Chi, Z., Coong, H., and Wang, B. (2024). Ultra-broadband metamaterial absorber in the far infrared. *Mater. Lett.* 355, 135518. doi:10.1016/j.matlet.2023.135518

Wu, B., Liu, Z., Du, G., Chen, Q., Liu, X., Fu, G., et al. (2020b). Polarization and angle insensitive ultra-broadband mid-infrared perfect absorber. *Phys. Lett. A* 384, 126288. doi:10.1016/j.physleta.2020.126288

Wu, J. (2020). A polarization insensitive dual-band tunable graphene absorber at the THz frequency. *Phys. Lett. A* 384, 126890. doi:10.1016/j.physleta.2020.126890

Wu, P. H., Wang, Y. Y., Yi, Z., Huang, Z., Xu, Z. S., and Jiang, P. P. (2020a). A near-infrared multi-band perfect absorber based on 1D gold grating fabry-perot structure. *IEEE Access* 8, 72742–72748. doi:10.1109/ACCESS.2020.2983394

Wu, Z., Liang, Z., Shi, X., Yang, F., Dai, R., Hou, E., et al. (2023). Broadband and energy-concentrated absorber based on hemispherical-embedded structure. *Adv. Photonics Res.* 4. doi:10.1002/adpr.202200301

Yu, P., Yang, H., Chen, X., Yi, Z., Yao, W., Chen, J., et al. (2020b). Ultra-wideband solar absorber based on refractory titanium metal. *Renew. Energy* 158, 227–235. doi:10.1016/j.renene.2020.05.142

Yu, Y., Yu, Z., and Sun, X. (2020a). Nonmetallic broadband visible-light absorbers with polarization and incident angle insensitivity. *IEEE Photonics J.* 12, 1–7. doi:10.1109/jphot.2020.3029213

Zeng, B. B., Huang, Z. Q., Singh, A., Yao, Y., Azad, A. K., Mohite, A. D., et al. (2018). Hybrid graphene metasurfaces for high-speed mid-infrared light modulation and single-pixel imaging. *Light. Sci. Appl.* 7, 51. doi:10.1038/s41377-018-0055-4

Zeng, L., Zhang, X., Ye, H., Dong, H., and Zhang, H. (2021). Design of ultra-broadband absorption enhancement in plasmonic absorber by interaction resonance of multi-plasmon modes and Fabry-Perot mode. *Opt. Express* 29, 29228–29241. doi:10.1364/OE.440172

Zhang, H. B., Du, J. S., Chi, Z. T., Cong, H. L., and Wang, B. (2024). Numerical design of a dual-wavelength confocal metalens with photonic crystal filter based on filter-substrate-metasurface structure. *Opt. Commun.* 554, 130157. doi:10.1016/j.optcom.2023.130157

Zhang, K. L., Zhang, J. Y., Hou, Z. L., Bi, S., and Zhao, Q. L. (2019). Multifunctional broadband microwave absorption of flexible graphene composites. *Carbon* 141, 608–617. doi:10.1016/j.carbon.2018.10.024

Zheng, Z., Luo, Y., Yang, H., Yi, Z., Zhang, J., Song, Q., et al. (2022). Thermal tuning of terahertz metamaterial absorber properties based on VO(2). *Phys. Chem. Chem. Phys.* 24, 8846–8853. doi:10.1039/d2cp01070d

Zhou, Y., Qin, Z., Liang, Z., Meng, D., Xu, H., Smith, D. R., et al. (2021). Ultra-broadband metamaterial absorbers from long to very long infrared regime. *Light Sci. Appl.* 10, 138. doi:10.1038/s41377-021-00577-8

frontiers | Frontiers in Astronomy and Space Sciences

TYPE Original Research
PUBLISHED 06 March 2024
DOI 10.3389/fspas.2024.1374951

OPEN ACCESS

EDITED BY
Hairen Wang,
Chinese Academy of Sciences (CAS), China

REVIEWED BY
Yuan Yu,
Chinese Academy of Sciences (CAS), China
Chunling Ding,
Wuhan Institute of Technology, China

*CORRESPONDENCE
Bin Wang,
robin_hust@126.com
Ning Li,
ning-99@163.com

RECEIVED 23 January 2024
ACCEPTED 19 February 2024
PUBLISHED 06 March 2024

CITATION
Li F, Wang S, Chi Z, Zhang T, Yu R, Wang B and Li N (2024), High-performance absorber with substitutable materials for short-wave infrared sensing.
Front. Astron. Space Sci. 11:1374951.
doi: 10.3389/fspas.2024.1374951

High-performance absorber with substitutable materials for short-wave infrared sensing

Fengjie Li[1], Shang Wang[2], Zongtao Chi[1], Tiqiang Zhang[1], Ruitao Yu[1], Bin Wang[1]* and Ning Li[1]*

[1]College of Electronic Information, School of Basic Medicine, Micro-Nano Technology College, Qingdao University, Qingdao, China, [2]College of Science, North China Institute of Science and Technology, Yanjiao, China

The optical absorption device plays a crucial role as a component of the infrared astronomical telescope and possesses a significant impact on astronomical observations. A simple metamaterial absorber with substitutable middle materials is made for short-wave infrared sensing. The absorber is designed as a hollow square column, using a patterning approach for the top-layer structure of metamaterials. The absorption characteristics are verified using the impedance matching method, which involves extracting S-parameters and then performing inverse calculations to determine the absorber's equivalent impedance. The result shows the highest absorption peak is at 3.25 μm, reaching 99.71%, with an impressive average absorption rate of 99.01% between 1.52 and 3.66 μm. The results demonstrate that this absorber shows polarization insensitivity while maintaining high absorption even at large angles of incidence. The distribution of the electromagnetic field within the absorber, the electromagnetic losses within individual layers, and their impact on the absorptive performance are analyzed in detail. Polarization angles, transverse magnetic polarization, and transverse electric polarization are further explored. The parameters of each layer have been discussed. An investigation of the intermediate dielectric layer has been conducted. The proposed absorber shows the potential to achieve exceptional absorption performance under various dielectric conditions, rendering it a promising candidate for use in astronomical observation, medical tests, infrared detection, invisible short-wave infrared systems, radar and various optical devices.

KEYWORDS

infrared, absorber, broadband, optical, astronomical

1 Introduction

The infrared telescope plays a crucial role in astronomical observation. (Honniball et al., 2022; Jakobsen et al., 2022). Infrared detection equipment assists researchers in discovering previously unknown stars, planets, and galaxies, as well as studying cosmic dust clouds and interstellar matter. As a crucial element of infrared detection equipment, the infrared absorber must not only possess high sensitivity, but also adhere to strict requirements regarding size, material and other factors. Metamaterials are a category of artificial composite materials with a subwavelength size (Bertoldi et al., 2017). In contrast to natural absorptive materials, metamaterials not only possess ultra-thin characteristics but also relatively small unit sizes. Metamaterial perfect absorbers (MPAS)

can achieve exceptional electromagnetic characteristics by manipulating their shape, structural parameters, and periodic arrangement. This resolves the constraints imposed by the inherent electromagnetic properties of materials. Owing to advancements in nanotechnology, research on metamaterials has made significant progress and has attracted increasing public interest in recent years. Light plays a pivotal role in our lives. The understanding and investigation of light have significantly deepened alongside the advancements in science and technology. Maxwell's equations reveal that light is a special form of electromagnetic wave from a mathematical perspective (Bliokh et al., 2016). The theoretical framework of electromagnetic waves has advanced significantly. Employing electromagnetic theory to investigate and explain optical phenomena has emerged as a reliable and effective methodology. MPAS demonstrate outstanding electromagnetic tunability and have garnered considerable attention in the field of optics.

In 2008, Landy and colleagues pioneered the design and implementation of MPAS within the millimeter-wave range (Landy et al., 2008). Over the last decade, many researchers have shown significant interest in the optical absorption properties of MPAS. The spectral research range of MPAS has been further expanded to include visible light (Cao et al., 2014; Lin et al., 2019), near-infrared (Ding et al., 2016; Lei et al., 2018), mid-infrared (Ma et al., 2013; Zhao et al., 2021; Li et al., 2023; Zhang et al., 2024), long-wavelength infrared (Ruan et al., 2021; Qin et al., 2022; Wang et al., 2024), terahertz (Liu and Song, 2021; Wang et al., 2022), and microwave (Hou et al., 2021; Xu et al., 2021) bands. Metamaterials have a wide range of applications in multiple fields, including solar energy absorption (Lin et al., 2020), filters (McCrindle et al., 2013), and imaging (Fan et al., 2017). Infrared sensors are an important component of thermal imagers and they can be used for military night vision reconnaissance (Gade and Moeslund, 2013). Infrared sensors can be used to detect biomolecules and prevent diseases, making them widely applicable in the medical field (Aslan et al., 2017). Infrared sensors can also be utilized for detecting combustion systems and are commonly employed in industrial settings (Goldenstein et al., 2017). As technological capabilities advance, the limitations of narrowband absorption are no longer sufficient to meet the demands of applications such as infrared detection and radar technology. In recent years, numerous research reports in the field of metamaterials have focused on achieving broadband absorption. Employing multilayer structures through stacking is an effective method for enhancing the absorption performance of MPAS. Su et al. utilized a combination of graphene and MgF_2 as a set of materials and integrated them into a multilayer structure, leading to the attainment of high broadband absorption in the terahertz band (Su et al., 2015). They explained the importance of electromagnetic resonance in the absorption of light energy by analyzing the distribution of the electromagnetic field. Liu et al. employed tungsten nanospheres in conjunction with SiO_2 as a set of materials for a metal-dielectric stack (Liu et al., 2017). They vertically assembled eight sets of metal-dielectric materials, achieving an absorption rate exceeding 90% across the visible light and near-infrared spectral ranges. The high absorption performance primarily arises from the presence of surface plasmon resonance and multilayer Fabry-Pérot (F-P) resonance cavities. Zou et al. employed a traditional metal-dielectric-metal structure with the Gosper curve as the top periodic pattern (Zou et al., 2020). The multi-size resonant coupling of the top periodic structure excites electric resonances at multiple wavelengths, resulting in high broadband absorption within the mid-infrared spectrum. Li et al. introduced a classic metal-insulator-metal (Cr-Al_2O_3-W) MIM structure (Li et al, 2022). The average absorption is 94.84% from 800 nm to 3,000 nm. The top layer featured a set of four metal rings, each of varying in size, used as periodic structures. The analysis of the electromagnetic field distribution reveals that localized plasmon resonance is a crucial factor that influences absorption performance across the entire desired wavelength range. Moreover, there are alternative approaches to achieve high broadband absorption in MPAS, such as incorporating metamaterial elements (Bakır et al., 2016; Khuyen et al., 2017) and utilizing unique materials like graphene (Li et al, 2022; Huang et al., 2022). Infrared technology is advancing towards interdisciplinary applications, and multi-band broadband absorption has the potential to broaden the range of applications for absorptive materials. Enhancing the absorption performance of MPAS remains a significant challenge, particularly in the context of achieving broadband absorption. While previous reports have described broadband absorbers in the short-wave infrared region, there is still potential for enhancing absorption performance. Previous studies on MPAS focused mainly on using fixed materials, providing limited alternative options. The substitutability of dielectric materials augments the absorber's potential for broader and more adaptable applications in related fields.

The proposed metal-dielectric-metal (MDM) absorber consists of a hollow square column. The characteristics of the proposed absorber are analyzed using the Finite-Difference Time-Domain (FDTD) method (Qian et al., 2021). The results indicate that the average absorption of our proposed absorber is as high as 99.01% in the wavelength range from 1.52 to 3.66 μm, with absorption rates exceeding 90% between 1.22 and 3.92 μm. Based on the impedance matching theory, we investigate the relationship between the equivalent impedance of the absorber and the impedance of free space. Our findings demonstrate that surface plasmon resonance improves absorption performance. This is determined by studying the distribution of the electromagnetic field at the absorption peaks. Additionally, Fabry-Perot cavities are involved in the absorption of incident light. In this paper, we investigate the impact of structural parameters on absorption performance. Furthermore, we discuss the polarization angles and incident angles for both transverse magnetic (TM) and transverse electric (TE) polarizations. InP, SiO_2, and Si_3N_4 can be used as alternative intermediate dielectric layers in addition to GaAs. The MPAS introduced in this paper exhibits polarization independence, insensitivity to wide incident angles, and broadband high absorption characteristics. We propose a broadband absorber with a periodic unit cell of hollow square columns based on a metal-dielectric-metal structure. The features of our proposed absorber position it for potential applications in various optical devices, such as astronomical observation, medical tests, and infrared detection.

2 Design and theory

The traditional metal-dielectric-metal (MDM) structure achieves excellent absorption performance in MPAS through the

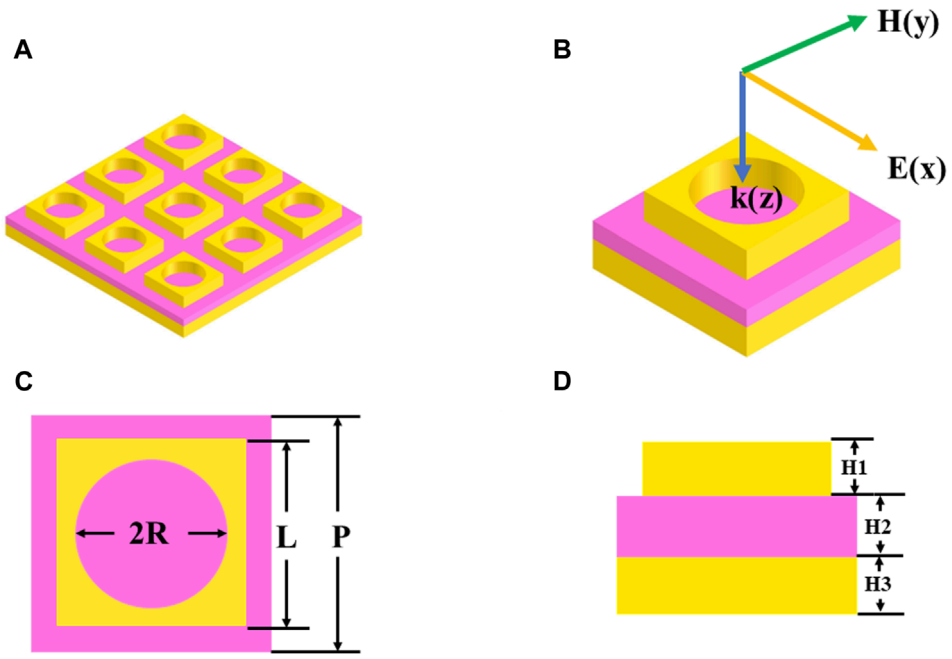

FIGURE 1
MPAS model structure. **(A)** Structural array of the proposed absorber. **(B)** 3D view of the unit structure. **(C)** Top view of the unit structure. **(D)** Side view of the unit structure.

implementation of a distinctive periodic structure on the upper plane (Yu et al., 2018). We propose a hollow square column absorber based on the MDM structure. The array structure of the proposed MPAS is shown in Figure 1A. Figures 1B–D represents the unit cell, the top view, and the side view of MPAS, respectively. Our proposed MPAS consists of titanium (Ti) as the metal layer and gallium arsenide (GaAs) as the dielectric layer. The bottom section of the MPAS is constructed using Ti as the metal component. The metal substrate is a square column with equal length and width and a thickness of H3 = 260 nm. The proposed absorber comprises a central dielectric layer with a thickness denoted as H2 = 110 nm. The top layer consists of a periodic structure made of hollow square columns, constructed from titanium metal. The square column on the top layer has a side length denoted as L = 380 nm. The inner cavity within the proposed absorber possesses a radius denoted as R = 180 nm. The thickness (H1) of the top periodic structure is 550 nm. The unit size (P) of the absorber is 660 nm. The mesh size is set 5 nm × 5 nm × 5 nm.

In this paper, the proposed absorber is modeled using FDTD calculation software. Periodic boundary conditions are applied in the x and y directions, while a perfect absorbing layer is set up in the z direction. The simulation periodicity size is defined as 660 nm. A reflectance monitor (R(ω)) is positioned 2 μm above the absorber, while a transmittance monitor (T(ω)) is situated 2 μm below the absorber. We choose a plane wave as the incident light source for the absorber. As illustrated in Figure 1A, the incident light travels in the negative direction of the Z-axis, with the electric field oriented along the X-axis and the magnetic field along the Y-axis. The absorption rate can be expressed as A(ω) = 1- R(ω)- T(ω). The thickness of the lower metal reflector in the absorber significantly exceeds the skin depth of the incident light. Virtually no light waves can penetrate the absorber. The absorption can be expressed as A(ω) = 1- R(ω). Our proposed MPAS consists of titanium (Ti) as the arsenide (GaAs) as the dielectric layer. Data for both Ti and GaAs are sourced from Palik's handbook (Palik, 1998). The real and imaginary components of the permittivity are shown in Figure 2. As an excellent lossy metal, Ti possesses a significantly large imaginary part of the permittivity in the infrared range, which enhances its absorption performance.

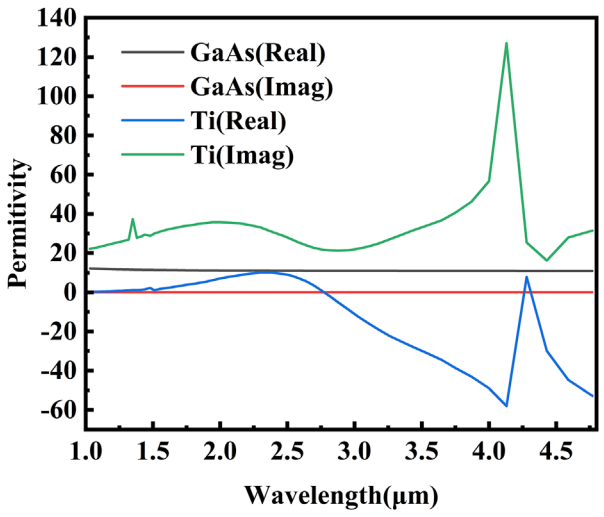

FIGURE 2
Permittivity data of Ti and GaAs.

We conduct extensive computational simulations and provide micromachining technology for the manufacturing and processes involved in this design. Ti film is deposited on a silicon substrate using ion beam sputtering. InP or GaAs thin films are deposited using Metal Organic Chemical Vapor Deposition (MOCVD). SiO_2 or Si_3N_4 are deposited using Plasma Enhanced Chemical Vapor Deposition (PECVD). The high-precision photolithography steps transfer the designed pattern, while Inductively Coupled Plasma (ICP) technology is used to, etch this pattern.

The MPAS has the capability to adapt the effective impedance of the absorber to align with the free-space impedance by designing a unique top periodic structure that incorporates multi-size resonant coupling. This ensures that incident light is absorbed by the MPAS with minimal reflection back into free space. To verify its absorption characteristics, we extract the S-parameters of the proposed absorber. S_{11} and S_{21} denote the reflection and transmission values, respectively. Figure 3 illustrates the equivalent impedance of the absorber. By impedance matching theory, the closer the equivalent impedance of the absorber is to the free-space impedance, the higher the absorption performance (Jung et al., 2015; Huang et al., 2020):

$$Z = \sqrt{\frac{(1+S_{11})^2 - S_{21}{}^2}{(1-S_{11})^2 - S_{21}{}^2}} \tag{1}$$

$$\Gamma = \frac{Z - Z_0}{Z + Z_0} \tag{2}$$

$$RL = 20 \lg \left| \frac{Z - Z_0}{Z + Z_0} \right| \tag{3}$$

$$A = 1 - \left| \frac{Z - Z_0}{Z + Z_0} \right|^2 \tag{4}$$

In Eqs 1–4, Z represents the normalized equivalent impedance of the absorber, Γ is the reflection coefficient, RL signifies the reflection loss and A represents absorption. As depicted in Figure 3B, the real part of the equivalent impedance closely approximates 1, while the imaginary part tends toward zero within the wavelength range of 1.22 μm–3.92 μm. It indicates that the proposed absorber achieves impedance matching with free space, leading to absorption performance that closely approaches perfection. To visually understand the impact of impedance matching on reducing the reflection of incident light waves, we calculate the reflection coefficient (Γ) and reflection loss (RL) through the utilization of S-parameters. As shown in Figure 3C, the reflection loss registers below −10 dB across the wavelength range from 1.22 to 3.92 μm. As depicted in Figure 3D, the absorption rate exceeds 90% across the wavelength range from 1.22 to 3.92 μm, and the average absorption rate reaches an impressive 99.01% between 1.52 and 3.66 μm within the wavelength spectrum. The results obtained from the calculation of equivalent impedance are consistent with the simulation results. This further confirms the authenticity of the results. Three absorption peaks are observed at wavelengths of 1.73, 2.53, and 3.25 μm. The reflection loss is RL = −25.62 dB, the effective impedance is Z = 0.92–0.072i, and the absorption is

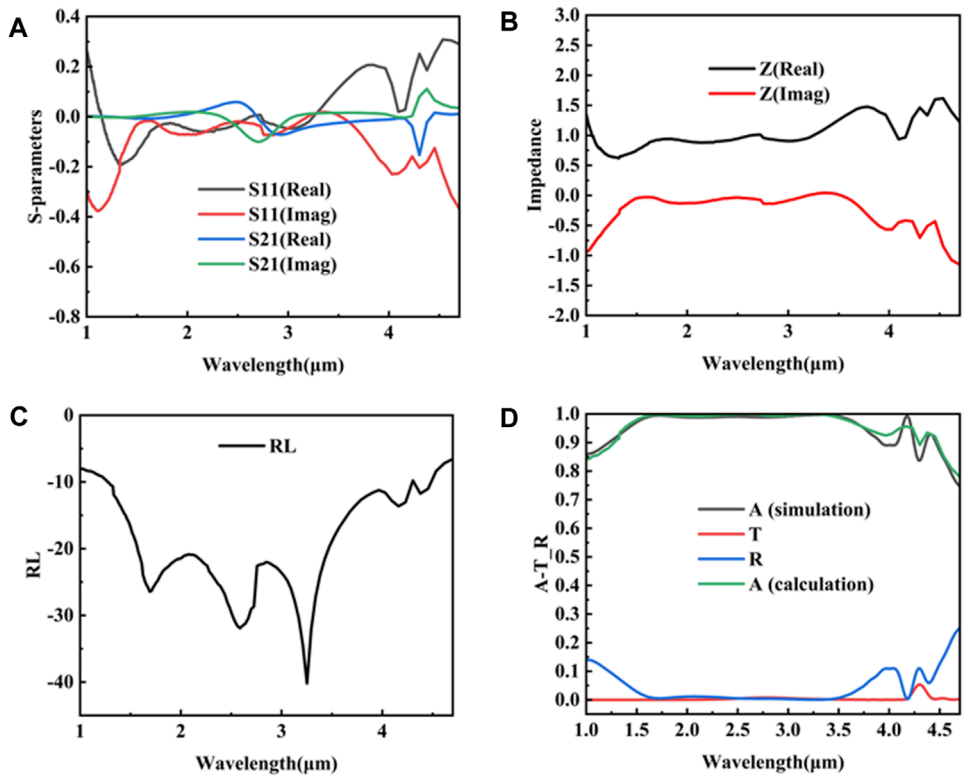

FIGURE 3
Parameter values of the absorber. **(A)** The values of S-parameters. **(B)** Equivalent impedance of the absorber. **(C)** The value of reflection loss. **(D)** Comparison of simulation and computational results. Absorption (A), Transmission (T) and Reflection (R) of the absorber.

A = 99.45% at 1.73 μm. The reflection loss is RL = −30.83 dB, the effective impedance is Z = 0.96–0.042i, and the absorption is A = 99.02% at 2.53 μm. The reflection loss is RL = −40.19 dB, the effective impedance is Z = 1.00–0.019i and the absorption is A = 99.71% at 3.25 μm.

To demonstrate the impact of the structure on absorption, we analyze the electromagnetic field distributions of the absorber at three absorption peaks. The incident light's influence triggers collective oscillations among groups of free electrons at the metal-dielectric interface, ultimately leading to the formation of surface plasmon resonance (SPR) (Zhang et al., 2007; Chen et al., 2014):

$$\lambda_{SPR} = \frac{P}{\sqrt{i^2 + j^2}} \left(\frac{\varepsilon_d \cdot \varepsilon_m}{\varepsilon_d + \varepsilon_m} \right)^{1/2} \quad (5)$$

In Eq. 5, P represents the unit size of the absorber, while i and j denote the order of SPR resonance. ε_d and ε_m stand for the permittivity values of the dielectric and metal, respectively. As shown in Figure 4, there is an electric field enhancement phenomenon occurring at the top layer. Electric field enhancement occurs at the four corners of the square column, while it is observed in the *y*-axis direction of a cylindrical cavity. The enhancement of the electric field in the top layer indicates the excitation of local surface plasmon resonance (LSPR), which contributes to absorption enhancement. The enhancement of the electric field within the cavity decreases progressively as the wavelength of light increases from 1.73 to 3.9 μm. The main factor contributing to absorption enhancement is the electric field enhancement induced by the LSPR at the outer boundary of the square pillar. Figures 5A–C shows the magnetic field distribution on the top layer. The magnetic field is primarily enhanced in the *Y*-axis direction within the cavity and at the boundary of the square pillar. Figures 5D–F shows the magnetic field distribution in the X-Z plane. It indicates that magnetic field enhancement occurs not only at the top layer but also at the intermediate dielectric layer. The increase in the magnetic field at the edge of the dielectric layer indicates the excitation of propagating surface plasmon resonance (PSPR). Both LSPR and PSPR synergistically enhance the absorption capabilities of our proposed absorber. Electromagnetic loss contributes to the absorption of incoming light. Figure 6 shows the energy consumption of the proposed absorber. This suggests that the primary cause of absorption is the electric loss from LSPR in the top layer, while the magnetic loss from PSPR in the middle dielectric layer also contributes to absorption.

3 Results and discussion

The influence of the structural parameters on absorption performance is discussed. The structure and size of the absorber impact LSPR. Modifying the structural parameters can alter the electromagnetic properties of the absorber. By making precise adjustments to the relevant structural parameters, the performance of the absorber can be optimized. To explore the specific effects of various structural parameters on the absorption performance, the controlled variables method is employed. We modify the value of one parameter while keeping the other parameters constant. The top-layer periodic structure not only influences the impedance matching between the absorber and free space but also contributes to the absorption of incident light by inducing SPR. Figure 7 illustrates the impact of different parameter values in the top-layer structure on the absorption performance. As shown in Figure 7A, the cavity radius increases from 20 to 180 nm in increments of 40 nm. The absorption bandwidth undergoes a redshift as the

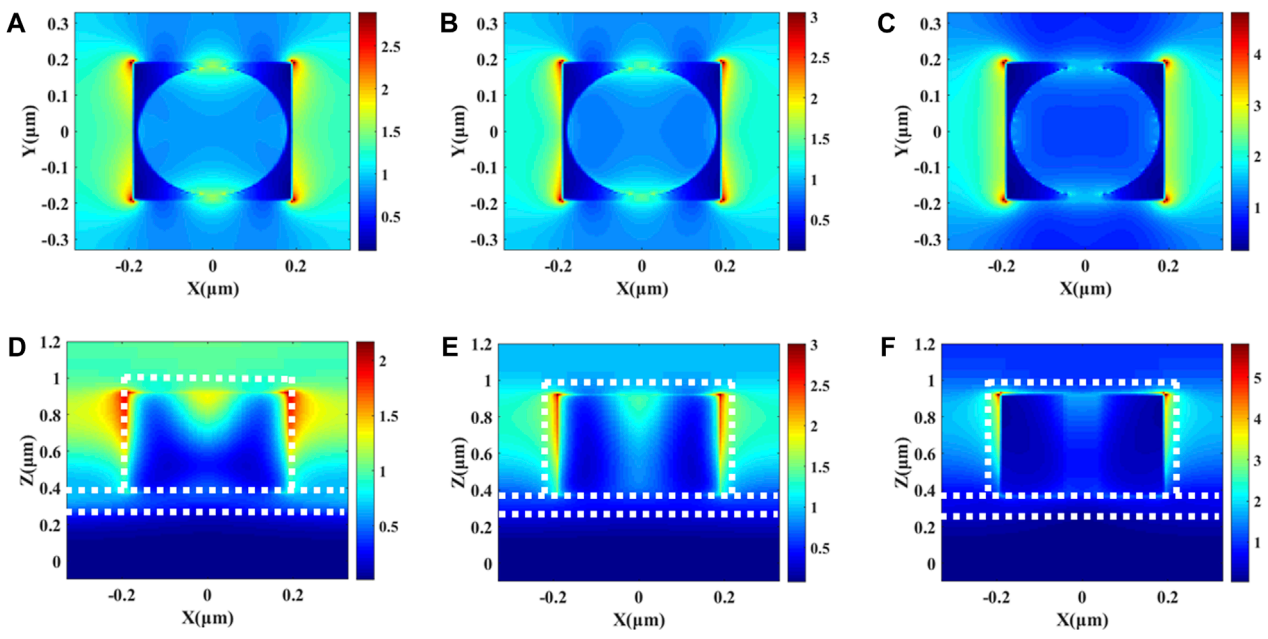

FIGURE 4
Electric field distribution at three absorption peaks. **(A–C)** Electric field distribution in the X-Y plane of the top layer at 1.73, 2.53 and 3.25 μm, respectively. **(D–F)** Electric field distribution in the X-Z plane at 1.73, 2.53 and 3.25 μm, respectively.

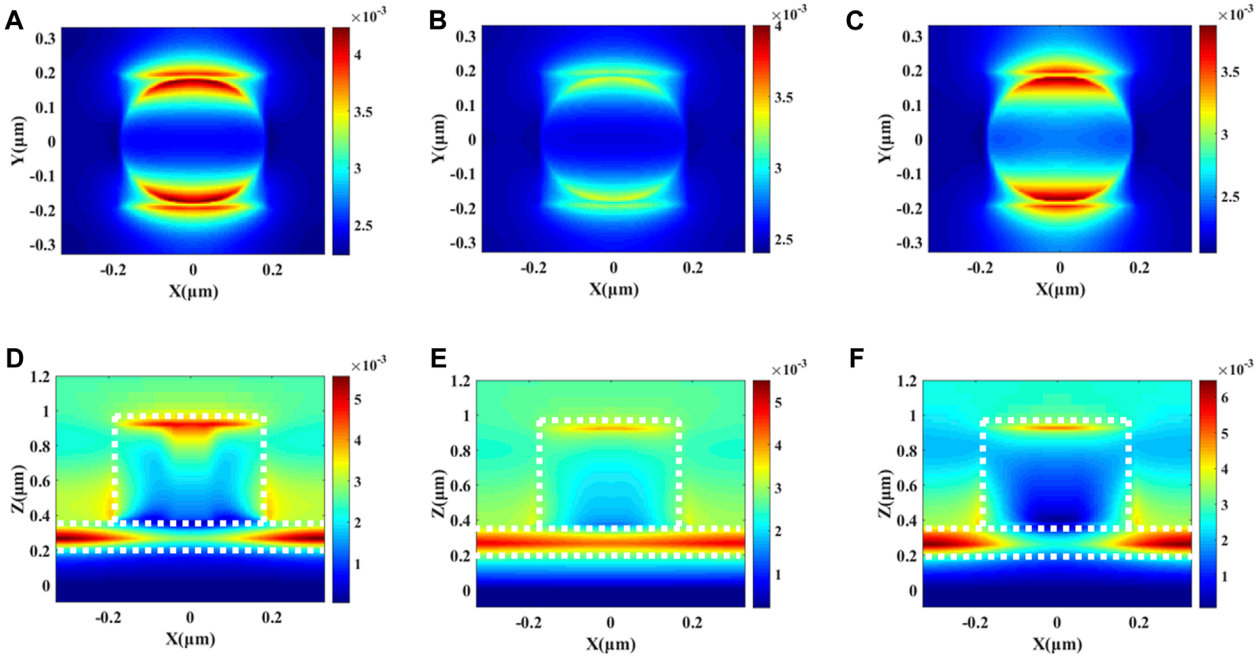

FIGURE 5
Magnetic field distribution at three absorption peaks. **(A–C)** Magnetic field distribution in the X-Y plane of the top layer at 1.73, 2.53 and 3.25 μm, respectively. **(D–F)** Magnetic field distribution in the X-Z plane at 1.73, 2.53 and 3.25 μm, respectively.

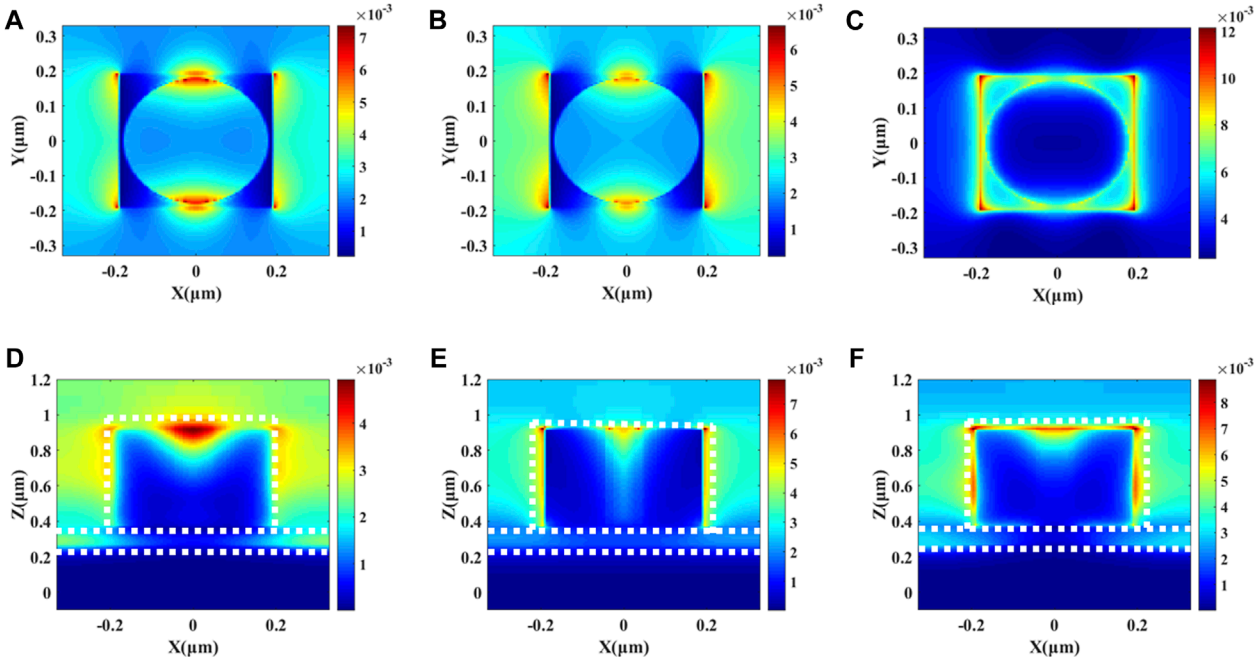

FIGURE 6
Power loss distribution at three absorption peaks. **(A–C)** Power loss distribution in the X-Y plane of the top layer at 1.73, 2.53 and 3.25 μm, respectively. **(D–F)** Power loss distribution in the X-Z plane at 1.73, 2.53 and 3.25 μm, respectively.

cavity radius increases, while the absorption performance remains largely unchanged at longer wavelengths. Based on the electric field distribution depicted in Figure 4, it is evident that the LSPR at the cavity edge is significantly attenuated at longer wavelengths. As the wavelength redshifts, the electric field at the cavity edge gradually becomes stronger. As shown in Figure 7B, the side length (L) of the square pillar increases from 380 nm to 580 nm in increments of 50 nm. As L increases, the absorption performance

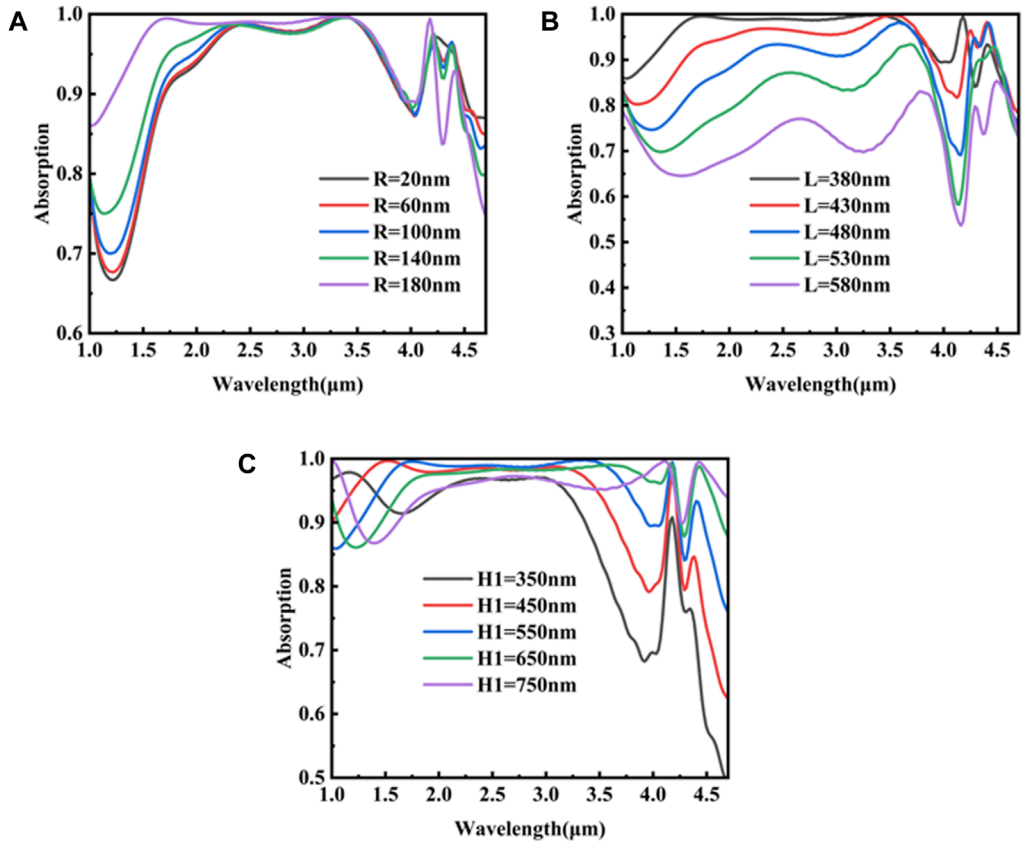

FIGURE 7
The impact of top layer structural parameters on the absorption performance. **(A)** The influence of cavity radius on the performance of absorption. **(B)** The influence of the top cube side length on the absorption performance. **(C)** The impact of the top layer thickness on the performance of the absorption.

steadily decreases across the entire wavelength range. The LSPR at the periphery of the square pillar significantly contributes to the absorption performance across the entire wavelength range. As L increases, it diminishes the plasma resonance at the periphery of the square pillar. On the other hand, the absorber experiences a greater impedance mismatch with free space. This leads to a higher reflection of incoming light back into free space, thereby reducing absorption performance. As shown in Figure 7C, when the thickness of the top layer increases from 350 to 550 nm, the average absorption gradually improves. However, the average absorption gradually decreases as the thickness increases from 550 to 750 nm, and the range of absorption exceeding 90% also diminishes. This indicates that both excessive and insufficient thickness of the top layer have adverse effects on plasmonic resonance. We selected a thickness of 550 nm as the optimal choice to achieve the best absorption performance.

The impact of dielectric thickness (H2) on absorption performance is depicted in Figure 8A. The H2 increases from 50 nm to 110 nm, leading to a gradual improvement in the average absorption rate and an expanded absorption bandwidth that exceeds 90%. When the dielectric layer thickness is increased from 110 nm to 170 nm, the average absorption rate progressively decreases. Based on the magnetic field distribution depicted in Figure 5, it is evident that PSPR occurs in the intermediate dielectric layer. This indicates that modifying the thickness of the dielectric layer can regulate PSPR and impact absorption performance. The reflection and interference of incident light between the top and bottom metal layers influence the configuration of the resonant cavity formed by the dielectric layer. Ultimately, we have chosen a thickness of 110 nm for the optimized dielectric layer. Figure 8B demonstrates the effect of unit size (P) on absorption performance. When p = 460 nm, the distance between adjacent top-layer periodic units is small. In addition to being influenced by incident light and LSPR, the cavity pillar of the top layer also experiences resonance coupling with the surrounding adjacent periodic units. This phenomenon leads to changes in the LSPR of each cavity pillar, ultimately reducing its absorption performance. When P increments from 560 nm to 860 nm in 100 nm intervals, there is a redshift in the absorption bandwidth. The range of wavelengths where absorption exceeds 90% decreases. The impact of different dielectrics on absorption performance is described in Figure 9. By fine-tuning the structural parameters, high absorption in the near-infrared to mid-infrared wavelength range is achieved using the same fundamental structure. The structural parameters of our proposed absorber with interchangeable materials are presented in Table 1. The substitutive capability of the dielectric material within the same structure significantly enhances the versatility of the absorber. The proposed absorber demonstrates an absorption rate of over 95% with four different dielectric materials.

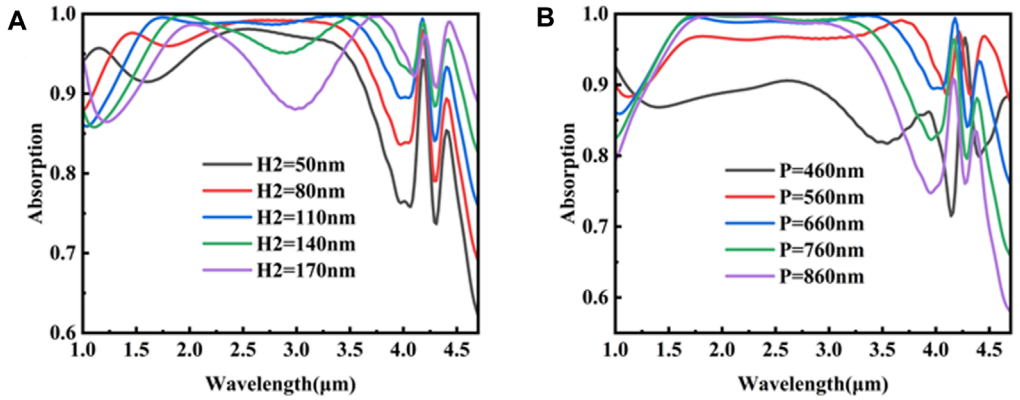

FIGURE 8
The influence of the dielectric layer and unit size on the performance of the absorption. **(A)** The influence of the dielectric layer thickness on the performance of absorption. **(B)** The effect of unit size on the performance of absorption.

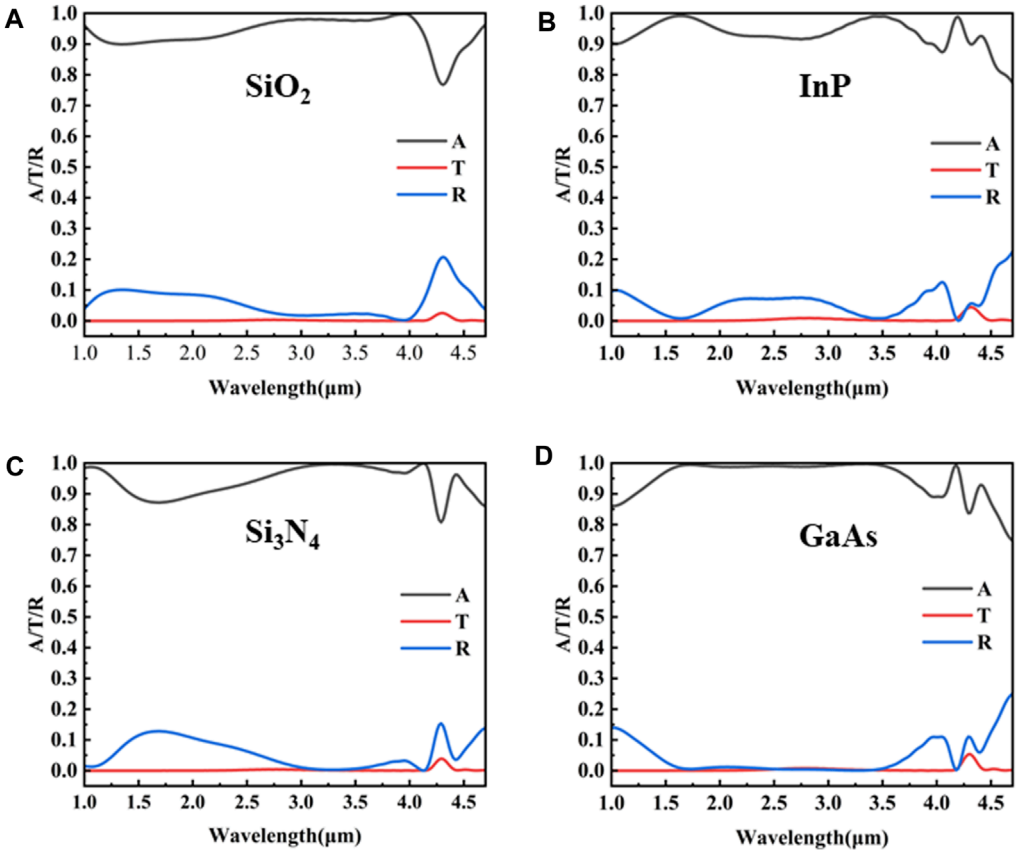

FIGURE 9
The absorption spectrum varies with different dielectrics based on the same hollow square column structure. **(A)** The absorption spectrum with a SiO_2 dielectric layer. **(B)** The absorption spectrum with an InP dielectric layer. **(C)** The absorption spectrum with a Si_3N_4 dielectric layer. **(D)** The absorption spectrum with a GaAs dielectric layer.

Therefore, we conclude that the proposed absorber demonstrates material substitution characteristics. As shown in Figures 10A, D, the polarization angles of the vertically incident light vary from 0° to 90°. The absorption performance of the top periodic structure is unaffected by the polarization angle due to its hollow square column shape, which is centrally symmetric. The polarization angles and incident angles of the incident light can vary significantly. Therefore, designing an absorber that is insensitive to changes in polarization angles and incident angles can accommodate various complex conditions. As shown in Figures 10B, E, the incident angles for TE polarization increase from 0° to 60°. As the incident angles increase, the absorption performance gradually decreases, and the absorption

TABLE 1 The parameters of the absorber with substitutable materials.

Substitutable materials	L (nm)	P (nm)	R (nm)	H1 (nm)	H2 (nm)	H3 (nm)	Operating bandwidth (μm)	Absorption value (%)
SiO_2	380	660	180	595	60	260	1.54–3.97	95.49
InP	370	610	175	450	160	260	1.37–3.75	95.33
Si_3N_4	380	660	180	680	60	260	2.11–4.18	96.77
GaAs	380	660	180	550	110	260	1.52–3.66	99.01

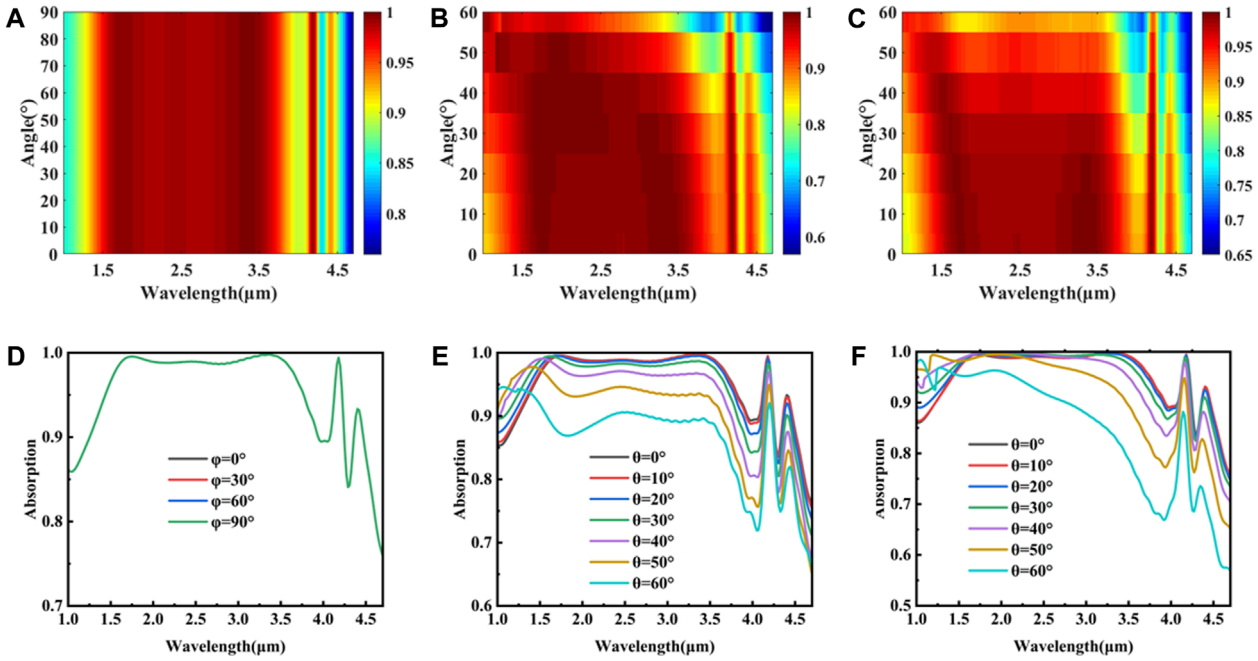

FIGURE 10
The influence of polarization angle (φ) and incident angle (θ). **(A, D)** The absorption spectrum with the polarization angle ranging from 0° to 90°. **(B, E)** The absorption spectrum with the incident angle ranging from 0° to 90° for TE polarization. **(C, F)** The absorption spectrum with the incident angle ranging from 0° to 90° for TM polarization.

TABLE 2 Reports about broadband infrared absorber.

Reference (year)	Operating bandwidth (μm)	Absorption value (%)	Incidence angles (absorption)	Polarization	Substitutability
Jia et al. (2022)	0.4–2.5	95	0°–50° (above 70%)	Insensitive	No
Zhang et al. (2015)	1.5–3.5	Above 80	0°–50° (above 80%)	Not discussed	No
Liu et al. (2019)	0.75–3.25	Above 80	Not discussed	Insensitive	No
Abou Houran et al. (2023)	1.15–2.50	Above 80	TE:0°–50° (above 70%) TM:0°–60°(above70%)	Not discussed	No
This work	1.52–3.66	99.01	TE:0°–60° (above 90%) TM:0°–60° (above 80%)	Insensitive	Yes

bandwidth undergoes a redshift. An absorption rate exceeding 90% is achieved within the bandwidth ranging from 1 μm to 3.47 μm when θ = 50°. However, the absorption sharply decreases when θ = 60°. As shown in Figures 10C, F, the TM polarization incident angles increase from 0° to 60°. With the increase in polarization angle, the absorption performance gradually decreases within the wavelength range of 1μm–4.7 μm. Even when θ = 60°, the absorption rate remains above 80%. The proposed absorber is insensitive to both TE and TM polarization angles. As shown in Table 2, our proposed absorber demonstrates excellent performance and material substitutability.

4 Conclusion

We proposed an absorber with a hollow square column based on the MDM structure. The average absorption is 99.01% within the wavelength range of 1.52–3.66 μm, with the highest absorption reaching 99.71% at 3.25 μm. The proposed absorber consists of a single metal material (Ti) and a single dielectric material (GaAs). The absorption curve has been verified and fits well based on impedance matching theory. Additionally, we investigated the distribution of the electromagnetic field at three absorption peaks, revealing the contribution of plasmonic resonances to the absorption performance. There is a regulating effect on the electromagnetic properties for structural parameters. We calculate the impact of the structural parameters of each part of the absorber on the absorption performance and determine the optimal parameter values. The study examines the impact of various dielectric materials on the performance of the absorber. By adjusting the structural parameters of the absorber while keeping the basic design unchanged, the substitution of different dielectric materials allows the absorber to maintain exceptional performance, achieving over 95% absorption. The proposed absorber is insensitive to polarization angles. Under TE and TM polarizations, with incident angles less than 50°, the absorption rate remains above 90%. A new structure that we proposed achieves near-perfect absorption in the short-wave infrared region. The substitutability of dielectrics allows the proposed absorber to have a wider range of potential applications in optical devices.

Data availability statement

The original contributions presented in the study are included in the article/Supplementary material, further inquiries can be directed to the corresponding authors.

Author contributions

FL: Formal Analysis, Writing–original draft, Writing–review and editing. SW: Software, Writing–original draft. ZC: Investigation, Writing–original draft. TZ: Data curation, Writing–original draft. RY: Project administration, Writing–original draft. BW: Supervision, Writing–review and editing. NL: Writing–review and editing.

Funding

The author(s) declare financial support was received for the research, authorship, and/or publication of this article. This work was supported by Qingdao Postdoctoral Application Research Project, the Chinese Ministry of Education's Industry School Cooperation Collaborative Education Project: 220606513074515.

Conflict of interest

The authors declare that the research was conducted in the absence of any commercial or financial relationships that could be construed as a potential conflict of interest.

Publisher's note

Supplementary material

The Supplementary Material for this article can be found online at: https://www.frontiersin.org/articles/10.3389/fspas.2024.1374951/full#supplementary-material

References

Abou Houran, M., Armghan, A., Baqir, M. A., Aliqab, K., Saqlain, M., and Alsharari, M. (2023). MXene nanorods-based metasurface wideband absorber for infrared regime. *Int. J. Therm. Sci.* 193, 108452. doi:10.1016/j.ijthermalsci.2023.108452

Aslan, E., Kaya, S., Aslan, E., Korkmaz, S., Saracoglu, O. G., and Turkmen, M. (2017). Polarization insensitive plasmonic perfect absorber with coupled antisymmetric nanorod array. *Sensors Actuators B Chem.* 243, 617–625. doi:10.1016/j.snb.2016.12.030

Bakır, M., Karaaslan, M., Dincer, F., Delihacioglu, K., and Sabah, C. (2016). Tunable perfect metamaterial absorber and sensor applications. *J. Mater. Sci. Mater. Electron.* 27 (11), 12091–12099. doi:10.1007/s10854-016-5359-7

Bertoldi, K., Vitelli, V., Christensen, J., and Hecke, M. V. (2017). Flexible mechanical metamaterials. *Nat. Rev. Mater.* 2 (11), 17066. doi:10.1038/natrevmats.2017.66

Bliokh, K. Y., Bekshaev, A. Y., and Nori, F. (2016). Corrigendum: dual electromagnetism: helicity, spin, momentum, and angular momentum. *New J. Phys.* 18 (8), 089503. doi:10.1088/1367-2630/18/8/089503

Cao, T., Wei, C. W., Simpson, R. E., Zhang, L., and Cryan, M. J. (2014). Broadband polarization-independent perfect absorber using a phase-change metamaterial at visible frequencies. *Sci. Rep.* 4, 3955. doi:10.1038/srep03955

Chen, S., Meng, L., Hu, J., and Yang, Z. (2014). Fano interference between higher localized and propagating surface plasmon modes in nanovoid arrays. *Plasmonics* 10 (1), 71–76. doi:10.1007/s11468-014-9779-z

Ding, F., Dai, J., Chen, Y., Zhu, J., Jin, Y., and Bozhevolnyi, S. I. (2016). Broadband near-infrared metamaterial absorbers utilizing highly lossy metals. *Sci. Rep.* 6, 39445. doi:10.1038/srep39445

Fan, K., Suen, J. Y., Liu, X., and Padilla, W. J. (2017). All-dielectric metasurface absorbers for uncooled terahertz imaging. *Optica* 4 (6), 601. doi:10.1364/optica.4.000601

Gade, R., and Moeslund, T. B. (2013). Thermal cameras and applications: a survey. *Mach. Vis. Appl.* 25 (1), 245–262. doi:10.1007/s00138-013-0570-5

Goldenstein, C. S., Spearrin, R. M., Jeffries, J. B., and Hanson, R. K. (2017). Infrared laser-absorption sensing for combustion gases. *Prog. Energy Combust. Sci.* 60, 132–176. doi:10.1016/j.pecs.2016.12.002

Honniball, C. I., Lucey, P. G., Arredondo, A., Reach, W. T., and Malaret, E. R. (2022). Regional map of molecular water at high southern latitudes on the moon using 6 μm data from the stratospheric observatory for infrared Astronomy. *Geophys. Res. Lett.* 49 (9), 97786. doi:10.1029/2022gl097786

Hou, T., Jia, Z., Feng, A., Zhou, Z., Liu, X., Lv, H., et al. (2021). Hierarchical composite of biomass derived magnetic carbon framework and phytic acid doped polyanilne with prominent electromagnetic wave absorption capacity. *J. Mater. Sci. Technol.* 68, 61–69. doi:10.1016/j.jmst.2020.06.046

Huang, J., Li, J., Yang, Y., Li, J., Li, J., Zhang, Y., et al. (2020). Broadband terahertz absorber with a flexible, reconfigurable performance based on hybrid-patterned vanadium dioxide metasurfaces. *Opt. Express* 28 (12), 17832–17840. doi:10.1364/OE.394359

Huang, X., Cao, M., Wang, D., Li, X., Fan, J., and Li, X. (2022). Broadband polarization-insensitive and oblique-incidence terahertz metamaterial absorber with multi-layered graphene. *Opt. Mater. Express* 12 (2), 811. doi:10.1364/ome.451450

Jakobsen, P., Ferruit, P., Alves de Oliveira, C., Arribas, S., Bagnasco, G., Barho, R., et al. (2022). The near-infrared spectrograph (NIRSpec) on theJames WebbSpace telescope. *Astronomy Astrophysics* 661, A80. doi:10.1051/0004-6361/202142663

Jia, Y., Wu, T., Wang, G., Jiang, J., Miao, F., and Gao, Y. (2022). Visible and near-infrared broadband absorber based on Ti3C2Tx MXene-Wu. *MXene-Wu. Nanomater. (Basel)* 12 (16), 2753. doi:10.3390/nano12162753

Jung, J. Y., Lee, J., Choi, D. G., Choi, J. H., Jeong, J. H., Lee, E. S., et al. (2015). Wavelength-Selective infrared metasurface absorber for multispectral thermal detection. *IEEE Photonics J.* 7 (6), 1–10. doi:10.1109/jphot.2015.2504975

Khuyen, B. X., Tung, B. S., Yoo, Y. J., Kim, Y. J., Kim, K. W., Chen, L. Y., et al. (2017). Miniaturization for ultrathin metamaterial perfect absorber in the VHF band. *Sci. Rep.* 7, 45151. doi:10.1038/srep45151

Landy, N. I., Sajuyigbe, S., Mock, J. J., Smith, D. R., and Padilla, W. J. (2008). Perfect metamaterial absorber. *Phys. Rev. Lett.* 100 (20), 207402. doi:10.1103/PhysRevLett.100.207402

Lei, L., Li, S., Huang, H., Tao, K., and Xu, P. (2018). Ultra-broadband absorber from visible to near-infrared using plasmonic metamaterial. *Opt. Express* 26 (5), 5686–5693. doi:10.1364/OE.26.005686

Li, F. J., Du, J. S., Wang, S., Yu, R. T., Wang, X., Zhang, T. Q., et al. (2023). Ultra-broadband infrared metamaterial absorber based on MDMDM structure for optical sensing. *Front. Astronomy Space Sci.* 10, 1338284. doi:10.3389/fspas.2023.1338284

Li, M., Wang, G., and Gao, Y. (2022a). An infrared ultra-broadband absorber based on MIM structure. *Nanomater. (Basel)* 12 (19), 3477. doi:10.3390/nano12193477

Li, Q., Cai, X., Liu, T., Jia, M., Wu, Q., Zhou, H., et al. (2022b). Gate-tuned graphene meta-devices for dynamically controlling terahertz wavefronts. *Nanophotonics* 11 (9), 2085–2096. doi:10.1515/nanoph-2021-0801

Lin, H., Sturmberg, B. C. P., Lin, K.-T., Yang, Y., Zheng, X., Chong, T. K., et al. (2019). A 90-nm-thick graphene metamaterial for strong and extremely broadband absorption of unpolarized light. *Nat. Photonics* 13 (4), 270–276. doi:10.1038/s41566-019-0389-3

Lin, K. T., Lin, H., Yang, T., and Jia, B. (2020). Structured graphene metamaterial selective absorbers for high efficiency and omnidirectional solar thermal energy conversion. *Nat. Commun.* 11 (1), 1389. doi:10.1038/s41467-020-15116-z

Liu, C., Zhang, D., Liu, Y., Wu, D., Chen, L., Ma, R., et al. (2017). Numerical study of an efficient solar absorber consisting of metal nanoparticles. *Nanoscale Res. Lett.* 12 (1), 601. doi:10.1186/s11671-017-2363-7

Liu, W., and Song, Z. (2021). Terahertz absorption modulator with largely tunable bandwidth and intensity. *Carbon* 174, 617–624. doi:10.1016/j.carbon.2020.12.001

Liu, X., Fu, G., Liu, M., Zhan, X., and Liu, Z. (2019). Titanium nanoholes meta-surface for ultra-broadband infrared absorption. *Results Phys.* 15, 102578. doi:10.1016/j.rinp.2019.102578

Ma, W., Wen, Y., and Yu, X. (2013). Broadband metamaterial absorber at mid-infrared using multiplexed cross resonators. *Opt. express* 21 (25), 30724–30730. doi:10.1364/OE.21.030724

McCrindle, I. J. H., Grant, J., Drysdale, T. D., and Cumming, D. R. S. (2013). Multi-spectral materials: hybridisation of optical plasmonic filters and a terahertz metamaterial absorber. *Adv. Opt. Mater.* 2 (2), 149–153. doi:10.1002/adom.201300408

Palik, E. D. (1998). *Handbook of optical constants of solids*. Academic Press.

Qian, Q., Wang, C., Fan, L., Cheng, L., Chen, H., and Zhao, L. (2021). An ultra-broadband metasurface perfect absorber based on the triple Mie resonances. *Opt. Mater.* 116, 111103. doi:10.1016/j.optmat.2021.111103

Qin, Z., Shi, X., Yang, F., Hou, E., Meng, D., Sun, C., et al. (2022). Multi-mode plasmonic resonance broadband LWIR metamaterial absorber based on lossy metal ring. *Opt. Express* 30 (1), 473–483. doi:10.1364/OE.446655

Ruan, X., Dai, W., Wang, W., Ou, C., Xu, Q., Zhou, Z., et al. (2021). Ultrathin, broadband, omnidirectional, and polarization-independent infrared absorber using all-dielectric refractory materials. *Nanophotonics* 10 (6), 1683–1690. doi:10.1515/nanoph-2020-0627

Su, Z., Yin, J., and Zhao, X. (2015). Terahertz dual-band metamaterial absorber based on graphene/MgF_2 multilayer structures. *Opt. Express* 23 (2), 1679–1690. doi:10.1364/OE.23.001679

Wang, B. X., Xu, C., Duan, G., Jiang, J., Xu, W., Yang, Z., et al. (2022). Miniaturized and actively tunable triple-band terahertz metamaterial absorber using an analogy I-typed resonator. *Nanoscale Res. Lett.* 17 (1), 35. doi:10.1186/s11671-022-03677-5

Wang, S., Du, J., Chi, Z., Coong, H., and Wang, B. (2024). Ultra-broadband metamaterial absorber in the far infrared. *Mater. Lett.* 355, 135518. doi:10.1016/j.matlet.2023.135518

Xu, X., Shi, S., Tang, Y., Wang, G., Zhou, M., Zhao, G., et al. (2021). Growth of NiAl-layered double hydroxide on graphene toward excellent anticorrosive microwave absorption application. *Adv. Sci. (Weinh)* 8 (5), 2002658. doi:10.1002/advs.202002658

Yu, P., Besteiro, L. V., Huang, Y., Wu, J., Fu, L., Tan, H. H., et al. (2018). Broadband metamaterial absorbers. *Adv. Opt. Mater.* 7 (3). doi:10.1002/adom.201800995

Zhang, H. B., Du, J. S., Chi, Z. T., Cong, H. L., and Wang, B. (2024). Numerical design of a dual-wavelength confocal metalens with photonic crystal filter based on filter-substrate-metasurface structure. *Opt. Commun.* 554, 130157. doi:10.1016/j.optcom.2023.130157

Zhang, Q., Bai, L., Bai, Z., Hu, P., and Liu, C. (2015). Theoretical analysis and design of a near-infrared broadband absorber based on EC model. *Opt. Express* 23 (7), 8910–8917. doi:10.1364/OE.23.008910

Zhang, W., Azad, A. K., Han, X. J., Chen, J. J., and Zhang, X. C. (2007). Direct observation of a transition of a surface plasmon resonance from a photonic crystal effect. *Phys. Rev. Lett.* 98 (18), 183901. doi:10.1103/PhysRevLett.98.183901

Zhao, Y., Liao, Y. L., Wang, P., Liu, Y., Gong, Y., and Sheng, W. (2021). Tunable ultra-narrowband mid-infrared absorber with graphene and dielectric metamaterials. *Results Phys.* 23, 104038. doi:10.1016/j.rinp.2021.104038

Zou, J., Yu, P., Wang, W., Tong, X., Chang, L., Wu, C., et al. (2020). Broadband mid-infrared perfect absorber using fractal Gosper curve. *J. Phys. D Appl. Phys.* 53 (10), 105106. doi:10.1088/1361-6463/ab57ea

frontiers | Frontiers in Astronomy and Space Sciences

TYPE Original Research
PUBLISHED 10 April 2024
DOI 10.3389/fspas.2024.1391070

OPEN ACCESS

EDITED BY
Hairen Wang,
Chinese Academy of Sciences (CAS), China

REVIEWED BY
Carlos Frajuca,
Federal University of Rio Grande, Brazil
Feng Wang,
Guangzhou University, China
Jun Nie,
University of Science and Technology of China, China

*CORRESPONDENCE
Hai-Long Zhang,
zhanghailong@xao.ac.cn

RECEIVED 24 February 2024
ACCEPTED 29 March 2024
PUBLISHED 10 April 2024

CITATION
Du X, Zhang H-L, Guo S-C, Zhang Y-Z, Li J, Wang J, Ye X-C, Wu H and Zhang T (2024), A sub-band division algorithm for ultra-wide bandwidth pulsar signals based on RFSoC. *Front. Astron. Space Sci.* 11:1391070. doi: 10.3389/fspas.2024.1391070

A sub-band division algorithm for ultra-wide bandwidth pulsar signals based on RFSoC

Xu Du[1,2], Hai-Long Zhang[1,2,3,4]*, Shao-Cong Guo[5], Ya-Zhou Zhang[1,2], Jian Li[1,2], Jie Wang[1,4], Xin-Chen Ye[1,2,4], Han Wu[1,2] and Ting Zhang[1,2]

[1]Xinjiang Astronomical Observatories, Chinese Academy of Sciences, Urumqi, China, [2]University of Chinese Academy of Sciences, Beijing, China, [3]Key Laboratory of Radio Astronomy, Chinese Academy of Sciences, Nanjing, China, [4]National Astronomical Data Center, Beijing, China, [5]Southeast University, Nanjing, China

In order to realize the real-time processing and analysis of astronomical ultra-wide bandwidth signals, this study proposes a sub-band division algorithm based on RFSoC. The algorithm uses Kaiser window to design FIR prototype low-pass filter, adopts critical sampling polyphase filter bank to decompose ultra-wide bandwidth signal into several sub-bands, and encapsulates each sub-band into VDIF data frame and sends it to GPU server. The algorithm is implemented on RFSoC platform, and its effectiveness is verified by simulation and actual observation. The experimental results show that the algorithm can divide the astronomical ultra-wide bandwidth signal into multiple sub-bands in real time, packetize and transmit them to GPU. This research provides reproducible design and project for ultra-wide bandwidth signal sub-band division with low spectrum leakage and aliasing, high data accuracy, and fast processing speed.

KEYWORDS

rfsoc, ultra-wide bandwidth signal, sub-band division, parallel processing, fourier transform

1 Introduction

Astronomical ultra-wide bandwidth signals are electromagnetic wave signals that cover a wide frequency range from radio waves to microwaves. They carry rich astrophysical information and can be used to detect various phenomena in the Universe, such as pulsars, radio bursts, gravitational waves, etc., which are of great significance for exploring the origin, structure and evolution of the Universe (Curyło et al., 2023). However, the acquisition, transmission and processing of astronomical ultra-wide bandwidth signals face huge challenges, mainly including high sampling rate, large data volume, low signal-to-noise ratio, multi-channel synchronization, etc. To effectively process these signals, they need to be pre-processed, that is, the signals are divided into channels, filtered, encapsulated, etc., to reduce the data volume, improve the signal quality, and facilitate subsequent analysis and storage (An et al., 2021).

Tohtonur et al. implemented a polyphase filter bank based on CUDA, using the powerful floating-point computation and efficient parallel execution capabilities of the graphics processor to effectively improve the processing capacity and computational efficiency of radio astronomical observation data (Tohtonur and Zhang, 2017). Hobbs et al. used the Xilinx Kintex FPGA development board to capture 3328M bandwidth data from the

ultra-wide bandwidth receiver and divide it into 26 128M sub-bands by using the critical sampling polyphase filter bank, and then transmit it to the Medusa GPU processing unit for data processing (Hobbs et al., 2020). The QTT (Qi-Tai Telescope) telescope plans to use an ultra-wide bandwidth receiver to observe astronomical signals in the 150 MHz–115 GHz frequency band. Its 704–4032 MHz ultra-wide bandwidth low-frequency receiver will be put into use first (Wang et al., 2023). Zhang et al. designed a signal division scheme for QTT ultra-wide bandwidth signals and verified the effectiveness of the channel division algorithm using ultra-wide bandwidth pulsar baseband simulation data (Zhang et al., 2023a). Zhang et al. give the details and simulation of ultra-wide bandwidth sub-band division algorithm based on critical sampling polyphase filter banks and oversampling polyphase filter banks, respectively (Zhang et al., 2023b).

This study proposes a sub-band division algorithm for astronomical ultra-wide bandwidth signals based on RFSoC (Radio Frequency System on Chip), which uses CPFB (Critical sampling Polyphase Filter Bank) to split the signal into channels, and then encapsulates it with VDIF format (VLBI Data Interchange Format) and Ethernet format to achieve signal division and transmission. RFSoC is a heterogeneous computing platform that integrates RF data converters, ARM processors and FPGA fabric, which can directly sample and process RF signals without external data converters, thus reducing the system complexity and power consumption, and improving the system integration and performance (Farley et al., 2017). CPFB is a low-pass filter bank implemented by using a polyphase structure, which can split the signal into channels at the Nyquist sampling rate, reducing the signal distortion and noise, and ensuring the signal quality and accuracy (Arnaldi, 2020). This study choose the Kaiser window function as the window function of CPFB, which has a fast side lobe decay rate, which can effectively suppress spectral leakage (Podder et al., 2014). VDIF is an international standard format for encapsulating astronomical data, which can perform checksum and encapsulation for astronomical signals, facilitating signal storage and transmission (Kettenis et al., 2008). Afterwards, Ethernet is used to achieve high-speed, reliable, and low-latency data communication. This study refers to Parkes ultra-wide bandwidth system and makes some improvements, which is the promotion of Zhang et al.'s work, and plans to be applied to QTT ultra-wide bandwidth sub-band division in the future. Currently, QTT is under construction, and simulation tests are carried out using the observation data of Nanshan 26 m telescope in advance.

2 Materials and methods

This study proposes a sub-band division algorithm for astronomical ultra-wide bandwidth signals based on RFSoC, whose flow chart is shown in Figure 1. The ADC in RFSoC is connected to the radio telescope receiver via SMA cable to receive dual-polarization ultra-wide bandwidth astronomical signals, and the satellite clock provides accurate time for RFSoC. In RFSoC, the sampling frequency of ADC is 2.56 GHz, the sampling accuracy is 12 bits, and the sampled signal is a real signal, containing only the real part. The commutator in RFSoC assigns each sample of the input signal to different polyphase branches in turn, realizing the polyphase decomposition of the input signal. The output of the commutator is 20 parallel signals, each with a sampling frequency and bandwidth of 128 MHz, and each sample is a 12-bit real signal. The polyphase filter in RFSoC performs low-pass filtering on each signal to suppress spectral aliasing and signal distortion, and the output of the polyphase filter is 20 parallel signals. The design of the polyphase filter adopts a FIR (Finite Impulse Response) prototype low-pass filter based on Kaiser window, with a cutoff frequency of 68 MHz, an order of 599, coefficients of 16-bit fixed-point numbers, an input sample frequency of 128 MHz for each sub-FIR filter, and an output data width of 28 bits. The 20-Point DFT (Discrete Fourier Transform) module in RFSoC performs an improved fast Fourier transform on each signal, with a length of 20, using the WFFT (Winograd fast Fourier Transform) algorithm and a pipeline structure, to improve the calculation speed and throughput, and obtain a single frequency sub-band carrying the original signal. The output of the 20-Point DFT module is 20 parallel signals, each with a 68-bit wide complex signal. The sub-band selection module in RFSoC performs sub-band selection on each signal to realize the transmission of signals in the specified frequency range. The input of the sub-band selection module is 20 parallel signals, and the default output is two signals in the 320–448 MHz and 448–576 MHz frequency bands, and the width is truncated to 32 bits. The data encapsulation module in RFSoC performs data encapsulation on each signal to realize the format conversion and verification of the signal. The input of the data encapsulation module is dual-polarization four parallel signals, and the output of the data encapsulation module is a serial signal, which is an Ethernet packet in VDIF format, with a size of 8278 bytes. The Ethernet card in RFSoC performs data distribution on the signal to realize the network transmission of the signal. The output signal of the Ethernet card has a data rate of 25 Gbps, and the Ethernet card connects the output signal to the GPU server via optical fiber, realizing high-speed, reliable, and low-latency data communication of the signal.

2.1 Acquisition of signal

Using the direct RF sampling capability of RFSoC, two channels of dual-polarization RAW data are captured by ADC0 and ADC1 on Tile 0 respectively. In order to recover the original signal with 1280 MHz bandwidth from the sampled signal, according to the Nyquist sampling condition $f_s \geq 2B$, the sampling rate is at least 2560 MSPS, which is also called critical sampling. The ADC output data format is set to real, single decimation mode, the number of sampling cycles per AXI4-Stream is 5, the AXI4-Stream clock is 512MHz, and the sampling is performed in the Nyquist first zone. The ADC calibration mode is mode 2, using square wave calibration, whose frequency and amplitude are proportional to the input signal. The AXI4-Stream master interface of the RF data converter IP is connected to the interface of the AXI Interconnect IP, the AXI4-Stream slave interface is connected to the polyphase filter bank, and the AXI Interconnect IP is connected to the Zynq UltraScale + MPSoC, and assigned a base address of 0xA0080000, to achieve data transmission and control between the RF data converter and the processor. The Signal_receive block design is shown in Figure 2.

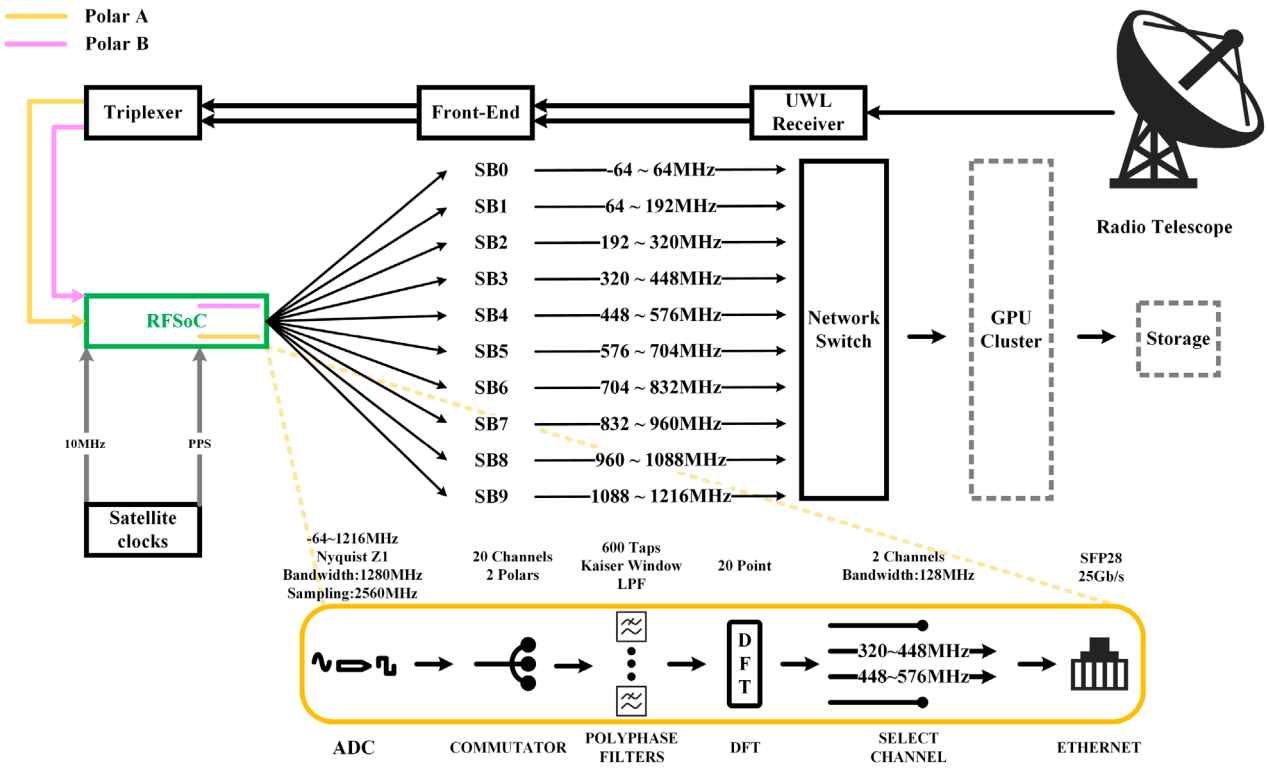

FIGURE 1
Flow chart of ultra-wide bandwidth signal sub-band division.

2.2 Sub-band division

The main difficulty in implementing sub-band division on FPGA is how to deal with the synchronization and switching problem between the high-speed input signal and the low-speed sub-band signal. The solution relies on the critical sampling polyphase filter bank. The algorithm implementation process adopts a pipeline and parallel architecture, which can fully utilize the parallel computing ability of FPGA, improve the operation speed and throughput of the polyphase filter bank, and reduce the hardware resource consumption and power consumption as much as possible. To realize the critical sampling polyphase filter bank in FPGA, it is necessary to design an analysis filter bank. Analysis filter bank includes a commutator and several low-pass filters. According to the Nobel identity, extracting first and then linear filtering is equivalent to linear filtering first and then extracting, as shown in **Equation 1**, where $\downarrow M$ represents the downsampling operation that takes one point for every M sampling points, and $*$ represents the convolution operation.

$$y(n) = x(n) \downarrow M * h(n) = x(n) * h(n) \downarrow M \tag{1}$$

This can replace the order of filtering and extraction, and perform M times extraction first, so that the data stream is in a low-speed state, and then output to the filter. The commutator decomposes the ultra-wide bandwidth high-speed digital signal into multiple low-speed digital signals, to achieve M times extraction, thereby reducing the data volume and processing complexity. The calculation formula is shown in Eqs 2–4, where $x_k(n)$ is the input signal of the k-th polyphase sub-filter, n is the time index after downsampling, and M is the number of sub-filters.

$$x_0(n) = x(nM) \tag{2}$$

$$x_1(n) = x(nM + 1) \tag{3}$$

$$\vdots$$

$$x_{M-1}(n) = x(nM + M - 1) \tag{4}$$

Figure 3 shows the structure diagram of the critical sampling polyphase filter bank, where the red part is the commutator, the blue part is the sub-filter, and the green part is the 20-point parallel DFT.

Since down-sampling will cause spectrum overlap, it is necessary to low-pass filter the input signal to suppress spectral aliasing and leakage, and eliminate the computation of invalid data. This study designs a finite impulse response low-pass filter based on the Kaiser window function. The advantages of the FIR filter are high stability, linear phase, and easy implementation. Its calculation formula is shown in Eq. 5, where $y(k)$ is the output signal, $x(k)$ is the input signal, $h(n)$ is the filter coefficient, which is the impulse response of the Kaiser window FIR low-pass filter, used to filter the input signal, n is the impulse response index, and k is the sample index.

$$y(k) = \sum_{n=0}^{N} h(n)x(k - n) \tag{5}$$

The Kaiser window is a commonly used window function, which can flexibly adjust the window function parameters

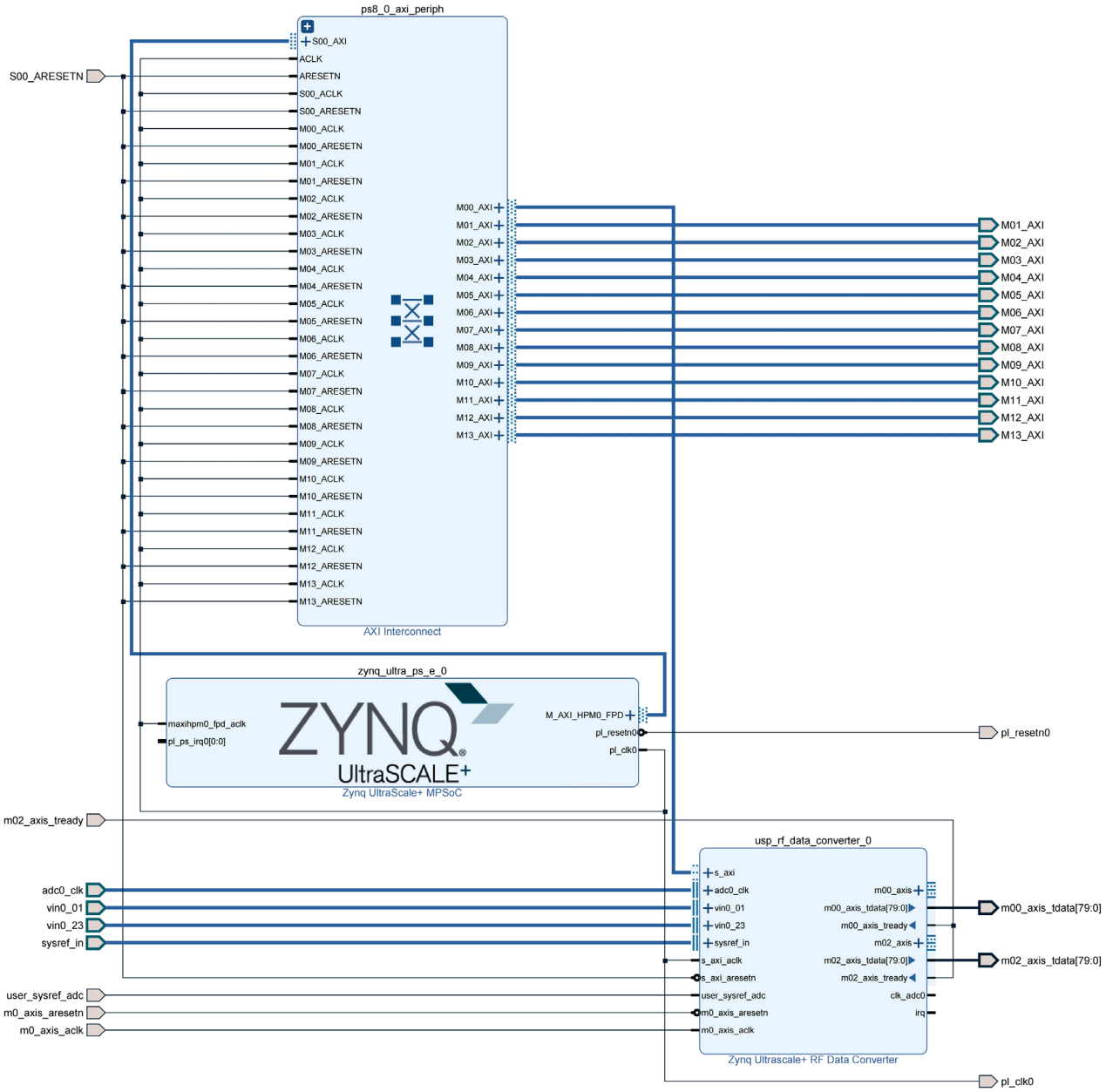

FIGURE 2
Signal_receive block design.

to balance the transition bandwidth and side lobe level. The order of the prototype filter is 599, with 600 coefficients. The stopband cutoff frequency is 68 MHz, $\beta = 5$, using fixed-point quantization, which brings some errors. Figure 4 shows the comparison between the amplitude-frequency response of fixed-point quantization of Kaiser window function and the double-precision floating-point reference amplitude frequency response. As it is difficult for a critically sampled polyphase filter bank to avoid aliasing between adjacent sub-bands through data reuse and channel overlap like an oversampled polyphase filter bank (Zhang et al., 2023), this study increases the attenuation amplitude of the first side lobe to −54db, and increases the filter order to 599 orders, which can also effectively reduce the impact of spectrum aliasing, leakage and influence of quantization errors.

The filtered data needs to go through the DFT module to obtain a single frequency sub-band carrying the original signal. This study uses Winograd FFT and Discrete Fourier Transform to jointly construct a 20-Point DFT module. WFFT is an efficient algorithm for computing the Discrete Fourier Transform of a signal, which reduces the number of multiplications operations at the cost of increasing the number of addition operations (Winograd, 1978). Due to the parallel structure of the FPGA, it can execute multiple addition operations simultaneously, while the multiplication operations are relatively slow and occupy more resources. The Winograd algorithm optimizes the computational

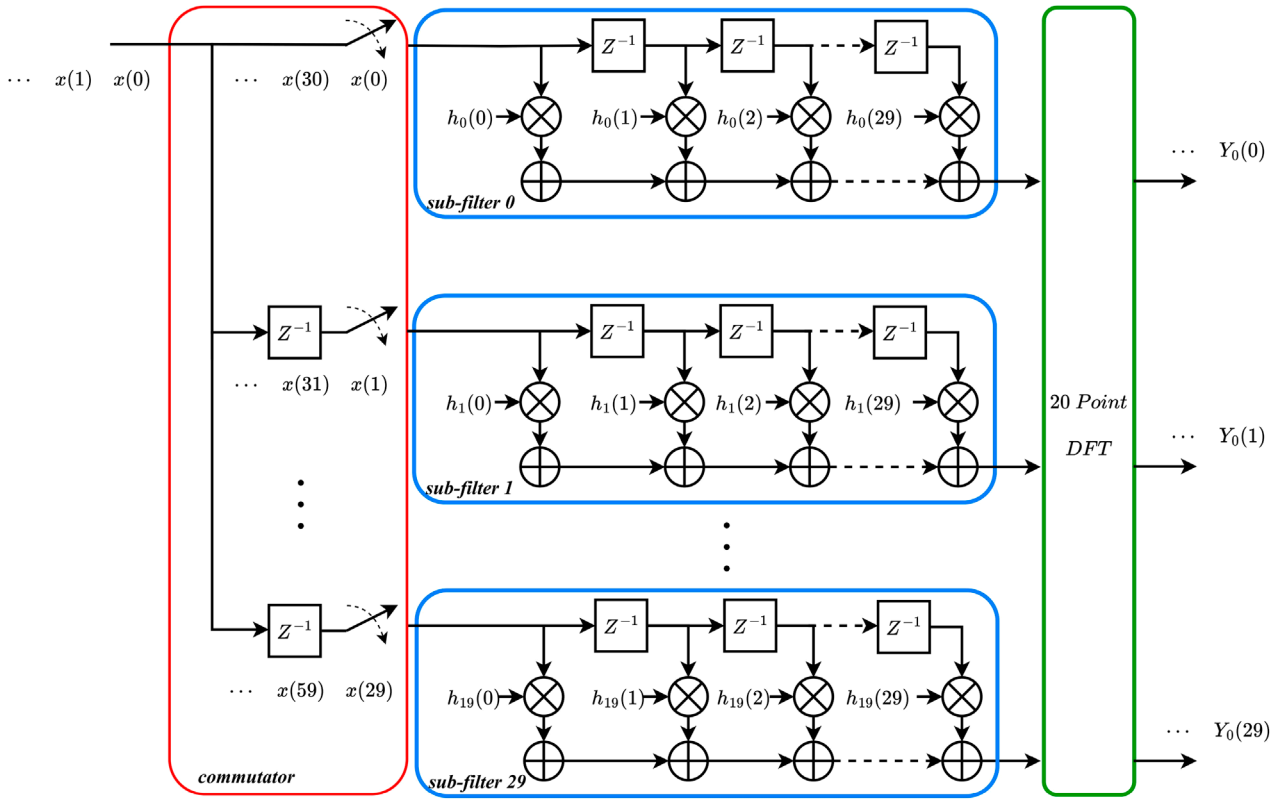

FIGURE 3
Structure diagram of the critical sampling polyphase filter bank.

efficiency by minimizing multiplication operations to improve the overall processing speed. Taking the five point WFFT as an example, the five point DFT is expressed in matrix form and converted to a cyclic correlation form. According to the periodicity of the symmetry factor, it is simplified as:

$$\begin{bmatrix} X_1 - X_0 \\ X_2 - X_0 \\ X_4 - X_0 \\ X_3 - X_0 \end{bmatrix} = \begin{bmatrix} W_5^1 - 1 & W_5^2 - 1 & W_5^4 - 1 & W_5^3 - 1 \\ W_5^2 - 1 & W_5^4 - 1 & W_5^3 - 1 & W_5^1 - 1 \\ W_5^4 - 1 & W_5^3 - 1 & W_5^1 - 1 & W_5^2 - 1 \\ W_5^3 - 1 & W_5^1 - 1 & W_5^2 - 1 & W_5^4 - 1 \end{bmatrix} \cdot \begin{bmatrix} x_1 \\ x_2 \\ x_4 \\ x_3 \end{bmatrix} \tag{6}$$

We assume:

$$\begin{cases} X_1 - X_0 = \varphi_1, X_2 - X_0 = \varphi_2, X_3 - X_0 = \varphi_3, X_4 - X_0 = \varphi_4 \\ W_5^1 - 1 = y_1, W_5^2 - 1 = y_2, W_5^4 - 1 = y_3, W_5^3 - 1 = y_4 \end{cases} \tag{7}$$

Then can get:

$$\begin{cases} s_1 = x_1 + x_3, s_2 = x_1 - x_3, s_3 = x_4 + x_2, s_4 = x_4 - x_2 \\ s_5 = s_1 + s_3, s_6 = s_1 - s_3, s_7 = s_2 + s_4 \\ m_1 = \dfrac{y_1 + y_2 + y_3 + y_4}{4} \cdot s_5, m_2 = \dfrac{y_1 - y_2 + y_3 - y_4}{4} \cdot s_6 \\ m_3 = \dfrac{y_1 + y_2 - y_3 + y_4}{2} \cdot s_2, m_4 = \dfrac{y_2 - y_4}{2} \cdot s_7, m_5 = \dfrac{y_1 - y_2 - y_3 + y_4}{2} \cdot s_4 \\ s_8 = m_1 + m_2, s_9 = m_1 - m_2, s_{10} = m_3 - m_4, s_{11} = m_4 + m_5 \\ s_{12} = s_8 + s_{10}, s_{13} = s_8 - s_{10}, s_{14} = s_9 + s_{11}, s_{15} = s_9 - s_{11} \\ \varphi_0 = x_0 + x_1 + x_2 + x_3 + x_4, \varphi_1 = s_{12}, \varphi_2 = s_{14}, \varphi_3 = s_{13}, \varphi_4 = s_{15} \end{cases} \tag{8}$$

Where $\varphi_0, \varphi_1, \varphi_2, \varphi_3, \varphi_4$ are the results of 5-Point WFFT.

The basic principle of the 20-Point DFT module is to decompose it into 4 five-point WFFTS and 5 four-point DFTS using the prime factor method and the Chinese remainder theorem mapping, where four and five are two coprime integers, avoiding the twiddle factors multiplication in the Cooley-Tukey algorithm (Bhagat et al., 2018). Suppose a sequence of length $N = 20$ is X(k), where N can be decomposed into the product of two prime factors 4 and 5. That is, $N = N1 * N2 = 4 * 5$, where $gcd(5, 4) = 1$. Therefore, the input index n and the output index k can be respectively mapped by the multi-factor simple mapping and the Chinese remainder theorem mapping, that is:

$$\begin{cases} n \equiv \sum_{i=1}^{2} \dfrac{N}{N_i} n_i N \\ k \equiv \sum_{i=1}^{2} \dfrac{N}{N_i} t_i k_i N \end{cases} \tag{9}$$

Where $(n_i, k_i = 0, 1)$, t_i satisfies $\sum_{i=1}^{2} \frac{N}{N_i} t_i \equiv 1 \, (mod N)$ and denote

$$\begin{cases} x(n_1, n_2) = x\left(\dfrac{N}{N_1} n_1 + \dfrac{N}{N_2} n_2\right) \\ X(k_1, k_2) = X(N_1 t_1 k_1 + N_2 t_2 k_2) \end{cases} \tag{10}$$

Then a 2D DFT can be obtained, that is:

$$X(k_1, k_2) = \sum_{n_1=0}^{N_1-1} \sum_{n_2=0}^{N_2-1} x(n_1, n_2) W_{N_1}^{n_1 k_1} W_{N_2}^{n_2 k_2} (k_i = 0, 1; i = 1, 2) \tag{11}$$

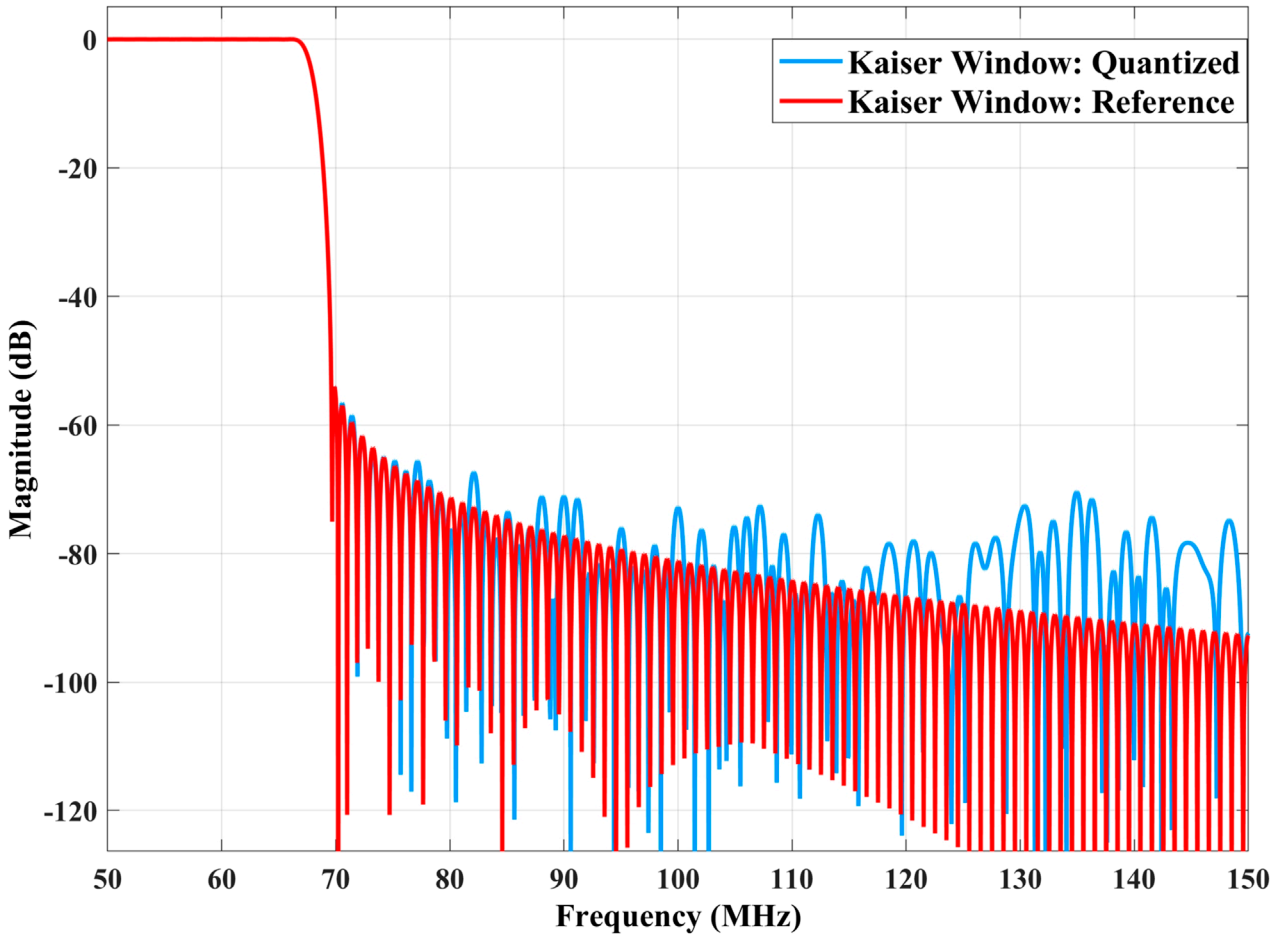

FIGURE 4
Comparison of the fixed-point quantization amplitude frequency response and the double-precision floating-point reference amplitude frequency response of the Kaiser window.

In the 20-Point DFT module, the 20 point sequence is decomposed into four five point sequences, and then WFFT is performed on each 5 point sequence to obtain four five point coefficients, and then these coefficients are rearranged into five four point sequences, and then DFT is performed on each 4 point sequence to obtain five four point coefficients, and finally these coefficients are rearranged into a 20 point coefficient, which is the final result. The 5-Point WFFT module and the 4-Point DFT module are implemented separately and combined to obtain the 20-Point DFT module, and its calculation structure is shown in Figure 5.

In the hardware implementation, the FIR filter uses the FIR Compiler IP core, with 20 sub-FIR filters, each with 30 coefficients. The coefficients are generated by splitting the coefficients of the FIR prototype low-pass filter based on the Kaiser window. The input sample frequency and clock frequency are both 128MHz, the input data width is 12 bits, the coefficient width is 16 bits, and the full precision mode is used. The filtered data is real and needs to be converted to complex form, to prepare the data for the subsequent 20-Point DFT. The Real2complex module written in Verilog is used to take the filtered real signal as the real part of the complex signal, and 0 as the imaginary part of the complex signal. To achieve real-time processing of ultra-wide bandwidth high-speed data streams, a 20-Point DFT module written in Verilog is used, which can realize real-time parallel DFT processing. The output data is conjugate symmetric, and only half of the data needs to be retained. This study uses ZCU111 board, chip model xzcu28dr-ffvg-1517-1-e, developed in Ubuntu 20.04 system. The IP developed by our team include Comutator, Selector, Real2complex, WFT, DFT, Ethernet _ MAC, Ethernet _ VDIF, Datasnapshot and so on. All IP and project have been publicly available on the gitee[1] website. PS block design as shown in Figure 6, the RFSoC receives and processes dual-polarization data, and the Polar_a block design of polarization A is shown in Figure 7.

1 https://gitee.com/WhataDavid/cspfb_on_rfsoc

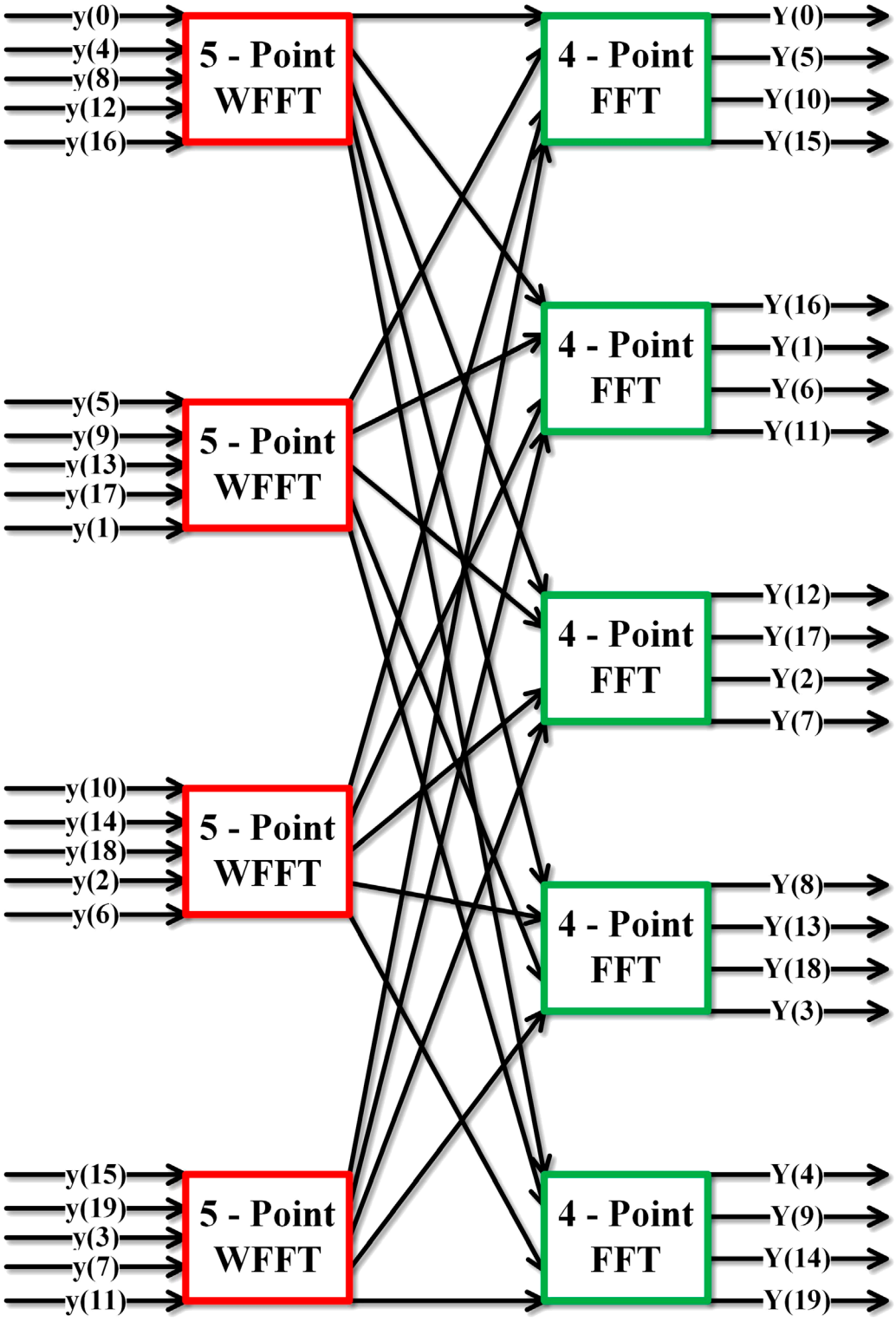

FIGURE 5
Implementation structure of 20-Point DFT.

2.3 Data distribution

The data after sub-band division needs to be sent to the GPU for data analysis via Ethernet. Before sending, the sub-band data is encapsulated. The Ethernet transmission of astronomical ultra-wide bandwidth signals not only requires the data packets to be encapsulated in Ethernet frames, but also in the general astronomical format VDIF, which is a standard format for

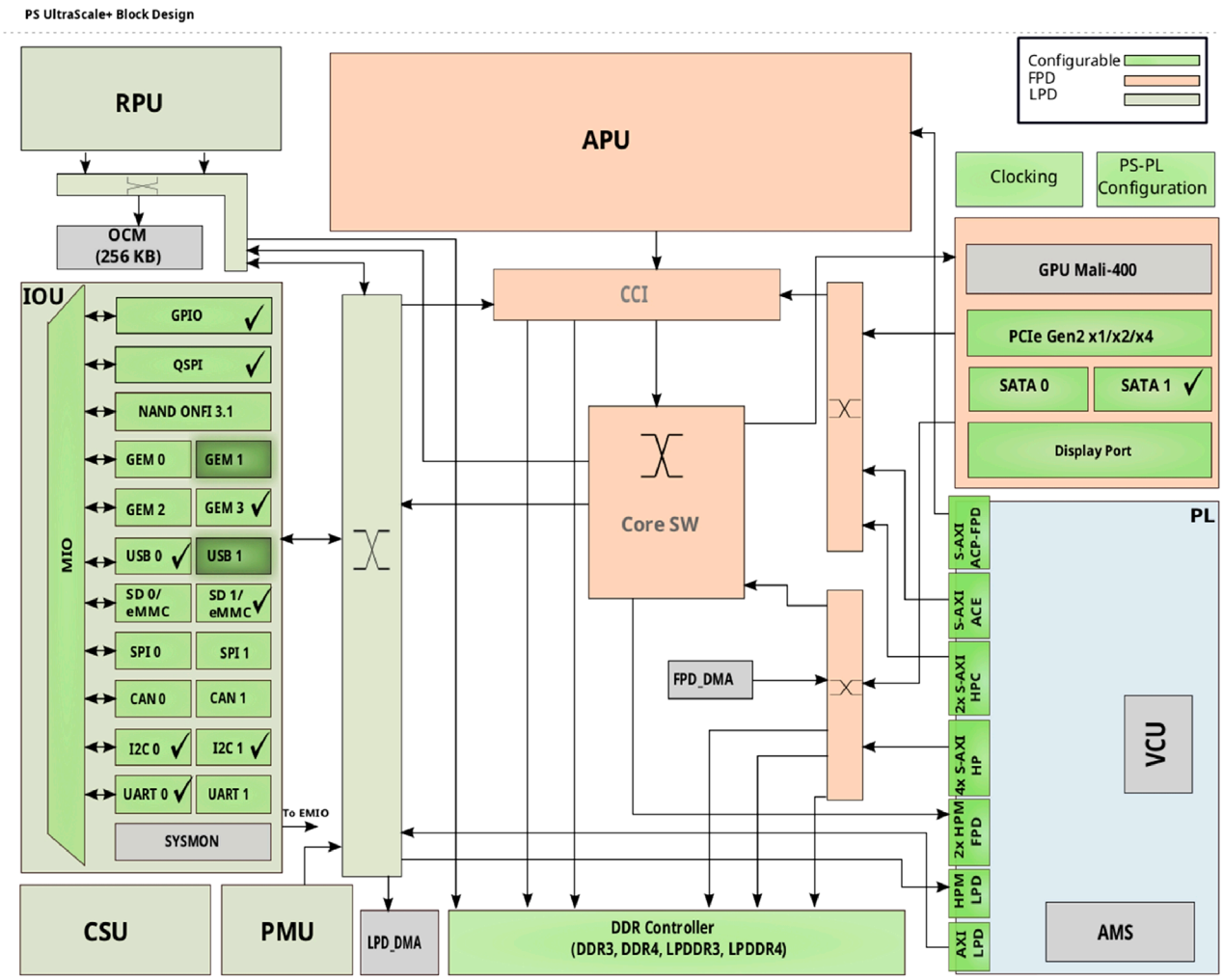

FIGURE 6
PS block design.

transmitting radio interferometry data. It can support various data types, such as time domain, frequency domain, polarization, etc., and various data transmission methods, such as UDP, TCP, etc. Ethernet frames are protocol data units of the network interface layer, which consist of three parts: frame header, data part, and frame tail. The frame header and tail contain some necessary control information, and the data part contains the data passed down from the upper layer. Different network layer protocols use different frame header formats for identification and processing. The TCP/IP protocol stack model diagram containing VDIF segments is shown in Figure 8.

The total length of the VDIF frame header in the application layer is 32 bytes, and the length of the data part is 8192 bytes, that is, the total length of the VDIF frame is 8224 bytes. UDP is a connectionless transport layer protocol. The total length of the UDP frame header is 8 bytes, and the length of the data part is 8224 bytes, that is, the total length of the UDP frame is 8232 bytes. The IP frame header in the network layer indicates the source IP address and the destination IP address. The total length of the IP frame header is 20 bytes, and the length of the data part is 8232 bytes, that is, the total length of the IP frame is 8252 bytes. The total length of the Ethernet frame header and tail is 26 bytes, which include preamble, start-of-frame delimiter, destination MAC address, source MAC address, type, frame check sequence, and interframe gap. The length of the data part is 8252 bytes, that is, the total length of the Ethernet frame is 8278 bytes.

In hardware implementation, data encapsulation mainly consists of three modules, namely, VDIF format encapsulation module, Ethernet encapsulation module and local data interaction module. Ethernet_vdif_ch0 is the VDIF format encapsulation module, which encapsulates the astronomical data according to the VDIF protocol and prepares the data for the Ethernet transmission layer. Ethernet_mac is an Ethernet frame encapsulation module, which adds UDP header, IP header, Ethernet header and tail to the VDIF encapsulated data, and adjusts the data format to the XGMII interface standard, preparing the data for the physical layer transmission. The XGMII interface includes an 8-bit xgmii_txc control interface and a 64-bit xgmii_txd data interface. Each bit of the xgmii_txc interface

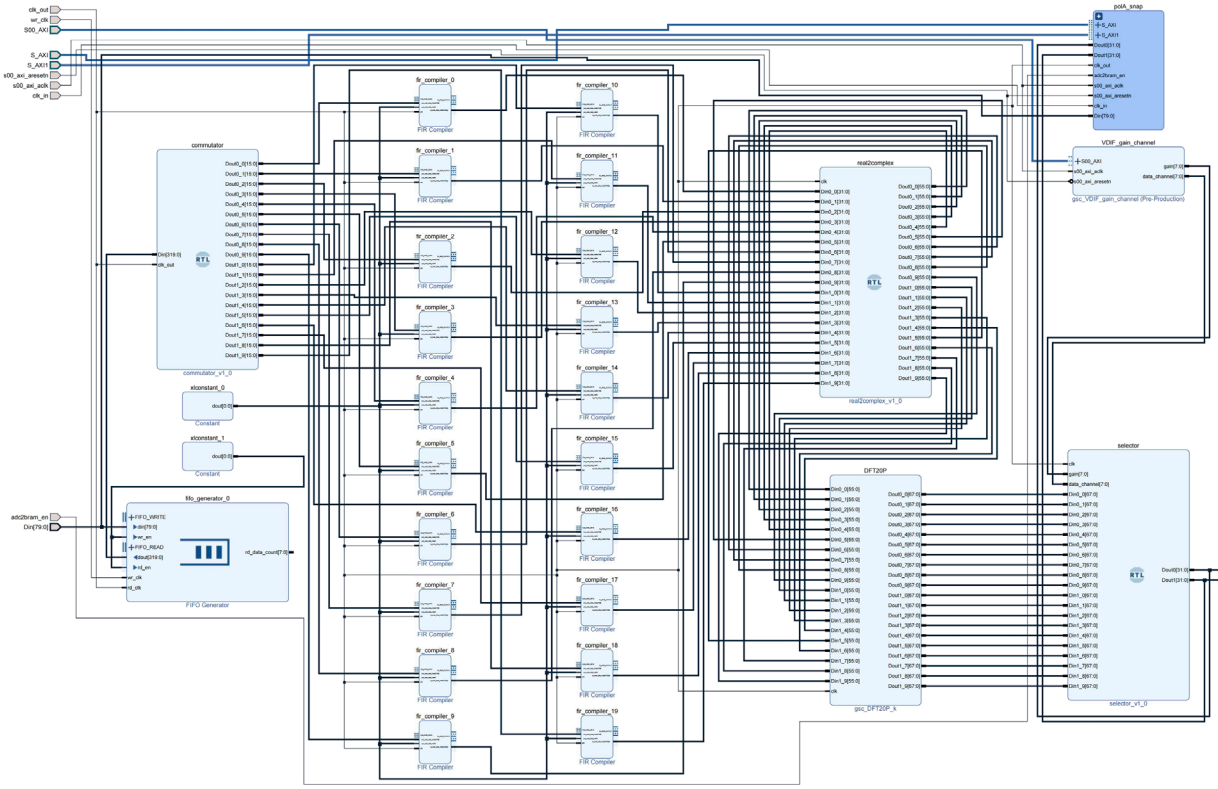

FIGURE 7
Polar_a block design.

Invalid Data	Legacy Mode	Seconds from Reference Epoch	Unassigned	Reference Epoch	Data Frames per Second	VDIF Version	Channels of Data Array	Data Frame length	Data Type	Bits per Sample	Thread ID	Station ID	Extended User Data	Data Array
1	1	30	2	6	24	3	5	24	1	5	10	16	128	65536

Source Port	Destination Port	Length	Checksum	Data
16	16	16	16	65792

Version	Internet Header Length	Type of Service	Total Length	Identification	Flags	Fragment Offset	TTL	Protocol	Header Checksum	Source IP	Destination IP	Data
4	4	8	16	16	3	13	8	8	16	32	32	65856

Preamble	Start of Frame Delimiter	Destination Mac	Source Mac	Type	Data	CRC	Interpacket Gap
56	8	48	48	16	66016	32	96

FIGURE 8
VDIF/TCP/IP protocol stack model diagram.

corresponds to one byte of data in the xgmii_txd interface. When it is 1, it indicates that the byte is control information, and when it is 0, it indicates that the byte is data. The sending state transition diagram is shown in Figure 9, where the meanings of the four states are:

IDLE_INTERFRAME: Send interframe gap to ensure that the GPU has enough time to process the previous frame data. The interframe gap is cyclically sent as 0 × 07, and the control interface values are all 1. After receiving the ready-to-send signal from the encapsulation module, it transitions to the SEND_PREAMBLE state.

SEND_PREAMBLE: Send preamble state, send 7 bytes of synchronization code and 1 byte of frame start symbol, and pull up the response signal, and transition to the SEND_DATA state.

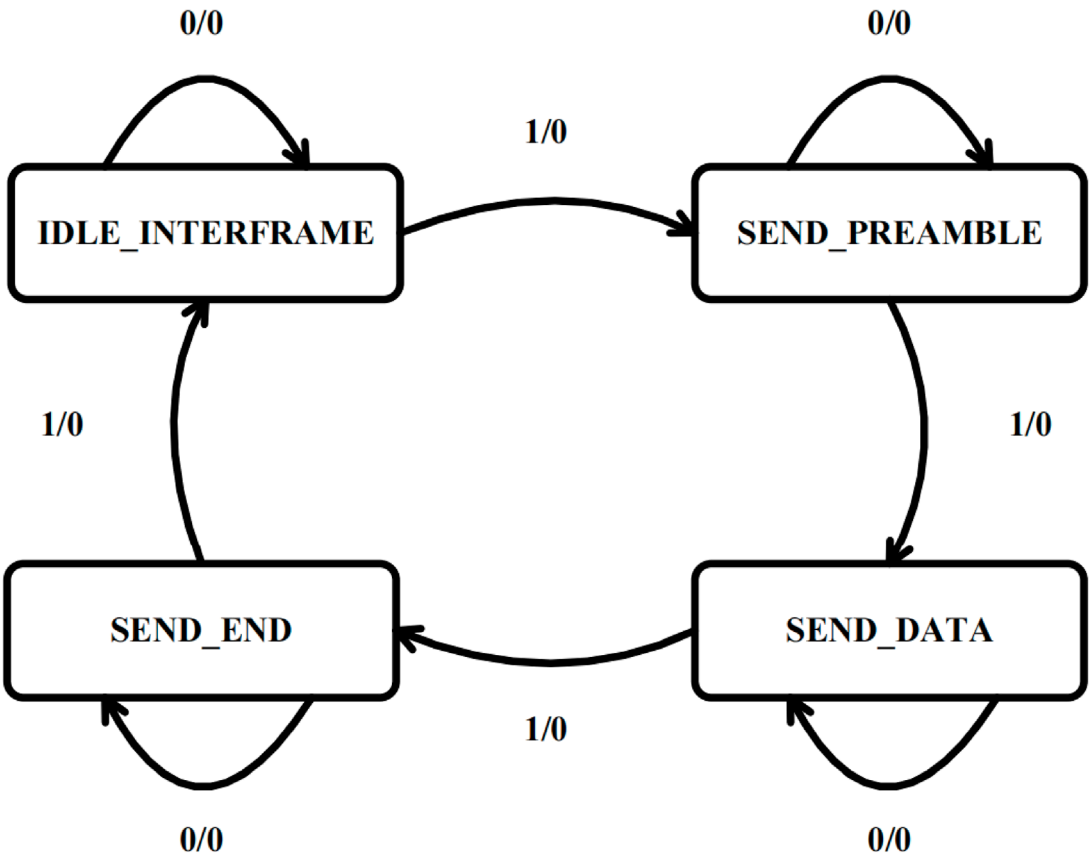

FIGURE 9
Sending state transition diagram.

SEND_DATA: Send data state, start sending the encapsulated data in byte order, until receiving the end signal, and transition to the SEND_END state.

SEND_END: Send end state, send the last data and 4-byte CRC32 check sequence, check whether the interframe gap is correct, receive the next ready-to-send signal in the IDLE_INTERFRAME state, and jump to the next state.

VDIF_Ctrl is a module that interacts with MPSoC to transfer data. Its function is to read the destination IP, destination MAC, port number, VDIF thread number and other information from the AXI bus of MPSoC, and then transmit them to the VDIF packaging module and Ethernet packaging module through the AXI Stream bus, which facilitates the transmission and control of the information within the frame, and improves the flexibility and compatibility of data transmission. MPSoC IP serves as a logical connection between PS and PL. This study implements the output of four-channel signals with dual polarization, and each channel signal needs to be packaged by VDIF and Ethernet. The Ch0_frame_pack_block design is shown in Figure 10.

The network card is configured by using the 10G/25G Ethernet Subsystem IP, selecting the Ethernet PCS/PMA 64-bit as the core architecture, processing the MAC separately, 25.78125 Gbps as the line rate, AXI4-Lite as the data interface, BASE-R as the physical layer standard, using optical fiber for transmission, configuring 156.25 MHz as the GT Refclk, selecting 128 MHz as the DRP Clocking, and turning off the FEC Logic, Auto Negotiation and IEEE PTP 1588V2.

After connecting and correctly configuring all the IPs, synthesize and implement the project, burn the bitstream to RFSoC, configure the LMK04208 and LMX2594 clock chips, only turn on CLKOUT0 and CLKOUT3, reduce the power consumption, and perform experimental analysis.

3 Result

3.1 Simulation test result

The algorithm divides the ultra-wide bandwidth data of 64–1344 MHz into 10 sub-bands. Total bandwidth of 1280 MHz and per sub-band width of 128 MHz. They are 64–192, 192–320, 320–448, 448–576, 576–704, 704–832, 832–960, 960–1088, 1088–1216 and 1216–1344 MHz sub-band. Among them, the signals of two sub-bands, 320–448 and 448–576 MHz, are encapsulated and transmitted to the GPU server. To test the effectiveness of the sub-band division, a sweep signal of 320–576 MHz is generated by the signal generator, with a step of 32 MHz, to obtain single-frequency signals of 320, 352, 384, 416, 448, 480, 512, 544, 576 MHz. To avoid the signal being at the edge of the sub-band, the spectrum diagrams of the sub-band division results are plotted when the test signal is at 352,

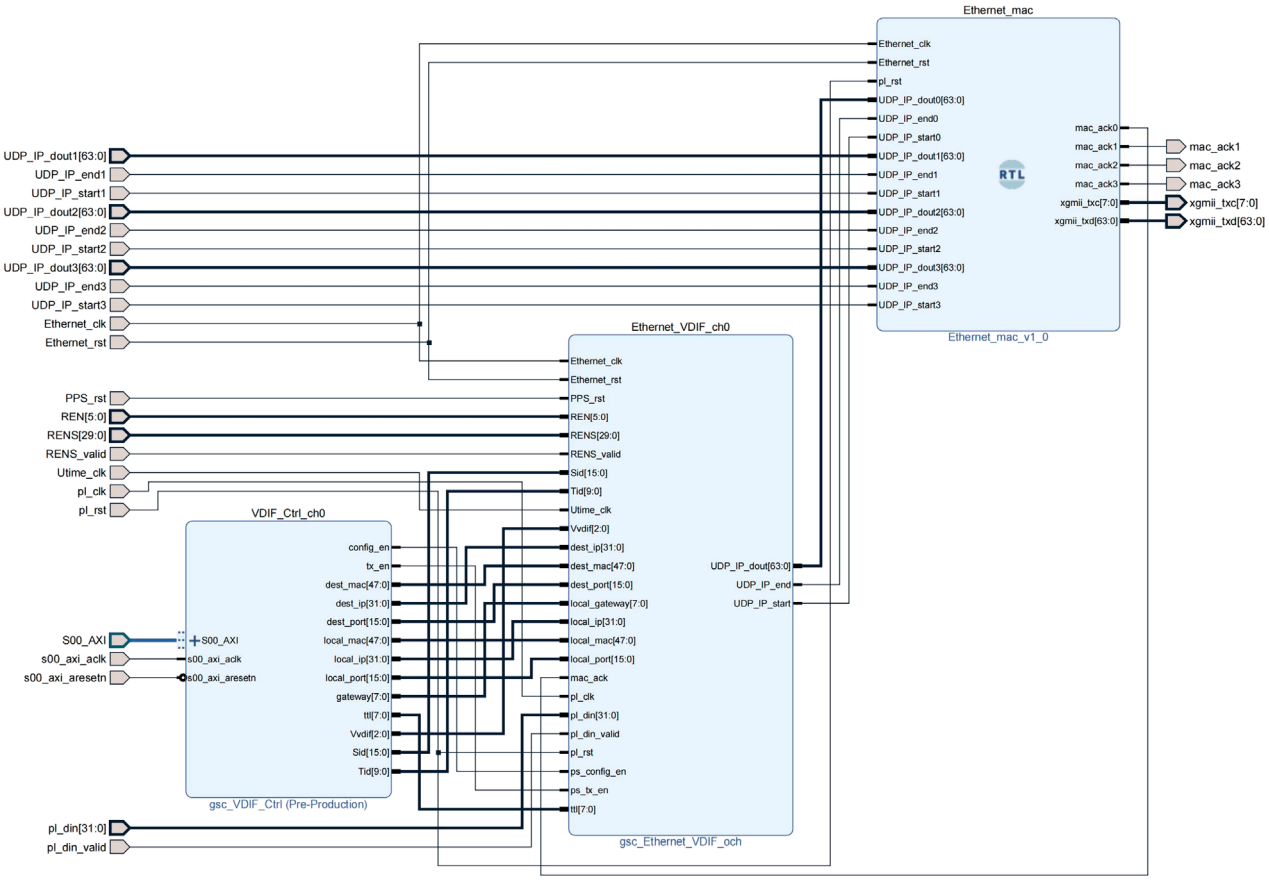

FIGURE 10
Ch0_frame_pack_block design.

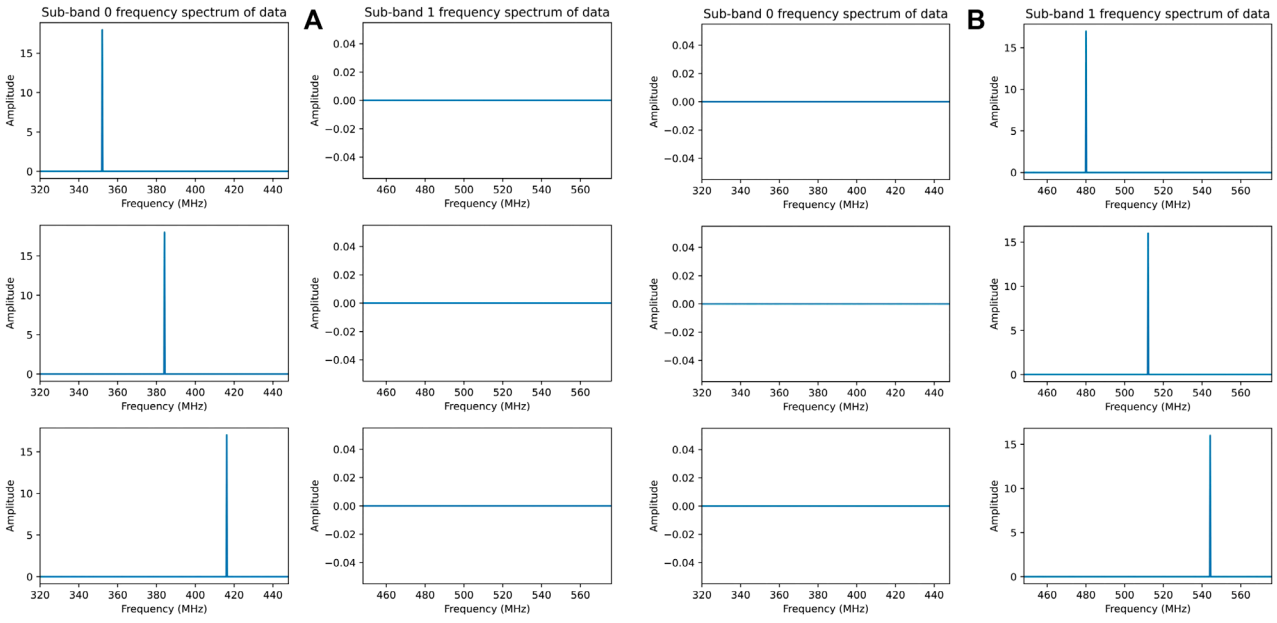

FIGURE 11
(A) Spectrum diagrams of the sub-band division results when the test signal is at 352, 384, 416 MHz. **(B)** Spectrum diagrams of the sub-band division results when the test signal is at 480, 512, 544 MHz.

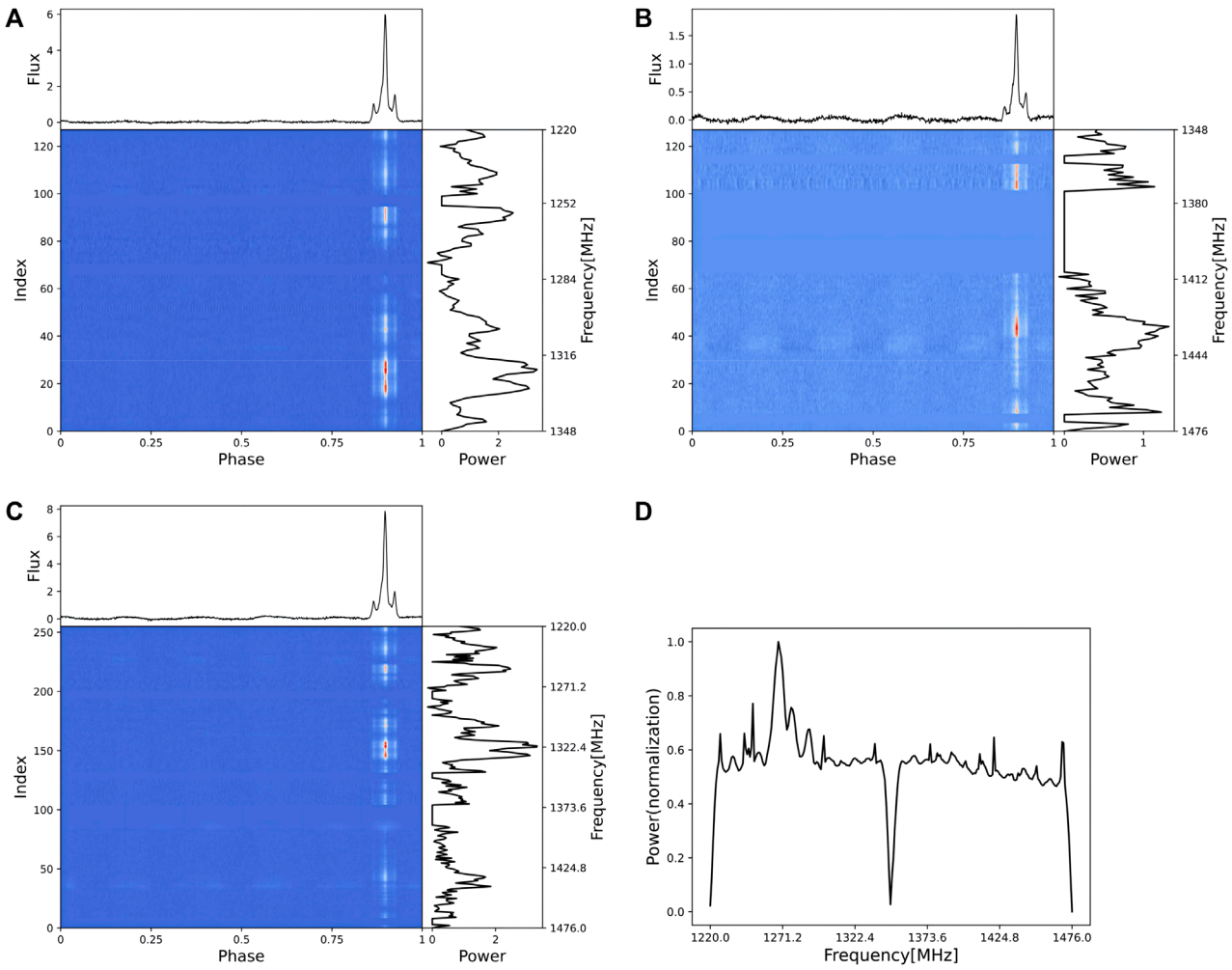

FIGURE 12
(A) J0332 + 5434 dynamic spectrum of sub-band 3. **(B)** J0332 + 5434 dynamic spectrum of sub-band 4. **(C)** J0332 + 5434 dynamic spectrum after merging sub-band three and sub-band 4. **(D)** J0332 + 5434 spectrum after merging sub-band three and sub-band 4.

384, 416 MHz and when the test signal is at 480, 512, 544 MHz. The data is read out from the memory after being divided into sub-bands by the polyphase filter bank. As shown in Figure 11A, when the test signal is in the 320–448 MHz range, the signal falls into the sub-band 0 range and has equal amplitude after the sub-band division. And there is no signal in the sub-band one range, indicating that the signal is effectively divided into sub-bands. As shown in Figure 11B, when the test signal is in the 448–576 MHz range, the signal falls into the sub-band one range and has equal amplitude after the sub-band division, and there is no signal in the sub-band 0 range, indicating that the signal is effectively divided into sub-bands.

3.2 Actual observation result

We tested the ultra-wide bandwidth signal sub-band division algorithm using the L-band 1 GHz bandwidth receiver of the 26-m radio telescope at Nanshan, Urumqi. By down-converting the Nanshan observation data, we used RFSoC to process 1280 MHz bandwidth data, divided the data into sub-bands, selected and output the 1220–1476 MHz dual-polarization sub-band data, and connected to the GPU server using $4 * 25$G SFP28 to 100G QSFP28 high-speed cables. We used the GPU server to receive the RFSoC sub-band data and plot the spectrum and dynamic spectrum.

We observed the pulsar source J0332 + 5434 for 5 min, and RFSoC divided the observation signal into sub-bands. We used DSPSR to process the received sub-band data, and after removing some channels that were interfered, we obtained the dynamic spectra of sub-band three and sub-band 4 as shown in Figure 12A and Figure 12B, respectively, where clear pulsar profiles can be observed. The dynamic spectrum after sub-band synthesis is shown in Figure 12C, and Figure 12D shows the spectrum of sub-band three and sub-band four merged, where two sub-bands can be clearly seen. The experimental results are consistent with the expectations. Due to the use of critical sampling polyphase filter bank, there will be sideband roll-off phenomenon at the sub-band edge connection,

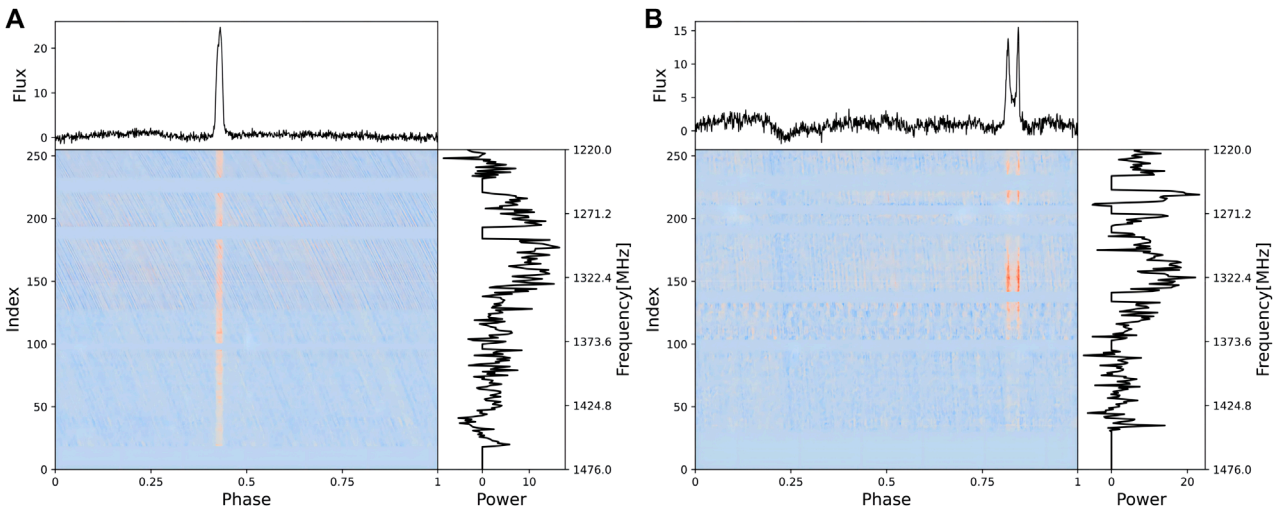

FIGURE 13
(A) J1935 + 1616 dynamic spectrum after merging sub-band three and sub-band 4. **(B)** J2022 + 2854 dynamic spectrum after merging sub-band three and sub-band 4.

and we plan to improve it by using oversampling polyphase filter bank in the future.

By switching the pulsar observation sources, we also observed J1935 + 1616 and J2022 + 2854, and the implemented RFSoC firmware can effectively perform the sub-band division function of astronomical ultra-wide bandwidth signals. The dynamic spectra are shown in Figure 13A and Figure 13B, respectively.

4 Conclusion

This study presents a sub-band division algorithm for astronomical ultra-wide bandwidth pulsar signals based on RFSoC, which solves the problems of real-time processing and transmission of astronomical ultra-wide bandwidth pulsar signals. The algorithm adopts a filter coefficient design method based on the Kaiser window function, with a FIR filter coefficient of 599 order, the first side lobe attenuation amplitude of −54 db, and uses a 12-bit wide ADC and a clock of 512 MHz, with low spectrum leakage and aliasing, high data accuracy, and fast processing speed. It uses CPFB and improved DFT to channelize the signals, which improves the quality and efficiency of the signals. Then it performs VDIF and Ethernet encapsulation on the signals, which realizes the division and transmission of ultra-wide bandwidth signals. Through simulation tests and actual observations, the feasibility, effectiveness and stability of the algorithm are verified.

Data availability statement

The original contributions presented in the study are included in the article/Supplementary material, further inquiries can be directed to the corresponding author.

Author contributions

XD: Conceptualization, Data curation, Formal Analysis, Funding acquisition, Investigation, Methodology, Project administration, Resources, Software, Supervision, Validation, Visualization, Writing–original draft, Writing–review and editing. H-LZ: Conceptualization, Data curation, Formal Analysis, Funding acquisition, Investigation, Methodology, Project administration, Resources, Software, Supervision, Validation, Visualization, Writing–original draft, Writing–review and editing. S-CG: Conceptualization, Data curation, Formal Analysis, Investigation, Methodology, Project administration, Resources, Software, Validation, Writing–original draft. Y-ZZ: Conceptualization, Data curation, Investigation, Methodology, Project administration, Resources, Validation, Writing–original draft. JL: Conceptualization, Software, Data curation, Methodology, Project administration, Resources, Validation, Writing–original draft. JW: Funding acquisition, Methodology, Project administration, Validation, Writing–original draft, Conceptualization, Investigation. X-CY: Resources, Conceptualization, Investigation, Methodology, Project administration, Validation, Writing–original draft. HW: Conceptualization, Formal Analysis, Methodology, Validation, Writing–review and editing. TZ: Investigation, Resources, Supervision, Validation, Writing–review and editing.

Funding

The author(s) declare financial support was received for the research, authorship, and/or publication of this article. This work is supported by the National Key R&D Program of China No. 2021YFC2203502 and 2022YFF0711502; the

National Natural Science Foundation of China (NSFC) (12173077 and 12003062); the Tianshan Innovation Team Plan of Xinjiang Uygur Autonomous Region (2022D14020); the Tianshan Talent Project of Xinjiang Uygur Autonomous Region (2022TSYCCX0095); the Scientific Instrument Developing Project of the Chinese Academy of Sciences, grant No. PTYQ2022YZZD01; China National Astronomical Data Center (NADC); the Operation, Maintenance and Upgrading Fund for Astronomical Telescopes and Facility Instruments, budgeted from the Ministry of Finance of China (MOF) and administrated by the Chinese Academy of Sciences (CAS); Natural Science Foundation of Xinjiang Uygur Autonomous Region (2022D01A360); the Chinese Academy of Sciences (CAS) "Light of West China" Program under No. 2022-XBQNXZ-012.

Acknowledgments

The software and software environment used in the experiment of this paper is from the National Astronomical Observatories of Chinese Academy of Sciences. Thanks to Teacher Ran Duan and his team members for their support and guidance.

Conflict of interest

The authors declare that the research was conducted in the absence of any commercial or financial relationships that could be construed as a potential conflict of interest.

The handling editor (HW) declared a shared parent affiliation with the author(s) (HZ) at the time of review.

Publisher's note

All claims expressed in this article are solely those of the authors and do not necessarily represent those of their affiliated organizations, or those of the publisher, the editors and the reviewers. Any product that may be evaluated in this article, or claim that may be made by its manufacturer, is not guaranteed or endorsed by the publisher.

References

An, X. M., Chen, M. Z., Pei, X., Li, J., and Duan, X. F. (2021). High-speed baseband data recording system for radar astronomy research. *Acta Astron. Sin.* 62 (5), 51. doi:10.15940/j.cnki.0001-5245.2021.05.005

Arnaldi, L. H. (2020). "Implementation of a polyphase filter bank channelizer on a ZYNQ FPGA," in 2020 Argentine Conference on Electronics (CAE), Buenos Aires, Argentina, 27-28 February 2020 (IEEE), 57–62. doi:10.1109/CAE48787.2020.9046377

Bhagat, N., Valencia, D., Alimohammad, A., and Harris, F. (2018). High-throughput and compact FFT architectures using the Good–Thomas and Winograd algorithms. *IET Commun.* 12 (8), 1011–1018. doi:10.1049/iet-com.2017.0837

Curyło, M., Pennucci, T. T., Bailes, M., Bhat, N. R., Cameron, A. D., Dai, S., et al. (2023). Wide-band timing of the Parkes pulsar timing array UWL data. *Astrophysical J.* 944 (2), 128. doi:10.3847/1538-4357/aca535

Farley, B., Erdmann, C., Vaz, B., McGrath, J., Cullen, E., Verbruggen, B., et al. (2017). "A programmable RFSoC in 16nm FinFET technology for wideband communications," in 2017 IEEE Asian Solid-State Circuits Conference (A-SSCC), Seoul, Korea (South), 06-08 November 2017 (IEEE), 1–4. doi:10.1109/ASSCC.2017.8240201

Hobbs, G., Manchester, R. N., Dunning, A., Jameson, A., Roberts, P., George, D., et al. (2020). *An ultra-wide bandwidth (704 to 4 032 MHz) receiver for the Parkes radio telescope*, 37. Australia: Publications of the Astronomical Society of Australia, e012. doi:10.1017/pasa.2020.2

Kettenis, M., Phillips, C., Sekido, M., and Whitney, A. (2008). *VLBI data Interchange format (VDIF) specification*.

Podder, P., Khan, T. Z., Khan, M. H., and Rahman, M. M. (2014). Comparative performance analysis of hamming, hanning and blackman window. *Int. J. Comput. Appl.* 96 (18), 1–7. doi:10.5120/16891-6927

Tohtonur, H. L., and Zhang, J. W. (2017). A design of polyphase filter bank for radio astronomy based on CUDA. *Astronomical Res. Technol.* 14 (1), 117–123. doi:10.14005/j.cnki.issn1672-7673.20160518.003

Wang, N., Xu, Q., Ma, J., Liu, Z., Liu, Q., Zhang, H., et al. (2023). The Qitai radio telescope. *Sci. China Phys. Mech. Astronomy* 66 (8), 289512. doi:10.1007/s11433-023-2131-1

Winograd, S. (1978). On computing the discrete Fourier transform. *Math. Comput.* 32 (141), 175–199. doi:10.2307/2006266

Zhang, H. L., Zhang, M., Zhang, Y. Z., Wang, J., Ye, X. C., Wang, W. Q., et al. (2023b). Channelization of wideband signal based on critical sampling polyphase filter banks. *J. Jilin Univ. Eng. Technol. Ed.* 53 (8), 2388–2394. doi:10.13229/j.cnki.jdxbgxb.20220274

Zhang, H. L., Zhang, Y. Z., Zhang, M., Wang, J., Li, J., Ye, X. C., et al. (2023a). Research on ultra-wide bandwidth low-frequency signal channelization for Xinjiang 110 m radio telescope. *Res. Astronomy Astrophysics* 23 (12), 125023. doi:10.1088/1674-4527/ad0427

Zhang, M., Zhang, H. L., Zhang, Y. Z., Wang, J., Guo, S. C., and Meng, Q. (2023c). Research on channelization techniques of radio astronomical wideband signal with oversampled polyphase filter banks. *Res. Astronomy Astrophysics* 23 (8), 085012. doi:10.1088/1674-4527/acd73b

frontiers | Frontiers in Astronomy and Space Sciences

TYPE Original Research
PUBLISHED 30 April 2024
DOI 10.3389/fspas.2024.1369368

OPEN ACCESS

EDITED BY
Shangqing Yang,
Huazhong University of Science and Technology, China

REVIEWED BY
Debi Prasad Choudhary,
California State University, United States
Victor De La Luz,
National Autonomous University of Mexico, Mexico

*CORRESPONDENCE
Changhui Rao,
chrao@ioe.ac.cn

RECEIVED 12 January 2024
ACCEPTED 08 April 2024
PUBLISHED 30 April 2024

CITATION
Rao C, Ji H, Bao H, Rao X, Yang J, Guo Y, Zhang L, Zhong L, Fan X, Zhang Q, Li C and Bian Q (2024), PASAT: pathfinder in solar adaptive telescope.
Front. Astron. Space Sci. 11:1369368.
doi: 10.3389/fspas.2024.1369368

PASAT: pathfinder in solar adaptive telescope

Changhui Rao[1,2,3]*, Haisheng Ji[3,4], Hua Bao[1,2], Xuejun Rao[1,2], Jinsheng Yang[1,2], Youming Guo[1,2], Lanqiang Zhang[1,2], Libo Zhong[1,2], Xinlong Fan[1,2], Qingmin Zhang[4], Cheng Li[1,2] and Qing Bian[1,2,3]

[1]National Laboratory on Adaptive Optics, Chengdu, Sichuan, China, [2]Institute of Optics and Electronics, Chinese Academy of Sciences, Chengdu, Sichuan, China, [3]School of Electronic, Electrical and Communication Engineering, University of Chinese Academy of Sciences, Beijing, China, [4]Purple Mountain Observatory, Chinese Academy of Sciences, Nanjing, China

In the forefront of quantitative solar physics research using large-aperture ground-based solar optical telescopes, high-contrast observation along with high-accuracy polarimetric measurement in the solar active region are required. In this paper, we propose a novel high-contrast imaging telescope construction with a 60 cm medium aperture, namely, the PAthfinder in Solar Adaptive Telescope (PASAT), in which a deformable secondary mirror is used as the adaptive optical correction device and a symmetrical optical path design is employed, leading to the least Muller matrix polarization instruments. The telescope can provide a high-resolution magnetic field with high accuracy for the solar active regions, as well as high-contrast images with a superior signal-to-noise ratio and photometric accuracy of the solar photosphere and chromosphere. These data will be directly used for a better understanding of the evolution and release of magnetic energy, which will help in improving space weather forecasting. Meanwhile, PASAT will accumulate the relevant techniques for constructing similar, larger solar telescopes in the future.

KEYWORDS

solar telescope, high resolution, adaptive optics, deformable secondary mirror, high contrast

1 Introduction

Solar activity is the source of space weather, and active bodies such as solar flares and coronal mass ejections are large-scale magnetic energy-releasing processes in the solar atmosphere. However, their energy accumulation and triggering are rooted in the chromosphere and photosphere and have smaller scales (Low, 2015; Wang et al., 2015; Choudhuri, 2017). Ground-based, large-aperture solar telescopes are still the best choice for studying the ultra-fine structure of solar active regions. Adaptive optical technology is also increasingly mature, which ensures the high-resolution observation of ground-based telescopes near the diffraction limit (Cao et al., 2010; Rimmele and Marino, 2011).

For solar observation, we not only need larger aperture telescopes to achieve higher spatial resolution and collect more photons, but we also need higher imaging contrast to achieve a higher detection signal-to-noise ratio and photometric accuracy. However, a prominent drawback of solar telescopes is the high scattered light, which makes the imaging contrast far from the requirements.

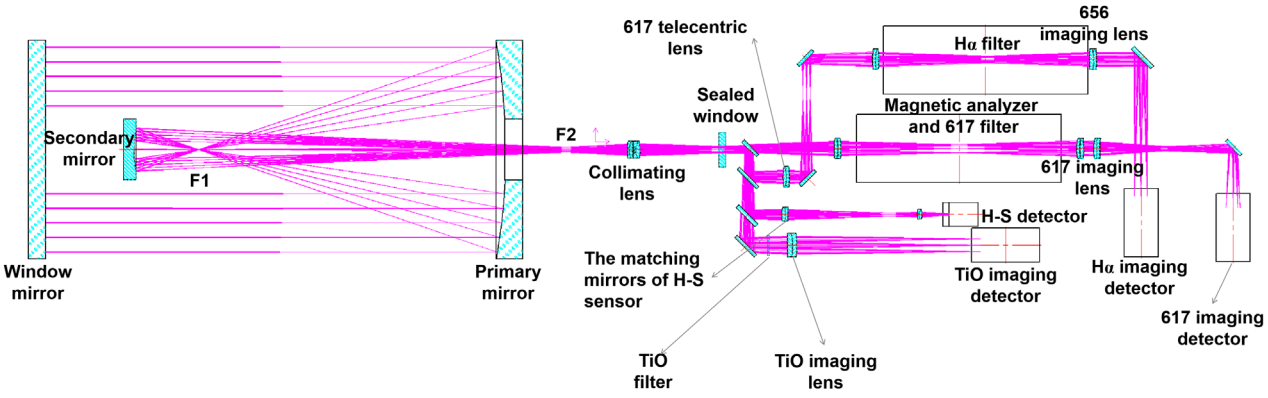

FIGURE 1
Optical configuration of PASAT.

The large-aperture ground-based solar telescopes that have been built internationally, such as the 1 m Swedish 1-m Solar Telescope (SST) (Scharmer et al., 2002), 1.5 m GREGOR (Schmidt et al., 2012; Schmidt et al., 2016; Kleint et al., 2020), 1.6 m Goode Solar Telescope (GST) (Rimmele et al., 2004; Cao et al., 2010; Shumko et al., 2014; Schmidt et al., 2017), 1 m New Vacuum Solar Telescope (NVST) (Liu et al., 2014), 1.8 m Chinese Large Solar Telescope (CLST) (Rao et al., 2020), 4 m Daniel K. Inouye Solar Telescope (DKIST) (Rimmele et al., 2020; Rast et al., 2021), and 2.5 m wide-field and high-resolution solar telescope (WeHoST) (Fang et al., 2019) under construction, are equipped with solar adaptive optical systems between the telescope and scientific terminal to correct atmospheric turbulence and the tracking and wavefront errors of the telescope itself. The optical path of this structural form is very complex, and there are also many optical mirrors for light passing through (taking the 1-meter new vacuum solar telescope as an example, a total of 21 optical mirrors are employed from the telescope to the back-end scientific instrument through an adaptive optics system). As a result, the spatial resolution of the obtained images can approach the optical diffraction limit, but the image contrast is severely limited.

In order to achieve high-contrast imaging of solar targets, it is necessary to strictly control the stray light of the system, as well as the wavefront residual error (especially high-frequency error) and non-common path aberration of the system, to achieve a high Strehl ratio (SR) of imaging. This article proposes using the deformable secondary mirror as an adaptive optical correction device, tightly coupling the telescope and adaptive optics, which can greatly simplify the optical path and significantly reduce the number of optical mirrors in the system, thereby reducing both the effects of stray light and the high-frequency wavefront aberration of the system. It is the best choice to achieve high-contrast solar target imaging. At the same time, the new solar adaptive telescope system has very high optical efficiency, which can reduce the exposure integration time of the imaging camera (especially for magnetic field measurement and limited imaging of weak light, such as the narrowband of the chromosphere), greatly improving the temporal resolution of telescope imaging. Therefore, the large-aperture solar adaptive telescope using a deformable secondary mirror can achieve continuous observation of solar targets with high contrast, high spatial resolution, and high temporal resolution simultaneously.

As good night vision and imaging occur in the infrared band, the deformable secondary mirror in a night astronomical telescope has low requirements for driver density. Due to the relatively poor daytime vision and imaging in the visible band, the deformable mirror requires a much higher driver density. Most of the night astronomical deformable secondary mirrors using voice-coil motors (Wildi et al., 2003; Esposito et al., 2011; Briguglio et al., 2013; Morzinski et al., 2014; Briguglio et al., 2018) have the disadvantage of large actuator spacing, leading to complex thermal control, and are not suitable for daytime solar applications. The piezoelectric deformable secondary mirror that we proposed can achieve high density and has low thermal radiation, making it especially suitable for high-contrast solar imaging applications. This deformable mirror with high driver density has been successfully tested on a night astronomical telescope and achieved high-contrast imaging with SR close to 0.5 in the 0.64 um wavelength band (Guo et al., 2016a; Guo et al., 2016b; Guo et al., 2023). In the field of solar observation, the 4 m European Solar Telescope (EST) (Soltau et al., 2010) is considered to use the deformable secondary mirror in multi-conjugate adaptive optics (MCAO) to carry out ground-layer corrections.

The solar adaptive telescope we proposed adopts our self-developed small-spacing and high-density piezoelectric deformable secondary mirror (PDSM). The optical components of the telescope and the adaptive optical system only consist of one primary mirror and one secondary mirror, making the optical path extremely simplified. It is particularly suitable for high-order correction of the wavefront disturbance induced by atmospheric turbulence, and it is very conducive to high-contrast imaging. Moreover, the optical path of the magnetic field measurement channel is completely symmetrical, and this will not introduce additional calibrations for polarization instruments, which can effectively improve the accuracy of the polarization measurement.

In this paper, the preliminary design of PASAT is introduced in Section 2. In Section 3, the key components are described, including the deformable secondary mirror, correlating Hartmann–Shack (HS) wavefront sensor, high-resolution photometric magnetism

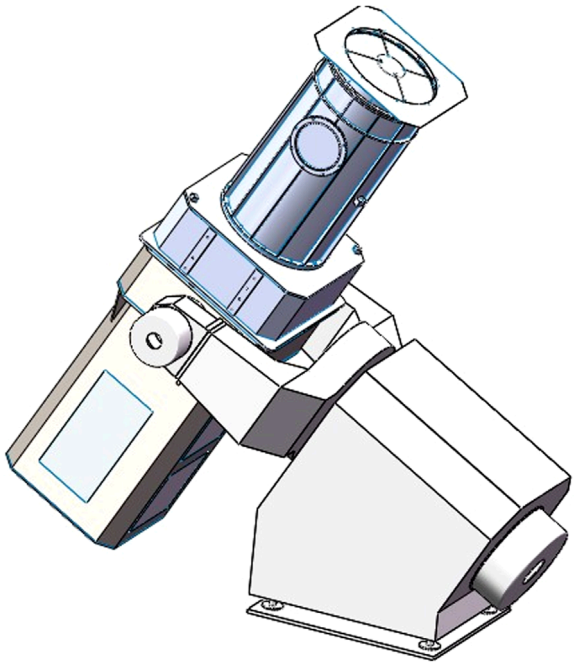

FIGURE 2
Overall structure diagram of the 60 cm solar adaptive telescope.

TABLE 1 Main technical parameters of the telescope.

No	Parameter	Value
1	Effective clear aperture	φ600 mm
2	Field	φ8′
3	Wavelength	0.6 μm–0.71 μm
4	Magnetic-field measurement	Central wavelength: 617.3 nm/spectral bandwidth: 0.008 nm
5	Photosphere imaging	Central wavelength: 705.8 nm/spectral bandwidth: 0.1 nm
6	Chromosphere imaging	Central wavelength: 656.28 nm/spectral bandwidth: 0.025 nm
8	Imaging resolution	<0.3"@ 705.8 nm @ r0 (0.50 μm) = 6 cm
9	Strehl ratio	>0.7 @ r0 (0.50 μm) = 10 cm/>0.4 @ r0 (0.50 μm) = 6 cm
10	Polarization measurement accuracy	5 × 10E-4

measurement, and high-resolution imaging systems. In Section 4, the system's performance is evaluated. Finally, we conclude the work in Section 5.

2 Preliminary optical design of PASAT

The optical configuration of PASAT, as shown in Figure 1, is composed of a 60 cm aperture primary mirror, a 163-element deformable secondary mirror, a correlating Hartmann–Shack wavefront sensor, a high-resolution photometric magnetism measurement at 617.3 nm, and two-channel high-resolution imaging systems at the Hα (656.28 nm) and TiO (705.8 nm) bands. The overall configuration of PASAT is shown in Figure 2. The vacuum tube for the primary optical system and the polar axis equatorial mount are used, and a thermal field stop and its active thermal control system are installed at the main focus F1 between the primary and secondary mirrors, which can reflect sunlight outside the imaging field of view from the optical system and effectively reduce the solar radiation power in the secondary mirror, relay optical components, and observation equipment. This technical solution has been successfully applied for the astronomical observation equipment of the Shanghai Astronomical Museum (Shanghai Science and Technology Museum Branch)—the Educational Adaptive Optics Solar Telescope (EAST) (Rao et al., 2022), which can ensure the stability of the optics of the instruments. The wavefront sensor and high-contrast imaging systems are fixed in the instrument box. The parameters of the primary mirror are clear aperture, 600 mm; vertex curvature radius, 1,800 mm; conic constant, K = 1.000; and central obscuration, 180 mm.

The main technical parameters of the PASAT are shown in Table 1.

3 Key components

3.1 Deformable secondary mirror

The 241-unit deformable secondary mirror has been successfully applied in the Lijiang 1.8 m night astronomical telescope system (Guo et al., 2023), which accumulated important technical experience for this project proposal. Referring to the 241-unit deformation secondary mirror experience of the Lijiang 1.8 m telescope, we conducted simulation calculations and design optimization on the actuator number and spatial layout of the deformation secondary mirror proposed in this project. We finalized that the PDSM actuators are arranged in a regular triangle configuration with a actuator spacing of 10.8 mm, and the total number of actuators is 163. The correction aperture is 130 mm, the central obscuration is 40 mm, and the single driver has a corrective stroke of ±3 μm. The arrangement of the PDSM actuators is shown in Figure 3. The influence function of the PDSM when driving an actuator is close to the Gaussian function, with a coupling of neighboring actuators of ~10.0% and a Gaussian index of ~2.2. The 241-unit deformation secondary mirror experience of the Lijiang 1.8 m telescope shows that the first 91 Zernike modes can be effectively corrected by this PDSM. The resonance frequency of the PDSM is larger than 4 kHz, and the error rejection bandwidth of the system would be mainly determined by the frame rate of the Hartmann–Shack wavefront senor. Table 2 lists the basic parameters of the PDSM design.

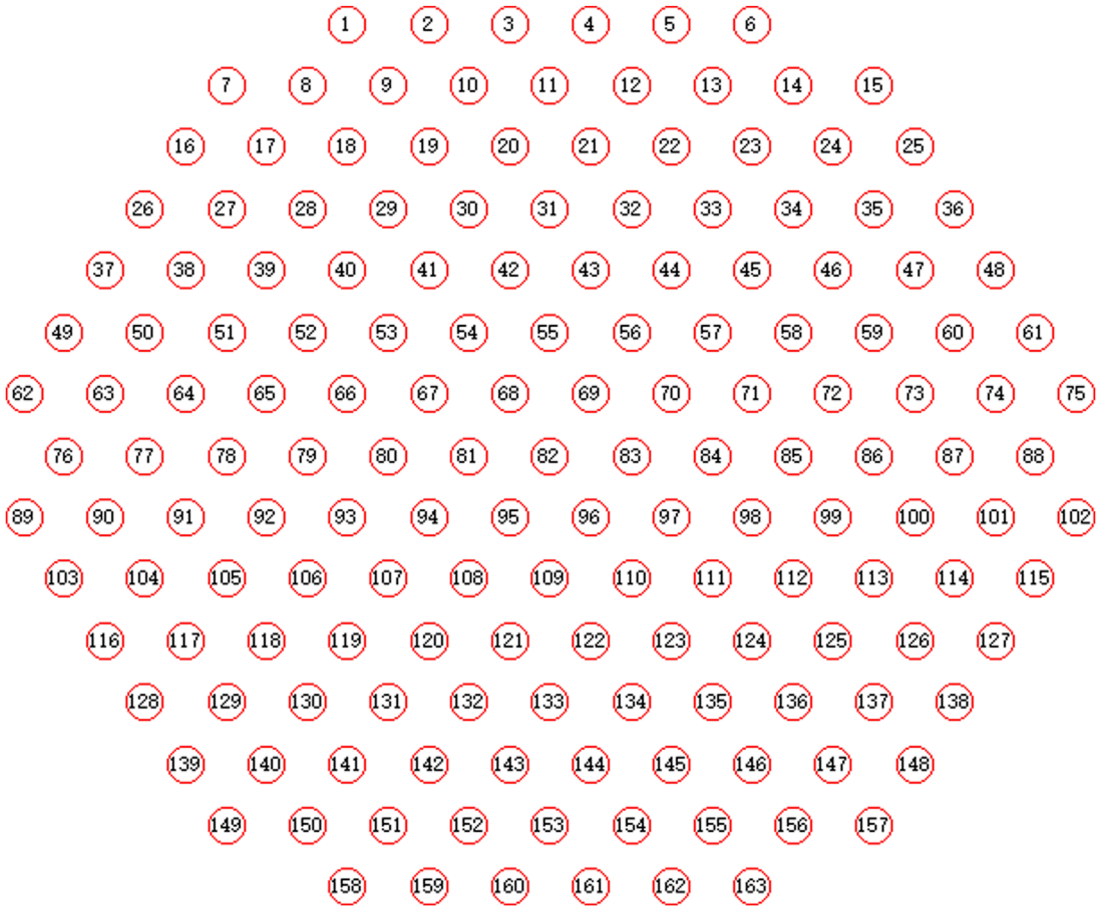

FIGURE 3
Arrangement of the PDSM actuators.

TABLE 2 Basic parameter requirements of high-density PDSM design.

No	Parameter	Value
1	Number of actuators	163
2	Arrangement pattern of actuators	regular triangle
3	Actuator spacing between actuators	10.80 mm
4	Clear aperture	130 mm
5	Vertex curvature radius	330.435 mm
6	Conic constant	−0.546
7	Estimated total mass	≈6 Kg

3.2 Correlating the Hartmann–Shack wavefront sensor

As one of the main components of the adaptive optics system, the performance of the wavefront sensor directly determines the final performance of the system. In solar adaptive optical systems, a Hartmann–Shack wavefront sensor based on the correlation algorithm is usually used. Our team has been conducting research on relevant wavefront sensors since 2009 (Rao et al., 2010) and has successfully developed correlating Hartmann–Shack wavefront sensors with sub-apertures ranging from 7 × 7 to 15 × 15 to 25 × 25. These wavefront sensors have successfully been applied in several solar adaptive optical systems, such as NVST (Rao et al., 2018; Zhang et al., 2023), EAST (Rao et al., 2022), and CLST (Rao et al., 2020), and have all achieved good wavefront detection results. In this project, we meet the requirements of small-field and high-order classic adaptive optics (CAO) correction and large-field and ground-layer ground-layer adaptive optics (GLAO) correction, and Figure 4 shows the layout diagrams of the two sub-apertures.

For the small-field and high-order CAO, the pixel resolution is initially determined to be 1.0"/pixel, with each sub-aperture corresponding to 24 × 24 pixels, and the corresponding detection field is approximately 24" × 24". The number of sub-aperture arrays is 15 × 15, the camera target surface is 360 × 360 pixels, and the camera frame rate can be more than 3,500 Hz. For the large-field and ground-layer GLAO, the maximum imaging area of the camera can reach more than 900 × 900 pixels under the condition that the wavefront detection frame rate is not less than 1,500 Hz.

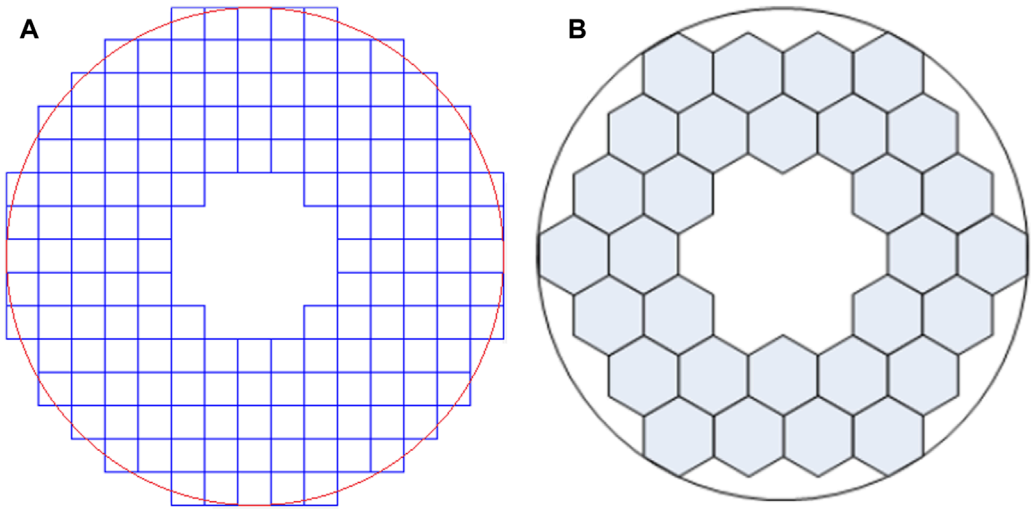

FIGURE 4
(A) Layout diagrams of small-field and high-order CAO sub-apertures; **(B)** layout diagrams of large-field and ground-layer GLAO sub-apertures.

TABLE 3 Main parameters of the Hartmann–Shack wavefront sensors.

Parameter type	Small-field and high-order	Large-field and ground-layer
Detection wavelength	600 nm–710 nm	600 nm–710 nm
Detection frame rate	≥3,500 Hz	≥1,500 Hz
Sub-aperture	15 × 15	7 × 7
Pixel resolution	~1.0"/pixel	~0.6"/pixel
Detection field	~24" × 24″	~74" × 85″
Number of guiding area	1	6–9

Combined with the detection speed of the camera and the previous experimental results of the adaptive optics (AO) system, the pixel resolution of the camera image is set as 0.6"/pixel, the number of sensor sub-aperture arrays is 7 × 7 so that each sub-aperture corresponds to 124 × 142 pixels, and the corresponding detection field is approximately 74" × 85". The main technical parameters of the Hartmann–Shack wavefront sensors are listed in Table 3.

3.3 High-resolution photometric magnetism measurement

The high-resolution magnetic field measurement subsystem is mainly composed of a pre-filter, imaging lens, polarization calibration unit, narrow-band filter, polarization analyzer, imaging camera, and magnetic field inversion unit.

The pre-filter is located at the front of the narrowband filter and is used to adjust the transmission wavelength of the filter. The specific requirements include the following: clear aperture ≥ 50 mm, central wavelength 617.3 nm, transmission spectral half-width of 2 nm, and transmission wavefront RMS ≤ 0.1λ.

The polarization analyzer has the following three types: mechanical rotation modulation based on the wave plates and polarizers, DKDP, and liquid crystal. In the first consideration, DKDP or the liquid crystal modulator is used.

The narrow-band filter adopts the scheme of a birefringent Lyot filter, which can achieve a transmission bandwidth narrower than the line width of the magneto-sensitive spectral line and can also contour scan the spectral lines by adjusting the central wavelength. The two-dimensional polarization spectral information of the Sun can be obtained through the combination of the polarization analyzer and the narrow-band adjustable filter, and thus, it inversely infers the two-dimensional magnetic field image of the Sun.

The basic parameter requirements of the magnetic field measurement system (including wavelength, polarization measurement accuracy, birefringent Lyot filter, and camera pixel count) are shown in Table 4.

3.4 High-resolution imaging systems

In this instrument, we selected two spectral lines, the Hα line and TiO line, which are commonly used for high-resolution

TABLE 4 Basic parameter requirements of the magnetic field measurement system.

No	Parameter	Value
1	Central wavelength	617.3 nm
2	Full width at half maximum (FHWM) of transmittance	≤0.008 nm
3	Shift range of the wavelength	±0.03 nm
4	Operating temperature	42°C ± 1°C
5	Aperture	≥40 mm
6	Polarization measurement accuracy	5 × 10E-4
7	Camera pixel count	4,096 × 4,096 pixels

TABLE 5 Parameters of the imaging optical system.

Parameter	High-resolution hα imaging	High-resolution TiO imaging
Wavelength	656.281 nm	705.8 nm
Bandwidth	0.025 mm	0.5 nm
FoV	56.5″	56.5″
Pixel resolution	0.106″	0.106″
Camera pixel count	4,096 × 4,096 pixels	4,096 × 4,096 pixels

TABLE 6 Analysis of the aberration correction results using the layout matching of deformable secondary mirror under different atmospheric coherence lengths (r0) conditions.

r0 (500 nm)	5 cm	8 cm	10 cm	12 cm	15 cm
Measurement error (nm)	44	30	25	21	17
Fitting error (nm)	41	28	23	20	16
Total error (nm)	60	41	34	29	24
Imaging SR (617 nm)	0.688	0.840	0.887	0.916	0.942
Imaging SR (656 nm)	0.719	0.857	0.899	0.926	0.949
Imaging SR (705 nm)	0.751	0.875	0.912	0.935	0.955

solar observation, to carry out high-contrast and high-resolution imaging observations of the solar active region. For high-resolution imaging at the Hα band, a scientific Lyot filter based on crystal birefringence will be used in the system, and the parameters of the high-resolution imaging optical system are shown in Table 5.

4 System performance evaluation

The closed-loop residual variance of the AO system is mainly composed of the measurement error of the HS sensors and the fitting error of PDSM (Hardy and Thompson, 2000), and we estimated the system performance based on the parameters of these two parts. The Strehl ratio of the 617 nm imaging system with the shortest wavelength is also better than 0.68 when r0 is only 5 cm, which ensures the high-contrast imaging of the solar target by this instrument. Table 6 shows the analysis of the aberration correction results using the layout matching of the deformable secondary mirror under different atmospheric coherence length (r0) conditions.

For the optical imaging system, the contrast of the imaging results is closely related to the SR of the point spread function of the imaging system. The higher the SR of the imaging system

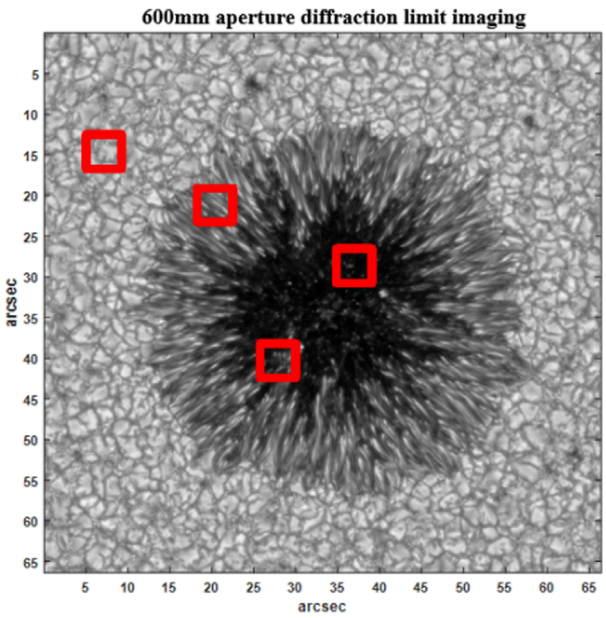

FIGURE 5
Target image that was used for simulation experiments.

is, the better the quality of the imaging results, the higher the contrast, and the clearer the discernible image details will be. Since image degradation is closely related to the residual aberration of the system, the simulation of system imaging is also carried out according to the real imaging process. In order to obtain the degenerative effects of different regions of a typical solar photosphere image with different correction capabilities, we selected a simulated solar image containing sunspot umbra, penumbra, and granulations, as shown in Figure 5. This image corresponds to the sunspot run presented in Rempel (2012), which was computed with the MURaM code (Vögler et al., 2005), and the simulation run is also publicly available (https://download.hao.ucar.edu/pub/rempel/sunspot_models/). The original simulated image has a total of 4,000 × 4,000 pixels, with a pixel resolution of 0.0166″, corresponding to a pixel size of 12 km. The simulated atmospheric turbulence distribution follows the Kolmogorov spectrum, where the atmospheric turbulence condition is D/r0 = 10, and in order to obtain the imaging results of different Strehl ratios, a variety of residual aberration conditions are obtained by setting different AO system correction capabilities. The residual aberration of the corrected system is used to calculate the corresponding PSF, and the degraded image is obtained by the convolution of the PSF and the original target image (Wöger, 2010). After that, the convolution of the point spread function and the diffraction-limited image of the 60 cm telescope were used to obtain the degraded image with different correction capabilities. The contrast of different regions of the degraded image was calculated to show the influence of the correction ability on the imaging system.

By simulating the situation of different atmospheric turbulence disturbances and different correction capabilities of the adaptive optics systems, the contrast of solar granulation and sunspots can be directly improved by enhancing the SR of the imaging system. Figure 6 shows the overall differential comparison of the different image qualities for the same solar target when the SR is gradually increased from 0.03 to 0.9. Figure 7 illustrates the differential comparison of the local details of solar granulation and sunspots under different SR conditions.

According to the simulation results, to obtain imaging results with high contrast and rich details, the solar telescope needs to be equipped with an advanced adaptive optics correction system. Only if the imaging system SR ≥ 0.5, the details between the solar granulation, especially between the sunspot internal, can be clearly identified. This also presents higher demands for the development of instrumental equipment. Achieving near-diffraction-limited imaging resolution in solar observation images while maintaining high SR at the same time is crucial for ensuring high measurement accuracy of the instrument, and this will provide more accurate measurement data for cutting-edge solar physics research.

Based on simulation experiments, the correction field of this instrument for high-order CAO is approximately 10″-20″ and that for large-filed GLAO imaging is around 2'. To achieve high-resolution imaging with an 8′ full FoV, post-processing techniques for image reconstruction must be employed. On the other hand, one important scientific objective of this equipment is to obtain high photometric accuracy and high-resolution images, particularly for the post-processing of Fe I magnetic field channel measurement data. This not only requires reconstruction algorithms to effectively improve image resolution but also requires the physical reality and light intensity reality of the reconstructed images. Phase diversity (PD) image reconstruction is to simultaneously collect one or more sets of images of the same target through different optical channels and reconstruct a clear target based on the measurement of the wavefront aberration that causes image distortion (Gonsalves, 1982; Löfdahl and Scharmer, 1994; Thelen et al., 2009; Löfdahl and Hillberg, 2022). Therefore, the PD image reconstruction method is a type of image reconstruction based on optical measurement, and its algorithm principle can ensure high photometric accuracy of the reconstructed results. We use a camera exposure external trigger control circuit to simultaneously capture the focus and defocus images and reconstruct a clear image from a degraded target based on accurate wavefront detection. On this basis, we can ensure image restoration with a large FoV and high photometric accuracy. Further research and experimental verification will be conducted in the future.

5 Conclusion and remarks

This paper reports a novel solar adaptive telescope, PASAT, and the systematic design and performance evaluation are also presented. The PASAT is planned to be put into operation in 2026 and built at the Wumingshan Observation Station in Daocheng, Sichuan, China, which has good meteorological conditions. After years of site selection, the Daocheng Wuming Mountain at an altitude of 4,800 m was chosen because it has natural advantages such as low atmospheric scattered light, an average daytime r0 value of 7.65 cm, and approximately

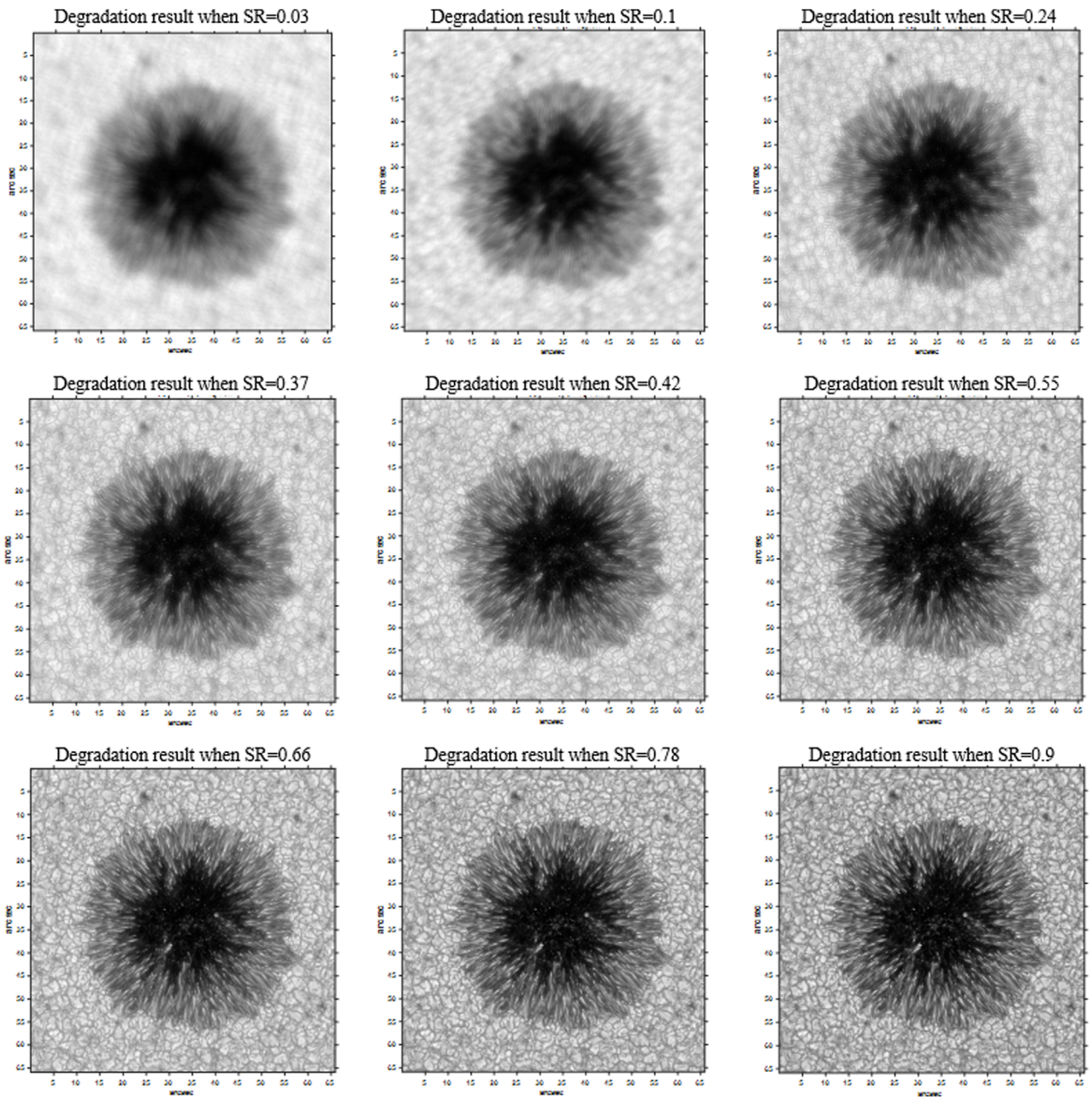

FIGURE 6
Degradation of the target by the point spread function under different Strehl ratios. From the graph in a large field of view of approximately 1′, it can be seen through an intuitive comparison that a higher Strehl ratio can retain more details and significantly improve the imaging resolution. Referring to the PASAT technical parameters, when the Strehl ratio is 0.4@ r0 (0.50 μm) = 6 cm, the imaging system can ensure that the results contain relatively complete, fine, and clear structures.

250 available sunny days throughout the year (Song et al., 2020). Many telescopes, such as the 2.5 m WeHoST, are planned to be placed at this station. After the completion of PASAT, it will become the first high-resolution magnetic field measurement solar-adaptive telescope without calibration units in the world.

The biggest technological innovation of this instrument is that it uses the simplest optical path to obtain richer deep-level image information while ensuring a certain degree of high spatial resolution and pursuing the ultimate image signal–noise ratio (SNR) and photometric accuracy. It can provide high-quality data support for space weather forecasting and early warning applications.

More importantly, PASAT provides an exploration of a new large solar telescope with the capability of high-contrast imaging as the pathfinder. Its accumulated relevant techniques can be applied to the construction of similar, larger solar telescopes in the future.

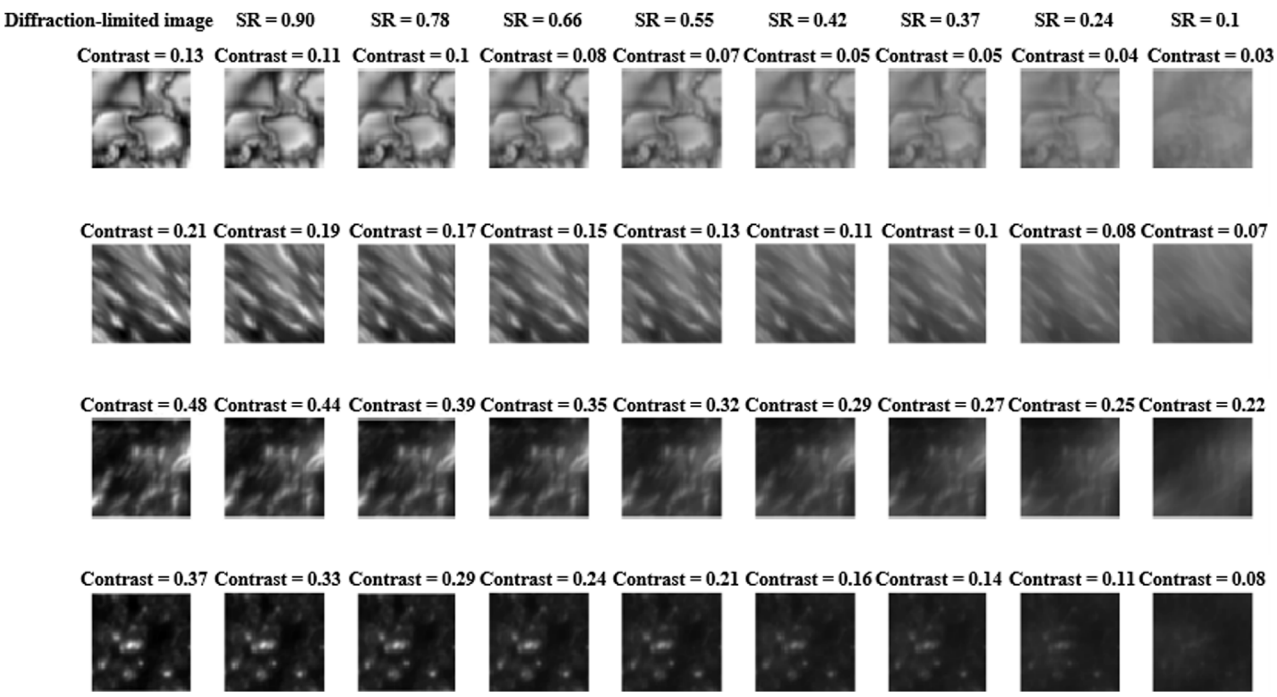

FIGURE 7
Contrast of the different regions (granulation, penumbra, and umbra, from top to bottom) as the Strehl ratio changes. It can be seen that the higher the Strehl ratio (from right to left), the better the correction effect of the system, and the higher the contrast of each sub-region. The size of the sub-region is 256 × 256 pixels, with a pixel resolution of 0.016″ and a corresponding field of view of approximately 4". Referring to the PASAT technical parameters, when the Strehl ratio is 0.4@ r0 (0.50 μm) = 6 cm, the contrast of granulation, penumbra, and umbra is larger than 5%, 11%, and 16%, respectively.

Data availability statement

The raw data supporting the conclusion of this article will be made available by the authors, without undue reservation.

Author contributions

CR: writing–review and editing, writing–original draft, visualization, validation, supervision, software, resources, project administration, methodology, investigation, funding acquisition, formal analysis, data curation, and conceptualization. HJ: writing–review and editing, visualization, validation, supervision, software, resources, project administration, methodology, investigation, funding acquisition, formal analysis, data curation, and conceptualization. HB: writing–review and editing, visualization, validation, supervision, software, resources, project administration, methodology, investigation, funding acquisition, formal analysis, data curation, and conceptualization. XR: writing–review and editing, formal analysis, data curation, and conceptualization. JY: writing–review and editing, formal analysis, data curation, and conceptualization. YG: writing–review and editing, investigation, data curation, and conceptualization. LaZ: writing–review and editing, investigation, data curation, and conceptualization. LiZ: writing–review and editing, data curation, and conceptualization. XF: writing–review and editing, data curation, and conceptualization. QZ: writing–review and editing, validation, investigation, data curation, and conceptualization. CL: writing–review and editing, investigation, data curation, and conceptualization. QB: writing–review and editing, validation, investigation, formal analysis, data curation, and conceptualization.

Funding

The author(s) declare that financial support was received for the research, authorship, and/or publication of this article. This work is funded by the National Natural Science Foundation of China (No. 12261131508) and the Laboratory Innovation Foundation of the Chinese Academy of Science (No. YJ22K002).

Acknowledgments

The authors would like to particularly thank Professor Pengfei Chen at Nanjing University for many helpful discussions and suggestions, and sincerely thank CAS Nanjing Astronomical Instruments Co., LTD for providing the polar axis frame design scheme and corresponding schematic diagram for this project.

Conflict of interest

The authors declare that the research was conducted in the absence of any commercial or financial relationships that could be construed as a potential conflict of interest.

Publisher's note

References

Briguglio, R., Quirós-Pacheco, F., Males, J. R., Xompero, M., Riccardi, A., Close, L. M., et al. (2018). Optical calibration and performance of the adaptive secondary mirror at the Magellan telescope. *Sci. Rep.* 8, 10835. doi:10.1038/s41598-018-29171-6

Briguglio, R., Xompero, M., Riccardi, A., Andrighettoni, M., Pescoller, D., Roberto, B., et al. (2013). "Optical calibration and test of the VLT deformable secondary mirror," in Proceedings of the Third AO4ELT Conference, Florence, Italy, 26-31 May 2013. doi:10.12839/AO4ELT3.13507

Cao, W., Gorceix, N., Coulter, R., Ahn, K., Rimmele, T. R., and Goode, P. R. (2010). Scientific instrumentation for the 1.6 m new solar telescope in big bear. *Astron. Nachr.* 331 (6), 636–639. doi:10.1002/asna.201011390

Choudhuri, A. R. (2017). Starspots, stellar cycles and stellar flares: lessons from solar dynamo models. *Sci. China Phys. Mech. Astron* 60, 019601. doi:10.1007/s11433-016-0413-7

Esposito, S., Riccardi, A., Pinna, E., Puglisi, A., Quirós-Pacheco, F., Arcidiacono, C., et al. (2011). Large binocular telescope adaptive optics system: new achievements and perspectives in adaptive optics. *Proc. SPIE* 8149, 814902. doi:10.1117/12.898641

Fang, C., Gu, B. Z., Yuan, X. Y., Ding, M. D., Chen, P. F., Dai, Z. G., et al. (2019). 2.5 m wide-field and high-resolution telescope. *Sci. China Phys. Mech. Astron.* 49 (5), 059603. doi:10.1360/SSPMA2018-00313

Gonsalves, R. A. (1982). Phase retrieval and diversity in adaptive optics. *Opt. Eng.* 21 (5), 829–832. doi:10.1117/12.7972989

Guo, Y. M., Chen, K. L., Zhou, J. H., Li, Z. D., Han, W. Y., Rao, X. J., et al. (2023). High-resolution visible imaging with piezoelectric deformable secondary mirror: experimental results at the 1.8-m adaptive telescope. *Opto-Electron Adv.* 6 (12), 230039. doi:10.29026/oea.2023.230039

Guo, Y. M., Zhang, A., Fan, X. L., Rao, C. H., Wei, L., Xian, H., et al. (2016a). First on-sky demonstration of the piezoelectric adaptive secondary mirror. *Opt. Lett.* 41 (24), 5712–5715. doi:10.1364/OL.41.005712

Guo, Y. M., Zhang, A., Fan, X. L., Rao, C. H., Wei, L., Xian, H., et al. (2016b). First light of the deformable secondary mirror-based adaptive optics system on 1.8m telescope. *Proc. SPIE* 9909, 99091D. doi:10.1117/12.2231842

Hardy, J. W., and Thompson, L. (2000). Adaptive optics for astronomical telescopes. *Phys. Today* 53 (4), 69. doi:10.1063/1.883053

Kleint, L., Berkefeld, T., Esteves, M., Sonner, T., Volkmer, R., Gerber, K., et al. (2020). GREGOR: optics redesign and updates from 2018-2020. *Astron. Astrophys.* 641, A27. doi:10.1051/0004-6361/202038208

Liu, Z., Xu, J., Gu, B. Z., Wang, S., You, J. Q., Shen, L. X., et al. (2014). New vacuum solar telescope and observations with high resolution. *Res. Astron. Astrophys.* 14 (6), 705–718. doi:10.1088/1674-4527/14/6/009

Löfdahl, M. G., and Hillberg, T. (2022). Multi-frame blind deconvolution and phase diversity with statistical inclusion of uncorrected high-order modes. Available at: https://arxiv.org/abs/2205.13650 (Accessed October 31, 2022).

Löfdahl, M. G., and Scharmer, G. B. (1994). Wavefront sensing and image restoration from focused and defocused solar images. *Astronomy Astrophysics Suppl* 107 (2), 243–264. doi:10.1086/117172

Low, B. C. (2015). Field topologies in ideal and near-ideal magnetohydrodynamics and vortex dynamics. *Sci. China Phys. Mech. Astron.* 58, 1–20. doi:10.1007/s11433-014-5626-7

Morzinski, K. M., Close, L. M., Males, J. R., Kopon, D., Hinz, P. M., Esposito, S., et al. (2014). MagAO: status and on-sky performance of the Magellan adaptive optics system. *Proc. SPIE* 9148, 914804. doi:10.1117/12.2057048

Rao, C. H., Gu, N. T., Rao, X. J., Li, C., Zhang, L. Q., Huang, J. L., et al. (2020). First light of the 1.8-m solar telescope–CLST. *Sci. China Phys. Mech. Astron* 63, 109631. doi:10.1007/s11433-019-1557-3

Rao, C. H., Rao, X. J., Du, Z. M., Bao, H., Li, C., Huang, J. L., et al. (2022). EAST-educational adaptive-optics solar telescope. *Res. Astron. Astrophys.* 22, 065003. doi:10.1088/1674-4527/ac65e8

Rao, C. H., Zhang, L. Q., Kong, L., Guo, Y. M., Rao, X. J., Bao, H., et al. (2018). First light of solar multi-conjugate adaptive optics at the 1-m new vacuum solar telescope. *Sci. China-Phys. Mech. Astron.* 61, 089621. doi:10.1007/s11433-017-9178-6

Rao, C. H., Zhu, L., Rao, X. J., Guan, C. L., Chen, D. H., Lin, J., et al. (2010). 基于云南天文台26厘米太阳精细结构望远镜的37单元太阳自适应光学系统. *Chin. Opt. Lett.* 8 (10), 966–968. doi:10.3788/COL20100810.0966

Rast, M. P., Bello González, N., Rubio, L. B., Cao, W., Cauzzi, G., DeLuca, E., et al. (2021). Critical science plan for the Daniel K. Inouye solar telescope (DKIST). *Sol. Phy.* 296, 70. doi:10.1007/s11207-021-01789-2

Rimmele, T. R., and Marino, J. (2011). Solar adaptive optics. *Living Rev. Sol. Phys.* 8, 2. doi:10.12942/lrsp-2011-2

Rimmele, T. R., Richards, K., Hegwer, S., Fletcher, S., Gregory, S., Moretto, G., et al. (2004). First results from the NSO/NJIT solar adaptive optics system. *Proc. SPIE.* 5171, 179. doi:10.1117/12.508513

Rimmele, T. R., Warner, M., Keil, S. L., Goode, P. R., Knölker, M., Kuhn, J. R., et al. (2020). The Daniel K. Inouye.solar telescope – observatory overview. *Sol. Phys.* 295, 172. doi:10.1007/s11207-020-01736-7

Scharmer, G. B., Bjelksjo, K., Korhonen, T. K., Lindberg, B., and Petterson, B. (2002). The 1-meter Swedish solar telescope. *Proc. SPIE.* 4853, 47. doi:10.1117/12.460377

Schmidt, D., Gorceix, N., Goode, P. R., Marino, J., Rimmele, T., Berkkefeld, T., et al. (2017). Clear widens the field for observations of the Sun with multi-conjugate adaptive optics. *Astron. Astrophys.* 597, L8. doi:10.1051/0004-6361/201629970

Schmidt, D., Gorceix, N., Marino, J., Berkefeld, T., Rimmele, T., Zhang, X. Y., et al. (2016). Progress in multi-conjugate adaptive optics at big bear solar observatory. *Proc. SPIE.* 9909, 1. doi:10.1117/12.2232087

Schmidt, W., Von der Lühe, O., Volkmer, R., Denker, C., Solanki, S. K., Balthasar, H., et al. (2012). The 1.5 meter solar telescope GREGOR. *Astron. Nachrichten* 333 (9), 796–809. doi:10.1002/asna.201211725

Shumko, S., Gorceix, N., Choi, S., Kellerer, A., Cao, W., Goode, P. R., et al. (2014). AO-308: the high-order adaptive optics system at Big Bear Solar Observatory. *Proc. SPIE.* 9148, 914835. doi:10.1117/12.2056731

Soltau, D., Berkefeld, T., Sánchez Capuchino, J., Collados Vera, M., Del Moro, D., Löfdahl, M., et al. (2010). Adaptive optics and MCAO for the 4-m European solar telescope EST. *Proc. SPIE.* 7736, 77360U. doi:10.1117/12.856851

Song, T. F., Liu, Y., Wang, J. X., Zhang, X. F., Liu, S. Q., Zhao, M. Y., et al. (2020). Site testing campaign for the Large Optical/infrared Telescope of China: general introduction of the Daocheng site. *Res. Astron. Astrophys.* 20 (6), 085. doi:10.1088/1674-4527/20/6/85

Thelen, B. J., Paxman, R. G., Carrara, D. A., and Seldin, J. H. (2009). Overcoming turbulence-induced space-variant blur by using phase-diverse speckle. *J. Opt. Soc. Am. A* 26 (1), 206–218. doi:10.1364/JOSAA.26.000206

Wang, J. X., Zhang, Y. Z., He, H., Chen, A. Q., Jin, C. L., and Zhou, G. P. (2015). Cluster of solar active regions and onset of coronal mass ejections. *Sci. China Phys. Mech. Astron.* 58, 599601. doi:10.1007/s11433-015-5682-7

Wei, X. Y., Noda, C., Zhang, L. Q., and Rao, C. H. (2023). Comparative analysis of image-shift measurement algorithms for solar shack–hartmann wavefront sensors. *Publ. Astronomical Soc. Pac.* 135, 114503. doi:10.1088/1538-3873/ad0451

Wildi, F. P., Brusa, G., Lloyd-Hart, M., Close, L. M., and Riccardi, A. (2003). First light of the 6.5-m MMT adaptive optics system. *Proc. SPIE* 5169, 17–25. doi:10.1117/12.507687

Wöger, F. (2010). Optical transfer functions derived from solar adaptive optics system data. *Appl. Opt.* 49 (10), 1818–1825. doi:10.1364/AO.49.001818

Zhang, L. Q., Bao, H., Rao, X. J., Guo, Y. M., Zhong, L. B., Ran, X., et al. (2023). Ground-layer adaptive optics for the new vacuum solar telescope:instrument description and first results. *Sci. CHINA-PHYSICS Mech. ASTRONOMY* 6, 200–210. doi:10.1007/s11433-022-2107-4

frontiers | Frontiers in Astronomy and Space Sciences

TYPE Original Research
PUBLISHED 06 May 2024
DOI 10.3389/fspas.2024.1402793

OPEN ACCESS

EDITED BY
Shengfeng Yang,
Indiana University, Purdue University Indianapolis, United States

REVIEWED BY
Wentao Luo,
University of Science and Technology of China, China
Ji Yao,
Shanghai Astronomical Observatory, Chinese Academy of Sciences (CAS), China

*CORRESPONDENCE
Binyang Liu,
byliu@pmo.ac.cn

RECEIVED 18 March 2024
ACCEPTED 12 April 2024
PUBLISHED 06 May 2024

CITATION
Hong Y, Yang C, Zhang M, Chen Y and Liu B (2024), Optimizing image processing for modern wide field surveys: enhanced data management based on the LSST science pipelines.
Front. Astron. Space Sci. 11:1402793.
doi: 10.3389/fspas.2024.1402793

Optimizing image processing for modern wide field surveys: enhanced data management based on the LSST science pipelines

Yuanyu Hong[1,2], Chao Yang[1,2], Miaomiao Zhang[1], Yanpeng Chen[1,2] and Binyang Liu[1]*

[1]Purple Mountain Observatory, Chinese Academy of Sciences, Nanjing, China, [2]School of Astronomy and Space Science, University of Science and Technology of China, Hefei, China

Introduction: In recent decades, numerous large survey projects have been initiated to enhance our understanding of the cosmos. Among these, the Vera C. Rubin Observatory's Legacy Survey of Space and Time (LSST) stands out as a flagship project of the Stage IV cosmology imaging surveys, offering an open-source framework for data management and processing adaptable to various instruments.

Methods: In this paper, we introduce the 'obs_mccd' software package, designed to serve as a bridge linking raw data from generic mosaic-CCD instruments to the LSST data management framework. The package also facilitates the deployment of tailored configurations to the pipeline middleware. To validate our data processing pipeline, we processed a batch of realistic data from a commissioning wide-field telescope.

Results: We established a prototype of the quality control (QC) system capable of assessing image quality parameters such as PSF size, ellipticity, and astrometric calibration. Our findings indicate that using a fifth-order polynomial for astrometric calibration effectively characterizes geometric distortion, achieving a median average geometric distortion residual of 0.011 pixel.

Discussion: When comparing the performance of our pipeline to our in-house pipeline applied to the same dataset, we observed that our new 'obs_mccd' pipeline offers improved precision, reducing the median average geometric distortion residual from 0.016 pixel to 0.011 pixel. This enhancement in performance underscores the benefits of the obs_mccd package in managing and processing data from wide-field surveys, and it opens up new avenues for scientific exploration with smaller, flexible survey systems complementing the LSST.

KEYWORDS

image processing pipeline, astrometry, survey telescopes, LSST, PSF (point spread function)

1 Introduction

The advancement of survey capabilities in optical telescopes, driven significantly by the introduction of wide field-of-view (FOV) Charge-Coupled Device (CCD) imaging technology, has been a critical breakthrough in modern astronomy. These comprehensive imaging surveys enable a wide spectrum of scientific research by allowing the identification of rare astrophysical phenomena and enabling the accurate quantification of astrophysical variables, despite the intrinsic noise present. They have revolutionized our approach to studying the universe, facilitating significant advances in areas like weak and microlensing, exoplanet discovery, transient phenomena, and identifying electromagnetic counterparts to gravitational waves (Abbott et al., 2016). Acquiring extensive datasets is essential for detecting unusual events and for the precise measurement of astronomical parameters.

However, generating a scientifically robust catalog from large-scale photometric surveys is challenging. The pursuit of rare astronomical objects, such as high-redshift quasars or strong gravitational lensing, is often hindered by the incidence of false positives, which primarily emerge from data processing anomalies like erroneous detections and insufficiently masked instrumental defects. Therefore, rigorous image processing techniques are necessary to filter the expansive dataset down to a viable set of candidates for in-depth analysis or subsequent observational verification.

Furthermore, validating these preliminary findings and extracting information pertinent to phenomena such as reionization and the substructure of dark matter require follow-up observations. At the same time, investigations of statistical phenomena like weak lensing and galaxy clustering demand exceptional accuracy in the measurement of galaxy morphologies and photometric properties, given their vulnerability to slight systematic deviations. As surveys broaden in scope and increase in depth, the margin for systematics narrows inversely to the anticipated statistical uncertainty, necessitating advancements in processing methodologies to effectively employ the full statistical power of the survey data.

Modern wide field surveys have imposed high demands on image processing systems during long-term observations, promoting the development of advanced software and algorithms. In the near future, as a flagship project of the Stage IV dark energy and dark matter surveys, the Rubin Observatory Legacy Survey of Space and Time (LSST) (Ivezić et al., 2019) will show its observing power in terms of not only its imaging quality but also its wide FoV from its 8-meter class aperture and 189 4 K × 4 K CCDs. To process the big data stream from LSST, the LSST Data Management Team is developing a next-generation data processing pipeline: the LSST Science Pipelines[1]. The LSST Science Pipelines represent a sophisticated and advanced pipeline (Bosch et al., 2019), inheriting from the Sloan Digital Sky Survey (SDSS) *Photo* pipeline (Lupton et al., 2001). Although the pipeline is intrinsically developed to process data from the LSST, the pipeline's well-designed architecture enables the processing of data from various instruments, a noteworthy example is the Hyper Suprime-Cam (HSC) (Bosch et al., 2018; Dalal et al., 2023). The data from HSC is processed using a customized version of the LSST Science Pipelines named hscPipe, demonstrating the adaptability of the LSST Science Pipelines. Both the hscPipe and the LSST Science Pipelines are open source, released under the GNU General Public Licence.

In the forthcoming LSST era, we anticipate numerous wide field imaging surveys that, while having smaller apertures and fewer CCDs compared to LSST, will play a complementary role to Stage IV surveys by filling gaps in timeline, bandpass, sky coverage, and enhancing imaging depth in specific areas. Achieving synergy among these diverse surveys necessitates a framework where data from various instruments can be homogeneously processed right from the level of detrended pixels, adhering to a unified data management schema. The infrastructure of the LSST Science Pipelines provides such a general-purpose, general-dataset platform to fulfill the possibility of data synergies among Stage III and Stage IV surveys.

Presently, the LSST Science Pipelines contain official interface packages for datasets from several telescopes and cameras, such as Sloan Digital Sky Survey (SDSS) (Gunn et al., 2006), Canada-France-Hawaii Telescope (CFHT) MegaCam (Erben et al., 2013), Dark Energy Camera (DECam) (Blum et al., 2016), and Subaru Suprime-Cam/HSC (Aihara et al., 2018; Aihara et al., 2019), all of which are tailored for CCD dimensions of approximately 2 K × 4 K. Drawing inspiration from the development of an interface package for the Gravitational Wave Optical Observer (GOTO) (Mullaney et al., 2021), we recognize a growing interest in smaller-scale, adaptable wide field imaging surveys featuring a reduced number of CCDs yet potentially larger individual CCD sizes. Our objective is to craft a bespoke pipeline that transitions imaging surveys from raw pixel data to refined source catalogs and implements quality control measures. This pipeline aims to extend the adaptability of the existing LSST Science Pipelines, offering customization for various instruments equipped with mosaic CCDs through minimal alterations. In the near future, this bespoke pipeline promises to be helpful across a multitude of survey initiatives. It seeks to reduce the cost associated with developing data processing software, while simultaneously fostering data synergy across projects with diverse scientific objectives.

In this paper, we present how to customize the LSST Science Pipelines to process data from a mosaic wide field CCD array. In Section 2 we briefly introduce the LSST Science Pipelines. In Section 3 we introduce the obs_mccd package, which serves as an interface connecting mosaic CCD data to the LSST Science Pipelines. In Section 4 we show how the mosaic CCD data is processed and evaluate the quality of data processing, and in Section 5 we summarize our work.

2 The LSST science pipelines

The Vera C. Rubin Observatory is a cutting-edge facility located on Cerro Pachón in Chile, home to the Simonyi Survey Telescope. With its impressive 8.4-meter primary mirror and a camera boasting a 9.6-degree field of view (FOV), the observatory is poised to undertake the Legacy Survey of Space and Time (LSST). This ambitious 10-year survey, expected to commence following the completion of construction and commissioning by 2025, aims to

1 https://pipelines.lsst.io/

revolutionize our understanding of four core scientific areas: the mysteries of dark matter and dark energy, hazardous asteroids and the remote Solar System, the transient optical sky, and the formation and structure of the Milky Way (Ivezić et al., 2019).

LSST will allocate 90% of its observation time to the deep-wide-fast survey, covering an area of 18,000 square degrees in the southern sky with a detection limit of approximately 24.5 magnitudes (*r* band) for individual images and around 27.5 magnitudes (*r* band) in the final coadded images. The remaining 10% of the time is reserved for special projects, such as Very Deep and Very Fast time domain surveys. In terms of data size, LSST anticipates generating 15 TB of raw data each night, resulting in an estimated 500 PB of image data and 50 PB of catalog data over the ten-year survey period. The final Data Release catalog is expected to be around 15 PB (Ivezić et al., 2019).

In the "big data" era, the volume of data requires the creation of specialized processing frameworks. The LSST Data Management Team has crafted the LSST Science Pipelines, an adaptable and advanced software suite designed to handle the extensive imaging data collected by the observatory. These pipelines play a pivotal role in delivering timely data products essential for time-domain astronomy and in producing annual releases of comprehensive deep coadd images and catalogs. They are engineered to perform a range of critical tasks including object detection and measurement, image characterization, calibration, image coadding, and image differencing, etc.

In conventional imaging data processing workflows, software is often tailored for use with a particular instrument or to achieve a specific scientific objective. Examples include IRAF (Massey, 1997), SExtractor (Bertin and Arnouts, 1996), SCAMP (Bertin, 2006), DAOPHOT (Stetson, 1987), SDSS *Photo* (Lupton et al., 2001), Pan-STARRS Image Processing Pipeline (IPP) (Magnier et al., 2006), DECam Community Pipeline (Valdes and Gruendl, 2014), THELI (Schirmer, 2013), *lens*FIT (Miller et al., 2007), each designed for processing data from specific surveys or addressing distinct science cases. However, integrating and analyzing raw data across different telescopic sources poses a significant challenge, necessitating the orchestration of various software tools to complete the journey from pixel to catalog. It is worth noting that the exploration of catalog-to-cosmology consistency has received attention, Chang et al. (2018) use unified pipelines on catalogs to show that a number of analysis choices can influence cosmological constraints.

For Stage IV cosmology surveys, there is a clear advantage in developing a comprehensive pipeline akin to the LSST Science Pipelines. Such a pipeline would be capable of handling data from a variety of telescopes within a unified data framework, streamlining the data processing workflow and enhancing the capability for joint analysis.

In addition to processing LSST data, the modular design, separating data processing software packages from the telescope's definition package (obs_package), enables the pipelines to process imaging data from other instruments. For example, the LSST Science Pipelines can process data from instruments like SDSS, CFHT, DECam (Fu et al., 2022; Fu et al., 2024), HSC (Jurić et al., 2017) and GOTO (Mullaney et al., 2021). The modification each instrument made is to develop an "obs_package" containing the necessary information related to the instrument that the pipelines require while processing data.

The following section provides an overview of our "obs_package" tailored for a standard mosaic CCD setup: obs_mccd. Within this prototype package, we employ a typical 3 × 3 CCD configuration as a model to showcase the operational flow. In particular, the newly commissioned 2.5-meter Wide Field Survey Telescope (WFST), which focus on time-domain events, such as supernovae, tidal disruption events (TDE), multi-messenger events; asteroids and the Solar System; the Milky Way and its satellite dwarf galaxies; cosmology and so on (Wang et al., 2023), equipped with its 3 × 3 array of 81-megapixel CCDs, serves as an ideal illustration of our obs_mccd package. Therefore, we have selected WFST as a case study to elaborate on the process of image handling at the CCD level.

3 The obs_mccd package

To process external data within the LSST Science Pipelines framework, our initial step involves creating an interface that serves as a bridge linking the specific dataset to the pipelines. This obs_package interface is also crucial for defining the data structure, which is managed by the data Butler (Jenness et al., 2022). The Butler system abstracts the complexities of data access for pipeline developers. The obs_package facilitates the pathway for the Butler to access both the raw data and subsequent intermediate data products.

The obs_package allows the LSST Science Pipelines to ingest and process raw data from different telescopes, using customized pipelines and task configurations for subsequent data processing steps. For example, obs_subaru[2] is one such obs_package empowering the LSST Science Pipelines to process Subaru Suprime-Cam and HSC data. Following the instructions provided by the LSST corporation[3], we developed the obs_mccd package. The obs_mccd contains telescope information (e.g., the layout of the focal plane and passbands), data types of raw data (e.g., integer or double-precision floating-point), and so on. In addition to the telescope information, obs_mccd also includes data processing workflow about the subtasks involved in data processing (in the format of YAML files), and the configuration of these subtasks. Below we detail the obs_mccd and our development environment employs the LSST Science Pipelines version v23.0.1.

3.1 Interacting with the LSST science pipelines

The initial step in the data processing workflow involves enabling the LSST Science Pipelines to ingest and register the raw data. This process comprises two key aspects: the interaction of header and data.

3.1.1 Interacting with header

To enable the LSST Science Pipelines to handle data from other instruments, it is necessary to interact with the headers of raw data. Due to variations of different instruments, the LSST

2 https://github.com/lsst/obs_subaru

3 https://pipelines.lsst.io/modules/lsst.obs.base/creating-an-obs-package.html

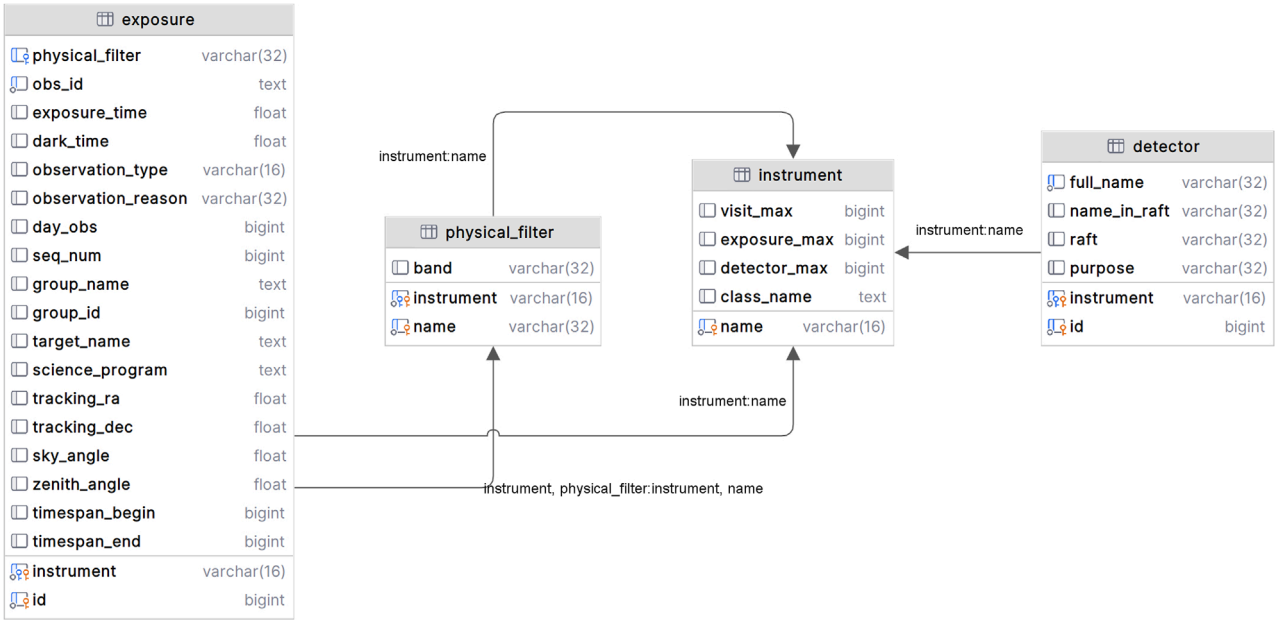

FIGURE 1
The LSST Science Pipelines utilizes SQLite3 to manage data. This figure illustrates the relationships between four tables: exposure, instrument, detector, and physical_filter. The relationships between these tables have been defined through the relations of primary and foreign keys. The keys marked with a yellow key pattern represent primary keys, while those with a blue key pattern represent foreign keys.

Science Pipelines has predefined a series of properties[4]. These properties are common information recorded in headers, such as telescope name, the physical filter used to observe, exposure time, RA and Dec of pointing, exposure ID, CCD number, etc. What we need to do is to convert the essential information stored in the headers, necessary for subsequent data processing, into the predefined properties. We implement this interaction by developing the MCCDTranslator based on the FitsTranslator[5]. The functionality of the MCCDTranslator is to tell the LSST Science Pipelines what headers should read and how to utilize the headers from our raw data. Then we can convert the required information in the headers of the raw data to the properties before finally writing them into the SQLite3 database. In the SQLite3 database, these properties correspond to the predefined keys.

Figure 1 shows an example illustrating four tables within the database. The diagram illustrates the relationships between these four tables: exposure, instrument, detector, and physical_filter. The relationships between these tables have been defined through the relationships between primary and foreign keys. A primary key is a column or a group of columns that make a record unique, and a foreign key is a column or a group of columns that provides a link between data in two tables. For example, the instrument and detector tables establish connections with each other by the key instrument name. In addition to the four tables, there are numerous other tables in the database. For example, the collection table and collection_chain table manage how to group a set of data; the dataset_type table manages the data type of the ingested data and the output data products containing the records related to dataset type like calexp, src, camera and so on. All these tables have well-defined relationships and are accessible by the pipelines. As the data processing advances, the outputs will be automatically written into the SQLite3 database.

3.1.2 Interacting with data

Along with processing header information, efforts are also focused on enabling the LSST Science Pipelines to effectively process the actual data part of the raw data. This is achieved by integrating detailed camera and CCD information, along with other necessary information into the obs_mccd module. This integration covers aspects such as the layout of the focal plane, camera geometry, CCD dimensions, pixel size, and more. A practical reference for this is the camera.py[6] script used for the HSC, which outlines the focal plane details and some CCD information.

In addition to camera.py, it is necessary for the LSST Science Pipelines to document specific details for each CCD amplifier, including the prescan region, science region, gain, saturation, readout direction, etc. Moreover, data about the telescope's passband information—like filter names, coverage ranges, effective wavelengths, etc., — is crucial. The system also allows for the logging of comprehensive optical system transmission data, including filter transmission, CCD quantum efficiency, and atmospheric transmission.

In our obs_mccd, we use the information of the engineering diagram as reference to our prototype obs_package (shown in

4 https://github.com/lsst/astro_metadata_translator/blob/main/python/astro_metadata_translator/properties.py

5 https://github.com/lsst/astro_metadata_translator/blob/main/python/astro_metadata_translator/translators/fits

6 https://github.com/lsst/obs_subaru/blob/main/hsc/camera/camera.py

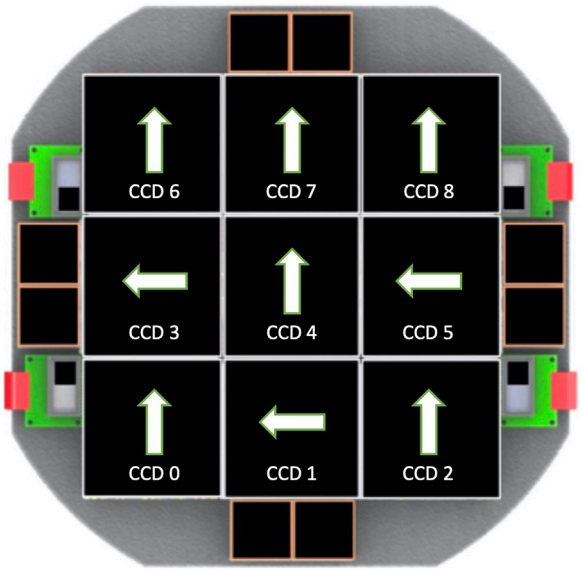

FIGURE 2
A sample CCD layout on the focal plane based on the engineering diagram of WFST (Lin et al., 2022). It specifies the CCD IDs, the gaps between any two adjacent CCDs, and the readout direction of each CCD.

Figure 2), which outlines the CCD layout and gaps. In our prototype obs_package, assigned CCD IDs are assigned according to the following specification: from left to right, the first three CCDs are numbered as 0, 1, 2; the next row is sequentially numbered as 3, 4, 5; and the final row is sequentially numbered as 6, 7, 8. The CCD and amplifier details have been meticulously encoded. As an example, within the camera.py file, we specify that the instrument is equipped with nine CCDs, each having dimensions of $9,216 \times 9,232$ and a pixel size of $10\mu m$ in both axes, with a pixel scale approximating $0.33''$. However, the actual layout of the focal plane may deviate from this design, for instance, during the processing of the engineering test data, we found numerous parameters needing modification. This update includes details such as the position of reference points (refpos_x(y)) and the physical coordinates of these points (offset_x(y)). Moreover, it was observed that the pixel scale is more accurately around $0.332''$, slightly larger than the designed $0.33''$, a discrepancy accounted for in the parameter transformDict. These values may require continual modification as changes occur during the operation and debugging of the instrument.

3.2 Defining the pipeline for processing data

After establishing the interaction between raw data and the LSST Science Pipelines, the next critical step is defining a detailed pipeline. This process is more than just a linear progression; it involves the strategic assembly and coordination of various subtasks that cater to distinct requirements of data processing. The pipeline's design is crucial because it dictates how data flows through the system, ensuring that each step is performed efficiently and accurately.

Pipelines are typically scripted in YAML files. An exemplary blueprint for a data release pipeline is the DRP-full.yaml[7] which serves as a guideline. Within the scope of this paper, we specifically engage in singleFrame processing. This processing is an intricate procedure broken down into three pivotal subtasks: the correction of instrumental effects (ISR), the identification of key image features (characterizeImage), and the comprehensive calibration of the image (calibrate). Each of these subtasks plays a significant role in ensuring the integrity and quality of the processed data.

The singleFrame processing flow is systematically illustrated in Figure 3, where the visual representation aids in understanding the complex interactions and dependencies among different data processing stages. In this flowchart, rectangles are utilized to represent the inputs and outputs at various stages of the pipeline, symbolizing the transformation of raw data into refined, useable information. The orange ellipses highlight the operations applied to the data, indicating the dynamic nature of the processing steps.

This approach underscores the modular and flexible nature of pipeline design in the LSST Science Pipelines. Each subtask is carefully crafted to perform specific functions, and their collective execution leads to a comprehensive processing of the raw data. The design of these pipelines, therefore, is not just a technical task but also a conceptual challenge, requiring a deep understanding of both the astronomical phenomena being observed and the intricacies of data processing technologies.

The SQLite3 database plays a crucial role in managing the myriad of data products, such as postISRCCD, calexp, src and others, which are integral to the processing workflow. The presence of these data types within the dataset_type table of the SQLite3 database exemplifies the structured and methodical approach required for handling vast datasets typical in contemporary astronomical surveys. This database-driven approach ensures not only the integrity and accessibility of the data but also facilitates the complex computations and transformations that are fundamental to the LSST Science Pipelines.

3.3 Configuration information

Following the successful interaction of data with the LSST Science Pipelines and the construction of the data processing pipelines, the focus shifts to a critical aspect of pipeline execution: the customization and adjustment of task-specific configuration settings. This step is not merely a procedural requirement; it is a crucial aspect that ensures the pipeline's performance is optimally tuned to the unique demands of the data and the specific objectives of the project.

Configuration settings act as the guiding parameters that dictate how each task within the pipeline processes the data. These settings can range from defining thresholds for data quality, setting parameters for image processing algorithms, to specifying criteria for data selection and analysis. Adjusting these configurations is a nuanced process that requires a deep understanding of both the nature of the data and the scientific goals of the project. It is where

7 https://github.com/lsst/drp_pipe/blob/main/pipelines/_ingredients/DRP-full.yaml

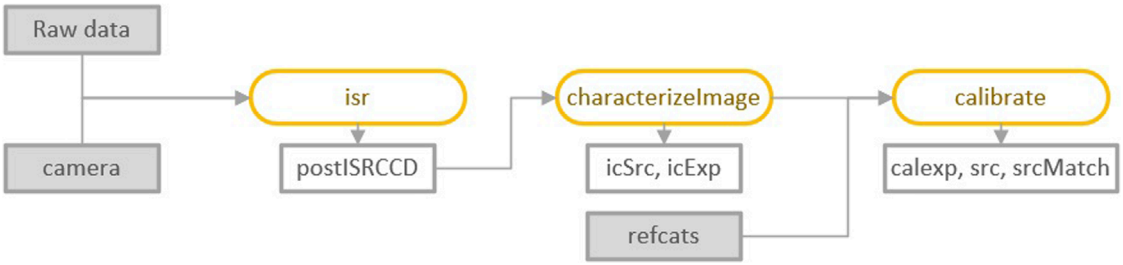

FIGURE 3
The flowchart of singleFrame processing, the rectangles represent input and output data, and the orange ellipses represent the operations to the data, the icSrc (SourceCatalog get by characterizeImage), icExp (ExposureF get by characterizeImage), calexp (calibrated exposureF) src (SourceCatalog get by calibrate) are all data types stored in the SQLite3 database.

the theoretical aspects of astronomy, computational methods, and practical considerations of data handling converge.

Moreover, the configuration process is iterative and often involves a series of trials and refinements. This iterative approach allows for the fine-tuning of the pipeline to accommodate the inherent variability and complexity of astronomical data. It is a process that may involve consultation with domain experts, experimentation with different parameter settings, and extensive testing to evaluate the impacts of these configurations on the data processing outcomes.

In Section 4 that follows, some exposition on configuring and optimizing these pipelines is provided. The importance of this step in the data processing workflow cannot be overstated. Proper configuration is essential to achieving high-quality data processing outcomes, which in turn, has a direct impact on the reliability and validity of the scientific results.

4 Data processing with the pipelines

Following the development and implementation of the obs_mccd package, the initial phase in the data processing workflow entails the ingestion of data into the LSST Science Pipelines. For this purpose, we utilize version v23.0.1 of the LSST Science Pipelines, which has transitioned to using Generation 3 for data organization and task execution, moving away from the previous Generation 2 framework as introduced in Bosch et al. (2018). This shift marks a significant evolution in the way data is handled and processed.

The preparation process before the actual data processing involves a series of actions and checks to ensure smooth data interaction and processing. This preparatory phase includes tasks such as verifying data compatibility with the pipelines, ensuring all necessary metadata is correctly formatted and available, and setting up the initial parameters and configurations that the pipelines will use to process the data.

This stage is essential for laying a solid foundation for subsequent data processing steps. It ensures that the data is properly aligned with the requirements of the pipelines and that the pipelines are appropriately calibrated to handle the specific characteristics of the data. This preparation, as detailed below,

1. Create a Butler repository by the cmd butler create.
2. Register the mosaic CCD camera (MCCDCamera) into the Butler repository.
3. Ingest both the raw data and the calibration data by the cmd butler ingest-raws.
4. Group the exposures into visits by the cmd define-visits.
5. Ingest the reference catalogs.

Subsequently, we advanced to the data processing stage of our investigation. In this phase, we meticulously processed a dataset derived from a dense star field. These images were captured during the engineering test period of WFST. It is important to emphasize that this dataset was exclusively used to evaluate the feasibility of the pipeline and test our prototype obs_package, and does not ultimately reflect the quality of scientific images. This processing follows the singleFrame steps, as detailed in Figure 3. The upcoming sections provide a detailed account of the main data products generated from this processing, along with an evaluation by our QC system.

4.1 Instrumental signature removal (ISR)

Utilizing the calibration data that has been ingested, we create the master calibration files, specifically for bias and flat fields. This is executed through pipelines specifically engineered by the LSST Data Management team. The generation of the master bias is guided by the cpBias subtask[8], while the creation of the master flat utilizes the cpFlat subtask[9].

Subsequently, we establish the validity periods for these calibrations using the command certify-calibrations. This designation ensures that exposures captured during these periods will be processed using the appropriate bias and flat calibrations. Figure 4 displays the master flat that we have obtained, particularly employing twilight flats. The pipeline is adept at managing star trails, efficiently synthesizing multiple images to mitigate their effects.

Beyond bias and flat, ISR includes adjustments for overscan areas, non-linearity in the detector response, crosstalk effects between different detector elements, and dark field corrections. Moreover, both variance and mask planes are generated for the subsequent data processing.

A key aspect of ISR is the identification and handling of defective pixels. Saturated and bad pixels are systematically detected, flagged,

8 https://github.com/lsst/cp_pipe/blob/23.0.1/pipelines/cpBias.yaml
9 https://github.com/lsst/cp_pipe/blob/23.0.1/pipelines/cpFlat.yaml

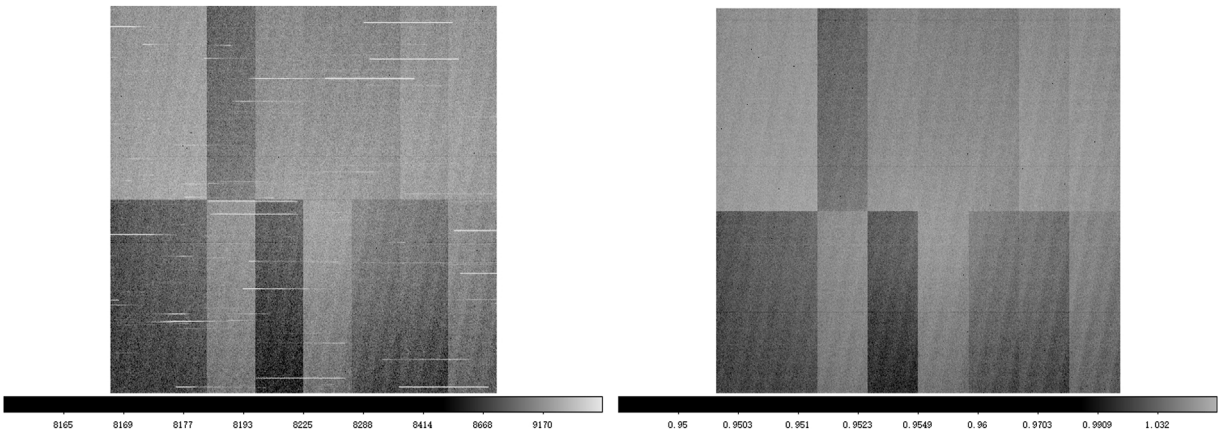

FIGURE 4
A sample flat image of CCD (ID 4), the left panel shows a single twilight flat, and the right panel is the resultant master flat combined by nine flats. The left image distinctly shows star trails, highlighting the initial quality of the single flat. The master flat demonstrates the effectiveness of the pipelines in mitigating such star trails. This improvement is achieved through the coaddition of multiple images, showcasing the capability of the pipelines to enhance image quality.

and then subjected to interpolation to minimize their impact on the final data. However, it is important to note that objects centered on these interpolated pixels might possess measurements that are deemed unreliable. To ensure data integrity, these objects are flagged in the catalogs to indicate potential measurement inaccuracies.

To preserve the integrity of the data and for future reference, a copy of the ISR-corrected images, along with the corresponding mask planes, is stored in the data repository. This archival ensures that the corrected data can be accessed and reanalyzed if necessary.

4.2 Image characterization (characterizeImage)

Once the instrumental signature has been removed from the raw image, the next step is to characterize the image, a process that involves a detailed assessment of its features. This step is visually represented in Figure 5 and entails a series of lower-level subtasks that are semi-iterative in nature. This means that many of these tasks are interdependent and cyclical. For instance, the source detection step can enhance background reduction, and conversely, more effective background reduction can lead to improved source detection.

The workflow for this task is intricate and involves several stages. Initially, the image undergoes a thorough background estimation and subtraction, which is critical for accurately identifying and measuring the sources in the image. Following this, source detection algorithms are applied to identify potential objects within the image. After sources are detected, the next step typically involves measuring their properties, such as their positions, shapes, and fluxes.

The characterization process also includes the identification and masking of artifacts and anomalies in the image, such as cosmic rays or satellite trails, which can otherwise affect the accuracy of source detection and measurement. Additionally, the task involves refining the Point Spread Function (PSF) model, which describes how a point source (like a distant star) appears in the image. An accurate PSF model is crucial for precise photometric and astrometric measurements.

The semi-iterative nature of these tasks allows for continuous refinement and improvement of the image characterization. As the process iterates, the accuracy of source detection, background estimation, and other measurements gradually improves, leading to a more precise and detailed characterization of the image. This iterative process is key to extracting the maximum amount of useful information from raw images, paving the way for in-depth analysis and research. The task workflow is shown as follows:

1. Background Subtraction: The process begins with the initial reading of the original background, considering that background subtraction is iterative. After masking the image, the background is recalculated and refitted for different bins.
2. PSF-Related Information: The task evaluates if the image contains PSF-related information. In the absence of such data, and if the configuration does not require PSF measurement, a default two-dimensional Gaussian PSF (11×11 pixels, with a standard deviation of 1.5 pixels) is assigned to the image at that point.
3. Cosmic Ray Repair: This involves detecting cosmic rays by analyzing the brightness gradient. The identified cosmic rays are then masked and interpolated, followed by a re-calculation of the background.
4. Source Detection: The goal here is to identify a group of bright stars for constructing the PSF model, setting the detection threshold at 50σ. This step includes a nested task for updating the sky background after source detection, improving the fitting of the sky background.
5. Star/galaxy Classification This phase concentrates on determining if a source in the image is a point source or an extended one. This classification is based on extendedness, which is the difference between the PSF magnitude and the CModel magnitude of the source. Once classified, the source is then appropriately flagged in the system.

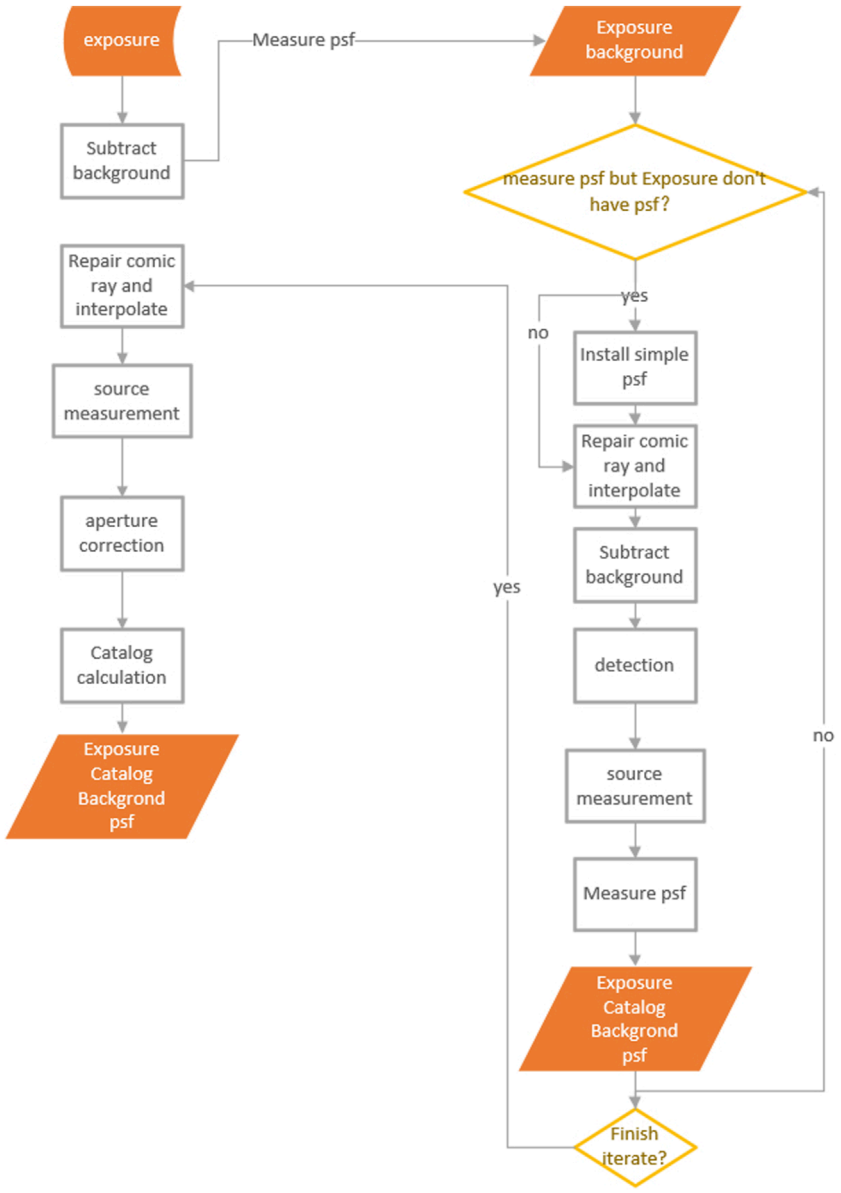

FIGURE 5
Flowchart of CharacterizeImageTask.

6. PSF Measurement: Measuring the PSF is iterative, with the number of iterations being selectable. Initially, if PSF information is absent, a simple Gaussian PSF is set. Subsequent tasks, like cosmic ray repair and source detection, are rerun, with the PSF being measured based on sources having a signal-to-noise ratio higher than 50σ.
7. Source Characteristic Measurement: In this step, various built-in algorithms can be chosen for calculating source features. For example, for flux calculation, options include aperture flux (base_CircularApertureFlux_12_0), PSF flux (base_PsfFlux), Gaussian flux (base_GaussianFlux), and CModel for galaxy photometry (Abazajian et al., 2004). Different algorithms can also be selected for measuring galaxy morphology.
8. Aperture Correction: This step is focused on aperture photometry, a fundamental technique in astrophysics for measuring the flux of astronomical objects. The process involves computing the ratios of different flux algorithm measurements to the measurement used for photometric calibration and using Chebyshev polynomials to interpolate.

Each of these steps is integral to the comprehensive processing and analysis of raw data, ensuring accurate and detailed characterization of the captured images.

4.2.1 Configurations of characterizeImage

Once the pipelines for data processing are outlined, the next step involves fine-tuning the configurations for various tasks, such as characterizeImage. This includes setting parameters for different stages of the process. For instance, during background subtraction, we can adjust the bin size for calculating the sky background,

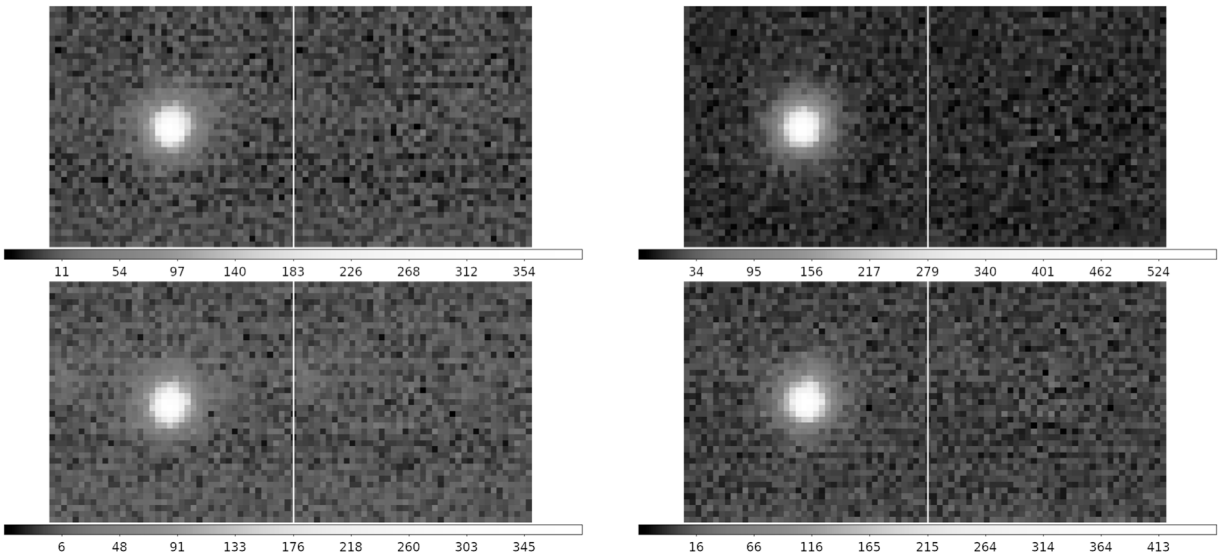

FIGURE 6
Four illustrative cases of PSF model residuals. The left part of each panel shows the original source image, while the right part displays the residuals remaining subsequent to the PSF subtraction. In the majority of instances, the residuals remaining after subtraction of the PSF model are negligible and merge with the background.

select the statistical method (like the default mean with clipping, or alternatives like mean without clipping or median), and choose the fitting algorithm for the sky background. Various functions can be used for this fitting, such as a single constant, a linear function, or spline functions like NATURAL_SPLINE or AKIMA_SPLINE, with AKIMA_SPLINE being the usual default. In tasks like PSF measurement and source characteristic measurement, we can also configure the size of the PSF. Similarly, for cosmic ray repair, settings include configuring the gradient to identify signals as cosmic rays and adjusting the threshold for source detection is also feasible.

In obs_mccd, it is essential to customize the configurations of different subtasks according to the specific characteristics of the instrument and the results obtained from preliminary data processing. This tailored approach ensures that the data processing is optimally aligned with the unique attributes of the instrument and the data, leading to more accurate and efficient processing outcomes.

4.2.2 PSF modeling and assessment

One of the most important products of characterizeImage is PSF. In the LSST Science Pipelines, PSF stars are selected via a k-means clustering algorithm (Bosch et al., 2018). PSF candidates are identified by rejecting objects with unusual brightness and size. After three iterations, PSF stars are determined across each CCD. In the output source catalogs, they are flagged as calib_psf_used=1. Intrinsically, the LSST Science Pipelines use PSFEx (Bertin, 2013) to model PSF stars on $41 \times 41-$ pixel postage stamps extracted from the post-ISR images. The PSF models on each CCD are established independently. In Figure 6, we show illustrative examples of PSF model residuals.

As a quality control, we fit a 2D Moffat function on each PSF star selected by the pipeline, and measure the FWHM to assess the PSF size. Meanwhile, we calculate the ellipticity of each PSF star from the characterizeImage output source catalogs. As a clarification, the ellipticity in this paper is defined using the distortion parameterization similar to (Bosch et al., 2018). In Figure 7, we demonstrate 2D plots of PSF FWHM and ellipticity for an example commissioning visit. The size and ellipticity are continuous across the entire focal plane. The central CCD has a relatively lower PSF size and ellipticity, whilst the PSF stars near the limbic and corner regions show larger values. In Figure 8, we plot the statistics of the FWHM and ellipticity.

For the purpose of static cosmology, a desired median PSF in r-band should have a size smaller than 1.2 arcsec, and ellipticity lower than 0.13 according to the criteria described in Fu et al. (2022). In this example of commissioning r-band PSF assessment, most PSF stars have FWHM lower than 1.05 arcsec and ellipticity lower than 0.13. For the official survey data release in the future, adaptive optics and scheduling observations for optimal conditions can mitigate impacts from atmospheric conditions. Fine-tuning instrumental calibration, PSF modeling, artifact handling, and background modeling can also improve the data quality and reliability of photometric measurements. We wish to clarify that the example data presented in this paper serves solely for the purpose of validating and demonstrating the pipeline; it should not be interpreted as formal scientific results or as a reflection of the ultimate image quality.

4.3 Calibrate

Following the image characterization, the next step is to engage in the calibration process, akin to the procedures in characterizeImage. The calibrate stage involves several subtasks, initiating with source detection. Contrasting with the source detection in characterizeImage, which targets sources with a signal-to-noise ratio above 50σ, this phase broadens its scope to include all

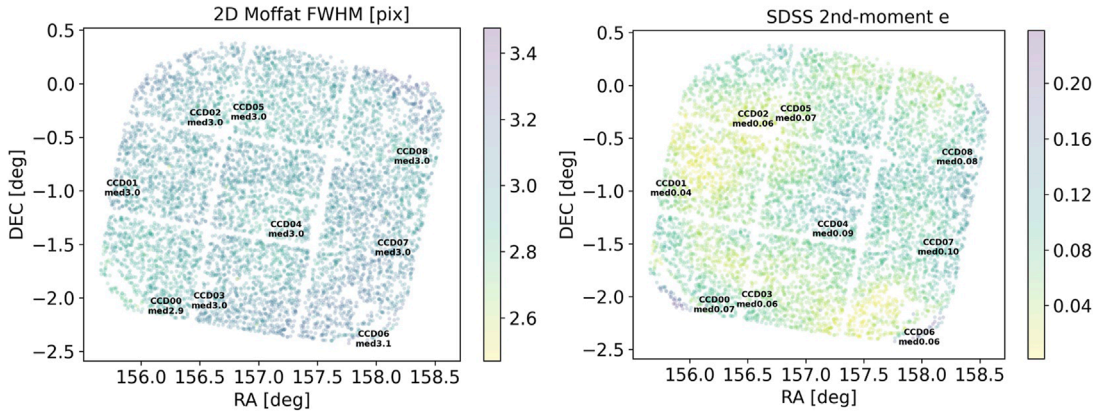

FIGURE 7
Example full FoV plots of PSF size (FWHM) and ellipticity. Each data point corresponds to the position of a PSF star. The color of the point represents the PSF size and ellipticity respectively. The median values of PSF size and ellipticity within each CCD are also labeled on the plots. Note: the plots are shown for validation of the QC system only.

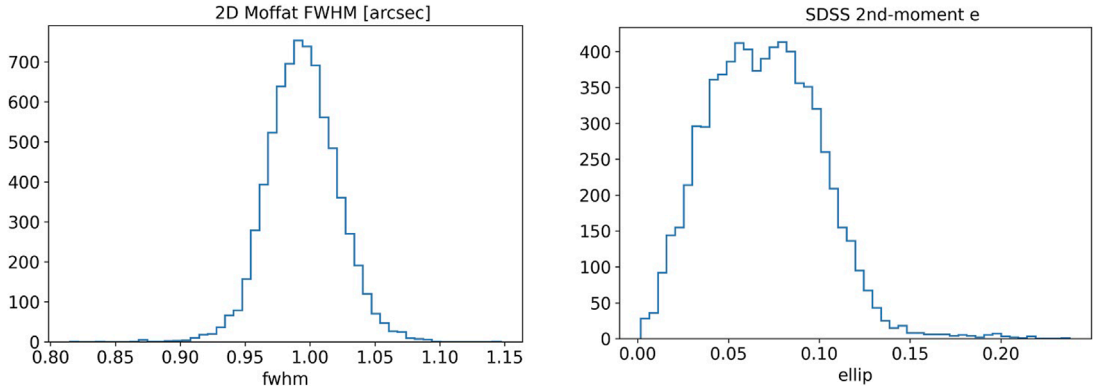

FIGURE 8
Example histogram plots of PSF size (FWHM) and ellipticity distribution. The FWHM is measured from the fitted 2D Moffat function on each PSF star selected by the pipeline. The ellipticity is calculated from the "SDSS 2nd-moments," which are the photometric measurements using the SDSS algorithm as described in Lupton et al. (2001). This algorithm is integrated into the LSST Science Pipelines along with other photometric measurements and shape measurements. Note: the plots are shown for validation of the QC system only.

sources with a signal-to-noise ratio greater than 5σ. The subsequent stages of the calibration process encompass tasks such as source deblending, aperture correction, and the measurement of source characteristics. The procedure culminates with astrometry and photometry calibration. In our study, particular attention is given to assessing the efficacy of astrometric calibration within the data processing workflow.

4.3.1 SIP convention

Astrometry plays a fundamental role in image processing, and its quality significantly influences subsequent steps in data processing. One primary task of astrometry involves correcting geometric distortion caused by the optical system. The general process for handling distortion is described in (Calabretta et al., 2004), distortions can be corrected in either the initial pixel coordinate system or the intermediate pixel coordinate system. Subsequently, the corrected coordinate system obtained can be transformed into a spherical coordinate system and then into the desired celestial coordinate system. Distortion correction commonly involves polynomial fitting, with various polynomial specifications for this purpose. Examples include the polynomial specification output by SCAMP (Bertin, 2006) which is represented by *PVi_j*, and the SIP (Simple Imaging Polynomial) convention (Shupe et al., 2005). However, these two conventions are essentially interchangeable (Shupe et al., 2012), the LSST Science Pipelines we employ adopt the SIP convention, which is denoted by Eqs 1–3:

$$\begin{pmatrix} x \\ y \end{pmatrix} = \begin{pmatrix} CD1\_1 & CD1\_2 \\ CD2\_1 & CD2\_2 \end{pmatrix} \begin{pmatrix} u + f(u,v) \\ v + g(u,v) \end{pmatrix} \quad (1)$$

$$f(u,v) = \sum_{p,q} A\_p\_q u^p v^q, p + q <= order \quad (2)$$

$$g(u,v) = \sum_{p,q} B\_p\_q u^p v^q, p + q <= order \quad (3)$$

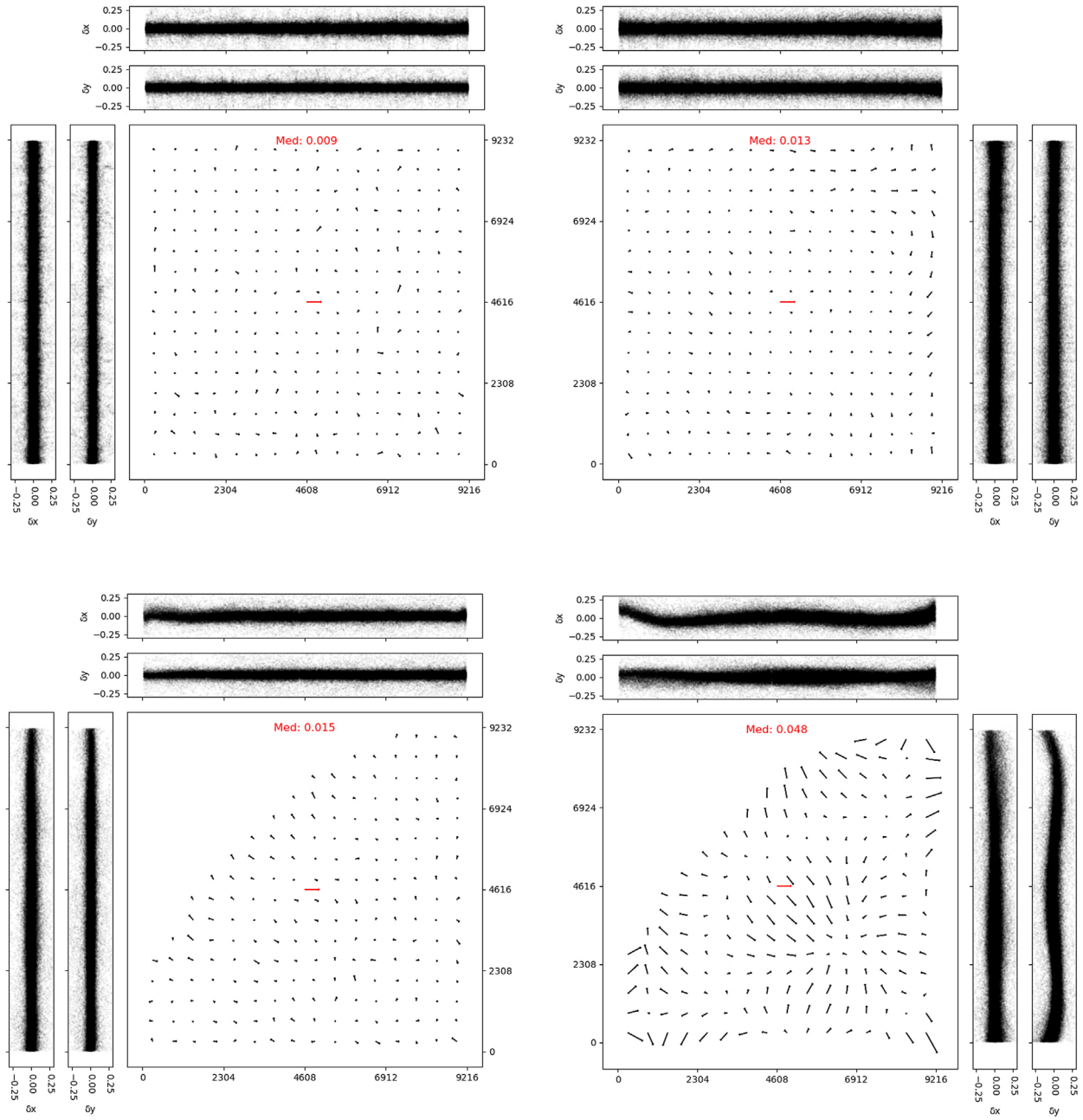

FIGURE 9
From top to bottom, the geometric distortion maps for CCD ID 4 and 0. The left panel displays residuals using the fifth-order SIP polynomial while the right panel shows results using the third-order SIP polynomial. The size of the residual vectors is magnified by a factor of 4,000, and the red vector in the center represents a residual of 0.1 pixel. The median of these vectors is displayed above the image. We also show the residual trends along the *X* and *Y*-axes. Units are in pixels.

4.3.2 Source matching

Fitting the SIP polynomial, which describes distortion, necessitates accurately determining the actual positions of stars in an image. This step requires correlating the stars detected in the image with their counterparts in the reference catalogs. The typical method for achieving this is by creating and comparing patterns constructed from stars in both the image and the reference catalog. This comparison process is known as "matching."

One common approach to matching is the construction of triangles using stars and then comparing specific geometric properties of these triangles. For example, a method involves comparing the ratio of the longest to the shortest side of the triangles, along with the cosine value of the included angles, as described by Groth (1986). Other methods have evolved from this, varying in the attributes compared. For instance, Valdes et al. (1995) developed a technique involving the comparison of ratios like b/a and c/a in

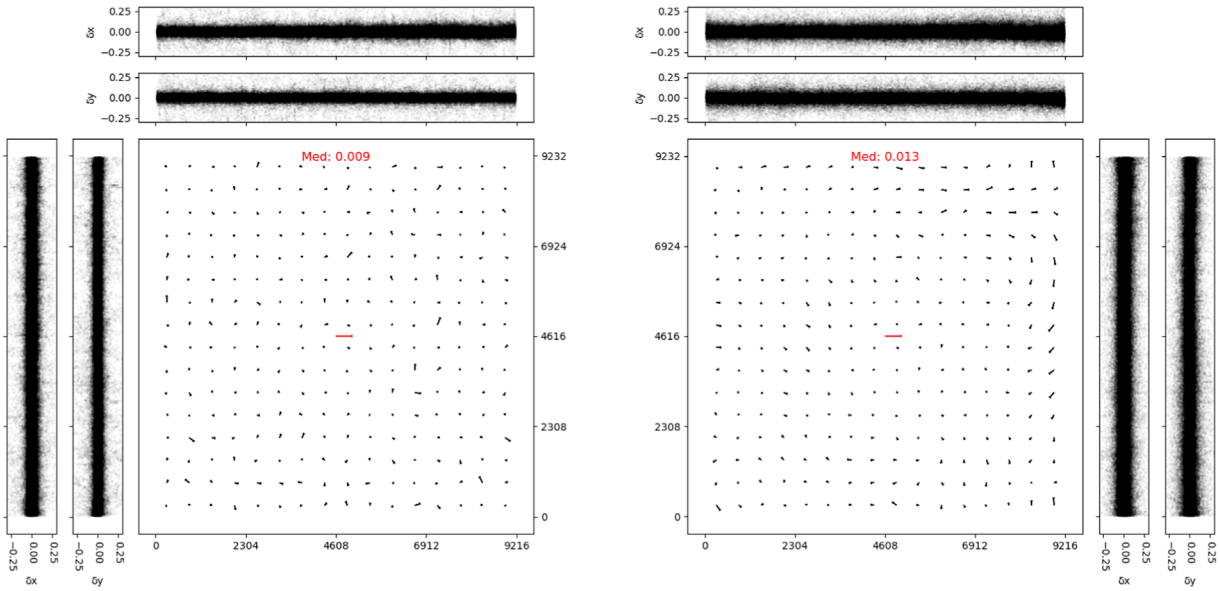

FIGURE 10
The geometric distortion maps for CCD ID 4 processed by two different pipelines. The left panel displays residuals using the LSST science pipelines while the right panel shows results using our in-house pipelines. The size of the residual vectors is magnified by a factor of 4,000, and the red vector in the center represents a residual of 0.1 pixel. The median of these vectors is displayed above the image. We also show the residual trends along the *X* and *Y*-axes. Units are in pixels.

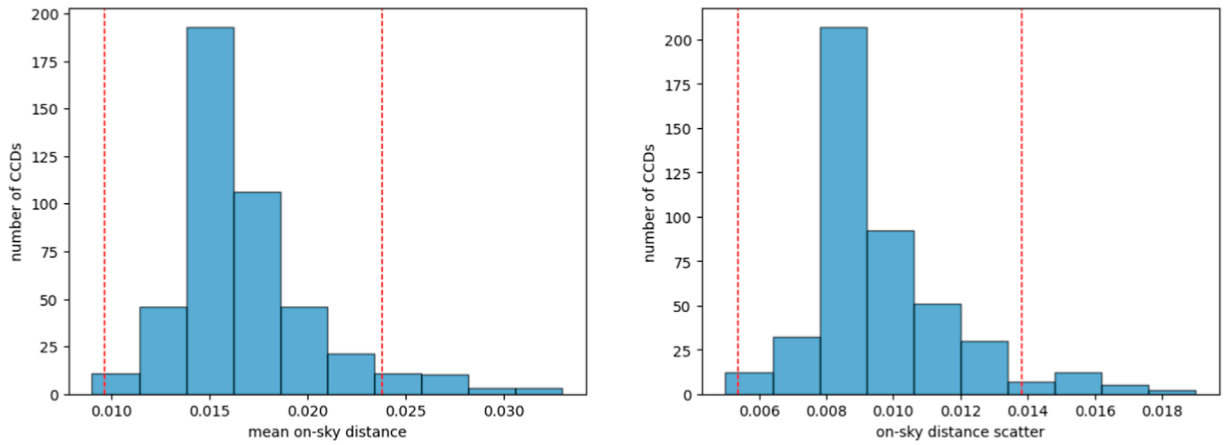

FIGURE 11
The distribution of mean on-sky distance and scatter is presented, with the red line indicating the 2σ level of this distribution. The units on the horizontal axis are in arcseconds.

patterns from two star catalogs, where *a*, *b*, and *c* represent the sides of the triangle in decreasing lengths.

These matching techniques are crucial for astrometric calibration, ensuring that the observed positions of stars align with their known positions in the celestial sphere, thereby enabling accurate distortion modeling in astronomical imaging. In addition to triangles, various other geometric patterns are employed for the matching process. For instance, the Optimistic Pattern Matching B (OPMb) algorithm uses a pinwheel pattern, as depicted in Figure 3 of the study by Tabur (2007). The matching process in OPMb involves comparing the separations of stars and their position angles (PA) relative to a central star in the pattern.

However, OPMb encounters difficulties in regions with high stellar density. To address this, the LSST Science Pipelines have adapted a modified version of this algorithm, known as the Pessimistic Pattern Matcher B (PPMb). PPMb is designed to be more robust in dense star fields. The steps of implementing the PPMb algorithm can be summarized as follows:

1. Determine the center of the loaded reference catalog based on the telescope pointing and rotation angle. The size of the

catalog is determined by the geometric description of the instrument in camera.py. During the loading process, a sky region marginally larger than described in camera.py is loaded, followed by the application of proper motion correction to the loaded reference star catalog.

2. In the source detection step, star catalogs are sorted by brightness in descending order for both the image and reference catalogs. The position of each star is then converted into x, y, z coordinates within a unit sphere coordinate system. Based on brightness, pinwheel patterns are created separately for the image and reference catalogs, facilitating the alignment and comparison process in astrometric analysis.
3. Automatically compute the matching tolerance dist_tol. Employ the previously constructed patterns and utilize cKDTree to find the two most similar patterns in the image catalog and calculate the average difference between these two patterns. Repeat the same process for the reference catalog. The final tolerance value is determined by selecting the smaller of the two differences. During the matching process of the patterns in the image catalogs and the reference catalog, the difference in spokes' lengths between two patterns must be smaller than the tolerance value to consider them as the same group of stars.
4. Set additional tolerances for the subsequent matches, including shift and rotation. During the iterative process, automatically relax the criteria when there are no matches.
5. The matching process starts with the catalog from the image, selecting reference stars for comparison based on their brightness. A spoke pattern is created using star pairs from the image, and similar patterns from the reference catalog are identified within a certain tolerance range as calculated in the second step. After this initial filtering, a further, more detailed comparison will be conducted, ultimately resulting in a list of matches, which is used for fitting the SIP polynomial for astrometric calibration.

We processed 50 exposures from a dense star field. Gaia DR3 catalog (Brown et al., 2021) was used as the reference catalog to test the correction quality of geometric distortion. Figures 9, 10 showcases the comparison between corrections using fifth-order and third-order SIP polynomials for distortion fitting. We divided each CCD into 16×16 bins, with the red line segment indicating a 0.1-pixel residual. For the central CCD (ID 4), employing a third-order polynomial to correct geometric distortions yields relatively satisfactory results. The outcomes derived from fitting the geometric distortions of the central CCD with a fourth-order polynomial are approximately equivalent to those obtained with a third-order polynomial, and employing a fifth-order polynomial, nonetheless, can improve the precision of the fit. However, for CCDs further from the center, the third-order polynomial fitting showed significant residuals, suggesting inadequate correction of distortion. In contrast, the fifth-order polynomial fitting more effectively accounted for the distortion. Based on these observations, we opted for a fifth-order polynomial for SIP fitting in our data processing. Figure 11 also present the distribution of mean on-sky distance and scatter for all these CCDs. After processing with the LSST science pipelines, the HSC's systematic error is approximately 10 mas. Our processed final results are on the same order of magnitude as those of the HSC.

In addition to employing the LSST pipelines for astrometry, we also utilize our in-house developed pipeline, which is based on Sextractor (Bertin and Arnouts, 1996), PSFEx, and SCAMP, to perform tasks such as source detection, PSF construction, and astrometry. Similar configurations are applied to process the results of the same data batch. For instance, we match stars with a signal-to-noise ratio greater than 40 and similarly employ a fifth-order polynomial for fitting. The final outcomes for the correction of geometric distortions are akin between the two approaches, the median average of nine CCDs obtained from processing with the LSST pipeline is $0.011''$, while the median average yielded by our in-house pipeline stands at $0.016''$. Both outcomes are satisfactory and exhibit a small discrepancy. However, considering that the LSST pipeline not only executes the aforementioned tasks but also offers a plethora of additional features and facilitates convenient data management through databases, we plan to adopt the LSST pipeline for data processing in future endeavors.

As previously stated, the sample data showcased in this paper is utilized strictly for the purposes of validating the pipeline and testing the astrometric calibration algorithms and configurations. It is important to note that these examples are not indicative of finalized scientific outcomes or the definitive quality of images.

5 Summary

In this study, with guidance and resources provided by the LSST community, including valuable comments and tutorials, and inspired by the successful implementation of these pipelines by the HSC team, we have adopted the LSST Science Pipelines for processing data from a mosaic CCD instrument. To showcase the workflow, we demonstrate the CCD-level processing of raw images from the engineering test of WFST. This paper outlines our development of the obs_mccd package and the execution of various data processing operations enabled by this package, such as ISR, characterizeImage, and calibrate. Additionally, we assess the outcomes of our data processing workflow, focusing on the PSF modeling and the correction of geometric distortion. Our findings recommend using a fifth-order polynomial for effective distortion correction in a realistic dataset.

The LSST Science Pipelines have proven their advanced capabilities and high-quality data processing, as evidenced by the HSC. In our data validation, data processing was conducted on a computer equipped with an AMD EPYC 7763 64-core processor and 1008 GB RAM. We present the wall-clock time for processing 450 CCDs at each stage on a single core: the calibration step averaged 293.0 s, the characterizeImage required an average of 123.2 s, and ISR took 77.3 s. On average, processing a single image took approximately 8 min. The obs_package makes the execution of LSST pipeline tasks more accessible to our instrument. Our work aims to serve as a practical guide and introduction for others interested in leveraging the LSST Science Pipelines for their observational data.

Furthermore, we recognize the untapped potential of the LSST Science Pipelines. They offer a wealth of features, such as utilizing multi-epoch data for improved calibrations and exploring functionalities like coaddition and forced photometry. Our future work will delve into these additional capabilities, expanding the scope and impact of our research with the LSST Science Pipelines.

Data availability statement

The data analyzed in this study is subject to the following licenses/restrictions: The data used for pipeline validation is from the engineering test of WFST and is not public due to relevant data policy. The data may be available upon request. Requests to access these datasets should be directed to BL, byliu@pmo.ac.cn.

Author contributions

YH: Writing–original draft, Writing–review and editing. CY: Writing–original draft, Writing–review and editing. MZ: Writing–original draft, Writing–review and editing. YC: Writing–original draft, Writing–review and editing. BL: Writing–original draft, Writing–review and editing.

Funding

The author(s) declare that financial support was received for the research, authorship, and/or publication of this article. This study is supported by the National Key Research and Development Program of China (2023YFA1608100), and the Cyrus Chun Ying Tang Foundations. YH acknowledges the scholarship from the Cyrus Chun Ying Tang Foundations.

Acknowledgments

We thank the referees and Prof. Xianzhong Zheng and Prof. Min Fang at Purple Mountain Observatory for their supervision and constructive discussion. We extend our heartfelt gratitude to the LSST community and the Data Management team. Their invaluable contributions, ranging from the development of cutting-edge tools to the supportive environment they foster, have been instrumental in our research. We would like to express our gratitude to the LSST Community Forum and its members for their enthusiastic, proactive, and prompt responses in addressing our questions and helping us navigate challenges encountered during the utilization and modification of LSST science pipelines. This paper makes use of LSST Science Pipelines software developed by the Vera C. Rubin Observatory. We thank the Rubin Observatory for making their code available as free software at https://pipelines.lsst.io.

Conflict of interest

The authors declare that the research was conducted in the absence of any commercial or financial relationships that could be construed as a potential conflict of interest.

The reviewer JY shared authors YH, CY, YC second affiliation at the time of review.

Publisher's note

References

Abazajian, K., Adelman-McCarthy, J. K., Agüeros, M. A., Allam, S. S., Anderson, K., Anderson, S. F., et al. (2004). The second data release of the sloan digital sky survey. *AJ* 128, 502–512. doi:10.1086/421365

Abbott, B. P., Abbott, R., Abbott, T., Abernathy, M., Acernese, F., Ackley, K., et al. (2016). Observation of gravitational waves from a binary black hole merger. *Phys. Rev. Lett.* 116, 061102. doi:10.1103/physrevlett.116.061102

Aihara, H., AlSayyad, Y., Ando, M., Armstrong, R., Bosch, J., Egami, E., et al. (2019). Second data release of the hyper suprime-cam subaru strategic Program. *PASJ* 71, 114. doi:10.1093/pasj/psz103

Aihara, H., Armstrong, R., Bickerton, S., Bosch, J., Coupon, J., Furusawa, H., et al. (2018). First data release of the hyper suprime-cam subaru strategic Program. *PASJ* 70, S8. doi:10.1093/pasj/psx081

Bertin, E. (2006). "Automatic astrometric and photometric calibration with SCAMP," in *Astronomical data analysis software and systems XV*. Editors C. Gabriel, C. Arviset, D. Ponz, and S. Enrique (San Francisco: Astronomical Society of the Pacific Conference Series), 351, 112.

Bertin, E. (2013). Psfex: point spread function extractor. *Astrophys. Source Code Libr.* 1301, 001.

Bertin, E., and Arnouts, S. (1996). SExtractor: software for source extraction. *Astron. Astrophys. Suppl. Ser.* 117, 393–404. doi:10.1051/aas:1996164

Blum, R. D., Burleigh, K., Dey, A., Schlegel, D. J., Meisner, A. M., Levi, M., et al. (2016). "The DECam legacy survey," in *American astronomical society meeting abstracts #228* (American Astronomical Society Meeting Abstracts).

Bosch, J., AlSayyad, Y., Armstrong, R., Bellm, E., Chiang, H.-F., Eggl, S., et al. (2019). "An overview of the LSST image processing pipelines," in *Astronomical data analysis software and systems XXVII*. Editors P. J. Teuben, M. W. Pound, B. A. Thomas, and E. M. Warner (San Francisco: Astronomical Society of the Pacific Conference Series), 523, 521. doi:10.48550/arXiv.1812.03248

Bosch, J., Armstrong, R., Bickerton, S., Furusawa, H., Ikeda, H., Koike, M., et al. (2018). The Hyper Suprime-Cam software pipeline. *PASJ* 70, S5. doi:10.1093/pasj/psx080

Brown, A. G., Vallenari, A., Prusti, T., De Bruijne, J., Babusiaux, C., Biermann, M., et al. (2021). *Gaia* early data release 3. *Astronomy Astrophysics* 649, A1. doi:10.1051/0004-6361/202141135

Calabretta, M. R., Valdes, F., Greisen, E. W., and Allen, S. L. (2004). "Representations of distortions in FITS world coordinate systems," in *Astronomical data analysis software and systems (ADASS) XIII*. Editors F. Ochsenbein, M. G. Allen, and D. Egret (San Francisco: Astronomical Society of the Pacific Conference Series), 314, 551.

Chang, C., Wang, M., Dodelson, S., Eifler, T., Heymans, C., Jarvis, M., et al. (2018). A unified analysis of four cosmic shear surveys. *Mon. Notices R. Astronomical Soc.* 482, 3696–3717. doi:10.1093/mnras/sty2902

Dalal, R., Li, X., Nicola, A., Zuntz, J., Strauss, M. A., Sugiyama, S., et al. (2023). Hyper suprime-cam year 3 results: cosmology from cosmic shear power spectra. *Phys. Rev. D.* 108, 123519. doi:10.1103/PhysRevD.108.123519

Erben, T., Hildebrandt, H., Miller, L., van Waerbeke, L., Heymans, C., Hoekstra, H., et al. (2013). Cfhtlens: the Canada–france–Hawaii telescope lensing survey – imaging

data and catalogue products. *Mon. Notices R. Astronomical Soc.* 433, 2545–2563. doi:10.1093/mnras/stt928

Fu, S., Dell'Antonio, I., Chary, R.-R., Clowe, D., Cooper, M. C., Donahue, M., et al. (2022). Lovoccs. i. survey introduction, data processing pipeline, and early science results. *Astrophysical J.* 933, 84. doi:10.3847/1538-4357/ac68e8

Fu, S., Dell'Antonio, I., Escalante, Z., Nelson, J., Englert, A., Helhoski, S., et al. (2024). Lovoccs – ii. weak lensing mass distributions, red-sequence galaxy distributions, and their alignment with the brightest cluster galaxy in 58 nearby x-ray-luminous galaxy clusters. arXiv.

Groth, E. J. (1986). A pattern-matching algorithm for two-dimensional coordinate lists. *AJ* 91, 1244–1248. doi:10.1086/114099

Gunn, J. E., Siegmund, W. A., Mannery, E. J., Owen, R. E., Hull, C. L., Leger, R. F., et al. (2006). The 2.5 m telescope of the sloan digital sky survey. *AJ* 131, 2332–2359. doi:10.1086/500975

Ivezić, Ž., Kahn, S. M., Tyson, J. A., Abel, B., Acosta, E., Allsman, R., et al. (2019). LSST: from science drivers to reference design and anticipated data products. *ApJ* 873, 111. doi:10.3847/1538-4357/ab042c

Jenness, T., Bosch, J. F., Salnikov, A., Lust, N. B., Pease, N. M., Gower, M., et al. (2023). "The Vera C. Rubin Observatory Data Butler and pipeline execution system," in Proc. SPIE 12189, Software and Cyberinfrastructure for Astronomy VII. August 29, 2022, 1218911. doi:10.1117/12.2629569

Jurić, M., Kantor, J., Lim, K. T., Lupton, R. H., Dubois-Felsmann, G., Jenness, T., et al. (2017). "The LSST data management system," in *Astronomical data analysis software and systems XXV*. Editors N. P. F. Lorente, K. Shortridge, and R. Wayth (San Francisco: Astronomical Society of the Pacific Conference Series), 512, 279. doi:10.48550/arXiv.1512.07914

Lin, Z., Jiang, N., and Kong, X. (2022). The prospects of finding tidal disruption events with 2.5-m Wide-Field Survey Telescope based on mock observations. *Mon. Notices R. Astronomical Soc.* 513, 2422–2436. doi:10.1093/mnras/stac946

Lupton, R., Gunn, J. E., Ivezić, Z., Knapp, G. R., and Kent, S. (2001). "The SDSS imaging pipelines," in *Astronomical data analysis software and systems X*. Editors J. Harnden, F. R., F. A. Primini, and H. E. Payne (San Francisco: Astronomical Society of the Pacific Conference Series), 238, 269. doi:10.48550/arXiv.astro-ph/0101420

Magnier, E., Kaiser, N., and Chambers, K. (2006). "The pan-starrs ps1 image processing pipeline," in The Advanced Maui Optical and Space Surveillance Technologies Conference, Wailea, Maui, Hawaii, September 10-14, 2006 (Maui: The Maui Economic Development Board), 50.

Massey, P. (1997). *A user's guide to ccd reductions with iraf*. Tucson: National Optical Astronomy Observatory.

Miller, L., Kitching, T., Heymans, C., Heavens, A., and Van Waerbeke, L. (2007). Bayesian galaxy shape measurement for weak lensing surveys–i. methodology and a fast-fitting algorithm. *Mon. Notices R. Astronomical Soc.* 382, 315–324. doi:10.1111/j.1365-2966.2007.12363.x

Mullaney, J. R., Makrygianni, L., Dhillon, V., Littlefair, S., Ackley, K., Dyer, M., et al. (2021). Processing GOTO data with the Rubin observatory LSST science pipelines I: production of coadded frames. *PASA* 38, e004. doi:10.1017/pasa.2020.45

Schirmer, M. (2013). Theli: convenient reduction of optical, near-infrared, and mid-infrared imaging data. *Astrophysical J. Suppl. Ser.* 209, 21. doi:10.1088/0067-0049/209/2/21

Shupe, D. L., Laher, R. R., Storrie-Lombardi, L., Surace, J., Grillmair, C., Levitan, D., et al. (2012). "More flexibility in representing geometric distortion in astronomical images," in *Software and cyberinfrastructure for astronomy II*. Editors N. M. Radziwill, and G. Chiozzi (Bellingham: Society of Photo Optical Instrumentation Engineers), 8451, 84511M. doi:10.1117/12.925460

Shupe, D. L., Moshir, M., Li, J., Makovoz, D., Narron, R., and Hook, R. N. (2005). "The SIP convention for representing distortion in FITS image headers," in *Astronomical data analysis software and systems XIV*. Editors P. Shopbell, M. Britton, and R. Ebert (San Francisco: Astronomical Society of the Pacific Conference Series), 347, 491.

Stetson, P. B. (1987). *Daophot: a computer program for crowded-field stellar photometry*. San Francisco: Publications of the Astronomical Society of the Pacific, 191.

Tabur, V. (2007). Fast algorithms for matching CCD images to a stellar catalogue. *PASA* 24, 189–198. doi:10.1071/AS07028

Valdes, F., and Gruendl, R. (2014). The decam community pipeline. *Astronomical Data Analysis Softw. Syst. XXIII* 485, 379.

Valdes, F. G., Campusano, L. E., Velasquez, J. D., and Stetson, P. B. (1995). FOCAS automatic catalog matching algorithms. *PASP* 107, 1119. doi:10.1086/133667

Wang, T., Liu, G., Cai, Z., Geng, J., Fang, M., He, H., et al. (2023). Science with the 2.5-meter wide field survey telescope (WFST). *Sci. China Phys. Mech. Astronomy* 66, 109512. doi:10.1007/s11433-023-2197-5

frontiers | Frontiers in Astronomy and Space Sciences

TYPE Original Research
PUBLISHED 23 May 2024
DOI 10.3389/fspas.2024.1406090

OPEN ACCESS

EDITED BY
Hairen Wang,
Purple Mountain Observatory, Chinese Academy of Sciences (CAS), China

REVIEWED BY
Kainan Wang,
Wuhan University, China
Hongchao Zhao,
Sun Yat-sen University, China

*CORRESPONDENCE
Erhui Qi,
qieh@ciomp.ac.cn

RECEIVED 24 March 2024
ACCEPTED 22 April 2024
PUBLISHED 23 May 2024

CITATION
Hu H, Zhou D, Zhao C, Qi E and Luo X (2024), Hetero-bonding strength investigation into opto-mechanical interface.
Front. Astron. Space Sci. 11:1406090.
doi: 10.3389/fspas.2024.1406090

Hetero-bonding strength investigation into opto-mechanical interface

Haifei Hu[1], Di Zhou[1], Chenchen Zhao[2], Erhui Qi[1]* and Xiao Luo[1]

[1]Changchun Institute of Optics, Fine Mechanics and Physics, Chinese Academy of Sciences, Changchun, China, [2]Changchun Vocational Institute of Technology, Changchun, China

Glass-metal hetero-bonding through optical epoxy adhesive is frequently used in opto-mechanics and requires high stability. However, the bonding stability is difficult to achieve and predict in massive use cases, where dozens to thousands of metal pads are bonded to mount large optics. Here a universal adhesive bonding technology was proposed and evaluated through reliability analyses based on a limited number of sample tests. Specimens were prepared and tested via standard procedures and equipment; afterward, the lower strength limits were calculated with high reliability. Nominal tensile (6.7 MPa) and shear (4.3 MPa) strength limits at 99.95% reliability were expected for ongoing 30 m aperture telescopes. This study may improve the quality of opto-mechanical interfaces and reduce the risk on constructing extremely large telescopes.

KEYWORDS

large aperture optics, metal-glass bonding, opto-mechanical interface, epoxy bonding, strength stability, safety factor

1 Introduction

Extremely large telescopes have been designed and utilized to achieve scientific goals such as searching for extrasolar planets, probing the formation of stars/galaxies/black holes, detecting water and organic molecules, measuring the acceleration of the Universe's expansion, etc. Nowadays, they have reached to tens of meters and their primary mirror consists of mirror segments involving massive opto-mechanical joints, mostly in glass-metal form between the optics and their mount structure (Nijenhuis et al., 2016).

Compared to typical linking methods such as optical contact, direct bonding, frit bonding, and mechanical fastening (Haisma et al., 2007; Kim and Schmitz, 2013; Wang et al., 2017), adhesive bonding is regarded as a smart attachment process that is compatible with almost all kinds of material (Ducousso et al., 2018) and is widely used for mounting large optics. As the interface is the weakest part of the whole opto-mechanical system in most cases, the durability of such composite structures often relates directly to the adhesive bond strength (Wetherhold et al., 2018).

Moreover, the Whiffletree-type multipoint support system (Meeks et al., 2016; Lan et al., 2017; Wang, 2017) is regarded as a standard choice for limiting the mirror deformations to

Abbreviations: TMT, the Thirty Meter Telescope; M1, the Primary mirror; E-ELT, the European Extremely Large Telescope; SSD, Sub-surface Damage; DOF, Degrees of Freedom; CMM, Coordinate Measuring Machine.

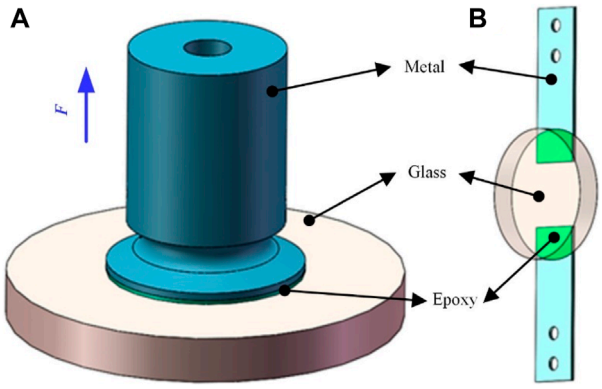

FIGURE 1
Glass-metal adhesive bonding samples under **(A)** tensile and **(B)** shear loads, where the lateral sample is a double-lap type.

some small fraction of the working wavelength (Wang et al., 2016a) for the mirror segments to stitch extremely large telescopes. For these segments, dozens to thousands of metal pads with carefully optimized postions (Wang et al., 2016b) are adhesively bonded to optics. For example, the Thirty Meter Telescope (TMT, aperture 30 m) primary mirror (M1) needs 13,284 pads (492 φ1.4 m segments and 27 pads per segment, with 1/6 segment symmetry) (Williams et al., 2008), while the European Extremely Large Telescope (E-ELT, aperture 39 m) M1 needs 21,546 pads (798 φ1.4 m segment and 27 pads/segment, with 1/6 segment symmetry) (Nijenhuis et al., 2016).

So massive bonding of metal pads onto optics requires a very precise, strong, and stable adhesive bonding technique. In the Whiffletree support structure mounting optical elements, all the small axial pads, made of invar, are bonded to the back or rear surface of the heavy optics and are then linked to the Whiffletree structure maintaining the optical surface figuration.

Low bonding strength involved in such cases represents a hazard, so researchers have been focusing on bonding strength and have found that it depends on many factors, such as the adhesive/primer effect (Hartman et al., 1998; He et al., 2015; Xiong et al., 2015), interfacial geometry (Wetherhold et al., 2018), surface preparation (Ende and Gubbels, 2014; Prolongo and Urena, 2009), and humidity, temperature, aging time, and loading speed (Goglio et al., 2008). These factors frequently can affect the strength such that it varies over a wide range (Afendi et al., 2013). The strength is generally unstable and is difficult to predict accurately by experiment or simulation (Swadener et al., 1999; Afendi et al., 2013; Xu and We, 2013).

Researchers have applied significant effort to improve the average bonding strength (Wang W. et al., 2016; Xu et al., 2019), but most have neglected the lower strength limit of an adhesive bonding, which is extremely important for dangerous cases such as the facing-down case (Bloemhof et al., 2009; Hu et al., 2018) and fast rotating case. Too low bonding strength can be catastrophic for expensive optics, so people usually over-design of the bonding region, usually by over 1,000 times larger size, of the joints to prevent any opto-mechanical interfacial damage.

Nevertheless, large glass-metal joints still broke frequently (Robinson, 2000; Laiterman et al., 2010; Meeks et al., 2016). Large joints also increase the cell weight and cause severe thermal distortion/stress concentration on the optical surface due to large CTE (coefficient of thermal expansion) difference. For example, it is reported that a team will require 18 years (2002–2020) at a cost of tens of millions of dollars to repair the 10-m twin Keck telescopes' bonding problems (Meeks et al., 2016).

Thus this study evaluates and discusses how to avoid adhesive breakage at opto-mechanical joints by seeking a stable bonding technique with a safe strength limit with high reliability. General

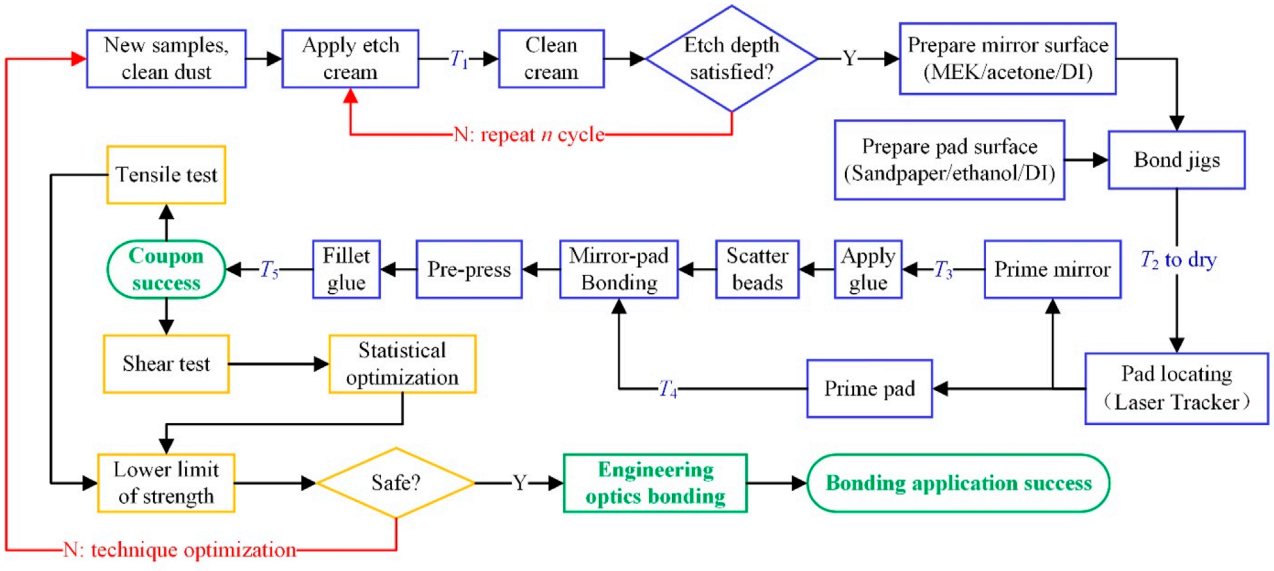

FIGURE 2
Bonding work flow for sample production and process optimization.

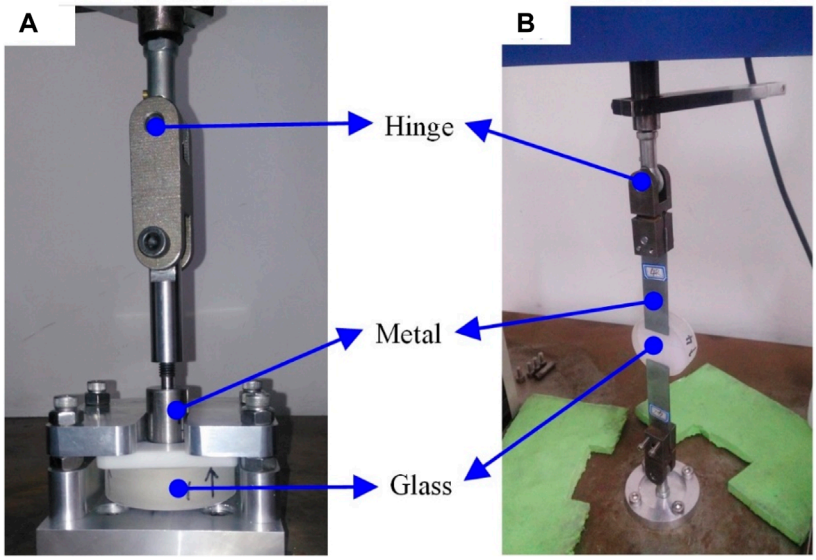

FIGURE 3
Test setup for glass-metal adhesive joint strength; **(A)** direct tensile and **(B)** tensile-shear tests.

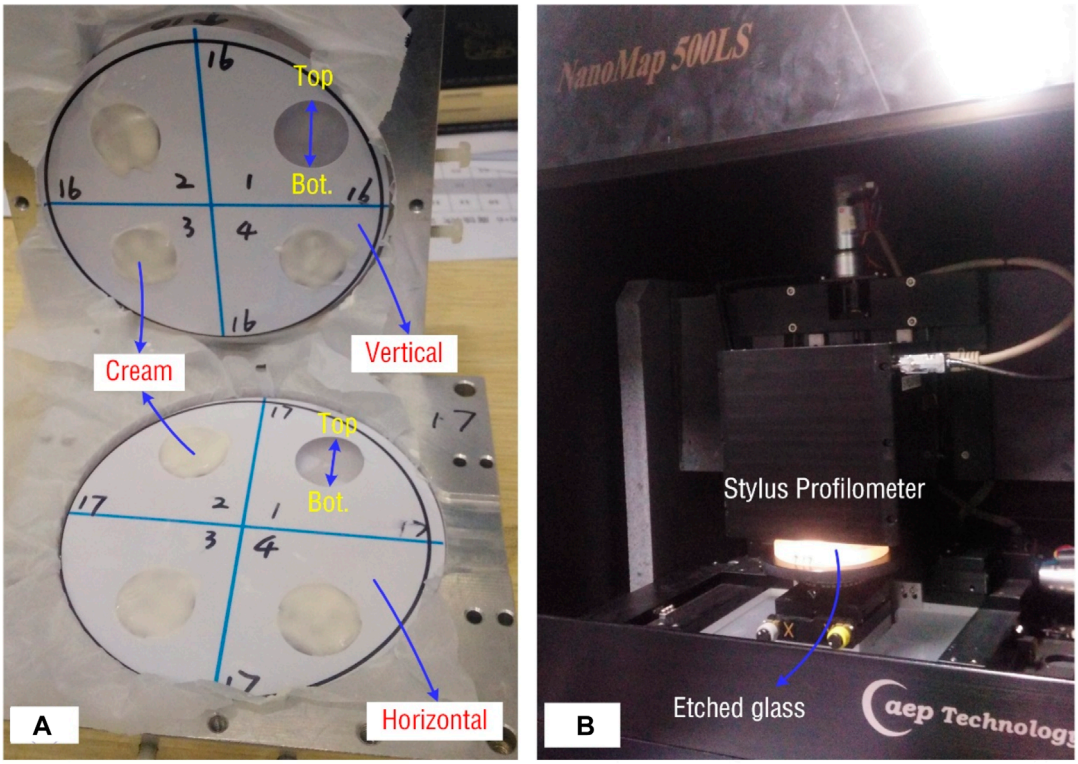

FIGURE 4
Test setup for the glass surface profiles after vertical/horizontal etching, **(A)** etching scheme, where the numbers 1-4 identify both the quadrant sequence and the number of, etch cycles applied to the region, **(B)** testing of the etched glass surface using a Stylus Profilometer, NanoMap 500LS.

procedures are introduced and specimens are prepared for strength testing, prior to which the main factors affecting the strength are carefully investigated and controlled, followed by the lower limit prediction based on the t-distribution assumption. The work may contribute an efficient means to evaluate and optimize the bonding safety and reliability of massive precision optics at low cost.

10.3389/fspas.2024.1406090

TABLE 1 Etch cycle effects on pit depth and profile, in μm.

Region	h_1	R_1	h_2	R_2	h_3	R_3	h_4	R_4
Vertical Top	5.4	4.5	13.0	5.3	22.5	8.2	29.1	9.5
Vertical Bottom	10.5		16.7		26.4		36.0	
Horizontal Top	7.3	2.7	19.7	6.5	28.8	8.8	38.0	12.7
Horizontal Bottom	9.5		18.9		28.5		35.2	

2 Methods

2.1 Samples preparation

Usually the epoxy adhesive's nominal shear strength is somewhat lower than its tensile strength, so several samples were designed for individual tensile and shear tests, as shown in Figure 1, with a bonding size of ~500 mm^2 for the former, and ~350 mm^2 for the latter.

The axial samples are designed as those of the TMT M1 and the shear samples follow the Chinese National Standard for testing an adhesive's shear strength GB/T 7124–2008 (same as ISO 4587:2003). For glass-metal joint applications, high strength, low stress, and viscous epoxy types are preferred (here, EC 2216 B/A Gray from 3M Corp. was used) and controlled to a bond line thickness of ~0.25 mm. The glass is fused silica from Corning and the metal pads are made of invar 4J32.

For avoiding the undesirable three damage styles in the glass-metal hetero-bonding interface, including the separation of glass/epoxy interface, the separation of metal/epoxy interface and the strength failure of glass sub-surface damage layer, namely, pursuing higher epoxy potentiality, a universal high quality bonding process is strongly recommended to be carried out in a clean room with a venting system to protect operators from hazardous chemicals such as HF and acetone, with as less pollution as possible. Operators should wear safety glasses, a face mask with organic/acidic filters, and plastic apron/gloves for protection. The work flow is outlined in Figure 2 and more detailed operations are presented by Laiterman et al. (2010). Some important notes for the key bonding processes of Figure 2 are given below.

1) Dust cleaning and optics protection: clean the glass and the metal with ethanol; paste protecting masks onto the optics, leaving the bonding regions uncovered.
2) Etching: apply the acid cream to the mask holes, wait until it dries, and remove the residue with a wet brush and deionized water (DI) in sequence until no visible cream remains. Repeat the process to remove all sub-surface damage (SSD) layers produced by the fabrication processes.
3) Glass cleaning: at the end of the final etching step, sponge the etching cream until the glass looks clean, and then use large amounts of DI water for further neutralization of any remaining acid.
4) Metal cleaning: abrade the pads' bonding region with sand paper, typically 240 grit. Flush the surface and perform the water break test. Afterward dry the metal with a hot-air gun.
5) Locating: place the locating jigs at their approximate locations and adjust the pad using the assistance of a laser tracker.
6) Priming: apply primer to the bonding region. Control the thickness of the primer to 1.5–2.5 microns or use the values recommended by the supplier.
7) Adhesive application: mix the A/B adhesive components uniformly, apply an adequate amount of mixture to each pad, and then scatter some glass micro-spheres for thickness control. An alternative choice using fishing line also works for thickness control.
8) Bonding operation: place a pad back to its predefined location.
9) After the pads are cured, remove all weights and locating jigs from the mirror.

Based on verifying the success of the coupons obtained from the above processes, mechanical strength tests can be performed, followed by bonding technique evaluation and optimization when needed.

2.2 Strength test and reliability-related limit prediction

Strength tests were carried out by a Chinese National Standard testing machine DDL10 with a load capacity of 10 kN at a resolution of 0.1 N, as shown in Figure 3. As the force was applied along a relatively long axis, two spherical hinges were involved to avoid creating any moment load.

Sample tensile strength values a_i are assumed to be normally distributed, and the corresponding population average $\overline{a}$ would follow the t-distribution, as explained in the Appendix. Then the limits of the average $\overline{a}_L$ and the lower single strength L_T could be determined by Eq. (1):

$$\begin{cases} \overline{a}_L = E(\boldsymbol{a}) - T_{p,\nu} S(\boldsymbol{a})/\sqrt{n} \\ L_T = \overline{a}_L - T_{p,m-1} S(\boldsymbol{a}) \end{cases}, \tag{1}$$

where n is the sample number, m is the number of pads to be bonded, $\boldsymbol{a}$ is a vector consisting of tested strength values, $E(\boldsymbol{a})$ and $S(\boldsymbol{a})$ are the mean value and the standard deviation of a respectively, $T_{p,\nu}$ is the single-side strength distribution region factor at probability p for n samples with $\nu = n - 1$ degrees of freedom (DOF), and $T_{p,m-1}$ is the factor at probability p for m pads. Here it defines $p = 1 - 1/m$ for presenting the marginal reliability, whose physical effect means that less than one (namely, none) of the m pads should break under the allowed stress (this stress itself usually has a safety

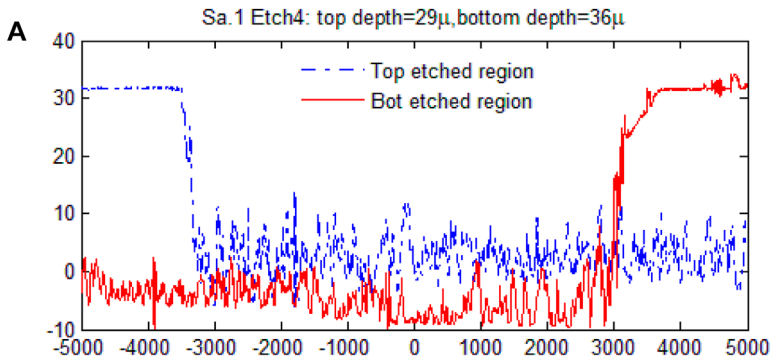

Surface profiles in both regions after 4 etching cycles for the vertical sample

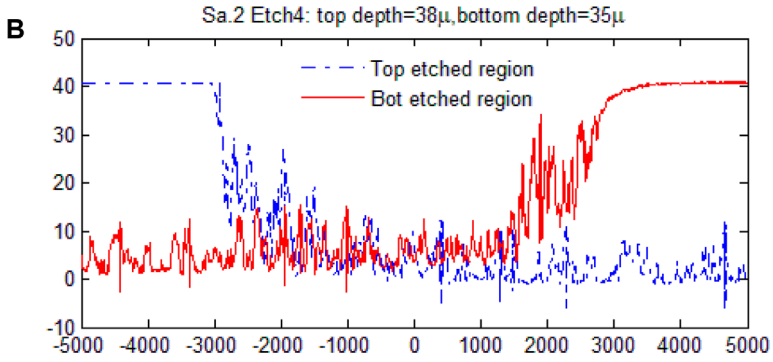

Surface profiles in both regions after 4 etching cycles for the horizontal sample

FIGURE 5
Surface profiles in both regions after four etching cycles(all axes in μm): **(A)** the vertical sample: etched depth of 29 μm on the top side and 35 μm on the bottom side; **(B)** the horizontal: etched depth of 38 μm on the top side and 35 μm on the bottom side.

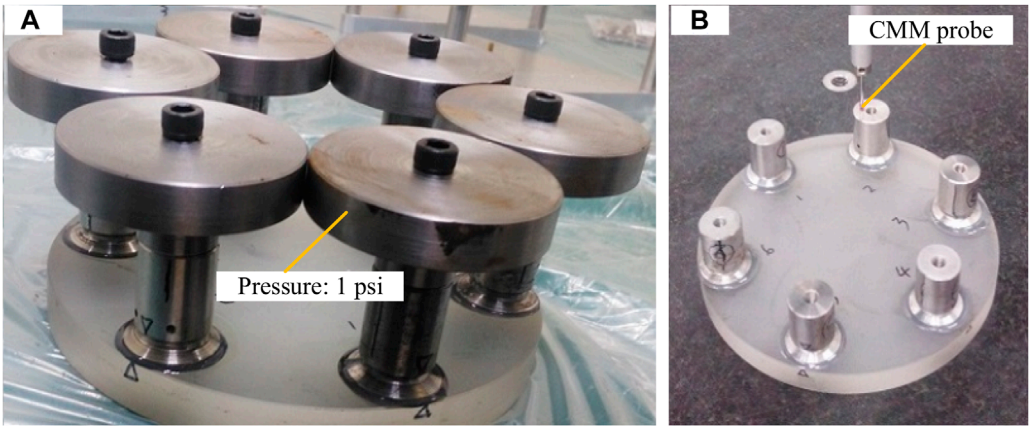

FIGURE 6
Bond line thickness test performed by CMM; **(A)** adhesive bonding controlled by glass beads and pressure of one psi, **(B)** measuring the adhesive thickness using the CMM 3 h after bonding.

factor of ≥4 in engineering application). It's noted that for the tensile test $m = n$, and for the shear test $m = 2n$

In double-lap shear tests, breakage occurs at one end and the strength x_i of the other end is unknown. The only knowledge is that it should be higher than the broken end's strength a_i, expressed as

$$x_i = a_i + t_i T_{p,v} S(\boldsymbol{a}), \text{with } t_i \in \text{rand}[0,1]. \quad (2)$$

TABLE 2 Bond line thickness tests for φ25 pads.

Sample	1	2	3	4	5	6
t/mm	0.28	0.27	0.26	0.21	0.21	0.25
α/Deg	0.06	0.06	0.05	0.04	0.01	0.02
Δt/μm	26	26	22	18	4.4	8.7

By setting up a parameter optimization model, the lower limit of shear strength L_S can be predicted as

$$\begin{aligned} &\text{Find}\,\boldsymbol{t} = \{t_1, t_2, \cdots, t_n\} \\ &\text{Min.}L_S = \overline{E}_L(\boldsymbol{t}) - T_{p,m-1}S(\boldsymbol{t}) \\ &\text{St.}\quad t_i \in \text{rand}[0,1] \\ &\overline{E}_L(\boldsymbol{t}) = E(\boldsymbol{t}) - T_{p,2v+1}S(\boldsymbol{t})/\sqrt{2n} \\ &E(\boldsymbol{t}) = \sum_{i=1}^{n} \frac{a_i + x_i}{2n} \\ &S(\boldsymbol{t}) = \sum_{i=1}^{n} \sqrt{\frac{[a_i - E(\boldsymbol{t})]^2 + [x_i - E(\boldsymbol{t})]^2}{2n-1}} \end{aligned} \quad , \tag{3}$$

where $E(\boldsymbol{t})$ is the n tested sample average strength, $\overline{E}_L(\boldsymbol{t})$ is the expected average limit for the whole $2n$ strength values(Note: n tested ends and n opposite ends), and $S(\boldsymbol{t})$ is the $2n$ values' variance.

3 Results and discussion

In order to obtain uniform and high bonding strength, all processes should be controlled very carefully. In this section, some significant factors affecting strength, such as etching pit depth, bond line thickness, primer thickness, and locating precision, were investigated in detail.

3.1 Etching depth

The SSD layer was removed by the etching process to strengthen the bonding.

Two pieces of φ150 mm glass were tested for evaluating the etching performance of the acid cream: one was etched horizontally, representing the case of axial pads, and the other was etched vertically, representing the case of lateral pads. Both were masked and a φ25 mm circular region was left open in each quadrant, as shown in Figure 4A, with the numbers 1, 2, 3, and four representing both the quadrant sequence and etching cycles. A Stylus Profilometer NanoMap 500LS from Aep Corporation was used to test the top-etched and the bottom-ethced regions for comparison, as shown in Figure 4B.

Surface profile information is provided in Table 1, where the variables hi and Ri represent the pit depth and surface roughness of the ith quadrant, respectively. Generally speaking, the vertical etching is weaker than the horizontal, not only in depth, but also in roughness. The pit depth increases in approximately linear fashion with the number of etching cycles. It is also noted that a higher number of etching cycles will produce a much rougher surface.

The final figure after the fourth etching is shown in Figure 5. It shows that vertical 4-cycle etching generates a pit depth of 29–36 μm with a roughness of 9.5 μm, while horizontal 4-cycle etching achieves a 35–38 μm pit depth with a roughness of 12.7 μm. According to the widely-accepted assumption that the thickness of the SSD layer is about 1.5–3 times that of the final grit size used for material surfacing, four, etch cycles are sufficient to thoroughly remove the SSD layer of glass surfaces ground/polished using a grit size smaller than 9 μm.

An unanticipated and interesting effect is found: the step width of the, etch zone edges is ~1 mm for the vertical case, and is ~3 mm for the horizontal case. This may be attributed to the fact that as we apply a large amount of, etch cream, with much of it exceeding the mask hole, the effective chemical component (such as HF) continuously flows into the etched zone under gravity, supplementing the consumed chemicals during the corrosion process.

Conservatively, this leads to the requirement that the mask hole be ~5 mm larger than the bonding edge, which has been described in item Eq. 1 of the notes in Section 2.1, as some additional space is needed to compensate for mask locating errors. Bonding the pads to the relatively flat etched zone will produce more uniform glue thickness and strength.

3.2 Bond line thickness

Hollow 250 μm glass beads were scattered onto the pad-applied adhesive for thickness control at a weight ratio of approximately 0.5%. A Coordinate Measuring Machine(CMM) test of six bonded samples was carried out to check the bond line thickness and uniformity, as shown in Figure 6 and Table 2.

The largest relative error of the bond line thickness measured is less than 10%, which may contribute to achieving a relatively uniform bonding strength.

3.3 Primer thickness

Priming is required to minimize the contamination risk of the glass bonding surface and to further guarantee good bonding. The primer was applied by optical swabs (TX-714A form Texwipe), and the primer thickness t_p was evaluated roughly by computing the fringes of the sodium light (wave length λ = 546 nm), as shown in Figure 7, where (a) illustrates the test principle of interferometry, (b) shows the initial fringe number $N_0 \approx 3$ from a viewing angle of 45°, and (c) shows the fringe number $N_1 \approx 12$ after priming viewed at the same angle. With the application of interferometry, t_p can be calculated by Eq. 4 as

$$t_p = \lambda \Delta N \sin(\theta)/2 \tag{4}$$

Substituting $\Delta N = N_1\text{-}N_0 \approx 9$ and $\theta \approx 45°$ into the equation, the result is $t_p \approx 1.74$ μm. As the primer works best at thicknesses in the range 1.5–2.5 μm, this control method proves satisfactory.

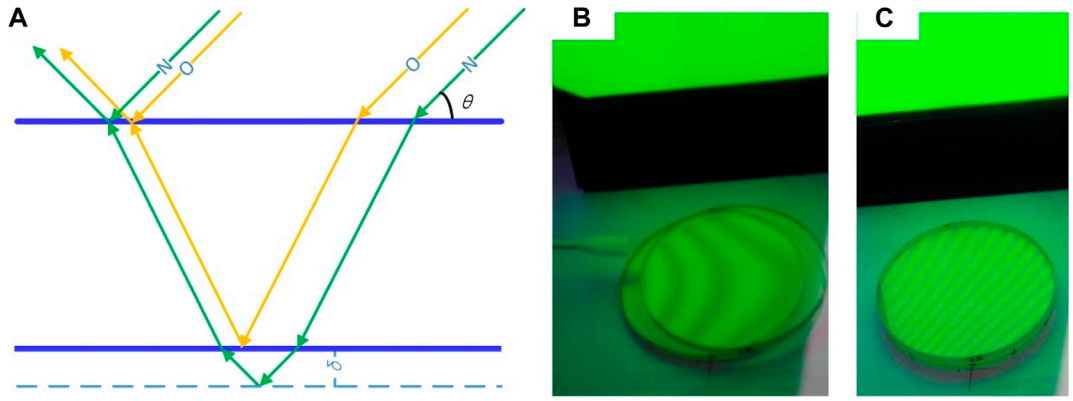

FIGURE 7
Primer thickness control through sodium light; **(A)** principle of the test, **(B)** priming operation with TX-714A optical swab viewing three fringes, and **(C)** interferometric graph after priming, viewing 12 fringes.

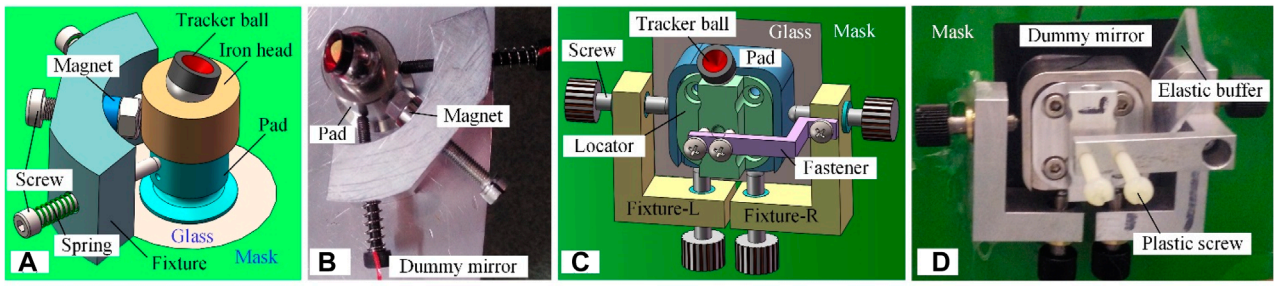

FIGURE 8
Universal pad locating method for arbitrary-shaped optics; **(A)** locating axial pads to a planar surface, **(B)** axial bonding test on dummy mirror, **(C)** locating lateral pads to a curved surface, and **(D)** lateral bonding test on dummy mirror assisted by an elastic buffer board.

3.4 Locating precision

The universal scheme for locating pads precisely onto optics is shown in Figure 8. For positioning the axial pads in Figures 8A, B, the magnet attracts the metal pad, stiffened by an iron head (optional, but important for diamagnetic material) and the pad position is adjusted by the double precision screws, each of which is fastened by a spring, according to the reading of the tracker ball. In Figures 8C, D, the lateral pads are adjusted by four precision screws, two of which are vertical and the other two are horizontal. Another two plastic screws are installed to provide pre-pressure during adhesive curing. In practice, as shown in Figure 8D, an additional elastic buffer is placed between the pad and one horizontal screw to avoid applying too high a fastening force by restraining the clearance of the horizontal screws, similar to the function of the springs in Figure 8A.

Locating precision tests for such jigs was performed for 21 pads (both axial and lateral), and all results are shown in Figure 9. The location error of axial pads ranges from −0.063 mm to 0.061 mm, averaging 0.003 mm, with a variance of 0.038 mm. The lateral pads location error ranges from −0.058 mm to 0.119 mm, averaging 0.013 mm, with a variance of 0.042 mm.

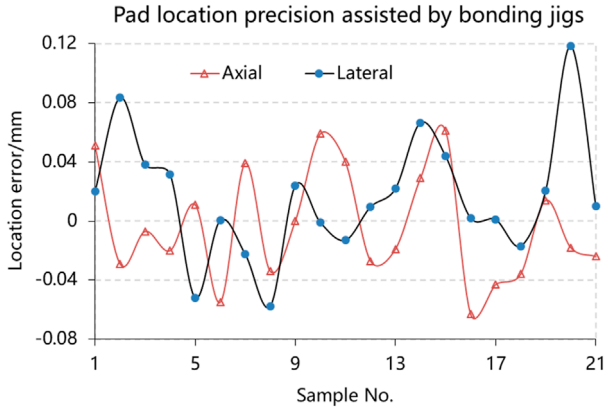

FIGURE 9
Pad location error test results for 21 pads.

All errors are within the distribution region of 3σ, so it is believed that no unacceptable value exits. Such small position errors have little effect on bonding strength uniformity.

TABLE 3 Tested strength values (in MPa).

Load	a_1	a_2	a_3	a_4	a_5	a_6
Tensile	13.2	14.3	14.5	14.4	13.0	14.8
Shear	11.4	11.4	11.1	12.2	12.2	12.0

TABLE 4 Strength limits for m pads based on n = 6 samples.

Load	m	$T_{p,v}$	$T_{p,m\text{-}1}$	E	$\overline{E}_L$	S	L
Tensile	18	1.93	1.68	14.0	13.4	0.74	12.0
	27	2.25	1.86		13.3		11.7
	2,214	7.02	3.32		11.9		6.67
Shear	18	1.73	1.68	11.9	11.6	0.75	10.3
	27	1.97	1.86	12.0	11.5	0.81	9.99
	2,214	4.50	3.32	12.8	10.4	1.84	4.28

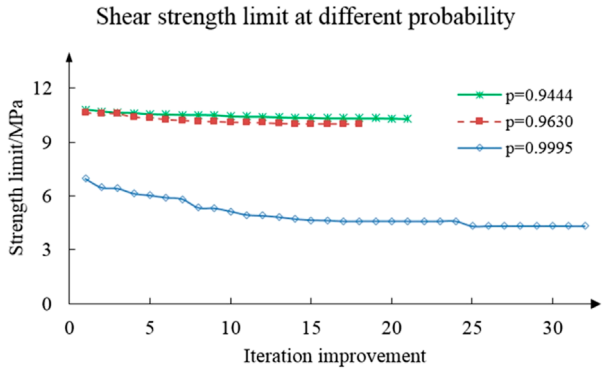

FIGURE 10
Objective function evolution to obtain the shear strength limit, starting at a random point.

3.5 Strength limits

For predicting the bonding strength limits, six samples (n = 6, v = 5) were prepared for tensile and shear tests, and all 12 strength values are listed in Table 3, with all undefined variables presented in the mm-N-s unit system hereafter.

For the tensile case, Eq. 2 can be applied directly for the limit calculation, and the results are shown in the second row of Table 4, where E is the sample average strength, $\overline{E}_L$ is the expected average limit for the whole population, S is the sample variance, and L is the population strength limit.

For the shear case, the optimization model defined by Eq. 3 is adopted for the limit searching procedure. The iterations were driven by the Multi-Island Genetic Algorithm followed by Sequential Quadratic Programming algorithm. Based on successful optimization implementation, all inputs and outputs for predicting shear strength limits are listed in the third row of Table 4 and shown in Figure 10, with p = 0.9444 for an 18-point Whiffletree structure (m = 18), p = 0.9630 for a 27-point Whiffletree (m = 27), and p = 0.9995 for 82 mirror segments, which is 1/6 symmetry of TMT's primary mirror and are all mounted using 27-point Whiffletrees (m = 2,214).

Table 4; Figure 10 indicate that the strength limits strongly depend on the reliability related to the quantity of pads involved in the opto-mechanical structure.

The proposed bonding technique is expected to have an average tensile strength of 14 MPa, a lower limit of 12.0 MPa for the 18-point Whiffletree application, 11.7 MPa for the 27-point Whiffletree, and 6.67 MPa for the 2,214 pads in the 82 copies of 27-point Whiffletrees. The corresponding lower shear strength limits in these applications are 10.3, 9.99, and 4.28 MPa, respectively, which demonstrates much stronger reliability dependence on the quantity of pads.

4 Conclusion

Universal adhesive bonding technology was investigated with regard to joining massive metal pads to mount large glass optics, paying special attention to controlling the main factors affecting the bonding safety and stability. Lower tensile/shear strength limits of 12/10 MPa for 1.5 m size optics and limits of 6.7/4.3 MPa for 30 m size mirrors are predicted for engineering application.

It is hoped that the proposed bonding technique and strength limit evaluation method can assist in setting a baseline to improve the bonding quality for massive use of mounting pads in giant telescope projects, such as TMT and E-ELT, and in other fields that rely heavily on a stable bonding technique.

Future work may focus on fatigue performance and temporal stability of the joints under cyclic loads, such as temperature change per day and per year and operational gravity change, especially for its practical applications in opto-mechanics over extended periods of operation, based on which the life prediction under dynamic loads can be made. It is believed that the strength limits is the priority for massive application, and the positioning error caused by temporal stability is inevitable, but it could be monitored by mirror edge sensors and compensated by active optics.

It should be pointed out that an alternative solution for deciding the shear strength limits is designing a new load structure to get the strength of the opposite end of the broken samples, whereas costing more time and expense.

Data availability statement

The raw data supporting the conclusion of this article will be made available by the authors, without undue reservation.

Author contributions

HH: Software, Resources, Project administration, Writing–original draft. DZ: Writing–review and editing, Data curation. CZ: Writing–review and editing, Visualization, Formal Analysis. EQ: Writing–review and editing, Methodology, Investigation. XL: Writing–review and editing, Visualization, Resources.

Funding

The author(s) declare that financial support was received for the research, authorship, and/or publication of this article. The work was financially supported by National Natural Science Foundation of China (Grant Nos 62175234 and 62127901) and the Scientific and Technological Development of Program of Jilin Province (Grant No. 20230508111RC) and the National Key R&D Program of China (Grant No. 2023YFC2206002).

Acknowledgments

The authors are grateful for the advices and help from Haixiang Hu, Peng Guo and Glen Cole on the bonding technique, for the financial support from Donglin Xue and Xuejun Zhang.

Conflict of interest

The authors declare that the research was conducted in the absence of any commercial or financial relationships that could be construed as a potential conflict of interest.

Publisher's note

All claims expressed in this article are solely those of the authors and do not necessarily represent those of their affiliated organizations, or those of the publisher, the editors and the reviewers. Any product that may be evaluated in this article, or claim that may be made by its manufacturer, is not guaranteed or endorsed by the publisher.

References

Afendi, M., Majid, M., Daud, A. R. R., and Teramoto, T. (2013). Strength prediction and reliability of brittle epoxy adhesively bonded dissimilar joint. *Int. J. Adhes.* 45, 21–31. doi:10.1016/j.ijadhadh.2013.03.008

Bloemhof, E., Lam, J., Feria, V., and Chang, Z. (2009). Extracting the zero-gravity surface figure of a mirror through multiple clockings in a flightlike hexapod mount. *Appl. Opt.* 48 (21), 4239–4245. doi:10.1364/ao.48.004239

Ducousso, M., Bardy, S., Rouchausse, Y., Bergara, T., Jenson, F., Berthe, L., et al. (2018). Quantitative evaluation of the mechanical strength of titanium/composite bonding using laser-generated shock waves. *Appl. Phys. Lett.* 112, 111904. doi:10.1063/1.5020352

Ende, D., and Gubbels, G. (2014). Fracture toughness of hydroxide catalysis bonds between silicon carbide and zerodur low thermal expansion glass-ceramic. *MATER Chem. Phys.* 143, 1236–1242. doi:10.1016/j.matchemphys.2013.11.028

Goglio, L., Peroni, L., Peroni, M., and Rossetto, M. (2008). High strain-rate compression and tension behaviour of an epoxy bi-component adhesive. *Int. J. Adhes.* 28, 329–339. doi:10.1016/j.ijadhadh.2007.08.004

Haisma, J., Hattu, N., Pulles, J., Steding, E., and Vervest, J. (2007). Direct bonding and beyond. *Appl. Opt.* 46 (27), 6793–6803. doi:10.1364/ao.46.006793

Hartman, N., Heimann, P., MacDowell, A., Franek, K., Grieshop, A., Irick, S., et al. (1998). Design, analysis, and performance of an epoxy-bonded, bendable mirror. *Proc. SPIE* 3447, 40–51. doi:10.1117/12.331128

He, P., Huang, M., Fisher, S., Yue, C., and Yang, J. (2015). Effects of primer and annealing treatments on the shear strength between anodized Ti6Al4V and epoxy. *Int. J. Adhes.* 57, 49–56. doi:10.1016/j.ijadhadh.2014.10.004

Hu, H., Qi, E., Luo, X., Zhang, X., and Xue, D. (2018). Rapid fabrication strategy for Ø15 m off-axis parabolic parts using computer-controlled optical surfacing. *Appl. Opt.* 57 (54), F37–F43. doi:10.1364/ao.57.000f37

Kim, H., and Schmitz, T. (2013). Shear strength evaluation of hydroxide catalysis bonds for glass-glass and glass-aluminum assemblies. *Precis. Eng.* 37, 23–32. doi:10.1016/j.precisioneng.2012.06.004

Laiterman, L., Radovan, M., and Cabak, G. (2010). Experimental investigation of adhesive bond strength between metal and optical glass. *Proc. SPIE* 7735, 773542. doi:10.1117/12.857775

Lan, B., Wu, X., Li, J., Ming, M., Liu, X., and Yang, H. (2017). Influence of axial-force errors on the deformation of the 4 m lightweight mirror and its correction. *Appl. Opt.* 56 (3), 611–619. doi:10.1364/ao.56.000611

Meeks, R., Doyle, S., Higginson, J., Hudek, J., Irace, W., McBride, D., et al. (2016). W.M. Keck observatory primary mirror segment repair project: overview and status. *Proc. SPIE* 9906, 990603. doi:10.1117/12.2233693

Nijenhuis, J., Braam, B., and Hamelinck, R. (2016). The opto-mechanical performance prediction of thin mirror segments for E-ELT. *Proc. SPIE* 10012, 1001203. doi:10.1117/12.2200931

Prolongo, S., and Urena, A. (2009). Effect of surface pre-treatment on the adhesive strength of epoxy-aluminium joints. *Int. J. Adhes.* 29, 23–31. doi:10.1016/j.ijadhadh.2008.01.001

Robinson, D. (2000). Minimizing gravity sag of a large mirror with an inverted hindle-mount. *Proc. SPIE* 4093, 142–150. doi:10.1117/12.405200

Swadener, J., Liechti, K., and Lozanne, A. (1999). The intrinsic toughness and adhesion mechanisms of a glass:epoxy interface. *J. Mech. Phys. SOLIDS* 47, 223–258. doi:10.1016/s0022-5096(98)00084-2

Wang, C., Wang, Y., Tian, Y., Wang, C., and Suga, T. (2017). Room-temperature direct bonding of silicon and quartz glass wafers. *Appl. Phys. Lett.* 110, 221602. doi:10.1063/1.4985130

Wang, H. (2017). Research on a bimorph piezoelectric deformable mirror for adaptive optics in optical telescope. *Opt. EXPRESS* 25 (7), 8115–8122. doi:10.1364/oe.25.008115

Wang, H., Cheng, J., Lou, Z., Qian, Y., Zheng, X., Zuo, Y., et al. (2016b). Multi-variable H-β optimization approach for the lateral support design of a wide field survey telescope. *Appl. Opt.* 55 (31), 8763–8769. doi:10.1364/ao.55.008763

Wang, H., Lou, Z., Qian, Y., Zheng, X., and Zuo, Y. (2016a). Hybrid optimization methodology of variable densities mesh model for the axial supporting design of wide-field survey telescope. *Opt. Eng.* 55 (3), 035105. doi:10.1117/1.oe.55.3.035105

Wang, W., Xiao, Y., Wu, X., and Zhang, J. (2016c). Optimization of laser-assisted glass frit bonding process by response surface methodology. *Opt. LASER Technol.* 77, 111–115. doi:10.1016/j.optlastec.2015.09.007

Wetherhold, R., Dargush, G., and Mhatre, T. (2018). Effects of free-edge interface angle on bi-material shear strength. *Int. J. Mech. Sci.* 144, 262–273. doi:10.1016/j.ijmecsci.2018.05.048

Williams, E., Baffes, C., Mast, T., Nelson, J., Platt, B., Ponchione, R., et al. (2008). Advancement of the segment support system for the thirty meter telescope primary mirror. *Proc. SPIE* 7018, 701810. doi:10.1117/12.790176

Xiong, Y., Zhuang, W., and Zhang, M. (2015). Effect of the thickness of cold sprayed aluminium alloy coating on the adhesive bond strength with an aluminium alloy substrate. *Surf. Coat. Tech.* 270, 259–265. doi:10.1016/j.surfcoat.2015.02.048

Xu, F., Liu, S., Fan, H., Xu, Y., and Ding, Y. (2019). Enhancement of the adhesion strength at the metal-plastic interface via the structures formed by laser scanning. *Opt. LASER Technol.* 111, 635–643. doi:10.1016/j.optlastec.2018.10.026

Xu, W., and We, Y. (2013). Influence of adhesive thickness on local interface fracture and overall strength of metallic adhesive bonding structures. *Int. J. Adhes.* 40, 158–167. doi:10.1016/j.ijadhadh.2012.07.012

10.3389/fspas.2024.1406090

Appendix: t-distribution

In statistics, the Student's t-distribution is defined as any member of a family of continuous probability distributions that arises when estimating the mean of a normally distributed population in situations where the sample size is small and population standard deviation is unknown.

Let $X_1, X_2, \ldots, X_n$ be an independent and identically distributed normal distribution of $N(\mu, \sigma^2)$, the sample's average/mean value could be defined by Eq. (5):

$$\overline{X} = \sum_{i=1}^{n} X_i / n, \tag{5}$$

and the sample variance could be defined by Eq. (6):

$$S^2 = \sum_{i=1}^{n} \left(X_i - \overline{X}\right)^2 / (n-1), \tag{6}$$

be the sample variance. Then the random variable defined by Eq. (7):

$$\left(\overline{X} - \mu\right) / \left(\sigma / \sqrt{n}\right) \tag{7}$$

has a standard normal distribution, and the random variable defined by Eq. (8):

$$\left(\overline{X} - \mu\right) / \left(S / \sqrt{n}\right) \tag{8}$$

has a Student's t-distribution with $v = n$-1 degrees of freedom (DOF).

The one-sided lower confidence limit of the mean value can be calculated using Eq. (9):

$$\overline{X}_L = \overline{X} - T_{p,v} S / \sqrt{n}. \tag{9}$$

$\overline{X}_L$ will be the lowest average value that will occur within a confidence interval $T_{p,v}$ at a given probability of p and DOF of v.

Many software packages, such as Excel and Matlab, provide the function for calculating $T_{p,v}$. Selected $T_{p,v}$ values for m pad bonds are given in Table 7 for average strength evaluation at a probability of $p = 1–1/m$.

Finally, the case of $v = m$-1 for optical segment joint strength limit prediction in massive bonding of m pads at probability p is given by Eq. (10):

$$X_L = \overline{X}_L - T_{p,m-1} S. \tag{10}$$

TABLE 7 *T* values for *m* pads based on six samples.

$T_{p,v}$	p =0.9444	p =0.9630	p =0.9995
v= 5	1.933	2.252	7.022
v= 11	1.732	1.974	4.499
v= m-1	1.681	1.861	3.324

frontiers | Frontiers in Astronomy and Space Sciences

TYPE Original Research
PUBLISHED 10 July 2024
DOI 10.3389/fspas.2024.1392970

OPEN ACCESS

EDITED BY
Hairen Wang,
Purple Mountain Observatory (CAS), China

REVIEWED BY
Mario Gai,
Osservatorio Astrofisico di Torino (INAF), Italy
Weiye Zhong,
Shanghai Astronomical Observatory (CAS), China
Jinqing Wang,
Shanghai Astronomical Observatory (CAS), China

*CORRESPONDENCE
Mao-Zheng Chen,
chen@xao.ac.cn

RECEIVED 28 February 2024
ACCEPTED 10 June 2024
PUBLISHED 10 July 2024

CITATION
Wu P, Li J and Chen M-Z (2024), Numerical model of the QiTai radio Telescope PAF receiver signal and simulation of interference mitigation.
Front. Astron. Space Sci. 11:1392970.
doi: 10.3389/fspas.2024.1392970

Numerical model of the QiTai radio Telescope PAF receiver signal and simulation of interference mitigation

Peng Wu[1,2,3], Jian Li[1,3] and Mao-Zheng Chen[1,3]*

[1]Xinjiang Astronomical Observatory, Chinese Academy of Sciences, Urumqi, China, [2]University of Chinese Academy of Sciences, Beijing, China, [3]Xinjiang Key Laboratory of Microwave Technology, Urumqi, China

Xinjiang Qitai is constructing a 110-m fully steerable radio telescope (QiTai radio Telescope [QTT]) equipped with a phased array feeds (PAF) receiver, which will install the focal plane operating from 0.7 to 1.8 GHz. In this article, we introduce a PAF receiver model for beamforming, and the numerical model of the internal and external noise for this PAF receiver is provided using electromagnetic field simulation software. The linear constraint minimum variance (LCMV) algorithm is used to simulate the interference mitigation. The interference mitigation rate is from 0.581 to 0.921, and the signal restoration rate is from 0.998 to 1.512 within the error range of an interference arrival angle of 10°. This conclusion can be used in the signal correction of the PAF receiver for interference mitigation.

KEYWORDS

QiTai radio Telescope, array signal processing, signal numerical model, linear constraint minimum variance, phased array feeds, beamforming, beamformer design

1 Introduction

The phased array feeds (PAF) receiver has been extensively studied worldwide as it is considered the next-generation receiver for telescopes. Compared to the horn receiver, which has a single-point receiving system, the PAF receiver is a multi-point (19–200) receiving system placed on the focal plane of telescopes (Warnick et al., 2016). The benefits of PAF receivers include a continuous field of view, flexible beam control, and active interference mitigation.

The search for faint astronomical signals is often limited by relatively large noise and interference in radio telescopes. The utilization of a PAF receiver in a telescope can result in increased system fluctuations, thereby leading to an increase in noise variance. This effect cannot be eliminated by integration (Jeffs et al., 2008). For single-dish radio telescopes, these noise sources include, but are not limited to, spillover noise observed by the PAF receiver from beyond the reflector edge; sky noise collected by the main and side beams of the telescope pattern, as shown in Figure 1; cross-coupling between the closely packed elements of the array (Warnick et al., 2009b); and additional noise due to resistance losses in the connector between the antenna, cable, and low-noise amplifier (LNA), as shown in Figure 2.

The QiTai radio Telescope (QTT), the largest fully steerable single-dish radio telescope currently under construction, has been selected by *Nature* as the most noteworthy science

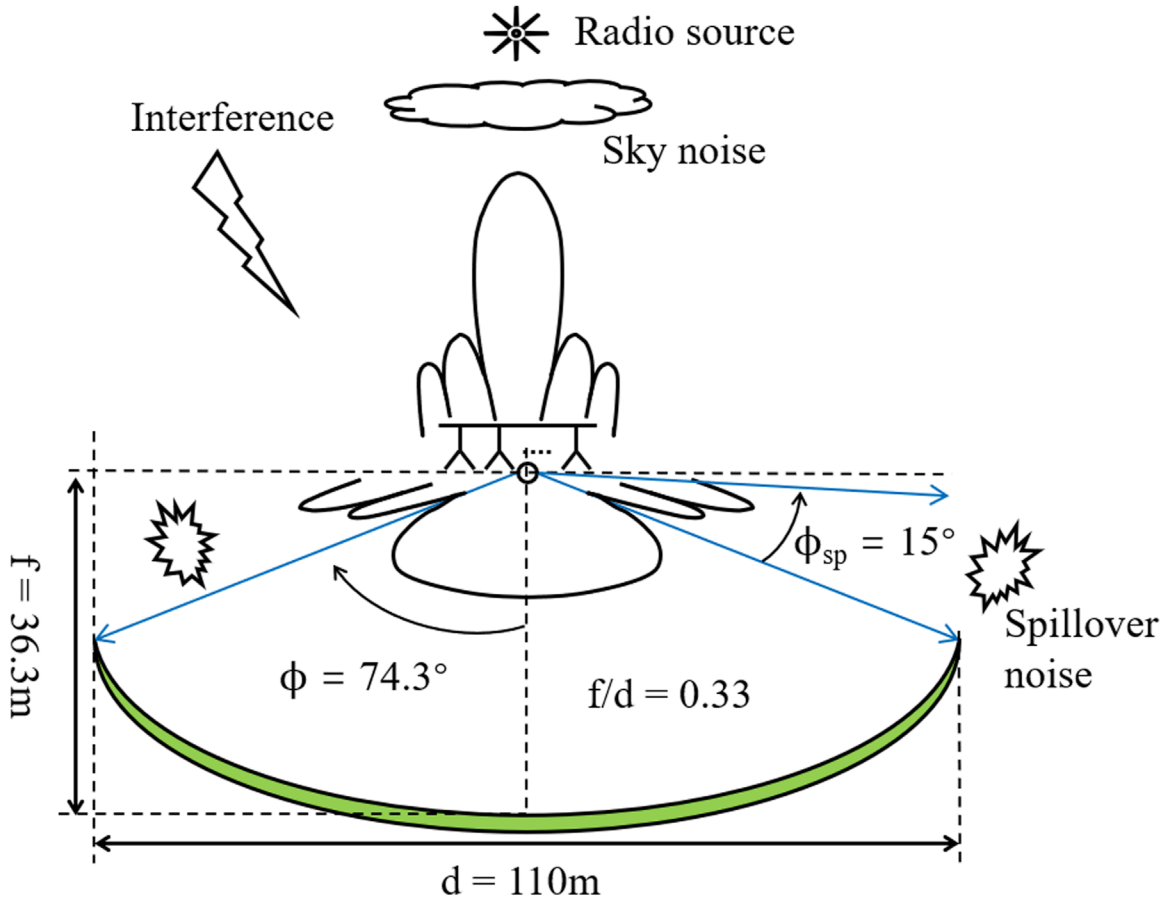

FIGURE 1
Sky noise and spillover noise diagram of the QTT-PAF receiver, when the telescope is pointed at the zenith.

project in 2023[1]. The QTT will install a 192-element (96 × 2) array dual-polarized PAF (QTT-PAF) receiver operating from 0.7 to 1.8 GHz (Wang, 2014; Ma et al., 2019). A parabolic antenna of 110 m and a single-polarized PAF composed of 25 Vivaldi antennas have been established and simulated, with a 2D model of a Vivaldi antenna being presented. Based on this model, the detailed noise environment of this telescope model is established, followed by the application of the linear constraint minimum variance (LCMV) algorithm for beamforming. The operational performance of the telescope is affected by errors arising from telescope pointing, receiver–telescope matching, and system phase shift, resulting in deviations in estimating the arrival angle of interference. Within the error range of 10° interference arrival angle, we calculate the interference mitigation rate and the signal restoration rate, which are valuable in the correction of cosmic signal power estimation.

This paper aims to investigate and establish the noise environment of the QTT-PAF receiver and to offer a numerical model for noise and interference mitigation in the design of the array and beamforming algorithm of the QTT-PAF receiver. At the same time, it is also important to obtain the relation between the interference arrival angle error, interference mitigation, and signal restoration, which is helpful in the correction of system errors and the estimation of cosmic signal power. Furthermore, this research can also provide theoretical validation and an experimental foundation for the pre-project research and development.

2 The mathematical principles of the PAF beamformer

2.1 Signal stream of the PAF receiver

Figure 2 shows a PAF receiving system with M elements. This system is divided into two parts: 1) analog front end, which consists of a reflector, PAF, and LNA, and 2) beamformer, which consists of a beamforming algorithm and power adder with complex weight. Here, $\boldsymbol{X} = [x_1, \ldots, x_M]^T$ represents the input of the beamformer (the output of the LNA), $[\cdot]^T$ for transpose. In addition, $\boldsymbol{w}^H = [w_1^*, \ldots, w_M^*]$ is the complex weight of the power adder (the LCMV algorithm output), and $[\cdot]^*$ and $[\cdot]^H$ represent the conjugate and conjugate transpose, respectively. It is obtained by using a beamforming algorithm to calculate sampling data in a short-time integration (STI) window. Therefore, the accuracy of the interference arrival angle is negatively correlated with the size of the STI window. At this point, the output of the beamformer is displayed as $y = \boldsymbol{w}^H \boldsymbol{X}$.

1 https://www.nature.com/articles/d41586-022-04444-3

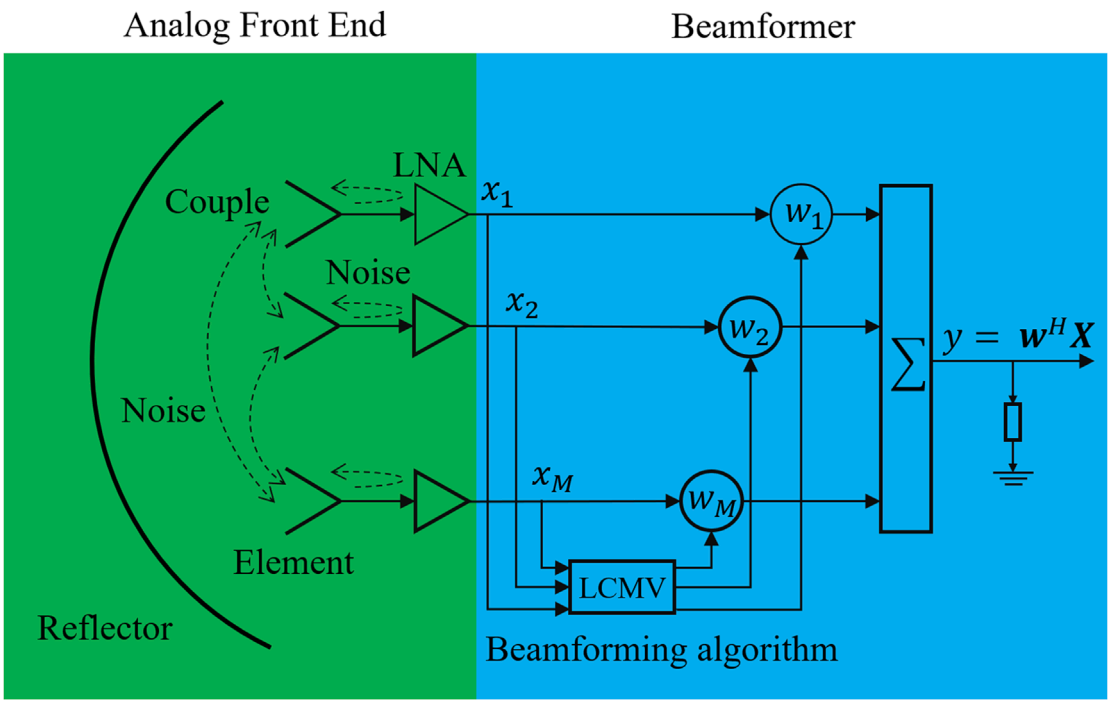

FIGURE 2
Beamforming schematic diagram of the PAF receiver. Here, the dashed line represents the noise caused by the coupling, connector, and LNA.

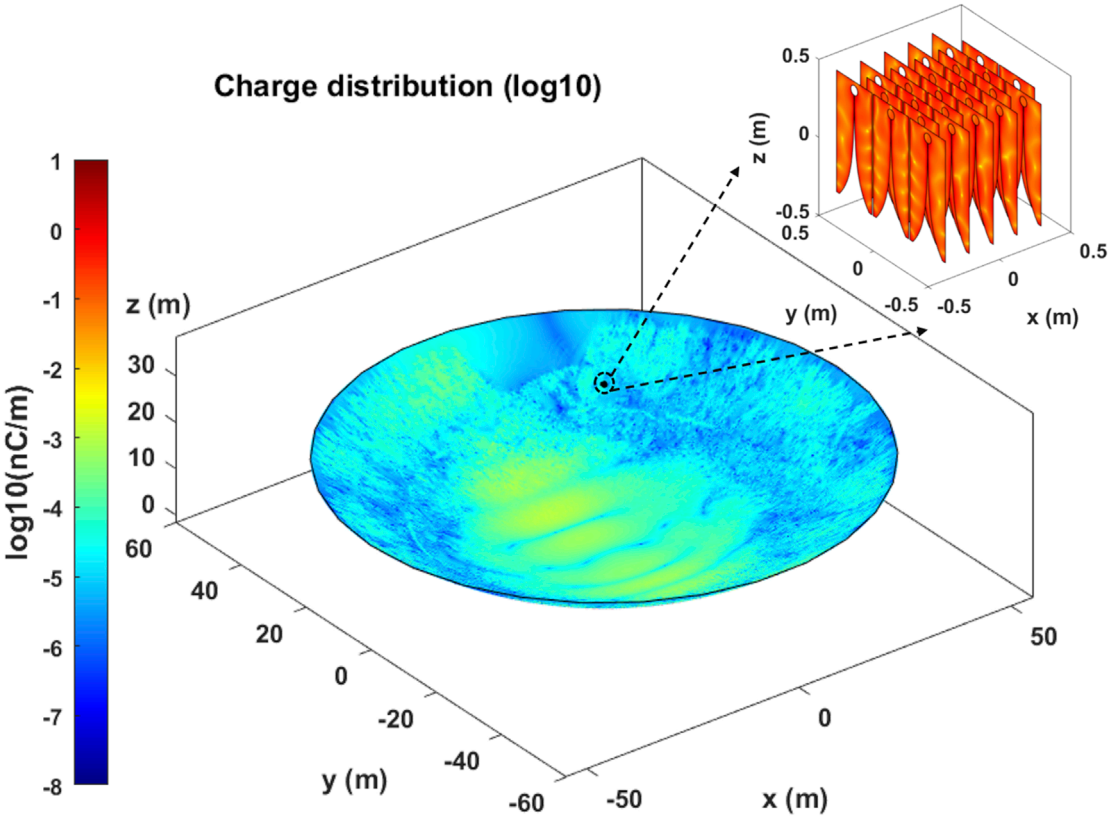

FIGURE 3
Charge distribution of a 110-m parabola antenna in the illumination of a PAF receiver consisting of 25 Vivaldi antennas. All Vivaldi antennas are unit-excited and operate at 1.25 GHz.

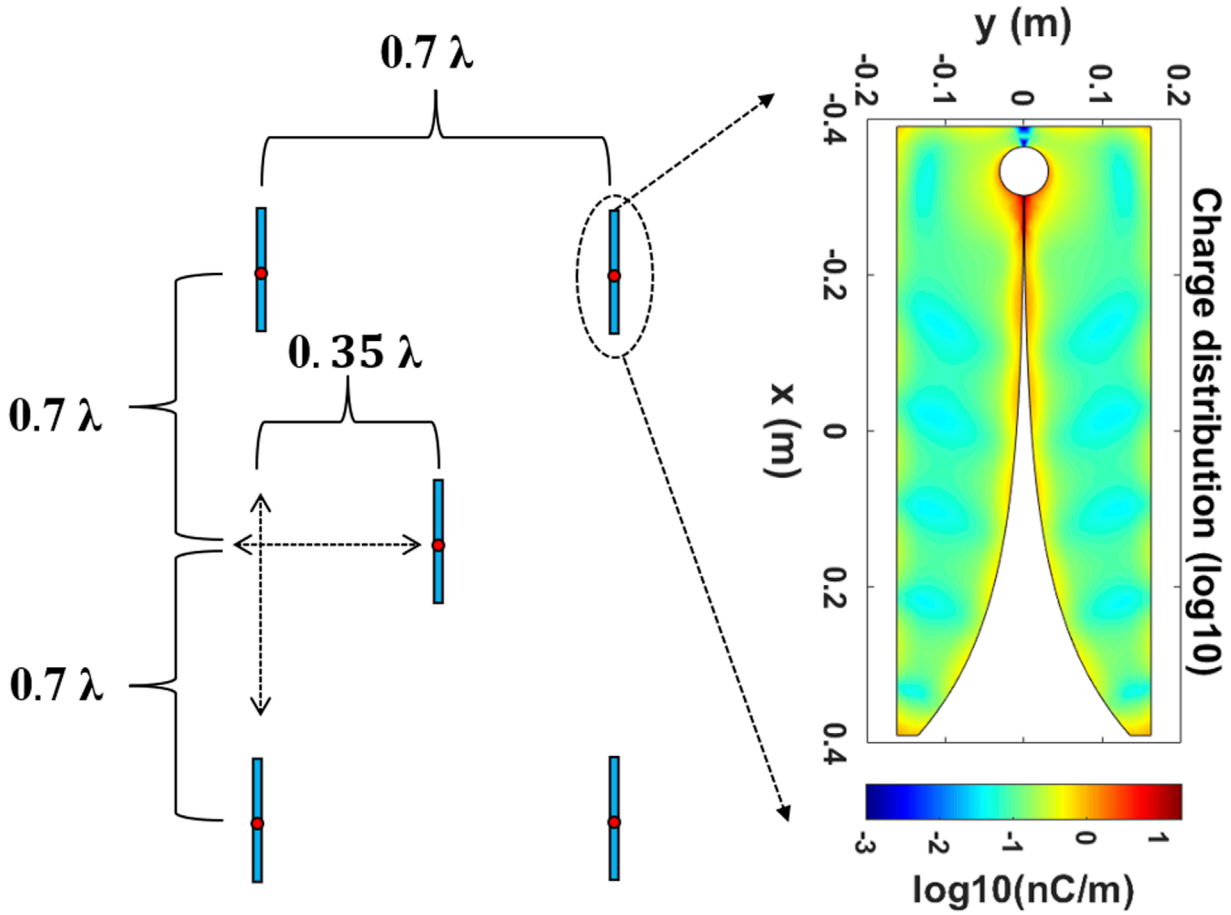

FIGURE 4
Planar diagram of the array and charge diagram of the 2D Vivaldi model (unit excitation).

2.2 Signal analysis

The sensitivity metric A_{eff}/T_{sys}, which is the effective area of the antenna system divided by the system equivalent noise temperature, can be expressed in terms of the signal-to-noise ratio (SNR) and the normalized flux density F_{source} of the radio source (in jansky, $1[Jy] = 10^{-26}[Wm^{-2}Hz^{-1}]$) as (Warnick and Jeffs, 2008)

$$\frac{A_{eff}}{T_{sys}} = \frac{2k_B}{F_{source}}\mathrm{SNR}, \mathrm{SNR} = \frac{\boldsymbol{w}\boldsymbol{R}_X\boldsymbol{w}}{\boldsymbol{w}\boldsymbol{R}_{n+I}\boldsymbol{w}}, \quad (1)$$

where k_B is Boltzmann's constant, $\boldsymbol{R}_X$ is the signal-of-interest (SOI) covariance matrix, and $\boldsymbol{R}_{n+I}$ is the sum of covariance matrix interference $\boldsymbol{R}_I$ and noise $\boldsymbol{R}_n$. Improving the SNR by matching $\boldsymbol{w}$ in Eq. 1 is the main method to improve the sensitivity. Eliminating $\boldsymbol{R}_I$ is the main work when interference is present. $\boldsymbol{R}_n$ is reduced as much as possible when there is no interference. At the same time, due to the pursuit of extreme sensitivity in radio astronomy, $\boldsymbol{R}_n$ cannot be described by a simple covariance matrix of white noise. It needs to reflect the contribution of the internal and external noise of a telescope, described as $\boldsymbol{R}_n = \boldsymbol{R}_{sp} + \boldsymbol{R}_{sky} + \boldsymbol{R}_{ant} + \boldsymbol{R}_{LNA}$. $\boldsymbol{R}_{sp}$ is a spillover noise matrix with non-white noise characteristics as the pattern of the PAF beamforming extends beyond the edge of the reflector surface, collecting unwanted signals from the spillover area within a limited range of angles. The main component of $\boldsymbol{R}_{ant}$ is LNA noise, which is due to the use of the high-gain LNA at the beginning of the receiver chain. The off-diagonal terms in $\boldsymbol{R}_{ant}$ are non-zero due to the LNA noise coupling back through array elements to neighboring closely packed antennas. As a result, the receiver noise temperature is increased by a mutual coupling noise penalty. $\boldsymbol{R}_{sky}$ is sky background noise, including atmospheric, constant cosmic microwave background (CMB), and galactic background (GB) noise. It enters mainly from the main and side beams of a telescope, and the non-diagonal parts of $\boldsymbol{R}_{sky}$ are also non-zero. $\boldsymbol{R}_{LNA}$ represents the noise power of a high-gain LNA at the beginning of the receiver chain. As the thermal motion power of the electron is independent of frequency, the covariance matrix exhibits non-zero values only on the diagonal (James, 2012).

2.3 Beamforming algorithm

At present, the main algorithms used in the beamformer are based on the maximum signal-to-noise ratio (MaxSNR), minimum variance distortionless response (MVDR), subspace projection (SP), and LCMV (Jeffs et al., 2008; Warnick et al., 2009a; Ivashina et al., 2011; Young et al., 2013). The LCMV algorithm can

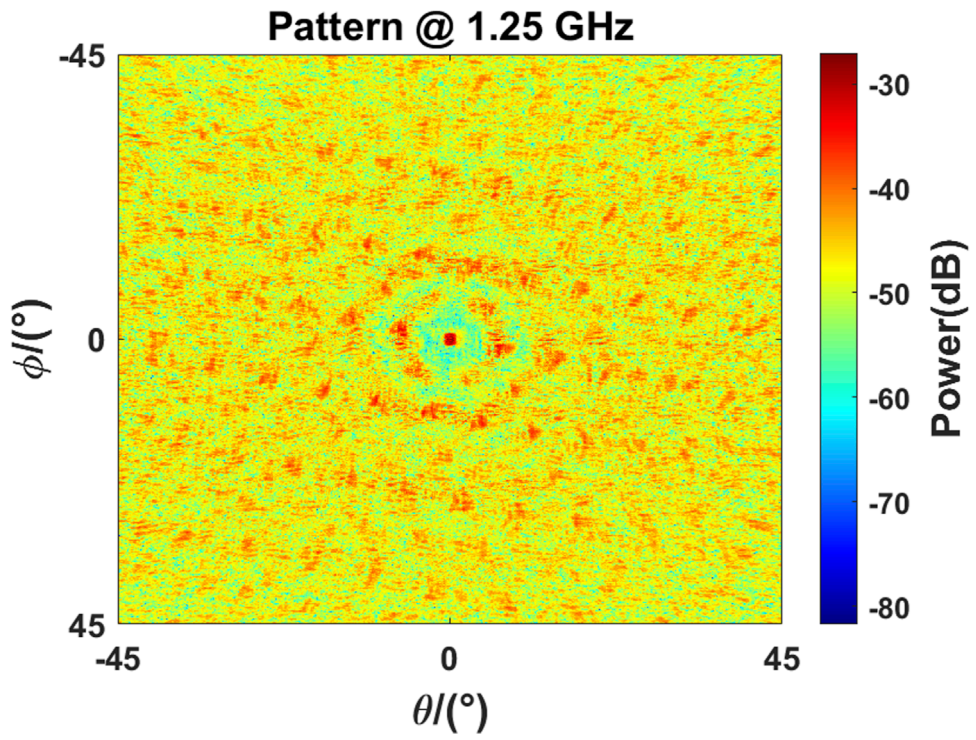

FIGURE 5
2D beam image in the model in Figure 3; the display range is 90 square degrees, and the operating frequency is 1.15 GHz.

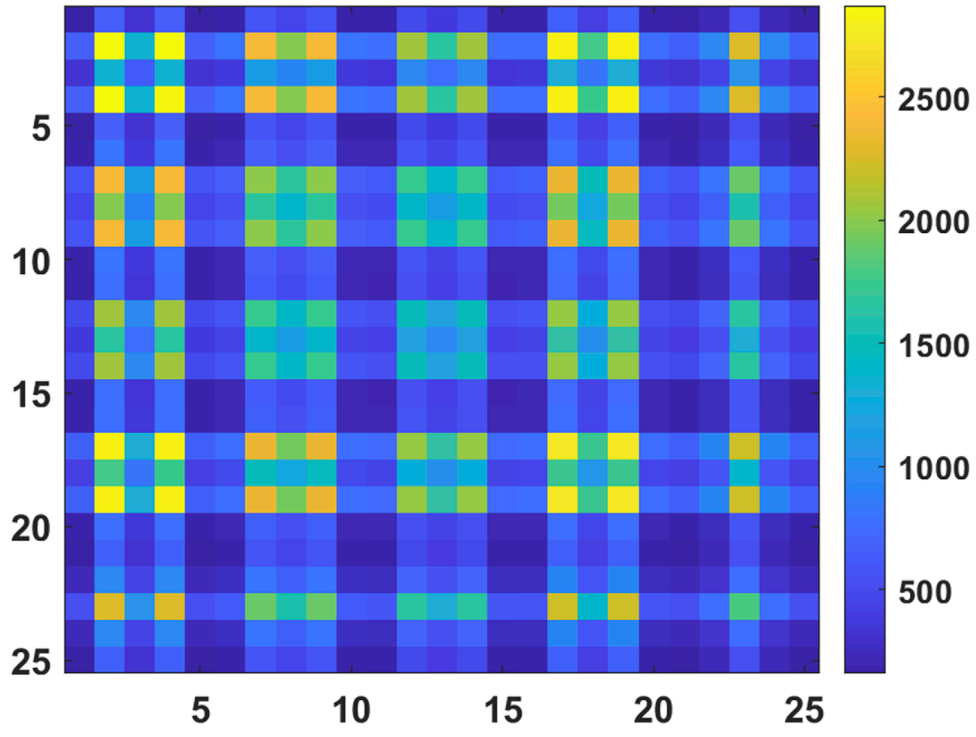

FIGURE 6
Correlation matrix of impedance coefficients of 25 elements.

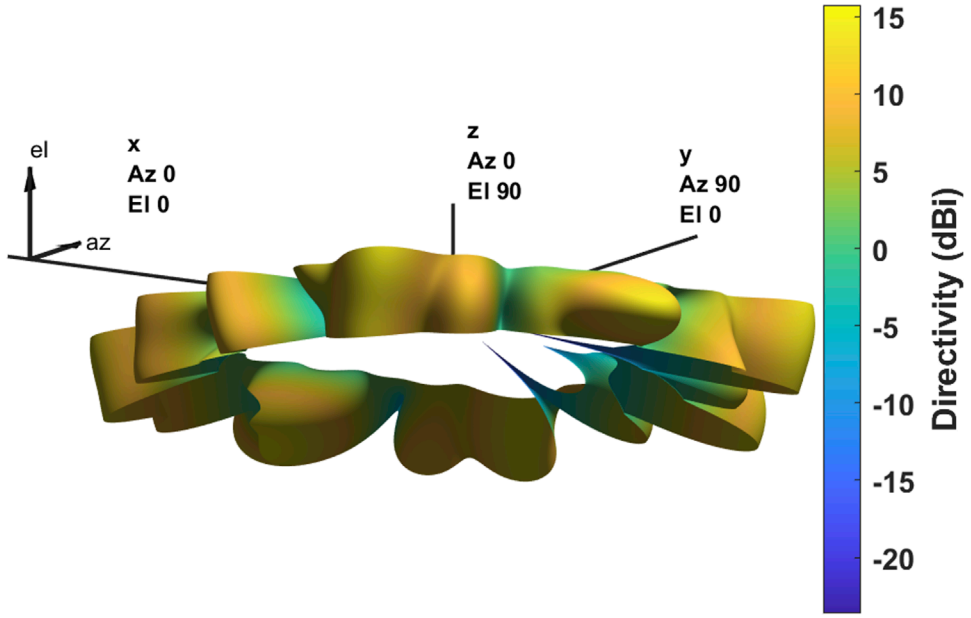

FIGURE 7
Pattern of PAF spillover noise, i.e., the pattern of ϕ_{sp} in Figure 1.

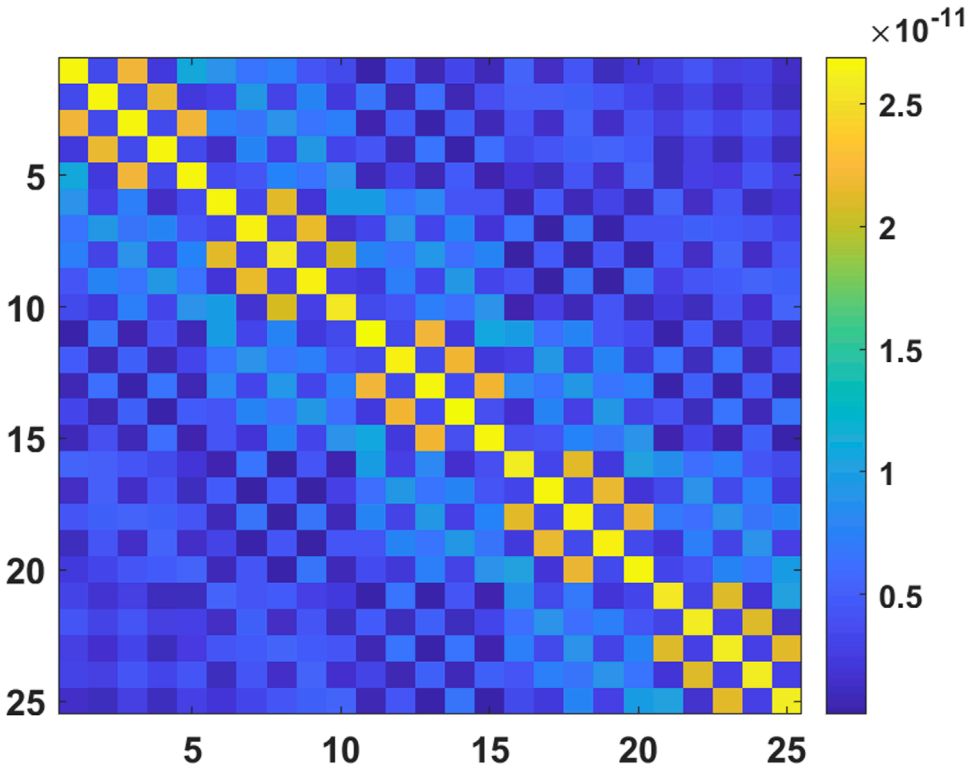

FIGURE 8
Covariance matrix of spillover noise in the telescope.

achieve interference mitigation without affecting the main beam response. When there is no interference, it is the MVDR algorithm. Suppressing the power of interference is equivalent to controlling the PAF pattern on interference orientation in a telescope. At the same time, because of the good control of the beam, it is also applied to the multi-beam joint optimization problem of PAF. Mathematically, the weight vector $\boldsymbol{w}_{LCMV}$ of the LCMV beamformer can be set by solving the following optimization problems:

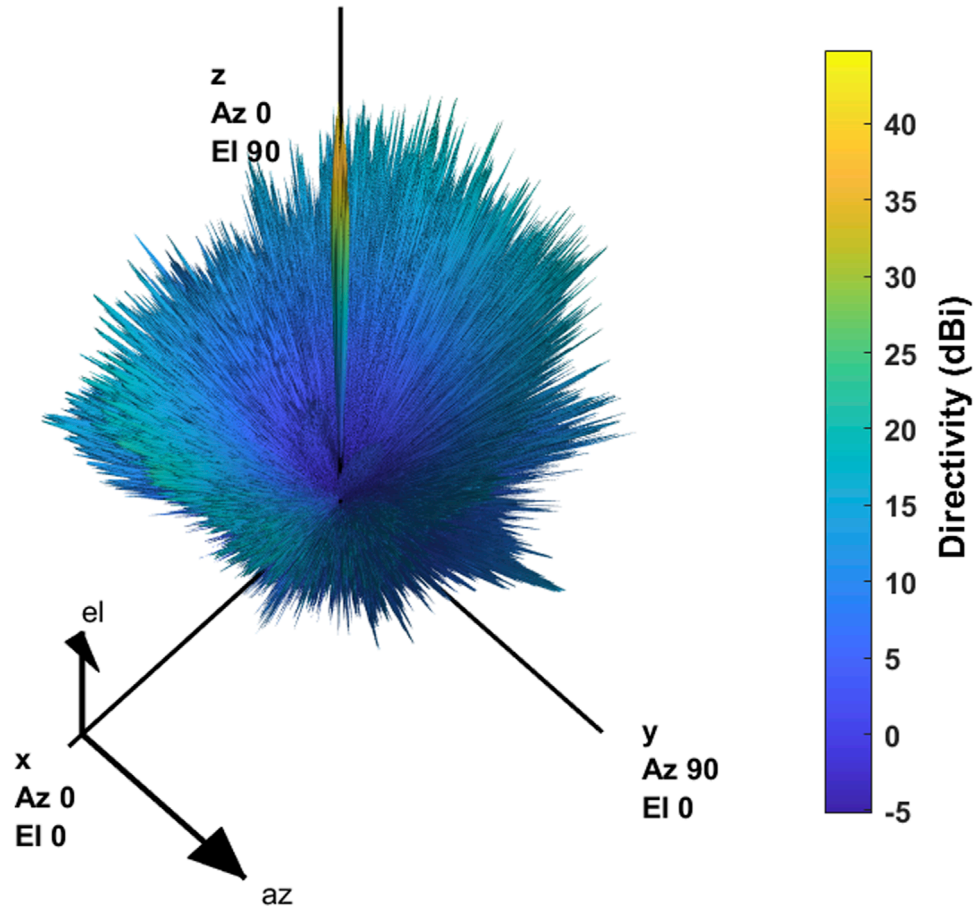

FIGURE 9
Pattern of the telescope-collected noise from the sky.

$$\begin{aligned} \boldsymbol{w}_{LCMV} &= \min_{\boldsymbol{w}} \boldsymbol{w}^H R \boldsymbol{w} \\ s.t. \quad & B(\theta_0, \phi_0, \boldsymbol{w}) = 1 \\ & B(\theta_k, \phi_k, \boldsymbol{w}) = 0, \quad k = 1, 2, \ldots, M-2, \end{aligned} \tag{2}$$

where θ_0 (azimuth) and ϕ_0 (elevation) are the solid angles of the SOI for the PAF receiver. θ_k and ϕ_k are k interference spherical angles. Since M arrays can provide $M-1$ constraints, the number of disturbances that need to be constrained should not exceed $M-2$ for a given astronomical information response constraint. Since all constraints are linear in the complex field, the solution can be obtained using the Lagrange multiplier method.

3 Simulation

This section presents the simulated signals used for beamforming and the hardware model to generate these signals. Antenna simulation software and the PAF signal generator mentioned by Wu et al. (2024) are mainly used in the experiment. Finally, the relationship between the interference arrival angle and interference mitigation and signal restoration in the LCMV beamfromer of Eq. 2 is calculated.

3.1 Model of the 110-m reflector and 25 Vivaldi PAF antennas

The QTT-PAF receiver is designed to operate at a center frequency of 1.25 GHz, with the array element being a Vivaldi antenna, and the operating temperature is 20 k in a cryogenic environment. The design of the QTT-PAF receiver has not yet been completed. The antenna model used for generating the simulation signal consists of 25 Vivaldi antennas arranged in a quadrilateral pattern on the focal plane of a 110-m parabolic reflector, as depicted in Figure 3. This section introduces a 2D Vivaldi antenna model, which does not compromise the principle of beamforming. Figure 4 illustrates the Vivaldi antenna model and the parameters of its quadrilateral arrangement. Due to computer memory constraints, the antenna model is divided into 192,680 grids. The pattern of all array elements under uniform excitation is shown in Figure 5.

3.2 The numerical model of noise

In radio astronomy, electric power is equated to temperature. The relationship between the average electrical power P per unit bandwidth and the temperature T is $P = k_B T$, when the

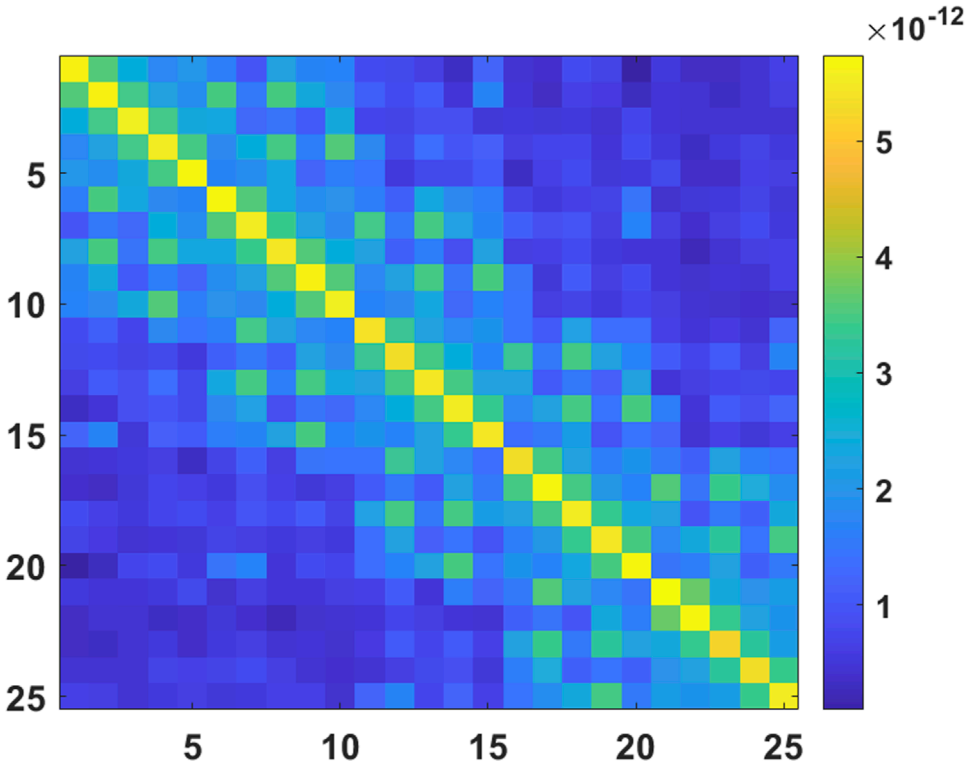

FIGURE 10
Covariance matrix of sky noise in the telescope.

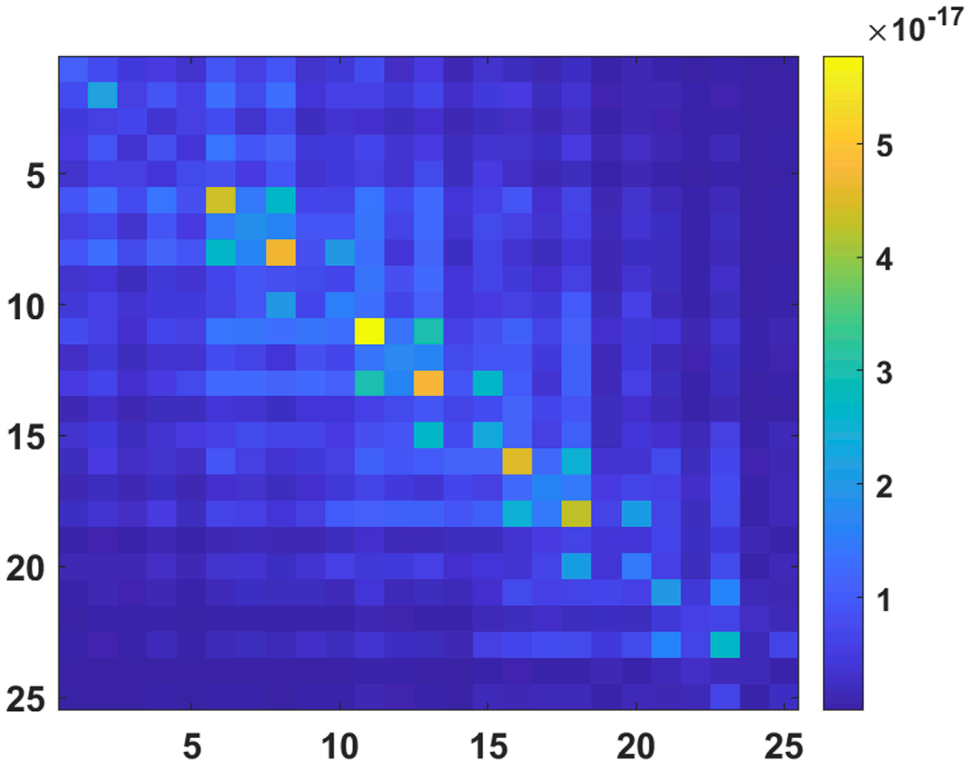

FIGURE 11
Covariance matrix of LNA noise in the PAF receiver.

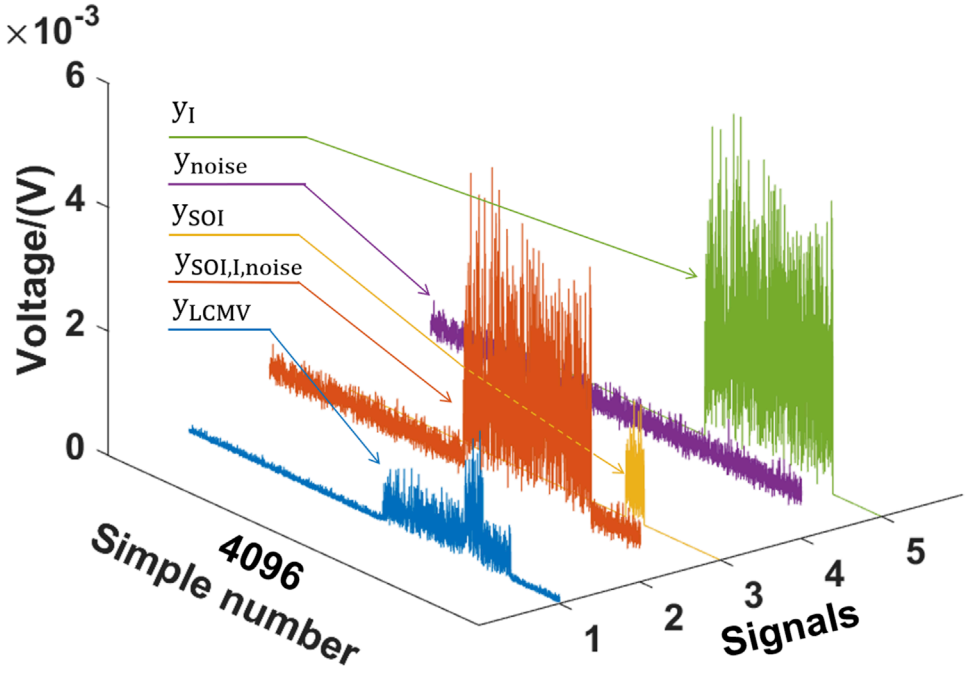

FIGURE 12
Voltage images of each signal over time, which are the average result of 10 STI windows. y_I, y_{noise}, and y_{SOI} are the given interference, noise, and SOI, respectively. $y_{SOI,I,noise}$ is the average output of the 25 ports of LNAs. y_{lcmv} is the output of the LCMV beamformer.

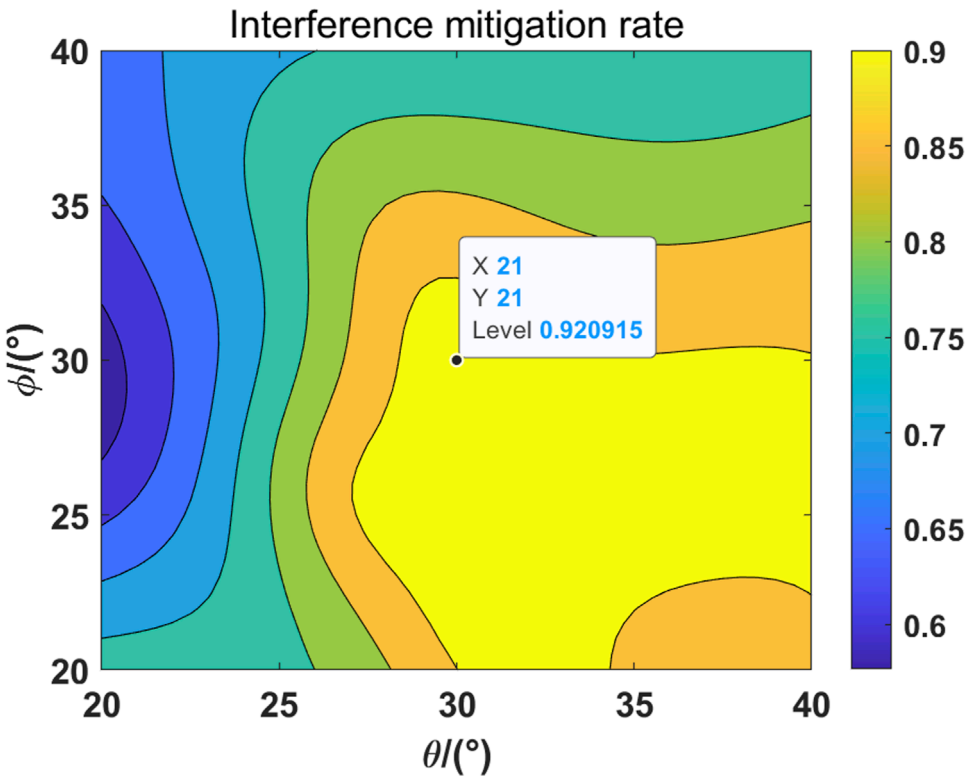

FIGURE 13
The relationship between the estimation of the interference arrival angle and the interference mitigation rate is plotted.

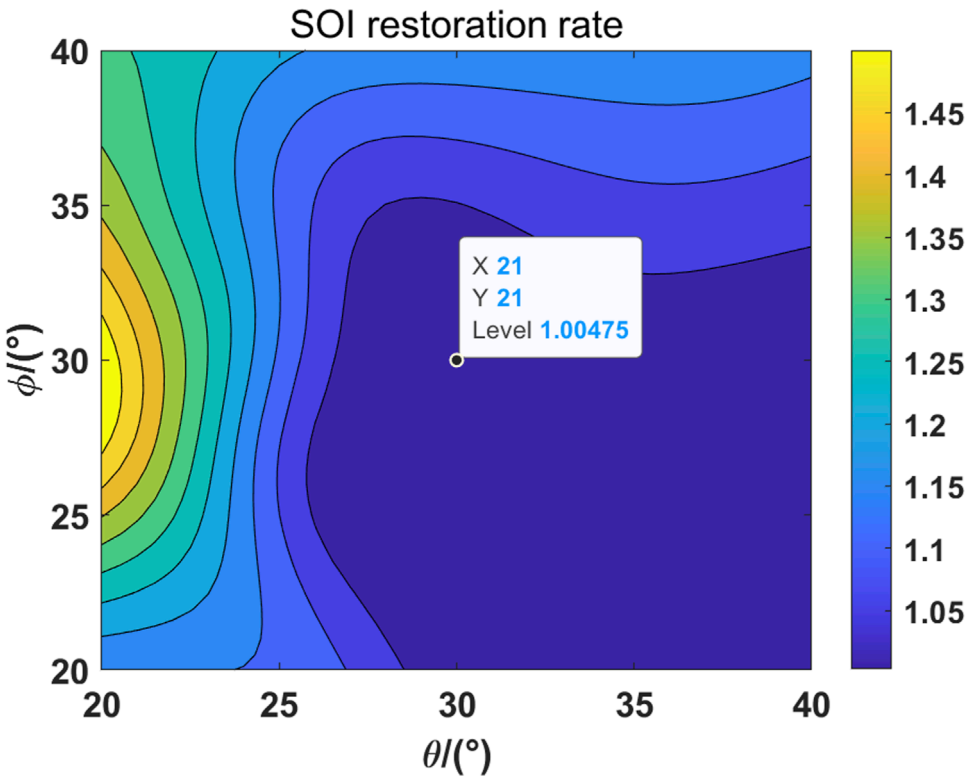

FIGURE 14
The relationship between the estimation of the interference arrival angle and the SOI restoration rate is plotted.

impedance is matched. The numerical model of PAF system noise can be established by using antenna analysis technology and electromagnetic field simulation software. According to the principle of electromagnetic reciprocity, the signal response of the array in the (θ,ϕ) orientation can be obtained from the pattern $P(\theta,\phi)$, which is the pattern of the array under unit excitation. Then, the array response in an orientation can also be obtained from $P(\theta,\phi)$. The correlation matrix of the signal response (Jeffs et al., 2008) of the non-point source is described as

$$R = 16k_B TB\mathfrak{C}A_\Omega\mathfrak{C}^H, \tag{3}$$

where B is the bandwidth, A_Ω is the integral matrix of the non-point source pattern, and $A_\Omega = \iint_\Omega p(\theta,\phi)p^*(\theta,\phi)d\theta d\phi$, where Ω is the solid angle of the noise reception. $\mathfrak{C}$ is the impedance coefficient vector calculated using electromagnetic field simulation software. Figure 6 shows a correlation matrix of impedance coefficients of 25 elements, i.e., $\mathfrak{C}\mathfrak{C}^H$. For $\boldsymbol{R}_{sp}$, the focal ratio of the 110-m parabolic antenna is 0.33, and the spillover angle of the PAF receiver ranges from 0° to −15.7°. To facilitate the calculation and avoid considering noise from long distances near the horizon, the spillover angle selected for the simulation ranges from −1° to −15°, as depicted in Figure 1. The angle interval used is 0.1°, consistent throughout the experiment. The spillover pattern of the 25 Vivaldi antennas under uniform excitation is shown in Figure 7. Assuming that the temperature of the warm ground is 298.5 K, the resulting $\boldsymbol{R}_{sp}$ is shown in Figure 8. For $\boldsymbol{R}_{sky}$, we consider noise entering the elevation range from 35° to 90°, which predominantly includes the main beam and several side beams. The pattern, shown in Figure 9, is obtained through the joint simulation of all array elements and the parabolic antenna under uniform excitation. Assuming that the atmospheric noise is 15 K and the cosmic microwave background (CMB) is 3 K, the resulting $\boldsymbol{R}_{sky}$ is depicted in Figure 10. For $\boldsymbol{R}_{LNA}$, the LNA of the QTT-PAF receiver has a design index of 6 k under cryogenic conditions, which cannot be represented by white noise only due to the mutual coupling, as shown in Figure 11. Due to the scope simulation, the loss of the antenna is not included. Finally, for the overall receiver operating temperature of 20 k, the remaining 14 k noise contribution is replaced by white noise.

3.3 Beamforming and interference mitigation

The minimum signal power that a radio telescope can detect is limited by the variance of the noise. Usually, the SOI enters along the main beam of a telescope, and the interference enters through the side beam, and these and the noise are uncorrelated to each other. The covariance matrix of the output signal of the PAF receiver can be described as $\boldsymbol{R}_x = \boldsymbol{R}_{SOI} + \boldsymbol{R}_I + \boldsymbol{R}_{noise}$, where $\boldsymbol{R}_{SOI}$ and $\boldsymbol{R}_I$ are the covariance matrix of the SOI and interference, respectively. The models for these two contributions are also described by Eq. 3, except that these are both considered point sources. The power of the SOI is limited to −20 dB below noise power and 30 dB above noise power for

interference. At the same time, the STI window size is set to 1,024. In this window, interference that occurs is 40% of the size, the SOI appears 20% of the size, and they are simultaneous in time. The output of the LCMV beamformer (assuming that the arrival angle of interference is unambiguous) is shown in Figure 12. We define the interference mitigation rate as $1-\frac{P_I^{LCMV}}{P_I}$, where P_I^{LCMV} is the average output power of the LCMV beamformer over the interference period and P_I is the average power of the input interference. The SOI restoration rate is defined as $\frac{P_{SOI}^{LCMV}}{P_{SOI}}$, where P_{SOI}^{LCMV} is the average output power of the LCMV beamformer during the time of SOI occurrence and P_{SOI} is the set average power of the SOI. Finally, we present the graphical depiction of the interference mitigation rate and SOI restoration rate when the error of the spherical angle of interference remains below 10°, as shown in Figures 13, 14. Here, the beamforming weight vector $\boldsymbol{w}_{LCMV}(\theta,\phi)$ for the telescope at the orientation (θ,ϕ) during one STI is obtained by the Hadamard product of the steering vector $\boldsymbol{w}(\theta,\phi)$ with the LCMV weight vector $\boldsymbol{w}_{LCMV}$. Mathematically, this can be expressed as $\boldsymbol{w}(\theta,\phi)^*\boldsymbol{w}_{LCMV} = \boldsymbol{w}_{LCMV}(\theta,\phi)$, where * is the Hadamard product operation.

By examining Figures 12–14, it becomes evident that when there is a clear interference orientation, the LCMV algorithm demonstrates significant interference reduction. The interference mitigation rate is 0.921, and the SOI restoration rate is 1.005. It should be noted that the ratio is greater than 1 due to interference. The interference orientation vector and the SOI orientation vector are not orthogonal. With the change in the spherical angle of interference, the interference mitigation rate and the SOI restoration rate show similar patterns. We believe that the primary factors are the pattern and single polarization of the telescope. Regarding the pattern, the telescope exhibits an approximately 10 dB variation in gain on the interference within the estimated range of interference orientations. Given that the telescope's overall dynamic range exceeds 50 dB, this change is not substantial. Furthermore, the PAF model considers only single polarization. Consequently, when the interference shifts in an orientation not aligned with the polarization, the telescope does not respond sensitively to these changes.

4 Conclusion

In this paper, the signal numerical model and interference mitigation verification under the QTT-PAF model are implemented. The PAF receiver and parabolic antenna composed of 25 array elements are co-simulated under the Vivaldi antenna model, and the internal and external noise of the system is given from the perspective of covariance. Finally, the noise is mixed into the SOI and interference, and the interference is mitigated by the LCMV algorithm. The mitigation results show that the LCMV algorithm has a good mitigation ability for interference under this model and has a small impact on the SOI, but the premise is that the interference orientation is accurately estimated.

Data availability statement

The original contributions presented in the study are included in the article/Supplementary Material; further inquiries can be directed to the corresponding author.

Author contributions

PW: writing–original draft and writing–review and editing. JL: funding acquisition and writing–review and editing. M-ZC: funding acquisition, project administration, supervision, and writing–review and editing.

Funding

The author(s) declare that financial support was received for the research, authorship, and/or publication of this article. This work was funded by the National Key R&D Program of China under Grant No. 2022YFC2205300, the National Natural Science Foundation of China (12073067), and the Chinese Academy of Sciences (CAS) "Light of West China" Program under Grant No. 2022-XBQNXZ-012.

Conflict of interest

The authors declare that the research was conducted in the absence of any commercial or financial relationships that could be construed as a potential conflict of interest.

Publisher's note

All claims expressed in this article are solely those of the authors and do not necessarily represent those of their affiliated organizations, or those of the publisher, the editors, and the reviewers. Any product that may be evaluated in this article, or claim that may be made by its manufacturer, is not guaranteed or endorsed by the publisher.

References

Ivashina, M. V., Iupikov, O., Maaskant, R., van Cappellen, W. A., and Oosterloo, T. (2011). An optimal beamforming strategy for wide-field surveys with phased-array-fed reflector antennas. *IEEE Trans. Antennas Propag.* 59, 1864–1875. doi:10.1109/TAP.2011.2123865

James, E. M. (2012) *Improved methods for phased array feed beamforming in single dish radio astronomy*. Provo, UT, United States; Brigham Young University. Ph.D. thesis.

Jeffs, B. D., Warnick, K. F., Landon, J., Waldron, J., Jones, D., Fisher, J. R., et al. (2008). Signal processing for phased array feeds in radio astronomical telescopes. *IEEE J. Sel. Top. Signal Process.* 2, 635–646. doi:10.1109/JSTSP.2008.2005023

Ma, J., Pei, X., Wang, N., Li, J., Wang, K., and Liu, Y. (2019). Ultra wideband and multi-beam signal receiving and processing system of qtt. *Sci. Sinica Phys. Mech. Astronomica* 49, 99502, 1–13. doi:10.1360/SSPMA-2019-0014

Wang, N. (2014). Xinjiang Qitai 110 m radio telescope. *Sci. Sinica Phys. Mech. Astronomica* 44, 783–794. doi:10.1360/SSPMA2014-00039

Warnick, K. F., and Jeffs, B. D. (2008). Efficiencies and system temperature for a beamforming array. *IEEE Antennas Wirel. Propag. Lett.* 7, 565–568. doi:10.1109/LAWP.2008.2001752

Warnick, K. F., Jeffs, B. D., Landon, J., Waldron, J., Jones, D., Richard Fisher, J., et al. (2009a). "Beamforming and imaging with the byu/nrao l-band 19-element phased array feed," in 2009 13th International Symposium on Antenna Technology and Applied Electromagnetics and the Canadian Radio Science Meeting, Banff, AB, February 15–18, 2009 (IEEE) 1–4. doi:10.1109/ANTEMURSI.2009.4805125

Warnick, K. F., Maaskant, R., Ivashina, M. V., Davidson, D. B., and Jeffs, B. D. (2016). High-sensitivity phased array receivers for radio astronomy, *Proc. IEEE* 104 (3), 607–622. doi:10.1109/JPROC.2015.2491886

Warnick, K. F., Woestenburg, B., Belostotski, L., and Russer, P. (2009b). Minimizing the noise penalty due to mutual coupling for a receiving array. *IEEE Trans. Antennas Propag.* 57, 1634–1644. doi:10.1109/TAP.2009.2019898

Wu, P., Li, J., and Chen, M.-Z. (2024). Simulation of rfi cancellation using subspace projection algorithm for paf receiver. *Res. Astron. Astrophys.* 24, 015019. doi:10.1088/1674-4527/ad0b84

Young, A., Ivashina, M. V., Maaskant, R., Iupikov, O. A., and Davidson, D. B. (2013). Improving the calibration efficiency of an array fed reflector antenna through constrained beamforming. *IEEE Trans. Antennas Propag.* 61, 3538–3545. doi:10.1109/TAP.2013.2255577

frontiers | Frontiers in Astronomy and Space Sciences

TYPE Original Research
PUBLISHED 30 July 2024
DOI 10.3389/fspas.2024.1407870

OPEN ACCESS

EDITED BY
Hairen Wang,
Purple Mountain Observatory, Chinese Academy of Sciences (CAS), China

REVIEWED BY
Dan Werthimer,
University of California, Berkeley, United States
Tao An,
Shanghai Astronomical Observatory, Chinese Academy of Sciences (CAS), China

*CORRESPONDENCE
Ji-Xia Li,
jxli@bao.ac.cn
Feng-Quan Wu,
wufq@bao.ac.cn
Hai-Jun Tian,
hjtian@hdu.edu.cn
Ju-Yong Zhang,
zhangjy@hdu.edu.cn
Zhi-Ping Chen,
chen_zp@hdu.edu.cn

RECEIVED 27 March 2024
ACCEPTED 25 June 2024
PUBLISHED 30 July 2024

CITATION
Wang Z, Li J-X, Zhang K, Wu F-Q, Tian H-J, Niu C-H, Zhang J-Y, Chen Z-P, Yu D-J and Chen X-L (2024), Design and implementation of a scalable correlator based on ROACH2 + GPU cluster for tianlai 96-dual-polarization antenna array.
Front. Astron. Space Sci. 11:1407870.
doi: 10.3389/fspas.2024.1407870

Design and implementation of a scalable correlator based on ROACH2 + GPU cluster for tianlai 96-dual-polarization antenna array

Zhao Wang[1,2,3,4], Ji-Xia Li[2]*, Ke Zhang[2,3], Feng-Quan Wu[2]*, Hai-Jun Tian[1,5]*, Chen-Hui Niu[4], Ju-Yong Zhang[5]*, Zhi-Ping Chen[5]*, Dong-Jin Yu[5] and Xue-Lei Chen[2]

[1]School of Science, Hangzhou Dianzi University, Hangzhou, China, [2]National Astronomical Observatories, Chinese Academy of Sciences, Beijing, China, [3]College of Electrical Engineering and New Energy, China Three Gorges University, Yichang, China, [4]Central China Normal University, Wuhan, China, [5]Big Data Institute, Hangzhou Dianzi University, Hangzhou, China

The digital correlator is one of the most crucial data processing components of a radio telescope array. With the scale of radio interferometeric array growing, many efforts have been devoted to developing a cost-effective and scalable correlator in the field of radio astronomy. In this paper, a 192-input digital correlator with six CASPER ROACH2 boards and seven GPU servers has been deployed as the digital signal processing system for Tianlai cylinder pathfinder located in Hongliuxia observatory. The correlator consists of 192 input signals (96 dual-polarization), 125-MHz bandwidth, and full-Stokes output. The correlator inherits the advantages of the CASPER system, for example, low cost, high performance, modular scalability, and a heterogeneous computing architecture. With a rapidly deployable ROACH2 digital sampling system, a commercially expandable 10 Gigabit switching network system, and a flexible upgradable GPU computing system, the correlator forms a low-cost and easily-upgradable system, poised to support scalable large-scale interferometeric array in the future.

KEYWORDS

interferometer, correlator, FPGA, signal processing, correlation, radio astronomy

1 Introduction

The digital correlator plays a crucial role in radio astronomy by combining individual antennas to form a large-aperture antenna, keeping large field of view, and providing high-resolution images. At present, many radio interferometric arrays in the world use CASPER (Collaboration for Astronomy Signal Processing and Electronics Research) hardware platform ROACH2 (Reconfigurable Open Architecture Computing Hardware-2) to develop correlators. For example, PAPER (Precision Array for Probing the Epoch of Reionization) in South Africa's Karoo Desert (Parsons et al., 2010; Ali et al., 2015). The 100 MHz FX correlator was originally based on iBOBs (Interconnect Break-out Boards) and later upgraded to ROACH, and then ROACH2 boards (Hickish et al., 2016). Currently, PAPER

uses 8 ROACH2 boards for channelization, followed by a GPU (Graphics Processing Unit)-based 'X' stage. Additionally, the 'large-N' correlator located in the Owens Valley Radio Observatory (LWA-OV) is designed to enable the Large Aperture Experiment to Detect the Dark Ages (LEDA) (Kocz et al., 2015). It features a 58 MHz, 512-input digitization, channelization, and packetization system using a GPU correlator backend.

The Tianlai project[1] is an experiment aimed at detecting dark energy by measuring baryon acoustic oscillation (BAO) features in the large-scale structure power spectrum, in which BAO can be used as a standard ruler (Ansari et al., 2012; Kovetz et al., 2019; Liu and Shaw, 2020). The basic plan is to build a radio telescope array and use it to make 21 cm intensity mapping observations of neutral hydrogen, which trace the large-scale structure of the matter distribution (Chen, 2011; Xu et al., 2015; Zhang et al., 2016; Das et al., 2018; Yu et al., 2024; Yu et al., 2023). Currently, two different types of pathfinder array have been built in a quiet radio site in Hongliuxia, Balikun county, Xinjiang, China (Wu et al., 2014). The cylinder array consists of three adjacent parabolic cylinder reflectors, each 40 m × 15 m, with their long axes oriented in the N-S direction. It has a total of 96 dual-polarization feeds, resulting in 192 signal channels (Cianciara et al., 2017; Li et al., 2020; Sun et al., 2022). The dish array includes 16 dishes with 6-m aperture. Each dish has a dual polarization feed, generating 32 signal channels in total (Wu et al., 2021; Perdereau et al., 2022; Kwak et al., 2024). In addition to the ability to survey the 21 cm Hydrogen sky, both antenna arrays are also capable of detecting fast radio bursts (Yu et al., 2022a; Yu et al., 2022b; Yu et al., 2022c). This paper is about the development of correlator for Tianlai cylinder pathfinder array.

The design of the Tianlai cylinder correlator is based on the prototype correlator of Niu et al. (2019), which has 32 inputs and was used for the Tianlai Dish pathfinder array. This 32-input prototype correlator is built upon the model of PAPER correlator, which creates a flexible and scalable hybrid correlator system. We expanded the prototype correlator from 32 to 192 channels, reprogrammed the network transport model, increased it from a single GPU server to seven GPU servers, solved the synchronization problem of multiple devices. It was eventually deployed in the machine room on the Hongliuxia site. The primary motivation behind the design of the PAPER correlator architecture is the scalability for large-scale antenna arrays, and it has been executed exceptionally well. Therefore, we have chosen to borrow ideas from the PAPER correlator. The Tianlai project is expanding and the number of single inputs will soon increase to more than 500.

The Tianlai cylinder correlator is a flexible, scalable, and efficient system, which has a hybrid structure of ROACH2+GPU+10 GbE network. A ROACH2 is an independent board, unlike a PCIe-sampling board which needs to be plugged into a computer server and often leads to some incompatible issues. A GPU card is dramatically upgrading, and it is almost the best choice among the current available hardwares, such as CPU/GPU/DSP (Digital Signal Processing), by comprehensively considering the flexibility, the efficiency and the cost. The module of the data switch network is easy to be upgraded, since the Ethernet switch has a variety of commercial applications. We have uploaded all the project files to Github.[2]

This paper gives a detailed introduction to the function and performance of the Tianlai 192-input cylinder correlator system. In Section 2, we introduce the general framework of the correlator system and show the deployment of the correlator. Then, in a sub-section, we provide a detailed introduction to the design and functions of each module. In Section 3, we evaluate the performance of the correlator. Section 4 summarizes the correlator system and presents the design scheme for correlator expansion in the future as part of the Tianlai project.

2 System design

The digital correlators can be classified into two types: XF and FX. XF correlators combine signals from multiple antennas and performs cross-correlation followed by Fourier transformation. XF correlators can handle a large number of frequency channels and have a relatively simple hardware design (Thompson et al., 2017). FX correlators combine signals from multiple antennas and perform the Fourier transformation followed by cross-correlation. FX correlators can handle a large number of antenna pairs and also have a relatively simple hardware design. The Tianlai cylinder correlator is an FX correlator.

The Tianlai cylinder correlator system can be divided into four parts, as shown in Figure 1. The first part is the control part which consists of a master computer and an Ethernet switch. The Ethernet switch is used for net-booting of the ROACH2, monitoring the status of F-engine and hashpipe[3], and synchronizing the running status of F-engine and X-engine.

The second part is the F-engine, which consists of six ROACH2 boards and one 10 GbE switch. The 192 input signals from the Tianlai cylinder array are connected to the ADC connectors on the ROACH2 boards. The main functions of the F-engine are to Fourier transform the data from the time domain into the frequency domain, and transmit the data to the GPU server through a 10 GbE switch.

The third part is the X-engine, which performs cross-correlation on the received Fourier data. Each GPU server receives packets from all ROACH2 boards. The details of network transmission will be explained later. The X-engine utilizes a software called hashpipe (MacMahon et al., 2018) to store, deliver and compute the cross-correlations.

The fourth part is the data storage part, which consists of seven GPU servers, an Ethernet switch, and a storage server (shared with the master computer). The GPU servers transmit data to the storage server via an Ethernet switch. We have developed a multi-threading program to collect and organize data packets from different GPU servers, and finally save them onto hard drives in HDF5 format.

The deployment of the correlator system is shown in Figure 2. It consists of six ROACH2 boards, an Ethernet switch, a 10 GbE

1 https://tianlai.bao.ac.cn

2 https://github.com/TianlaiProject

3 https://github.com/david-macmahon/hashpipe

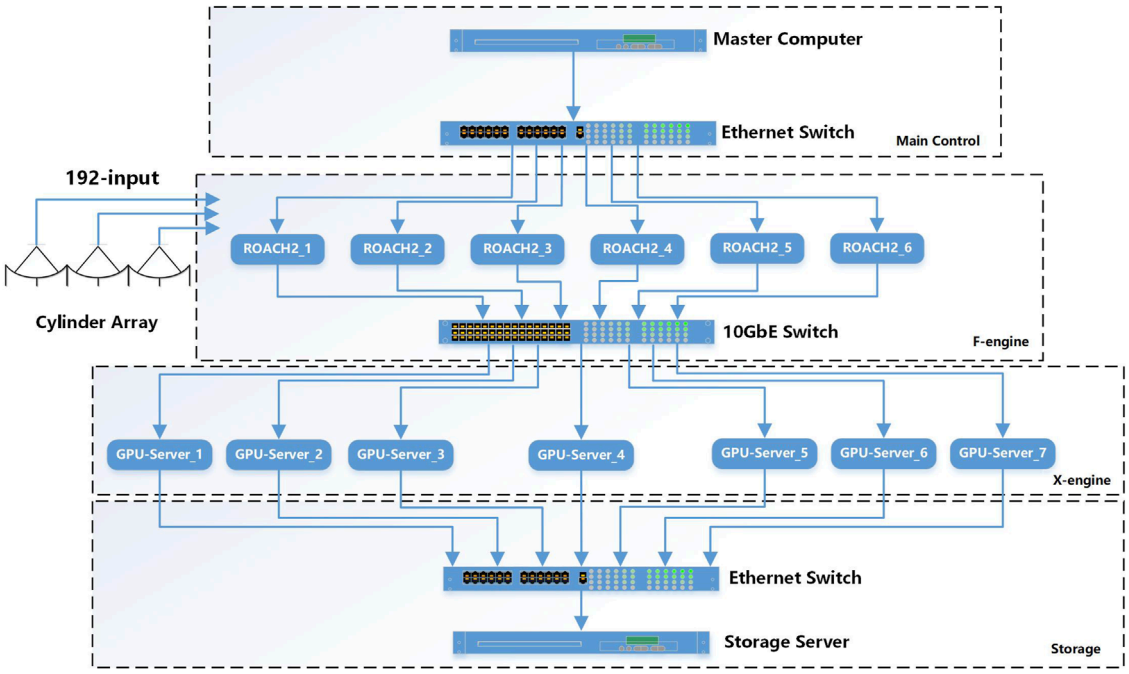

FIGURE 1
This block diagram illustrates the Tianlai cylinder array correlator. The master computer communicates with ROACH2 boards, a 10 GbE switch, and GPU servers through an Ethernet switch. Six ROACH2 boards receive 192 input signals from the antenna. After the signal processing is completed, the UDP(User Datagram Protocol) data is sent to the 10 GbE switch. Seven GPU servers receive the UDP data to calculate the cross-correlation, sending results back to the Ethernet switch after the computations are finished. Finally, the data is transmitted to the master computer for storage via the Ethernet switch.

switch, a master computer, and seven GPU servers, arranged from top to bottom. The yellow "ROACH2" label in Figure 2A represents the front panel of the ROACH2 board. (In our case, a connector transformer panel has been specifically designed to conveniently connect to the radio cables.) The ADC connector of the ROACH2 is connected to a blue RF (Radio Frequency) cable that transmits the analog signal. Figure 2B shows the back side of the ROACH2 board. On the far left is the power line. The light orange RF cable is the clock cable. The 250 MHz clock of the ROACH2 board is output by a VALON 5008 dual-frequency synthesizer module, and it is split by a 12-way power splitter. The short blue-black cable connects to the synchronization port between the ROACH2 boards. We use synchronization ports in F-engine functional block design to ensure that the six ROACH2 boards work at the same clock. The signal of the synchronization port is provided by a time server. The time server sends out a 1-PPS (Pulse Per Second) signal, which is used to initialize the synchronization module of the F-engine system. After running the F-engine control script, the 1 PPS signal drives the F-engine and synchronizes the operational state of the six ROACH2 boards. The bandwidth of the antenna signal input to the ROACH2 board is 125 MHz. According to the Nyquist sampling law, the input signal can be completely recovered by a 250 Msps sampling rate. In Figure 2C, seven GPU servers are vertically stacked, consisting of six Supermicro servers with a size of 4 U (Unit) and one Dell server with a size of 2U. These devices are used to implement X-engine functionality. The number of servers is determined by the total frequency channel count and the frequency channel processing capacity of each server. In terms of computational performance, each GPU server runs 4 hashpipe threads, processing a total of 128 frequency channels. At this configuration, the computational performance accounts for approximately 46% of the theoretical peak performance. In terms of data transfer performance, the server's PCIe is of version 3.0, with a transfer rate close to 8 GB/s. This is comparable to the maximum transfer rate between the host and the device.

2.1 F-engine

The diagram of the F-engine module is shown in Figure 3. The Tianlai cylinder correlator system is an improvement upon the Tianlai dish correlator system, with enhancements including an increased number of input signals and additional new functions. The Tianlai dish correlator is very similar to the PAPER experiment correlator, which also uses the ROACH2 system. Please refer to (Niu et al., 2019) for details. Here, we provide a concise overview of the F-engine's process and the functionality of the CASPER yellow block.

Each ROACH2 board is connected with two ADC boards through Z-DOK + connectors. The ADC board is the adc16 × 250-8 coax rev2 Q2 2013 version, which uses 4 HMCAD1511 chips and provides a total of 16 inputs. It samples 16 analog signal inputs with 8 bits at a rate of 250 Msps.

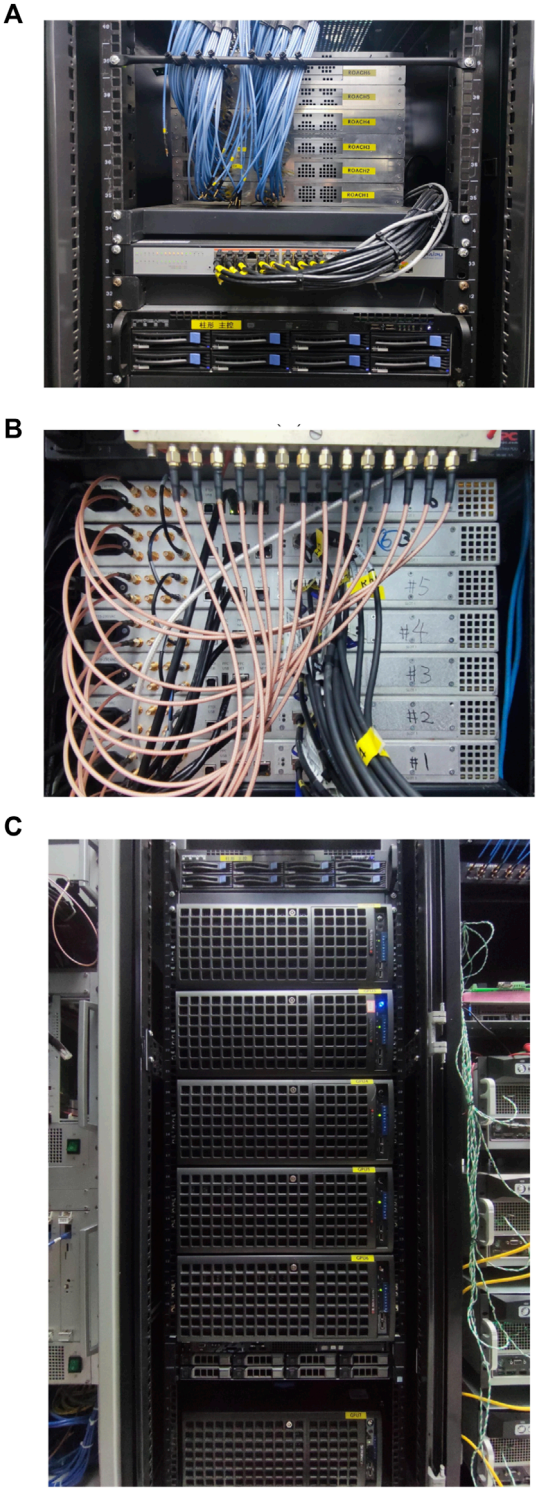

FIGURE 2
(A) Six ROACH2 boards are connected to 192 input signals. The two switches are positioned on the same layer, with the Ethernet switch in the front and the 10 GbE switch at the rear. The master computer is located below. **(B)** Clock and synchronization cable connections on the rear panel of ROACH2 boards. **(C)** Seven GPU servers are vertically stacked, consisting of six Supermicro servers with a size of 4U and a Dell server with a size of 2U.

The output digital signal of the adc16 × 250 block is Fix_8_7 format, which indicates an 8-bit number with 7 bits after the decimal point. The ADC chip is accompanied by a control program developed by David MacMahon from the University of California, Berkeley. This program is responsible for activating the ADC, selecting the amplification level, calibrating the FPGA input delay, aligning the FPGA SERDES blocks until data is correctly framed, and performing other related tasks. A comprehensive user's guide for the ADC16 chip is accessible on the CASPER website[4]. According to the actual range of input signal power, we conducted linearity tests on the ADC at various gain coefficients and also assessed the linearity of the correlator system. Ultimately, the ADC gain coefficient was set to 2.

The analog-to-digital converted data from the ADC is transmitted to the PFB (Polyphase Filter Bank) function module. PFB is a computationally efficient implementation of a filter bank, constructed by using an FFT (Fast Fourier Transform) preceded by a prototype polyphase FIR filter frontend (Price, 2021). The PFB not only ensures a relatively flat response across the channels but also provides excellent suppression of out-of-band signals. The PFB is implemented using the models pfb_fir and fft_biplex_real_2x from the CASPER module library.

Each pfb_fir[5] block (the signal processing blocks mentioned in this article can all be linked to the detailed page from here) processes two signals, configured with parameters including a PFB size of 2^{11}, a Hamming window function, four taps, input width of 8 bits, an output width of 18 bits, and other settings. Each block takes two input signals, and a total of 16 `pfb_fir` blocks are used to process 32 input signals. Each fft_biplex_real_2x block processes four input data streams and outputs two sets of frequency domain data. Configured with parameters including an FFT size of 2^{11}, an input width of 18 bits, an output width of 36 bits, and other settings. The parameter settings are based on the scientific requirements of the Tianlai project, which calls for a signal resolution of less than or equal to 0.2 MHz. There are eight fft_biplex_real_2x blocks, with each block taking in four data streams and outputting two sets of frequency domain data. The PFB module is flexible, making it very easy to adjust the parameters according to one's requirements, such as the FFT size, PFB size, and the number of taps in the CASPER block.

The data output of the PFB module is 36 bits, which essentially represents a complex number with 18 bits for the real part and 18 bits for the imaginary part. Considering factors such as data transmission and hardware resources, the data is usually effectively truncated. In our case, we will truncate the complex number to have a 4-bit real part and a 4-bit imaginary part. Prior to quantizing to 4 bits, the PFB output values pass through a scaling (i.e., gain) stage. Each frequency channel of each input has its own scaling factor. The purpose of the scaling stage is to equalize the passband before quantization, so this stage is often referred to as EQ. The

4 https://casper.astro.berkeley.edu/wiki/ADC16x250-8_coax_rev_2

5 https://casper.astro.berkeley.edu/wiki/Block_Documentation

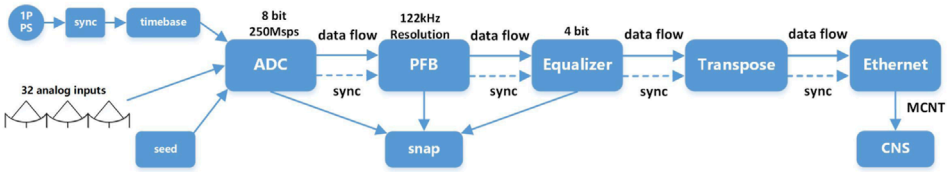

FIGURE 3
Data flow block diagram of each F-engine.

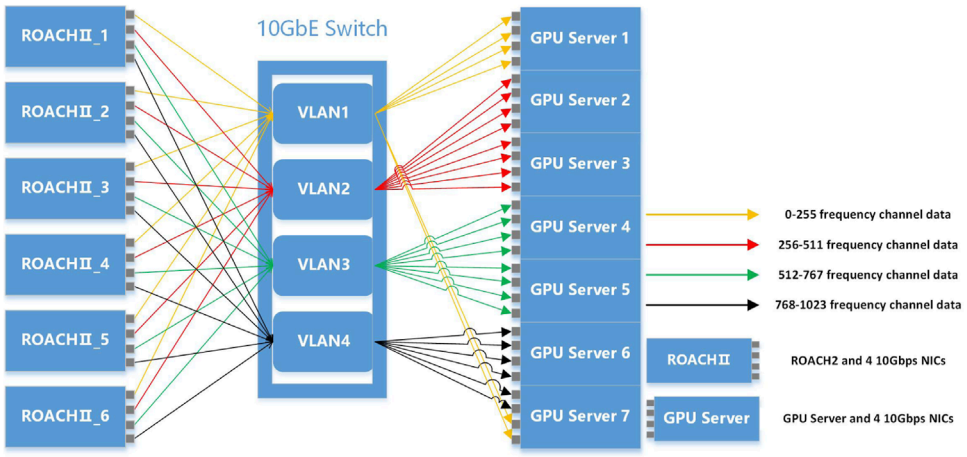

FIGURE 4
Diagram of data transmission between X-engine and F-engine. Each ROACH2 board has 4 10 GbE ports, and each port transmits data from 256 frequency channels. The 10 GbE switch is configured with 4 VLANs (Virtual Local Area Networks), which offers benefits in simplicity, security, traffic management, and economy. Each VLAN receives UDP data from 256 frequency channels and sends them to the GPU servers.

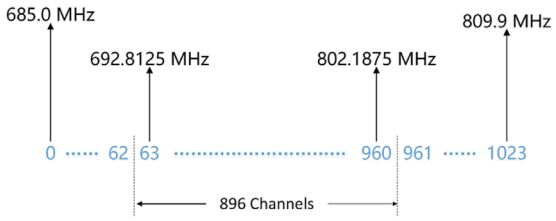

FIGURE 5
The relationship between the FFT channels and the radio frequency. There are a total of 1,024 frequency channels, and the input signal's effective frequency range is 700-800 MHz. The correlator's actual processing frequency range is 692.8125-802.1875 MHz, which includes a total of 896 frequency channels.

TABLE 1 List of X-engine equipment.

	Supermicro (4U)	Dell (2U)
PCIe	3.0	4.0
Graphics Card	Dual GTX 690	One RTX 3080
CPU	Dual Intel E5-2670	Dual Intel E5-2699
NIC	Dual 2-port 10 GbE	Dual 2-port 10 GbE
Memory	128 GB RAM	256 GB RAM
OS	Centos7	Rocky8

scaling factors are also known as EQ[6] coefficients and are stored in shared BRAMs.

The quantized data cannot be sent directly to the X-engine. Before sending it, we divide the frequency band and sort the data in a format that facilitates the relevant calculations. This module is called Transpose, and it is divided into four submodules. Each submodule processes 1/4 of the frequency band, resulting in a total of 256 frequency channels. The number of submodules corresponds to the number of 10 GbE network interface controllers (NICs) on the ROACH2 board, with each NIC used to receive and send data from the output of a transpose submodule. This module performs the data transpose, also known as a "corner turn" to arrange the data in the desired sequence. Additionally, it is responsible for generating the packet headers, which consist of MCNT (master counter), Fid (F-engine id), and Xid (X-engine id). The current

6 https://casper.astro.berkeley.edu/wiki/PAPER_Correlator_EQ

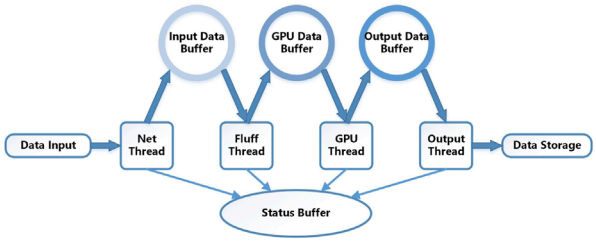

FIGURE 6
Hashpipe thread manager diagram.

parameter configuration of the sub-module is tailored for scenarios with 256 inputs or fewer. However, David MacMahon, the researcher behind the PAPER correlator system, has included sufficient spare bits in the design, enabling the adjustment of model parameters based on specific input conditions and accommodating scalability and additional use cases.

The data is already in a form that is easy for X-engine to compute, we want to send it to X-engine, so the data comes to the Ethernet module. It contains four sub-modules and receives data from four transpose sub-modules. Each submodule has a Ten_GbE_v2 block, where we can set the MAC address, IP address, destination port and other parameters using Python or Ruby script.

2.2 Network

The data of the F-engine module is sent out through the ROACH2 network port and transmitted to the network port of the target GPU server through the 10 GbE switch. The network transmission model of the correlator system is dependent on the bandwidth of a single frequency channel and the number of frequency channels calculated by the GPU server. The diagram of data transfer from F-engine to X-engine is shown in Figure 4.

The frequency domain data in F-engine has a total of 1,024 frequency channels. Given the 250 Msps sampling rate, each frequency channel has a width of $\Delta\nu = 125/1{,}024$ MHz = 122.07 kHz. Each GPU node processes 128 frequency channels with a bandwidth of 128×122.07 kHz = 15.625 MHz. The number of frequency channels processed by the GPU server is determined by hashpipe.

The analog part of the Tianlai digital signal processing system uses replaceable bandpass filters, with the bandpass set to 700 MHz ~ 800 MHz. We have chosen to utilize seven GPU nodes to implement the X-engine component. These seven GPU nodes process data for the central 896 frequency channels, covering a bandwidth of approximately 109.375 MHz from 692.8125 MHz to 802.1875 MHz, as shown in Figure 5. The final GPU node is dedicated to receiving data from the first 32 and last 32 frequency channels out of the 896 frequency channels.

The data transfer rate of a single network port of the ROACH2 board is 8.0152 Gbps, so the total data transfer rate of 6 ROACH2 boards is 6×4 ports $\times$ 8.0152 Gbps = 192.3648 Gbps. The data reception rate of a single network port on the GPU node is 192.3648 Gbps/(8×4) = 6.0114 Gbps. At present, the number of input signals for the correlator system ranges from 32 to 256. While our correlator system is designed for 192 input signals, we conducted data transmission simulations with 256 input signals. Under these conditions, the data reception rate of a single network port on the GPU node stands at 8.0152 Gbps.

In our system, each GPU server has four 10 GbE ports. For the Tianlai cylinder correlator system, we require a total of 6 ROACH2 boards $\times$ 4 ports + 7 GPU servers $\times$ 4 ports = 52 ports on a 10 GbE switch. So we selected the Mellanox SX1024 switch which has 48 ports of 10 GbE and 12 ports of 40 GbE. Ports 59 and 60 on the switch can be subdivided into four 10 GbE ports, providing ample capacity for our application.

The transpose module is designed with extra bits reserved in the blocks related to the parameter `fid`. The number of bits in the `fid` parameter is directly linked to the maximum number of F-engines in the correlator system. By utilizing these additional bits, the correlator can be configured to accommodate a greater number of input signals. In terms of the F-engine, theoretically, there could be an infinite number of input channels, and the number of ROACH2 boards can be increased based on the input channel number. The capacity of X-engine determines the upper limit of input channels, depending on the processing capacity of the GPU servers for a single frequency point. Since each frequency point should contain all the input channel information, the processing capability of the GPU servers for a single frequency channel affects maximum number of input channels. Currently, a single server theoretically has the capability to handle over 20,000 input channels if it only processes one frequency channel. However, this may need an extremely large-scale switch network.

The relationship between the number of input channels and the output data rate is as shown in Eq. 1:

$$\frac{1}{2} \times N(N+1) \times f\_ch \times 2 \times f\_b / Integration\_time \tag{1}$$

where N represents the number of input channels, f_ch represents the number of frequency channels, f_b represents the number of bytes in a single frequency channel. The multiplying factor 2 is because frequency channels are complex numbers.

2.3 X-engine

The primary role of the X-engine is to perform cross-correlation calculations. The X-engine receives the data from the F-engine in packets, which are then delivered to different computing servers, where the conjugate multiplication and accumulation (CMAC) are done. The hardware for this part consists mainly of six Supermicro servers and one Dell server. We list the main equipment of the X-engine in Table 1.

The X-engine part consists of seven GPU nodes. To ensure that they integrate the data at exactly the same time duration, they must be synchronized together. A script has been developed to achieve this, and its basic procedure is as follows. First, initialize the hashpipes of 7 GPU nodes; Second, start the hashpipe program of the first GPU node; Third, read out the

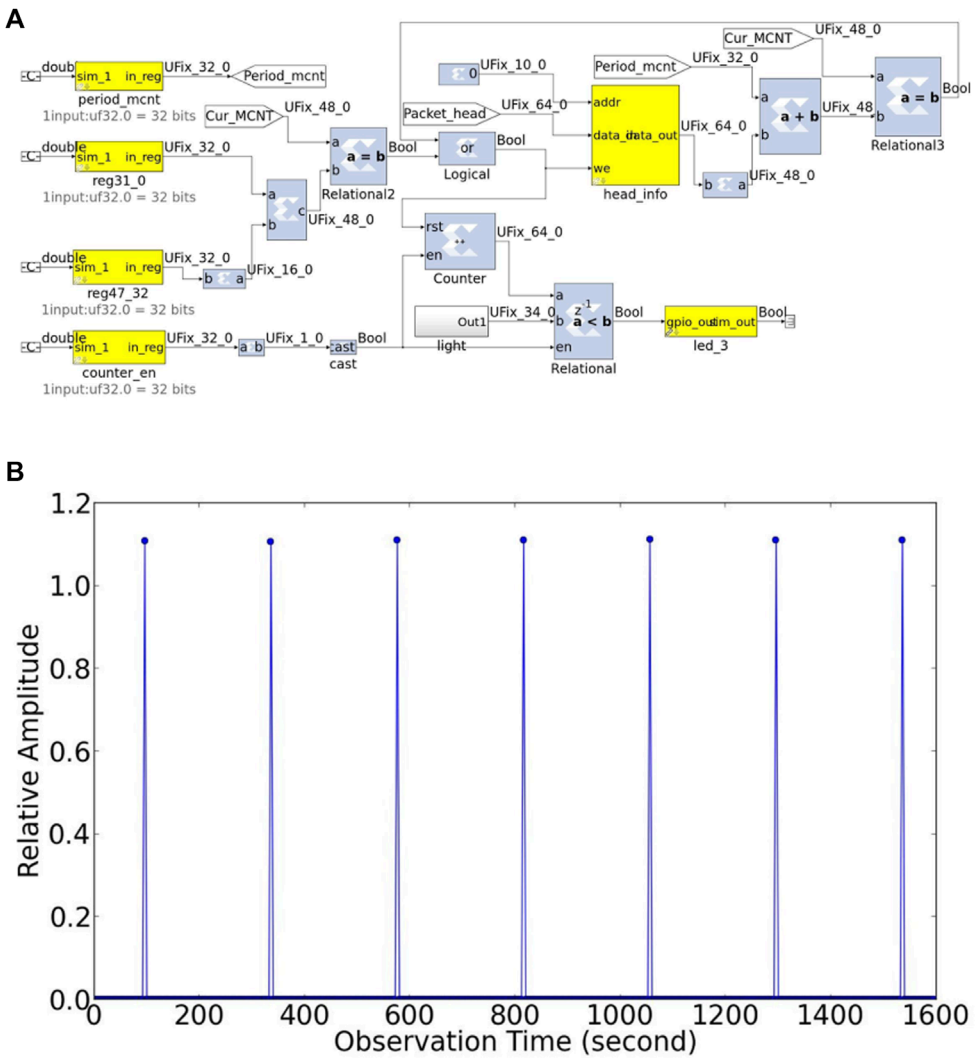

FIGURE 7
(A) Design of the calibrator noise source control module. **(B)** The periodic CNS signal in the cross-correlation results is aligned with the integration time.

MCNT value in the current packet and calculate a future (several seconds later) MCNT value to act as the aligning time point. Finally, all GPU nodes work simultaneously when their hashpipe threads receive a packet contains the calculated aligning MCNT value.

The data operation in the X-engine is managed by the hashpipe software running on CPU and GPU heterogeneous servers. Hashpipe was originally developed as an efficient shared pipe engine for the National Astronomical Observatory, the Universal Green Bank Astrospectrograph (Prestage et al., 2009). It was later adapted by David MacMahon of U.C. Berkeley, it can be used for FX correlators (Parsons et al., 2008), pulsar observations (Pei et al., 2021), Fast Radio Bursts detection (Yu et al., 2022a) and the search for extraterrestrial civilizations (Price et al., 2018). The core of the hashpipe is the flexible ring buffer. It simulates contiguous memory blocks, realizes data transmission and sharing among multiple threads, and uses the central processing unit to control startup and shutdown, etc. The ring buffer is used to temporarily store and deliver the data packets to ensure that the data is captured quickly and distributed in the correct order.

Each hashpipe instance in our system has a total of four threads and three buffers, as shown in Figure 6. To process the four 10 GbE ports data stream, four hashpipe instances are created. In each instance, the basic data process can be concluded as follows. First, net_thread receives the packets from the GPU server's 10 GbE port. According to the packet format, the valid data is extracted and the packet header is analyzed. Packets are time-stamped, and if they arrive at the GPU server out of order, they can be rearranged into the appropriate time series and written to the input data buffer, which is passed onto the next thread once a consecutive block of data is filled. The fluff thread "fluffing" the data, fluffs 4bit+4bit complex data into 8bit+8bit complex data in the thread. The data is "fluffed" and temporarily stored in the GPU input data buffer until it is fetched by gpu_thread. Then gpu_thread transfers the data to the graphics processor to perform complex calculations and then writes the results to the output data buffer. The CMAC

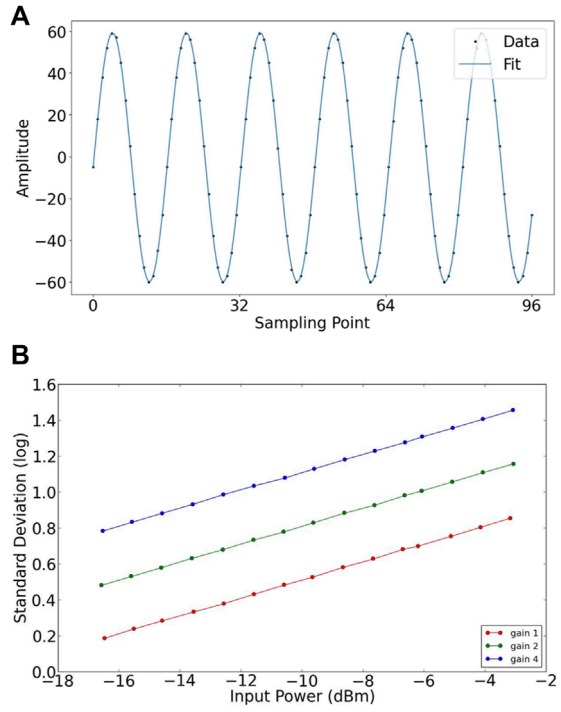

FIGURE 8
(A) The ADC output data points and the fitting curve. **(B)** the logarithm of the standard deviation of the ADC output with gain coefficient 1, 2, and 4 was plotted at different input power levels.

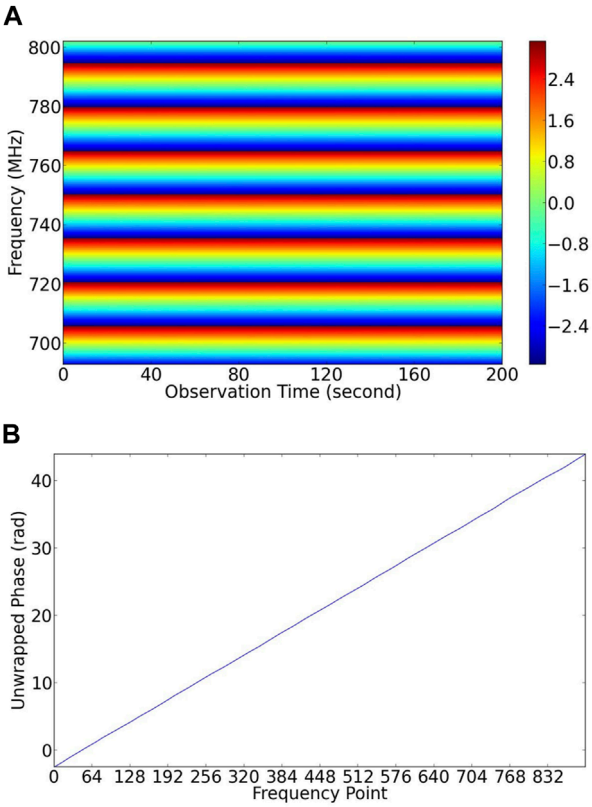

FIGURE 9
Phase correctness check of the correlator by two signals with fixed phase difference. The measured phase is consistent with the length difference of the two cables. **(A)** Phase fringes of the two input signals. **(B)** The relationship between frequency and phase.

process uses the xGPU[7](Clark et al., 2013), which is written in CUDA-C and is optimized on GPU memory resources by specific thread tasks. The cross-correlation algorithm involves computing the cross-power spectrum at a specific frequency observed by a pair of stations, known as a baseline. By processing a sufficient number of baselines, a detailed power spectrum representation can be derived, enabling the generation of an image of the sky through an inverse Fourier transform in the spatial domain. The algorithm's implementation on Nvidia's Fermi architecture sustains high performance by utilizing a software-managed cache, a multi-level tiling strategy, and efficient data streaming over the PCIe bus, showcasing significant advancements over previous GPU implementations. The output thread gets the data from the output data buffer and transmits it to the storage server through the switch. Hashpipe provides a status buffer that extract key-value pairs in each thread. This key value is updated every running cycle. The status can be viewed using a GUI monitor that has been written in both Python and Ruby.

2.4 Data storage

At the beginning of the design, two schemes for data storage were considered. One is that the data is stored on each GPU server, and it is read and combined when used. Due to the large number of GPU servers, this method is too cumbersome. The other is that the data is transmitted from each GPU server to the master computer in real-time, and the data is stored in the master computer. This method is convenient for data use and processing, so the second scheme is adopted.

Each GPU node has 4 hashpipe instances, and the output thread of each hashpipe instance sends data to a dedicated destination port. A total of 28 different UDP ports are used for the 7 GPU servers. The data acquisition script, written in Python, collects data from all 28 UDP ports and combines them. Currently, the integration time is set to approximately 4 s, resulting in a data rate of about 150 Mbps for each network port. The total data rate for all seven servers with 28 ports amounts to approximately 4.2 Gbps. Therefore, a 10 GbE network is capable of handling the data transmission. Finally, the data are saved onto hard drives in the HDF5 format. Additional information such as integration time, observation time, telescope details, and observer information is also automatically saved in the file.

2.5 CNS control module

During the drift scan observation of the Tianlai cylinder array, the system needs to be calibrated by a calibrator noise source (CNS).

7 https://github.com/GPU-correlators/xGPU

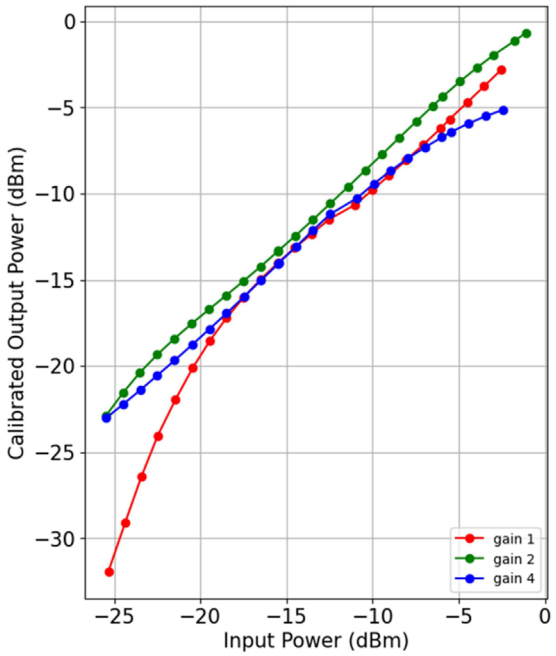

FIGURE 10
Linearity of correlator system. The ADC gain coefficients of 1, 2, and 4 were used for system linearity testing. A gain coefficient of 2 was selected as the daily operational parameter value for the correlator.

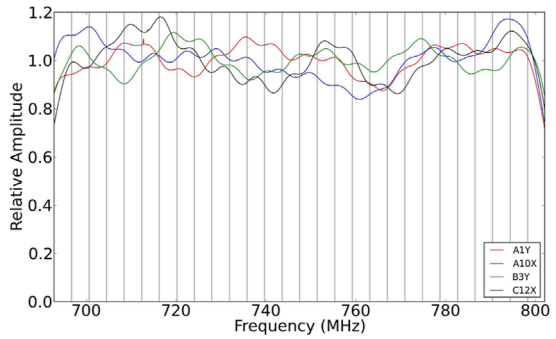

FIGURE 11
Spectral response of feed A1Y, A10X, B3Y, and C12X.

The CNS periodically broadcasts a broadband white noise of stable magnitude from a fixed position, so the system gain can be recovered (Zuo et al., 2021; Zuo et al., 2019). One requirement in the data processing part is to let the CNS's signal fall exactly in one integration time interval, so it needs to be aligned to the integration time. To achieve this, a logical ON/OFF signal from the cylinder correlator is necessary. In order to meet this requirement, we have introduced a noise source control function to the correlator system. This control function is implemented through the noise_source_control block in the F-engine, as shown in Figure 7A.

First, the script enables counter_en block to initialize the module. Second, the hashpipe instance on the GPU node returns the MCNT value of its current packet. The script uses this value to calculate the CNS MCNT value (an MCNT value at a future time, when the MCNT value in the F-engine is equal to this value, the CNS is turned ON) and sets that CNS MCNT to reg31_0 block and reg47_32 block. Third, the CNS on/off period is converted to the change value of MCNT and set period_mcnt block to this value. Fourth, set the GPIO's working time to light block, which is on the ROACH2 board. Finally, the GPIO periodically sends out a logical signal to turn the CNS on or off.

We tested the accuracy of the CNS control module and its actual output result, as shown in Figure 7B. The CNS is activated based on a pre-set MCNT value and is aligned precisely with the integration time interval.

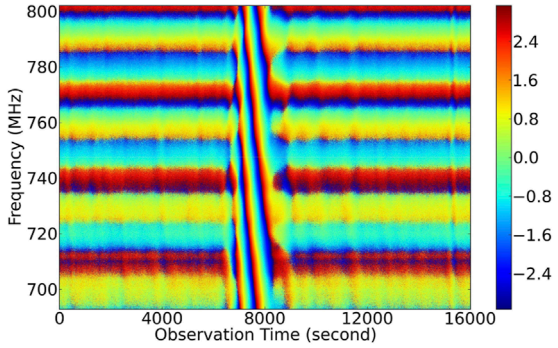

FIGURE 12
Observational phase of Cassiopeia A at around 8000th second.

3 Testing and experimentation

3.1 ADC testing

The importance of ADCs lies in their quality and performance, as these factors bear a direct impact on the overall functionality of the systems they inhabit. To verify the sampling correctness of the ADC, we input a 15.625 MHz sinusoidal wave signal into the ADC and fit the digitized data. The sampling points and fitting result are shown in Figure 8A. The correlator system requires the ADCs to have linearly sampled output at different signal levels. We plot the logarithm of the standard deviation of the ADC output with three different gain coefficients as a function of different input power levels, and the results are shown in Figure 8B. No obvious nonlinearity is found in the testing power range.

3.2 Phase testing

We verify the phase of the visibility (cross-correlation result) by two input signals, whose phase difference is determined by a cable length difference. We use a noise source generator to output the white noise signal and the signal is divided into two ways by a power splitter. Then, the two signals are fed into the ROACH2 board through two radio cables of different lengths. The cable length difference is 15 m. The two signals can be depicted as $S_1 = A_1 e^{i(2\pi f t+\phi_0)}$ and $S_2 = A_2 e^{i(2\pi f(t+\tau)+\phi_0)}$, where A is the wave amplitude,

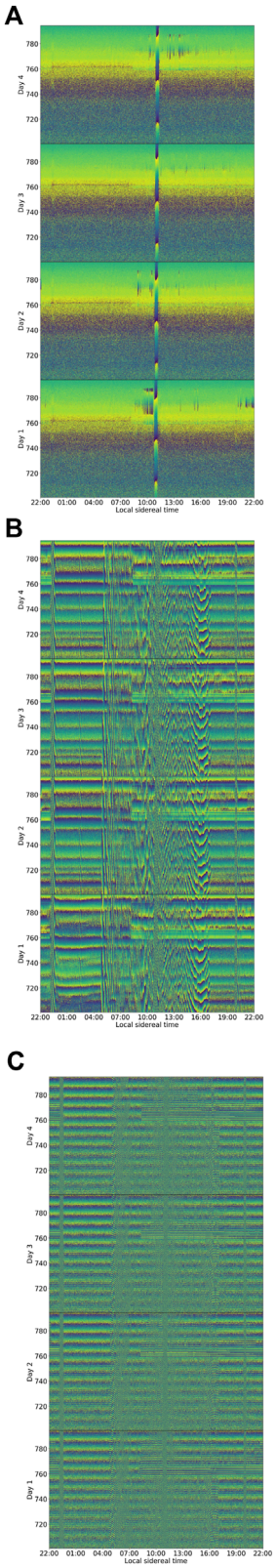

FIGURE 13
Typical phase of raw visibilities as a function of LST and frequency for 4 days starting from Sept. 6th, 2023. **(A)** Baseline A3Y-A15Y; **(B)** Baseline A3Y-B18Y; **(C)** Baseline A3Y-C15Y.

ϕ_0 is an arbitrary initial phase, f is frequency, τ is the delay incurred by the unequal-length RF cables. The visibility of two signals is

$$V =< S_1^* \cdot S_2 >= A_1 A_2 e^{i2\pi f\tau} \tag{2}$$

The cable length difference of the two input signals is fixed, so the delay τ is constant over time. As Eq. 2 shows, the phase $\Phi = 2\pi\tau \cdot f$, Φ is a linear function of frequency, and the slope $k = 2\pi\tau$. The delay $\tau = \Delta l/\tilde{c}$, where Δl is the cable length difference, $\tilde{c}$ is the propagation speed of RF signal in coaxial cable.

The measured waterfall 2D plot of phase of visibility output by our correlator in this experiment is plotted in Figures 9A, 1D plot (at one integration time) of phase as a function of frequency is shown in Figure 9B. By calculating the curve slope in Figure 9B, we obtain a propagation speed in the coaxial cable of about 0.78c (0.78 times speed of light in vacuum), which is consistent with the specification of the RF cable.

3.3 Linearity of correlator system

The linearity of our correlator is verified by comparing the input power levels and the output amplitudes. The results are shown in Figure 10. Considering multiple factors, we have set the ADC gain coefficient for the correlator to 2. We can draw the conclusion that the linear dynamic range of our correlator is between −22 dBm and 0 dBm within the 125 MHz bandpass. In realistic observations, power levels output from the receivers vary 10 dB at most, so the 22 dB dynamic range of our correlator can satisfy our observation requirement.

3.4 Sky observation

The whole frequency band of each feed ranging from 692.8125 to 802.1875 MHz, is divided to 28 sub-bands. These sub-band have been sent to different hashpipe instances for correlation calculation. The final spectra are the combination of these 28 sub-bands. Some spectra of feeds (A10X, A19Y, B27X, and C12X) are plotted in Figure 11. The Tianlai cylinder array is aligned in the N-S direction and consists of three adjacent cylinders. They are designated as A, B and C from east to west, and have 31, 32, and 33 feeds respectively. Each dual linear polarization feed generates two signal outputs. We use "X" to denote the output for the polarization along the N-S direction and "Y" along E-W direction. Spectra of the selected feeds in Figure 11 are from three cylinders, and are smooth in adjacent frequency sub-bands. No obvious inconsistent processing amplitude in different sub-bands are found.

In these spectra, a periodic fluctuation of about 6.8 MHz can be seen. They have been confirmed to result from the standing wave in the 15-m feed cable (Li et al., 2021).

We made 4.4 h (16,000 s) of continuous observation since the night of August 7th, 2023, and the data are shown in Figure 12. The fringe of radio bright source Cassiopeia A occurred around 8000th second.

The continuous operation ability of the correlator is tested, and there is no fault in continuous operation for a month. We plot 4 days' continuous observation data of three baselines as a function of LST (Local sidereal time) and frequency, as shown in Figure 13. The subplots from top to bottom show the baselines for two feeds (a) on the same cylinder, (b) on two adjacent cylinders, and (c) on two non-adjacent cylinders. Each subplot shows the result of four consecutive days starting from September 6th, 2023; each day is a sub-panel from bottom to top.

3.5 Power consumption

All devices are powered by PDU (Power Distribution Unit), and the voltage and current usage of the devices can be monitored through the PDU management interface. The entire correlator system uses a total of 3 PDUs. The six ROACH2 boards and the master computer are connected to one PDU. The first 7 GPU servers and the 10 GbE switch are connected to another PDU. The last 7 servers and the 1 GbE Ethernet switch are connected to the third PDU.

The total power of the F-engine is 220 V × 3.5 A = 770 W, including six ROACH2 boards and one master computer. The total power of X-engine is 220 V × 17.5 A = 3850 W, including seven GPU servers, one 10 GbE switch, and one 1 GbE switch. Therefore, the total power of the whole correlator system is 770 W + 3850 W = 4,620 W for 192 inputs. This is very energy-efficient for such a large-scale interferometer system.

4 Summary

In this paper, the correlator is designed and deployed for the cylinder array with 192 inputs. Based on the basic hybrid structure of the ROACH2-GPU correlator, we have realized the data acquisition and pre-processing function by F-engine, which consists of six ROACH2 boards. The F-engine part is tested, debugged, and analyzed, works in the suitable linear range and the calibrator noise source is controlled in a cadence according to integration time. We conducted hardware testing and data storage design for the X-engine part and realized the complete and orderly data storage of 7 GPU servers. We use a DELL 2020 server, NVIDIA GeForce RTX3080 graphics card, and Rocky 8 system to achieve the X-engine function.

As Tianlai radio interferometric array is currently extending its scale, the correlator we design can increase the number of ROACH2 boards according to the number of input signals, and set the appropriate number of frequency points and the size of data packets. The X-engine part can use higher-level servers and graphics cards to combine multiple tasks and increase the work tasks of a single server to reduce the number of servers. Our future work is to implement it on larger systems.

Data availability statement

The raw data supporting the conclusions of this article will be made available by the authors, without undue reservation.

Author contributions

ZW: Writing–original draft. J-XL: Writing–review and editing. KZ: Software, Writing–original draft. F-QW: Writing–review and editing. Haijun H-JT: Writing–review and editing. C-HN: Writing–review and editing. J-YZ: Writing–review and editing. Z-PC: Writing–review and editing. D-JY: Writing–review and editing. X-LC: Writing–review and editing.

Funding

The author(s) declare that financial support was received for the research, authorship, and/or publication of this article. We acknowledge the support by the National SKA Program of China (Nos 2022SKA0110100, 2022SKA0110101, and 2022SKA0130100), the National Natural Science Foundation of China (Nos 12373033, 12203061, 12273070, 12303004, and 12203069), the CAS Interdisciplinary Innovation Team (JCTD-2019-05), the Foundation of Guizhou Provincial Education Department (KY (2023)059), and CAS Youth Interdisciplinary Team. This work is also supported by the office of the leading Group for Cyberspace Affairs, CAS (No. CAS-WX2023PY-0102) and CAS Project for Young Scientists in Basic Research (YSBR-063).

Conflict of interest

The authors declare that the research was conducted in the absence of any commercial or financial relationships that could be construed as a potential conflict of interest.

Publisher's note

References

Ali, Z. S., Parsons, A. R., Zheng, H., Pober, J. C., Liu, A., Aguirre, J. E., et al. (2015). PAPER-64 constraints on reionization: THE 21 cm power spectrum ATz= 8.4. *ApJ* 809, 61. doi:10.1088/0004-637X/809/1/61

Ansari, R., Campagne, J. E., Colom, P., Le Goff, J. M., Magneville, C., Martin, J. M., et al. (2012). 21 cm observation of large-scale structures at$z$ ∼ 1: instrument sensitivity and foreground subtraction. *A&A* 540, A129. doi:10.1051/0004-6361/201117837

Chen, X. (2011). Radio detection of dark energy—the Tianlai project. *Mech. Astronomica* 41, 1358–1366. doi:10.1360/132011-972

Cianciara, A. J., Anderson, C. J., Chen, X., Chen, Z., Geng, J., Li, J., et al. (2017). Simulation and testing of a linear array of modified four-square feed antennas for the Tianlai cylindrical radio telescope. *J. Astron. Instrum.* 6, 1750003. doi:10.1142/S2251171717500039

Clark, M. A., Plante, P. L., and Greenhill, L. J. (2013). Accelerating radio astronomy cross-correlation with graphics processing units. *Int. J. high Perform. Comput. Appl.* 27, 178–192. doi:10.1177/1094342012444794

Das, S., Anderson, C. J., Ansari, R., et al. (2018). "Society of photo-optical instrumentation engineers (SPIE) conference series," in *Millimeter, submillimeter, and far-infrared detectors and instrumentation for astronomy IX*. Editors J. Zmuidzinas, and J.-R. Gao, 10708. doi:10.1117/12.23130311070836

Hickish, J., Abdurashidova, Z., Ali, Z., et al. (2016). A decade of developing radio-astronomy instrumentation using CASPER open-source Technology. *J. Astronomical Instrum.* 5, 1641001. doi:10.1142/S2251171716410014

Kocz, J., Greenhill, L., Barsdell, B., et al. (2015). Digital signal processing using stream high performance computing. *J. Astronomical Instrum.* 4, 1550003. doi:10.1142/S2251171715500038

Kovetz, E., Breysse, P. C., Lidz, A., et al. (2019). Astrophysics and cosmology with line-intensity mapping. *BAAS* 51, 101. doi:10.48550/arXiv.1903.04496

Kwak, J., Podczerwinski, J., Timbie, P., Ansari, R., Marriner, J., Stebbins, A., et al. (2024). The effects of the local environment on a compact radio interferometer I: cross-coupling in the Tianlai dish pathfinder array. *J. Astron. Instrum.* 13, 2450002. doi:10.1142/S2251171724500028

Li, J., Zuo, S., Wu, F., Wang, Y., Zhang, J., Sun, S., et al. (2020). The Tianlai Cylinder Pathfinder array: system functions and basic performance analysis. *Mech. Astronomy* 63, 129862. doi:10.1007/s11433-020-1594-8

Li, J.-X., Wu, F.-Q., Sun, S.-J., Yu, Z. J., Zuo, S. F., Liu, Y. F., et al. (2021). Reflections and standing waves on the Tianlai cylinder array. *Astronomy Astrophysics* 21, 059. doi:10.1088/1674-4527/21/3/059

Liu, A., and Shaw, J. R. (2020). Data analysis for precision 21 cm cosmology. *PASP* 132, 062001. doi:10.1088/1538-3873/ab5bfd

MacMahon, D. H., Price, D. C., Lebofsky, M., Siemion, A. P. V., Croft, S., DeBoer, D., et al. (2018). The breakthrough listen search for intelligent life: a wideband data recorder system for the robert C. Byrd Green Bank telescope. *Publ. Astron. Soc. Pac.* 130, 044502. doi:10.1088/1538-3873/aa80d2

Niu, C.-H., Wang, Q.-X., MacMahon, D., Wu, F. Q., Chen, X. L., Li, J. X., et al. (2019). The design and implementation of a ROACH2+GPU based correlator on the Tianlai dish array. *Res. Astron. Astrophys.* 19, 102. doi:10.1088/1674-4527/19/7/102

Parsons, A., Backer, D., Siemion, A., Chen, H., Werthimer, D., Droz, P., et al. (2008). A scalable correlator architecture based on modular FPGA hardware, reuseable gateware, and data packetization. *Publ. Astronomical Soc. Pac.* 120, 1207–1221. doi:10.1086/593053

Parsons, A. R., Backer, D. C., Foster, G. S., Wright, M. C. H., Bradley, R. F., Gugliucci, N. E., et al. (2010). THE PRECISION ARRAY FOR PROBING THE EPOCH OF RE-IONIZATION: EIGHT STATION RESULTS. *Astronomical J.* 139, 1468–1480. doi:10.1088/0004-6256/139/4/1468

Pei, X., Li, J., Wang, N., Ergesh, T., Duan, X. F., Ma, J., et al. (2021). Design of a multi-function high-speed digital baseband data acquisition system. *Res. Astron. Astrophys.* 21, 248. doi:10.1088/1674-4527/21/10/248

Perdereau, O., Ansari, R., Stebbins, A., Timbie, P. T., Chen, X., Wu, F., et al. (2022). The Tianlai dish array low-z surveys forecasts. *MNRAS* 517, 4637–4655. doi:10.1093/mnras/stac2832

Prestage, R. M., Constantikes, K. T., Hunter, T. R., King, L., Lacasse, R., Lockman, F., et al. (2009). The Green Bank telescope. *Proc. IEEE* 97, 1382–1390. doi:10.1109/jproc.2009.2015467

Price, D. C. (2021). in *The WSPC handbook of astronomical instrumentation: volume 1: radio astronomical instrumentation* (World Scientific), 159–179.

Price, D. C., MacMahon, D. H., Lebofsky, M., Croft, S., DeBoer, D., Enriquez, J. E., et al. (2018). The Breakthrough Listen search for intelligent life: wide-bandwidth digital instrumentation for the CSIRO Parkes 64-m telescope. *Publ. Astron. Soc. Aust.* 35, e041. doi:10.1017/pasa.2018.36

Sun, S., Li, J., Wu, F., Timbie, P., Ansari, R., Geng, J., et al. (2022). The electromagnetic characteristics of the Tianlai cylindrical pathfinder array. *Astronomy Astrophysics* 22, 065020. doi:10.1088/1674-4527/ac684d

Thompson, A. R., Moran, J. M., and Swenson, G. W. J. (2017). *Interferometry and synthesis in radio astronomy*. 3rd Edition. doi:10.1007/978-3-319-44431-4

Wu, F., Li, J., Zuo, S., Chen, X., Das, S., Marriner, J. P., et al. (2021). The Tianlai dish pathfinder array: design, operation, and performance of a prototype transit radio interferometer. *MNRAS* 506, 3455–3482. doi:10.1093/mnras/stab1802

Wu, F., Wang, Y., Zhang, J., et al. 2014, Site selection for the Tianlai experiment proceedings of the XXXIst URSI general assembly and scientific symposium to be held in Beijing, China (CIE), August 17–23, 2014in 2014 XXXIth URSI General Assembly and Scientific Symposium (URSI GASS). 16-23 August 2014. Beijing, China, 1–4.

Xu, Y., Wang, X., and Chen, X. (2015). FORECASTS ON THE DARK ENERGY AND PRIMORDIAL NON-GAUSSIANITY OBSERVATIONS WITH THE TIANLAI CYLINDER ARRAY. *ApJ* 798, 40. doi:10.1088/0004-637X/798/1/40

Yu, K., Wu, F., Zuo, S., Li, J., Sun, S., Wang, Y., et al. (2023). A simulation of calibration and map-making errors of the Tianlai cylinder pathfinder array. *Astronomy Astrophysics* 23, 105008. doi:10.1088/1674-4527/acf032

Yu, K., Zuo, S., Wu, F., Wang, Y., and Chen, X. (2024). Application of regularization methods in the sky map reconstruction of the Tianlai cylinder pathfinder array. *Res. Astron. Astrophys.* 24, 025002. doi:10.1088/1674-4527/ad1223

Yu, Z., Deng, F., Niu, C., et al. (2022b). *Astronomer's Telegr.* 15758, 1.

Yu, Z., Deng, F., Sun, S., Niu, C., Li, J., Wu, F., et al. (2022a). A fast radio burst backend for the Tianlai dish pathfinder array. *Res. Astron. Astrophys.* 22, 125007. doi:10.1088/1674-4527/ac977c

Yu, Z., Deng, F.-R., Niu, C.-H., et al. (2022c). Detection of a bright FRB with the Tianlai cylinder pathfinder array. *Astronomer's Telegr.* 15342, 1.

Zhang, J., Zuo, S.-F., Ansari, R., Chen, X., Li, Y. C., Wu, F. Q., et al. (2016). Sky reconstruction for the Tianlai cylinder array. *Astronomy Astrophysics* 16, 158. doi:10.1088/1674-4527/16/10/158

Zuo, S., Li, J., Li, Y., Santanu, D., Stebbins, A., Masui, K., et al. (2021). Data processing pipeline for Tianlai experiment. *Astronomy Comput.* 34, 100439. doi:10.1016/j.ascom.2020.100439

Zuo, S., Pen, U.-L., Wu, F., Li, J., Stebbins, A., Wang, Y., et al. (2019). An eigenvector-based method of radio array calibration and its application to the Tianlai cylinder pathfinder. *Astronomical J.* 157, 34. doi:10.3847/1538-3881/aaf4c0

frontiers | Frontiers in Astronomy and Space Sciences

TYPE Original Research
PUBLISHED 09 August 2024
DOI 10.3389/fspas.2024.1411810

OPEN ACCESS

EDITED BY
Shengfeng Yang,
Purdue University Indianapolis, United States

REVIEWED BY
Nan Li,
National Astronomical Observatories, Chinese Academy Of Sciences, China
Wei Du,
Shanghai Normal University, China

*CORRESPONDENCE
Binyang Liu,
binyang_liu@alumni.brown.edu
Ian Dell'Antonio,
ian_dell'antonio@brown.edu

RECEIVED 03 April 2024
ACCEPTED 08 July 2024
PUBLISHED 09 August 2024

CITATION
Liu B, Dell'Antonio I, Chotard N and Clowe D (2024), Measurement and calibration of non-linear shear terms in galaxy cluster fields. *Front. Astron. Space Sci.* 11:1411810. doi: 10.3389/fspas.2024.1411810

Measurement and calibration of non-linear shear terms in galaxy cluster fields

Binyang Liu[1,2]*, Ian Dell'Antonio[1]*, Nicolas Chotard[3] and Douglas Clowe[4]

[1]Department of Physics, Brown University, Providence, RI, United States, [2]Purple Mountain Observatory, Chinese Academy of Sciences, Nanjing, China, [3]CNRS/IN2P3, Villeurbanne, France, [4]Department of Physics and Astronomy, Ohio University, Athens, OH, United States

Introduction: Galaxy cluster lensing is a powerful tool for measuring the mass of galaxy clusters, but accurate shear measurement and calibration are critical to obtaining reliable results. This study focuses on the measurement and calibration of weak lensing shears to improve mass estimates in cluster lensing. To deal with the problem, we first developed an image simulation pipeline, jedisim, which utilizes galaxy images extracted from the Hubble Space Telescope (HST) Ultra Deep Field (UDF) and the Cosmic Assembly Near-infrared Deep Extragalactic Legacy Survey (CANDELS).

Methods: The simulations represent realistic galaxy distributions and morphologies as input sources. The foreground halo with a Navarro–Frenk–White (NFW) profile is constructed such that the lensing signals of background galaxies can be measured by the Vera C. Rubin Observatory's Legacy Survey of Space and Time (LSST) Science Pipelines. By comparing the measured reduced shear g^{meas} and the true reduced shear g^{true}, we observe non-linearity up to $g \lesssim 0.6$. We fit polynomials to the data with quadratic correction adequate to $g \lesssim 0.4$. Meanwhile, we conduct mass estimates using the pzmassfitter code on four different clusters.

Results: The mass estimate results are significantly improved after applying the shear calibration derived from the present work—from $4.954 \pm 0.504 \times 10^{14} M_{\odot}$ to $10.507 \pm 0.498 \times 10^{14} M_{\odot}$ after calibration for a simulated cluster with the mass of $10 \times 10^{14} M_{\odot}$. In multiple cases of validation, the estimated results are all consistent with true cluster mass.

Discussion: This study yields the first relationship between reality and shape measurement of the LSST Science Pipelines and serves as the first step toward the overall goal of mass calibration in cluster lensing. By addressing the challenges in shear measurement and calibration, we aim to enhance the accuracy and reliability of mass estimates in galaxy cluster lensing studies.

KEYWORDS

galaxy clusters, gravitational lensing, image processing, observational cosmology, systematic uncertainties

1 Introduction

Although the ΛCDM cosmological model shows phenomenological success, the nature of its two main components, dark matter and dark energy, is unknown. Therefore, physicists consider understanding these components as the major scientific driver in high-energy experiments and cosmological surveys. As an upcoming cosmological survey, the Vera C. Rubin Observatory Legacy Survey of Space and Time (LSST)[1] will provide an opportunity to understand the nature of dark matter and dark energy through its survey of the southern-hemisphere sky area (LSST Science Collaboration, 2009). Together with other space- and ground-based telescopes (*e.g.*, the Nancy Grace Roman Space Telescope (Spergel et al., 2015) and the Euclid mission (Laureijs et al., 2011)), we will be able to acquire abundant high-resolution observational data in a wide sky area.

In LSST and another stage IV dark energy surveys, gravitational lensing plays a critical role, which describes the phenomenon that light from distant objects is bent by the gravitational field of intermediate-mass before arriving at the observers (Albrecht et al., 2006). Gravitational lensing provides a direct probe to determine the mass distribution in the Universe based solely on the gravitational effects of baryonic matter and dark matter. This probe is impartial and unbiased regarding the details of how the mass interacts (Van Waerbeke and Mellier, 2003).

Galaxy clusters, as the largest virialized structure, are formed in the relatively recent epoch of the cosmological age. Based on the observations and measurements from galaxy clusters, we can study the late-time evolution of the Universe and constrain cosmological parameters if the masses of the clusters are measured accurately. Among the analysis methods, weak gravitational lensing is an important and effective probe to estimate the masses (Joudaki et al., 2009). The most common measurement in weak lensing is the shape distortion (or shear) of galaxies, which describes the lensing effect. Therefore, to estimate the mass with high accuracy, we need to map the shapes of source galaxies to the mass of lenses. Before mapping, it is important to understand and restrict the systematics of shear measurements. To evaluate and improve the impacts of systematic bias, several data challenges, such as the Shear Testing Program (STEP) (Heymans et al., 2006; Massey et al., 2007) and the Gravitational Lensing Accuracy Testing (GREAT) (Bridle et al., 2009; 2010), have been conducted. In these data challenges, shear measurement biases are investigated and discussed in terms of the presence of realistic galaxy morphology, finite galaxy postage stamps, and galaxy types, among other factors, via different measurement methods (Mandelbaum et al., 2015). These data challenges have resulted in estimates for the calibration of shear measurements. These calibrations have been adopted for some recently completed and ongoing surveys (Heymans et al., 2006; Bridle et al., 2010; Mandelbaum et al., 2015). In general, the next-generation surveys are designed to measure the properties of dark energy at an order of magnitude of one percent accuracy, which can be considered the motivation of shear calibration (Bridle et al., 2009).

Taking the Hyper Suprime-Cam Subaru Strategic Program (HSC-SSP)[2] as an example, a set of simulations for shear calibration was analyzed by Mandelbaum et al. (2017), where realistic galaxy morphologies and nearby galaxies were taken into account with an effective source number density of 21.8 arcmin^{-2}. As an upcoming wide-area sky survey, LSST is capable of providing the largest and most uniform cluster sample with shape measurements to date. In the case of cluster weak lensing, the observational data will include weak lensing measurements for ~40 galaxies arcmin^{-2} behind low redshift clusters (LSST Science Collaboration, 2009). Here, we evaluate the performance of the LSST Science Pipelines (LSP)[3] in terms of both shear measurement and follow-up cluster mass reconstruction.

In this paper, we produce image simulations of cluster lensing. Real galaxy postage stamps are generated from Hubble Ultra Deep Field (HUDF) (Beckwith et al., 2006) and CANDELS (Grogin et al., 2011; Koekemoer et al., 2011) data release at the pixel scale of HST. These postage stamps are used to construct the background galaxies. A model foreground cluster is placed at a redshift between the observer and background galaxies. A ray-tracing algorithm is then adopted to apply the shear from the cluster to the background galaxies and simulate the lensed images. This simulation pipeline, known as jedisim[4], is designed to output images under the observational conditions of LSST with the corresponding resolution.

The simulated images are processed and analyzed using the LSST Science Pipelines. Reduced shear is measured using the *shapeHSM* algorithm (Hirata and Seljak, 2003; Mandelbaum et al., 2017), and shear calibration biases can be derived by comparing the measured shear and true shear.

Before jedisim, there were already several well-developed image simulation pipelines for strong lensing effects, such as Pipeline for Images of Cosmological Strong (PICS) lensing, (Li et al., 2016) and SkyLens (Meneghetti et al., 2016; Plazas et al., 2019), as well as for weak lensing, such as GalSim (Rowe et al., 2015). Each of these simulation pipelines has its own advantages and is developed based on the necessary assumptions to optimize computational efficiency on a specific physics topic.

Our approach necessarily differs from the traditional simulation approach for weak lensing or strong lensing because massive galaxy clusters considerably distort galaxies located behind their central regions. Consequently, galaxies are not only more elliptical but also exhibit higher-order distortions (*e.g.*, flexion), causing them to deform into rings or multiple images. One of our primary objectives is to investigate the impact of neglecting these higher-order distortions on cluster mass estimates, necessitating simulations that accurately reproduce the distortions. Because higher-order distortions can result in significant magnification of faint galaxies and noise features, we require that the template galaxies be free from noise. At the same time, we require that the galaxies have sufficient structures so that sub-image magnification can be handled correctly. Therefore, we developed our own image simulation pipeline.

Jedisim aims to simulate both strong and weak lensing effects in observations of a cluster field, where the galaxies retain the

1 https://www.lsst.org

2 http://hsc.mtk.nao.ac.jp

3 http://dm.lsst.org

4 https://github.com/rbliu/jedisim

morphologies and properties of HUDF and CANDELS images. In addition, we apply the observational conditions of LSST to the simulation procedure and process the data with the entire analysis pipeline developed for LSST. Hence, the results are compatible with LSST and enlighten us to understand the output of the data analysis pipeline.

The remainder of this paper is organized as follows: in Section 2, we provide a brief review of the calculations and approximations in weak gravitational lensing, which are the fundamentals of the image simulation. The image simulation pipeline is described in Section 3. The methodology of the analysis pipeline is presented in Section 4. We summarize our results and conclusions in Sections 5, 6, respectively. Finally, we discuss systematics in Section 7 and present our conclusions in Section 8. Throughout this paper, we adopt the ΛCDM cosmology and assume $\Omega_m = 0.315$, $\Omega_\lambda = 0.685$, and $H_0 = 67.8 km\ s^{-1} Mpc^{-1}$ (Collaboration et al., 2020).

2 Gravitational lensing and the NFW profile

In this section, we provide a concise review of the calculations and approximations fundamental to weak gravitational lensing, which form the basis of our image simulation. Understanding these concepts is crucial for accurately modeling the lensing effects observed in galaxy clusters. We will discuss the equations and assumptions involved in weak lensing, highlighting their relevance to our simulation methodology.

2.1 Basic formalism of gravitational lensing

In the weak gravitational field limit, the gravitational lensing effect is described by the lens equation or ray-tracing equation denoted by Eq. 1 (Narayan and Bartelmann, 1996):

$$\boldsymbol{\beta}(\boldsymbol{\theta}) = \boldsymbol{\theta} - \boldsymbol{\alpha}(\boldsymbol{\theta}), \tag{1}$$

where $\boldsymbol{\beta}$ is the true angular position, $\boldsymbol{\theta}$ is the observed angular position, and $\boldsymbol{\alpha}$ is the deflection angle. It is usually assumed that these two-component angles are small enough that the curvilinear nature of this coordinate system can be neglected.

Based on the thin lens approximation, where all the mass is in a single plane P orthogonal to the direction of light and between the source and observer, we can treat space as Euclidean. In addition, because the deflection occurs in a small region compared to the path length, we can approximate the light path as a single deflection. Suppose that the projected mass density distribution on P is given by $\Sigma(\boldsymbol{\xi})$, where $\boldsymbol{\xi}$ is a vector in P.

Often, the mass distribution will not be planar but will be concentrated near the plane P. More precisely, let z be a coordinate parallel to the path of the light. Then, the mass distribution is given by $\rho(\boldsymbol{\xi}, z)$ where $\rho = 0$ for $|z| \geq \varepsilon$, where ε is some distance which is smaller than the distance between the mass and the observer. This holds in almost all astronomical situations. In this case, Σ is given by integrating ρ over the line-of-sight:

$$\Sigma(\boldsymbol{\xi}) \equiv \int_{-\infty}^{\infty} \rho(\boldsymbol{\xi}, z)\, dz, \tag{2}$$

and $M(r)$, the mass enclosed within radius r, can be calculated by $\Sigma(\boldsymbol{\xi})$. In our simulations and observations, the distances involved are large enough that thin plane approximation is reasonable.

The angular diameter distances from the observer to the lens, observer to the source, and lens to the source are given by D_ℓ, D_s, and $D_{\ell s}$, respectively. For a two-dimensional gravitational lensing potential ψ, the deflection angle can be written as $\boldsymbol{\alpha}(\boldsymbol{\theta}) = \nabla\psi$. The dimensionless surface mass density is represented as the *convergence* κ denoted by Eq. 3:

$$\kappa = \frac{1}{2}\left(\psi_{11} + \psi_{22}\right) = \frac{\Sigma}{\Sigma_{crit}}, \tag{3}$$

where $\psi_{ij} = \partial^2\psi / \partial\theta_i \partial\theta_j$, and the critical surface mass density is given by Eq. 4

$$\Sigma_{crit} = \frac{c_s^2}{4\pi G} \frac{D_s}{D_\ell D_{\ell s}}, \tag{4}$$

where c_s is the speed of light.

The *shear* γ represents the tidal gravitational field of the lens and can be written as a complex notion $\gamma = \gamma_1 + i\gamma_2$. These two components can be derived from the second derivatives of the lensing potential shown in Eqs 5, 6:

$$\gamma_1 = \frac{1}{2}\left(\psi_{11} - \psi_{22}\right), \tag{5}$$

$$\gamma_2 = \psi_{12} = \psi_{21}, \tag{6}$$

and the complex reduced shear is introduced as $g = \gamma/(1-\kappa)$. Without a measurement of the intrinsic size or magnification of a galaxy, we are only able to measure g but not γ (Schneider et al., 2000). Considering the weak lensing regime where $\kappa \ll 1$ and $\gamma \ll 1$, the image distortion due to the lensing cluster is usually much smaller than the intrinsic shapes of background sources. The convergence can be recovered by the shear γ of background images through the inverse two-dimensional Laplacian to the potential ψ (Fahlman et al., 1994; Kaiser et al., 1995; Fischer and Tyson, 1997). The distortion of the background image can be calculated by a Jacobian matrix denoted by Eq. 7 (Kaiser and Squires, 1993):

$$\mathbb{A} = (1-\kappa)\begin{pmatrix} 1-g_1 & -g_2 \\ -g_2 & 1+g_1 \end{pmatrix}. \tag{7}$$

Therefore, the distorted shape is a function of reduced shear g rather than κ or γ separately. To describe the shapes of lensed galaxies, measuring their reduced shear along the tangential direction, $g_{\tan}$, is more physically motivated than measuring g_1 and g_2, and $g_{\tan}$ can be computed by the ellipticities of lensed sources (Schneider et al., 2000).

The measured ellipticity of a galaxy can be decomposed into two components: $e_1 = e\cos(2\theta)$ along x and y axes and $e_2 = e\sin(2\theta)$ along $y = \pm x$ directions, where θ is the position angle of the galaxy measured counter-clockwise from the x axis. Furthermore, the shear of a galaxy can be quantified by its E-mode component, *tangential ellipticity*:

$$e_{\tan} = -\left(e_1\cos(2\phi) + e_2\sin(2\phi)\right), \tag{8}$$

where ϕ is the azimuthal angle measured from the lens center and the factors of $\cos(2\phi)$ and $\sin(2\phi)$ project e_1 and e_2 to the tangential

direction, respectively. The weak lensing effect on the background sources produces a curl-free stretching in the tangential direction to the line-of-sight. An image should have no systematic B-mode shear in background galaxies. If we omit the lens plane and assume the absence of intrinsic alignment of the background galaxies, the average tangential ellipticity should equal zero as a statistical result. Therefore, we can use $\langle e_{\tan} \rangle$ as an unbiased measurement of reduced shear. It is feasible to recover the convergence of a foreground galaxy cluster by calculating the non-zero average tangential ellipticity with a given sample of lensed background galaxies (Jarvis et al., 2003).

2.2 NFW profile

The Navarro–Frenk–White (NFW) profile is frequently used in mass distributions, as it is a good approximation to the average profile of clusters in N-body simulations and fits observations well. The profile has several dependent parameters, any two of which are sufficient (Navarro et al., 1996; 1997).

The NFW profile at redshift z is defined as

$$\rho(r) \equiv \frac{\delta_c \rho_c(z)}{(r/r_s)(1+r/r_s)^2}, \tag{9}$$

where δ_c, ρ_c, and r_s are parameters. The dimensionless characteristic density δ_c is given by

$$\delta_c \equiv \frac{200}{3} \frac{c^3}{\ln(1+c) - \frac{c}{1+c}}, \tag{10}$$

where c is the concentration parameter. ρ_c is the critical density for closure of the Universe at redshift z with units of mass density. It is given by Eq. 11

$$\rho_c \equiv \frac{3H^2(z)}{8\pi G}, \tag{11}$$

where $H(z)$ is the Hubble parameter at redshift z. Furthermore, r_s is a scale radius for the profile, with units of length and is given by $r_s \equiv \frac{r_{200}}{c}$, where r_{200} is the radius within which the mean density of the halo is 200 times the critical density ρ_c. The mass enclosed by this radius is given by

$$M_{200} \equiv M(r_{200}) = \frac{800\pi}{3} \rho_c r_{200}^3. \tag{12}$$

The NFW profile is given in three spatial dimensions; however, to use it with the thin lens approximation, we can compress it along the line-of-sight. Let P be some plane through the origin and z be the perpendicular direction through its origin. Let R be the radial distance on the plane from the origin. Then, $\Sigma(R)$, the surface mass density, is given by Eq. 2, except with R instead of $\boldsymbol{\xi}$ because of radial symmetry. To perform the integration, it is necessary to introduce the dimensionless distance variable $x \equiv R/r_s$. This integral is performed by Wright and Brainerd (2000), giving a complex but analytic expression:

$$\Sigma_{\rm NFW}(x) = 2 r_s \delta_c \rho_c \times \begin{cases} \frac{1}{x^2-1}\left(1 - \frac{2}{\sqrt{1-x^2}} \operatorname{arctanh}\sqrt{\frac{1-x}{1+x}}\right) & 0 \le x < 1 \\ \frac{1}{3} & x = 1 \\ \frac{1}{x^2-1}\left(1 - \frac{2}{\sqrt{x^2-1}} \arctan\sqrt{\frac{x-1}{1+x}}\right) & 0 \le x < 1 \end{cases}, \tag{13}$$

where the constant $\frac{1}{3}$ is chosen to ensure continuity at $x = 1$.

M_{200} and c are used to determine the deflection due to this profile since any two parameters are sufficient to describe the profile. Hence, $\Sigma_{\rm NFW}$ is integrated to calculate the enclosed mass. Since $R = r_s x$, the enclosed mass is is derived as Eqs 14, 15

$$\begin{aligned} M_{\rm NFW}(x) &= 2\pi \int_0^x \Sigma_{\rm NFW}(x)\, R\, dR \\ &= 2\pi r_s^2 \int_0^x \Sigma_{\rm NFW}(x')\, x'\, dx' \\ &= 2\pi r_s^2 2 r_s \delta_c \rho_c \int_0^x dx'\, x' \\ &\quad \times \begin{cases} \frac{1}{x'^2-1}\left(1 - \frac{2}{\sqrt{1-x'^2}} \operatorname{arctanh}\sqrt{\frac{1-x'}{1+x'}}\right) & 0 \le x' < 1 \\ \frac{1}{3} & x' = 1 \\ \frac{1}{x'^2-1}\left(1 - \frac{2}{\sqrt{x'^2-1}} \arctan\sqrt{\frac{x'-1}{1+x'}}\right) & x' > 1 \end{cases} \\ &= 4\pi r_s^3 \delta_c \rho_c \mathbb{X}_{NFW} \\ &= \frac{M_{200}}{\ln(c+1) - \frac{c}{c+1}} \mathbb{X}_{NFW}, \end{aligned} \tag{14}$$

where

$$\mathbb{X}_{NFW} = \ln\frac{x}{2} + \begin{cases} \frac{2}{\sqrt{1-x^2}} \operatorname{arctanh}\sqrt{\frac{1-x}{1+x}} & 0 \le x < 1 \\ 1 & x = 1 \\ \frac{2}{\sqrt{x^2-1}} \arctan\sqrt{\frac{x-1}{1+x}} & x > 1 \end{cases}, \tag{15}$$

with the first and third piecewise parts giving the entire expression, except at $x = 1$. Due to the logarithm term, the enclosed mass diverges as $x \to \infty$, albeit quite slowly. Usually, the distribution is truncated to account for this, or $M_{200} = M_{\rm NFW}(c)$ is used to describe the mass of clusters.

3 Simulations

The simulation pipeline, jedisim, was used to generate simulated cluster lensing images for Analysis of Realistic Cluster Lensing through Extensive Training Simulations (ARCLETS[5]). Simulated sheared galaxies and clusters are constructed to test for mass bias due to non-linearities in shear calibration. More details on implementation are included in Supplementary Appendix-1.

Any simulation is only as accurate as the model and parameters used to create it. Systemic biases are inevitably introduced by whatever differences exist between the simulation and actual galaxy clusters, as well as the errors in the galaxy properties of source galaxies. The best way to counteract this and reduce biases is to make the model and its parameters as physically accurate as possible. In practice, this is limited by the computational power available and the precision of the parameters used to calibrate the model. Judicious selection of what approximations and simplifications are used is required to make the model.

5 http://www.het.brown.edu/people/ian/ClustersChallenge

The jedisim pipeline models the effect of a foreground galaxy cluster on the shapes of background galaxies. Broadly, there are three main components of the simulation:

1. Making the field of supersampled background galaxies (Section 3.1);
2. Each galaxy image is then sub-pixel sampled, and the subpixels are separately ray-traced to model the process of distorting the light from the background galaxies in accordance with a specified mass distribution (Section 3.2);
3. The individual distorted galaxies are assembled into an image and then resampled onto an appropriate pixel scale, also accounting for the blurring and distortion due to the point spread function (PSF) and noise (Section 3.3).

The three steps are performed as independently as possible so that the model can be improved in a modular fashion. To enable strong lensing in practice, we have devised an efficient reverse-tracing technique that links the output sub-pixels to the input image, thereby allowing multiple imaging. Galaxies are simulated individually and combined into a single image at a late stage so that redshift-dependent effects can be included.

Furthermore, the simulation is generated across a wide sky area of 1200×1200 arcsec^2, which is large enough that no lensing signal will be artificially removed by the image boundaries but small enough that the coordinates can be treated as flat. In the final step of the simulation, images are created with the observational conditions of LSST (see Section 3.3). To ensure that there are no pixelization effects when generating the galaxy light profiles, the first two steps are carried out at HST UDF resolution. The image is rescaled to LSST resolution in a subsequent step.

3.1 Background inputs

The background galaxy field is simulated one galaxy at a time. To create realistic lensed shapes, individual galaxies in the HDF/UDF and GOODS sky areas of CANDELS are identified by SExtractor. They are extracted and converted to 600×600 pixel^2 postage stamps. The stamps are applied with a mask thresholded at 5σ (per pixel), which is calculated based on the standard deviation in the sampled background sky area. This procedure aims to make sure that each postage stamp is noise-free and that the morphology feature of the galaxy is not artificially altered. In addition, distant sources and bright pixels that do not belong to the target galaxy are also masked out. Hence, each cleaned stamp has one isolated galaxy on a blank background, as shown in Figure 1.

In this paper, we present simulation results only in r-band (552–691 nm) images for LSST. However, the database of jedisim contains postage stamps from HST WFPC2 (Wide Field and Planetary Camera 2) F450W, ACS (Advanced Camera for Surveys) F606W, and ACS F814W bands, which enable the potential of multi-band simulation (we discuss the simulation for the next step in Section 8). All the postage stamps are at an HST resolution of 0.03 arcsec per pixel. The sample repository contains 738 extracted galaxies, which can provide a fairly diverse set of galaxy shapes and orientations. More galaxy samples are planned to be included to increase the diversity in morphology, as discussed in Section 8.

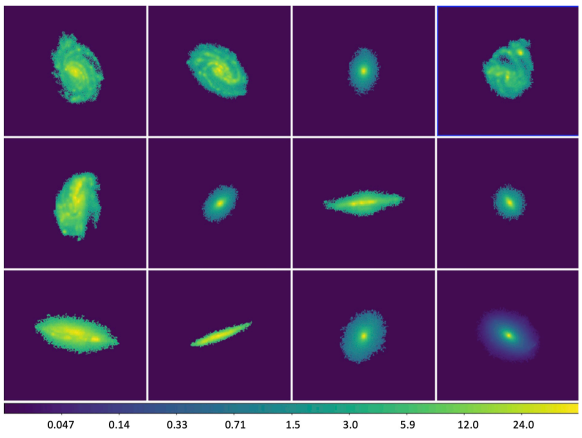

FIGURE 1
Sample 600×600 pixel postage stamps cut out and cleaned from HST UDF with a pixel scale of 0.03 arcsec per pixel.

The simulation aims to generate galaxies at the coadded depth with an r-band magnitude from 22 to 28.5, which is 1 mag deeper than the final coadded survey depth given by the LSST Science Book (LSST Science Collaboration, 2009). We calculate the AB magnitude for each galaxy postage stamp and convert them to magnitudes in LSST bands. When the sky is observed, a significant number of galaxies of high magnitude will be relatively faint. The noise level will then render them indistinguishable from the background. Because we generate simulations for both LSST 1-year and 10-year survey depths, they have different corresponding noise levels (see Section 3.3). So, we include the faint galaxies with a magnitude up to 28.5 to make sure the simulated sky has more realistic features. Based on the LSST Science Book (LSST Science Collaboration, 2009), ~40 galaxies per arcmin^2 behind the clusters are expected to be observed and measured. With this approximation of galaxy number density, ~6000 sources should be measured within a ~150 arcmin^2 simulation output, which is in good accordance with the results, as discussed in Section 6.

By using real galaxies as the materials of simulation, we retain the most morphological details in the galaxies. We have a finite dataset of the galaxy postage stamps with a sufficiently high signal-to-noise ratio from the HST field. Hence, it is necessary to increase the variety of samples in the simulation. Based on the originally extracted galaxy postage stamps, we create varied galaxies with realistic features. Each simulated galaxy is specified by six parameters detailed below:

- **Magnitude:** The magnitude of each galaxy is selected in the range of $22 \leq M \leq 28.5$ with the distribution given by the power law denoted by Eq. 16:

$$P(M + dM) \propto 10^{BM}, \tag{16}$$

where M is the r-band magnitude and $B = 0.33 \ln 10$ is an empirical constant (Benitez et al., 2004).

- **Half-light radius:** For each galaxy, the effective radius or half-light radius, r_{50}, is selected from the database of galaxy radii

described by Kubo and Dell'Antonio (2008). This database is generated based on the galaxy magnitude-size distribution from HST UDF (Coe et al., 2006). Specifically, for statistical convenience, the database is binned by the integer part of the magnitude, and a list of radii is generated for each magnitude (the database is included in the source code of jedisim). Since each postage stamp is already assigned a magnitude, it has a corresponding bin, and an r_{50} radius is chosen randomly from that bin. Then, the galaxy postage stamp is scaled to the new size using an interpolation routine.

- **Image:** A postage stamp image is chosen at random from those postage stamps whose r_{50} value is larger than r_{50} assigned to the galaxy. Hence, the images are always sized down to avoid interpolation errors.
- **Redshift:** The database of galaxy redshift from the zCOSMOS redshift survey is used and binned by magnitude (Iovino et al., 2010). For each galaxy, a redshift is selected from the corresponding magnitude bin. Alternatively, a single redshift (*i.e.*, $z = 1.5$) can be chosen for all galaxies. This parameter can be controlled in the configuration file of jedisim. When $z = 1.5$ is selected for the source galaxies, their luminosities and pixels are rescaled according to their intrinsic redshifts.
- **Position:** The center of the postage stamp is selected as a pair of uniformly distributed floating points (for x and y positions in pixel). The range of position is restricted to ensure that the entire galaxy postage stamp lies completely within the simulated image.
- **Orientation:** Each galaxy is randomly oriented by choosing an angle uniformly from the range $[0, 2\pi)$. The orientation of galaxies has at least three degrees of freedom, but since we are dealing with two-dimensional projections of galaxies, we can only make the orientation random in one degree of freedom, with some additional variability coming from the diverse orientations of the postage stamps.

Once these parameters are chosen for each galaxy, an image is made that satisfies those parameters. The postage stamp is rotated at the assigned angle, scaled down to the correct r_{50} radius (using bilinear interpolation), and its flux is adjusted to the correct magnitude. The galaxy is then appropriately cropped so that the image consists of the smallest rectangle that contains all non-zero pixels of the galaxy. Each transformed postage stamp galaxy is saved as a FITS image, along with the six parameters that characterize it.

Therefore, we have all the information on the background simulation image: a catalog of galaxies whose sizes, magnitudes, orientations, positions, and (optionally) redshifts are distributed in accordance with observations.

3.2 Lensing model

The next step in the simulation is to emulate the effects of gravitational lensing caused by a galaxy cluster. As mentioned in Section 2.1, the lens equation can be written as Eq. 17

$$\boldsymbol{\beta}(\boldsymbol{\theta}) = \boldsymbol{\theta} - \boldsymbol{\alpha}(\boldsymbol{\theta}) = \boldsymbol{\theta} - \frac{D_{\ell s}}{D_s}\widehat{\boldsymbol{\alpha}}(\boldsymbol{\theta}), \tag{17}$$

where the deflection term $\widehat{\boldsymbol{\alpha}}$ is a vector quantity in a radially symmetric mass distribution as in Eq. 18.

$$\widehat{\boldsymbol{\alpha}}(\boldsymbol{\theta}) = \alpha(r)\hat{\boldsymbol{r}}, \tag{18}$$

where $\alpha(r)$ is the radial deflection which depends on the mass distribution, r is the distance from the center of the mass distribution to $\boldsymbol{\theta}$, and $\hat{\boldsymbol{r}}$ is the unit vector from the center of the mass distribution to $\boldsymbol{\theta}$. Both r and $\alpha(r)$ have units of pixels.

We implement the density distribution profile as a separate module in the code, which enables jedisim to simulate different types of galaxy clusters. In this work, we use the NFW profile (Navarro et al., 1996; 1997) to generate the images, as it provides a well-established model for the mass distribution of galaxy clusters. Additionally, the specific cluster field we are studying is not significantly affected by the potential issues associated with the central density divergence of the NFW profile.

For an NFW profile cluster, given Eqs 9, 10, 12, its virial mass can be written in terms of the concentration $c$shown in Eq. 19:

$$M_{200} = 4\pi\rho_c\delta_c r_s^3\left[\ln(1+c) - \frac{c}{1+c}\right]. \tag{19}$$

Then, the density is expressed as $\rho(r; M_{200}, c)$. The deflection in pixels by the NFW profile is given by Eq. 20

$$\frac{\alpha(r; M_{200}, c)}{r} = \frac{4GM_{200}\delta_c'}{9\times 10^5 D_\ell\, r}\times \mathbb{X}_{NFW}, \tag{20}$$

where r is the radius in pixels, D_ℓ is the angular diameter distance of the cluster for a given cosmology, and δ_c' is a modification of the density parameter, which is given by Eq. 21

$$\delta_c' = \frac{1}{\ln(1+c) - \frac{c}{1+c}}, \tag{21}$$

and x, as defined in Eq. 13, is calculated by Eq. 22

$$x = \frac{ScD_\ell}{10.0}\left(\frac{G}{H_0^2}\right)^{-1/3} r, \tag{22}$$

where H_0 is the Hubble constant at the present time and S is the conversion factor between pixels and radians given by Eq. 23

$$S = \frac{\pi}{180\,(\text{degree})}\,\frac{3600\,(\text{arcsec/degree})}{\text{resolution}\,(\text{arcsec/pixel})}. \tag{23}$$

An arbitrary number of lenses can be present simultaneously, whose center positions, redshifts, and profile parameters are all specified by a configuration file. In this work, we use a single symmetric lens to produce simulations. In the future, however, we plan to enable the potential probability to simulate substructures of clusters or the light cone of multiple lensing planes. The lenses can be distributed at any redshift, as described in the configuration file. To simplify the mass reconstruction process at this first stage, all lenses share the same redshift in the current simulation. The deflection then becomes the superposition of the deflections from each of the lenses: if there are N lenses with deflection functions α_i for $i = 1, \ldots, N$, then the deflection term becomes Eq. 24

$$\widehat{\boldsymbol{\alpha}}(\boldsymbol{\theta}) = \sum_{i=1}^{N}\alpha_i(r_i)\hat{\boldsymbol{r}}_i, \tag{24}$$

where r_i is the distance from the center of the i^{th} mass distribution to $\boldsymbol{\theta}$ and $\hat{\boldsymbol{r}}_i$ is the corresponding unit vector.

The lensed image is calculated by applying Equation (17) to the subsampled background image produced in Section 3.1. This is done as follows. For now, assume that all background galaxies

lie at a single redshift. Then, we can consider the Universe as consisting of three parallel planes: the source plane, where the background galaxies lie; the lens plane, where the mass distribution lies; and the observation plane, which is near Earth but above the atmosphere.

Any light traveling from the source plane to the observation plane will pass through the lens plane and be deflected, forming a distorted image of the source plane on the observation plane. A straightforward way to determine what this distorted image will be is to trace the path of individual photons from the source image to the observation image. Unfortunately, this is non-deterministic because of the phenomenon of multiple images and is thus extremely inefficient. However, it is possible to go backward. Concretely, let I and J be the scalar-valued intensity function on the source and observation planes, respectively, and let $\hat{\boldsymbol{\alpha}}$ be the vector-valued deflection function on the lens plane. Then, with $\boldsymbol{\theta} = (x, y)$,

$$J(x,y) = I(\boldsymbol{\beta}(x,y)) = I\left((x,y) - \frac{D_{ls}}{D_s}\hat{\boldsymbol{\alpha}}(x,y)\right). \tag{25}$$

This Eq. 25 contains the assumption from above that all background objects have a single redshift. In a more realistic case where there are background galaxies at multiple redshifts, there is a separate source plane for each redshift, and a corresponding observation plane can be calculated for each one. Hence, the total observation intensity is the sum of all these planes.

3.3 PSF and noise

To emulate the actual atmospheric and telescopic effects in observation, we make a non-varying point spread function using PhoSim[6] with a δ-function input (Peterson et al., 2015). The distorted, denoised galaxy postage stamps are assembled into the final sky area and then convolved with this PSF kernel.

By modifying the parameters of PhoSim, the PSF kernel is generated at the HST resolution with the observational conditions of LSST. The resulting PSF is normalized to a total intensity of unity, as illustrated in Figure 2.

To ensure that the final simulation image at the LSST resolution has a smooth and realistic PSF, the PSF image we generate at the HST resolution has a size of 1024×1024 pixels, so it is computationally impractical to convolve straight from the double-sum two-dimensional discrete convolution. At a small loss of precision, it is more efficient to utilize the convolution theorem. A strip with a width of 1024 pixels is added to each image so that no information is lost. Using the FFTW3 library, each image is Fourier transformed, multiplied with the transform of the PSF, and transformed back. The image is then trimmed by 1024 pixels to recover the original dimension. Because this image is still at HST resolution (0.03 arcsec per pixel), it is resampled to the LSST resolution of 0.2 arcsec per pixel by block averaging.

6 https://www.lsst.org/scientists/simulations/phosim

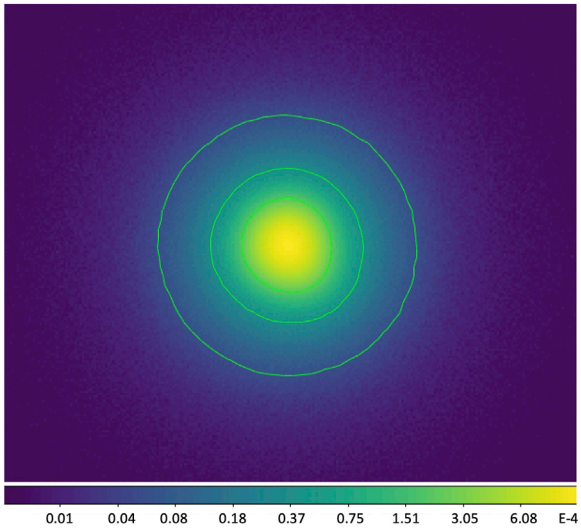

FIGURE 2
Normalized PSF convolution kernel at the HST resolution, generated by PhoSim and displayed in the log-scale.

In this process of generating PSF, the size of seeing is set at 0.7 arcsec based on the observational condition of LSST (LSST Science Collaboration, 2009). The PSF ellipticity is $e_1 = -0.0020$ and $e_2 = -0.0050$ (measured by SExtractor). In a later step, we simulate stars based on this PSF kernel.

In addition, we add Poisson noise to each pixel. To acquire an empirical estimate of the noise level, we measure the variance of background noise from random samples of the sky area in the Dark Energy Camera (DECam) r-band images of Abell 3128 with 1-year depth (McCleary et al., 2015). By calculating the average value, we use this variance λ as the parameter in our simulation images with 1-year depth and downscale the parameter for images with 10-year depth accordingly. The size of the sampled sky area is varied according to the local distribution of detectable objects to make sure that no distinguishable galaxy or star is included and is not significantly contaminated by undetected objects.

For validation, the simulations have an average number density of ~39.8 arcmin^{-2} for detectable background sources in 10-year coadded depth as measured by the LSST Science Pipelines, which is consistent with our expected value for LSST. More measurement parameters are described in Section 4.3.

3.4 Cluster simulations

On the basis of NFW-profile galaxy clusters, as discussed in Section 3.2, we generate four groups of cluster simulations with a size of 12.2×12.2 arcmin^2 (24576×24576 pixels at the HST resolution). The foreground cluster in each group has a virial mass of $5, 10, 15, 20 \times 10^{14} M_{\odot}$, respectively. The concentration of all clusters is set to 4.0.

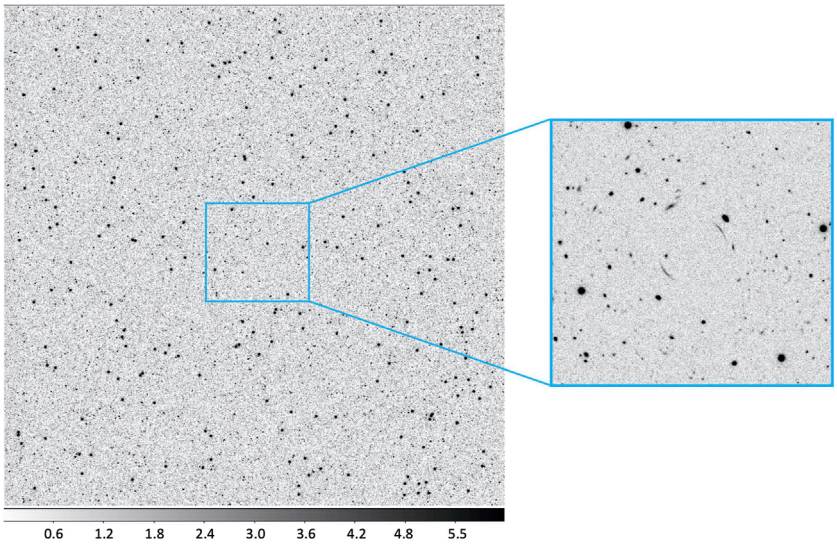

FIGURE 3
One cluster simulation with $M_{200} = 20 \times 10^{14} M_{\odot}$ in 10-year depth. *Left*: the full $12.2' \times 12.2'$ field of view of the cluster ($z = 0.3$) and background galaxies ($z = 1.5$) at an LSST resolution ($0.2''$/pixel). *Right*: zoomed-in view of the central $2.3' \times 2.3'$ area, which shows strong lensing arcs. The image is displayed in the z-scale.

The clusters are placed at $z = 0.3$ with only dark matter halo such that no extra bias is introduced due to foreground–background blending. The background galaxies are sampled from our HST ACS F606W postage stamp database. The background source plane is set at $z = 1.5$ with 30,000 galaxies as raw input, whose r-band magnitudes range from 22 to 28. The galaxy number count is extrapolated from ACS observations by Benitez et al. (2004), where 799,663 galaxies per square degree are detected in the F606W filter with a magnitude up to 27.29.

After lensing, the output is down-scaled from HST resolution to LSST resolution by interpolation. All images are convolved with the LSST PSF kernel and have background noise added, as introduced in Section 3.3. For each simulation, images for both 1-year and 10-year survey depths are generated. An example is shown in Figure 3 with cluster virial mass $M_{200} = 20 \times 10^{14} M_{\odot}$.

To diminish the intrinsic shape bias of the background galaxy sample and increase computational efficiency, we generate variant simulations where each selected background galaxy is rotated by 90° before lensing and assemble a separate simulated image with other parameters unchanged.

3.5 Grid simulations

The cluster simulations described in Section 3.4 are capable of simulating lensing distortion from weak to strong lensing regimes. However, similar to realistic cluster fields, there are blendings between background galaxies in these simulations. Hence, we also generate simulated images in a grid layout in addition to the cluster simulations to study the mapping between measured tangential ellipticity and true reduced shear.

In the grid-layout simulations, every single galaxy is assigned a known true reduced shear $g^{\rm true}$. To achieve this, each background galaxy is generated via the same ray-tracing simulation pipeline, as introduced in Section 3.4. Then, postage stamps of the lensed galaxies are cut out and assembled into a grid layout. The range of $g^{\rm true}$ is designed from 0.02 to 0.60, which covers from weak lensing to strong lensing regime. After lensing, the distorted galaxies are rescaled to the LSST resolution and arranged in a grid layout with the size of 1900×1900 pixels. Similarly, the images are convolved with the LSST PSF kernel. For a higher signal-to-noise ratio in detection, we only add sky noise at the level of the 10-year survey depth. An example is illustrated in Figure 4.

As discussed in Section 3.4, a parallel set of grid simulations is produced with each galaxy postage stamp rotated by 90° before lensing to suppress intrinsic shape noise. Furthermore, to reduce bias in the intrinsic orientation of the galaxy sample, postage stamps are placed at different azimuthal angles (*i.e.*, 0°, 60°, 120°, 180°, 240°, and 300°) with respect to the cluster center. A total of 410 grid simulations in the F606W band are generated, including 60 sets of simulations per azimuthal angle plus 50 sets for null tests. Each simulated image contains 300 to 1,000 individual galaxies, depending on their actual sizes and separations. To make it possible to be processed by the analysis pipeline, normalized PSF stars are added in the gaps between separate galaxies, such that they can be detected and measured by the LSST Science Pipelines. We will demonstrate in the next section how to measure the calibration biases from the simulations.

4 Methods of analysis

To analyze the simulations, we process the images using the LSST Science Pipelines with appropriate configurations. By processing the images through LSP, we obtain shape measurement outputs, which

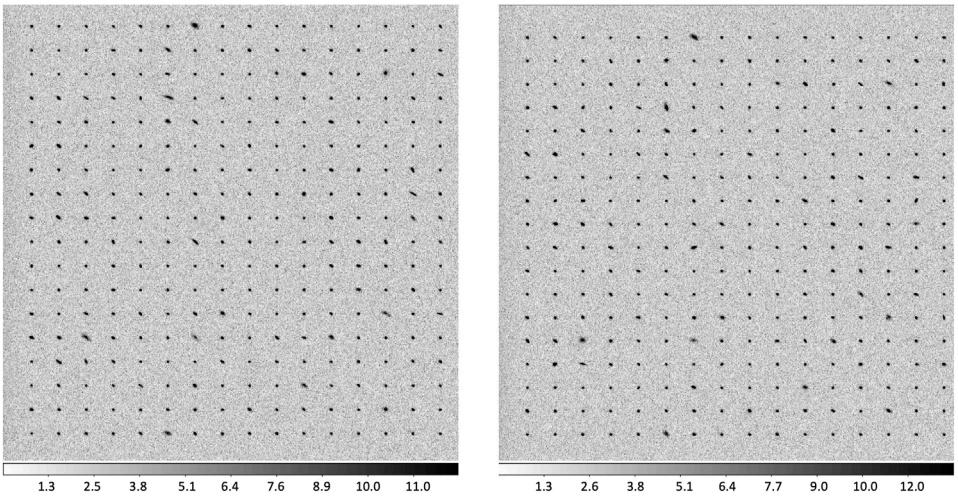

FIGURE 4
Grid simulation generated with $g = 0.4$ in 10-year depth. *Left*: the full $1,900 \times 1900$ pixel image at an LSST resolution ($0.2''$/pixel). *Right*: the corresponding parallel image with each galaxy rotated by 90° before lensing. In both images, the individual galaxies are placed at an azimuthal angle of 60° relative to the cluster center. Because the given reduced shear is relatively strong, it is noticeable that the lensed galaxies share the same trend of distortion. Images are displayed in the z-scale.

enable us to conduct a series of analyses. These analyses allow us to estimate the reduced shear and derive the mass of the galaxy clusters.

4.1 LSST Science Pipelines

The LSST Science Pipelines are developed to satisfy the rapid cadence and scale of the LSST observing program for image and data processing. A prototype of the LSST Science Pipelines is also used as the fundamental codebase of the HSC Pipeline to reduce HSC Subaru Strategic Program (SSP) data. Details about the software architecture, algorithms, and processing tasks are described by Jurić et al. (2015) and Bosch et al. (2017).

In the analysis of our simulations, we use an LSP installation of the v17.0 release, together with the obs_file[7] package as an interface to ingest and process the simulation images. The obs_file package was developed explicitly for the work presented in this paper. Because we have perfect knowledge of the PSF kernel and background noise, several tasks in the LSST Science Pipelines can be simplified. Specifically, the CCD processing step consists of instrumental signal removal (ISR), source detection, PSF measurement, aperture correction, deblending, and source measurement.

In the context of the LSST Science Pipelines, a sky area with all pixels above the detection threshold is defined as a footprint. One footprint can include one or multiple peaks. Although foreground–background blending situations are eliminated in our cluster simulations, blending instances between background galaxies still occur. In this case, a footprint with multiple peaks is considered a "parent" source, while the deblended sources and single-peak footprints are "children" sources.

The images are generated to simulate the coadded exposures in 1-year and 10-year depths, so they do not require joint calibration through the pipeline. Therefore, the tasks invoked in this pipeline are equivalent to single-frame processing subtasks, followed by coaddition detection and measurement. In the simulation images, each FITS file only includes the image extension but not the mask or variance extensions. Hence, the primary parameter as an input is the estimated background noise given in analog-to-digital unit (ADU), which is an estimate of the background field required by ISR such that some isolated noise pixels are not detected as cosmic rays. According to the original average noise used to generate the simulations and the measured background variance in the simulated images, we set this input sky noise level as `isr.noise` = 5.0 for 10-year depth and `isr.noise` = 15.0 for 1-year depth. Since these noise values are used as initial estimates that the pipeline can update afterward, there is a slight tolerance in them, but the estimates still should be made reasonably. Theoretically, there is no cosmic ray added when generating the simulated images. As a result, the pipeline identifies 0 cosmic rays in CCD processing as expected.

4.2 Astrometry and PSF modeling

The simulations are originally produced with no World Coordinate System (WCS) coordinates because, with the obs_file package, images are processed and measured at pixel level without R.A./Dec. information. Accordingly, the measured x/y positions and second-order moments are in pixel coordinates.

However, in the later steps of mass estimation, the pipeline requires WCS information in R.A. and Dec. Given the relatively small dimensions of the simulated images, we add flat WCS coordinates to the image headers with a pixel scale of $0.2''$.

7 https://github.com/SimonKrughoff/obs_file

In addition, the LSST Science Pipelines require a PSF model for shape measurement. We add 200 PSF stars randomly into the $12.2' \times 12.2'$ field of view of cluster simulations. The stars are generated, as described in Section 3.3. For the PSF measurement, a maximum-likelihood detection algorithm is adopted with a 50σ threshold and $1''$ full width at half maximum (FWHM) Gaussian as the smoothing filter (Bosch et al., 2017). Two iterations of the PSF star selector are implemented with updated median background values to determine the sources used as PSF. Consequently, only enough bright stars are selected for PSF modeling and fed into PSFEx based on analysis of the measured sizes (Bertin, 2013). To confirm the accuracy of the PSF measurement, we compare the positions and the size of the detected PSF stars with their ground truth inputs.

4.3 Image processing

Once the data are ingested appropriately, each CCD is processed independently, producing a calibrated image and its corresponding source catalog. A long series of semi-iterative subtasks are included in this task. To process the simulations, we invoke ISR, source detection, aperture correction, background subtraction, deblending, and source measurement. Due to a relatively simple instrument signature, no brighter-fatter or crosstalk corrections are employed in ISR. A 5σ threshold is applied for detected positive sources, which are recorded as footprints.

The deblender algorithm is applied if a footprint contains more than one peak. The flux of the footprint is apportioned such that one "child" image is created for each peak as a distinct source. Both "parent" and "children" sources are measured and stored: each "parent" together with its "children" sources is assigned a unique parent ID, while the number of "children" sources in each deblended "parent" source is recorded as deblend_nChild. Some important parameters and features of the LSST Science Pipelines are listed in Table 1.

The primary data outputs of CCD processing are calexp (calibrated exposures) and src (source catalogs). The calexp files are the output FITS images with multi-extensions after CCD processing. They contain calibration and correction information, as well as objects for PSF modeling. The src files are in the format of the FITS table, where each source is stored as one entry. The columns in the catalogs represent characterizations and measurements of the objects. The catalogs also contain an array of flags, in which a flag of calib_psfCandidate indicates whether the source is selected as a PSF candidate. To obtain a clean catalog that has only distinct galaxy sources, we apply a filter with criteria `deblend_nChild` = 0 and `calib_psfCandidate` = `False` on the src catalogs.

TABLE 1 Parameters in process CCD.

Parameter	Value
charImage.doApCorr	True
charImage.doMeasurePsf	True
charImage.detection.thresholdType	Standard deviation
charImage.detection.thresholdValue	5.0
charImage.detection.includeThresholdMultiplier	10.0
charImage.detection.thresholdPolarity	Positive
charImage.deblend.edgeHandling	Ramp
charImage.deblend.maxFootprintArea	1,000,000
charImage.deblend.strayFluxRule	Trim
starSelector ['objectSize'].widthStdAllowed	0.15
starSelector ['objectSize'].kernelSize	21
starSelector ['objectSize'].fluxMin	12,500.0
psfDeterminer.name	pca
psfDeterminer ['pca'].kernelSizeMax	45
psfDeterminer ['pca'].kernelSizeMin	25
psfDeterminer ['pca'].nIterForPsf	3

4.4 Shape measurements

This version of the LSST Science Pipelines employs the *shapeHSM* algorithm (HsmMoments) to measure the adaptive Gaussian moments, where the Gaussian elliptical weight functions are iteratively calculated and matched to the measured moments (Bosch et al., 2017). The adaptive moments $\mathbb{M}$ are calculated with the least-squares deviation from the image pixels. Hence, the ellipticity tensor $(e_+, e_\times)$ can be determined by the second moments as shown in Eqs 26–28.

$$e_+ = \frac{M_{xx} - M_{yy}}{T}, \tag{26}$$

$$e_\times = \frac{2M_{xy}}{T}, \tag{27}$$

where T is the trace,

$$T = \left(M_{xx} + M_{yy}\right), \tag{28}$$

and ellipticity e used in this paper is the same as χ in Schneider (2006).

The HsmMoments output is implemented from the HSM measurement in GalSim (Rowe et al., 2015). In this algorithm, the PSF-corrected ellipticities are estimated in addition to adaptive moments so that the PSF-corrected shears can be calculated as output. Explicitly, `ext_shapeHSM_HsmShapeRegauss_e1` and `ext_shapeHSM_HsmShapeRegauss_e2` are the results using the re-Gaussianization method, as described in Hirata and Seljak (2003).

The HSM measurement has the following advantages:

- Robustness and validation: The HSM measurement has been rigorously tested and validated across various datasets and surveys (Miller et al., 2013; Mandelbaum et al., 2018). Its performance and reliability are well-documented, making it a dependable choice for shear measurement in our study.

- Simplicity and efficiency: Compared to forward modeling and machine learning methods, re-Gaussianization is computationally less intensive and easier to implement, allowing for efficient processing of large datasets.
- Baseline comparability: Using a well-established method like HSM measurement provides a baseline for comparison with other studies in the field, facilitating the validation and interpretation of our results within the broader context of weak lensing research.

We realize and consider other shape measurement methods. Forward modeling techniques involve generating model images of galaxies and fitting these models to the observed data to extract shear estimates. This method is advantageous as it allows for the direct incorporation of complex PSF models and galaxy morphologies, potentially leading to more accurate shear measurements (Bernstein and Jarvis, 2002a; Miller et al., 2007; Voigt and Bridle, 2010). Machine learning approaches, such as convolutional neural networks (CNNs), have been increasingly explored for shear measurement. These methods can learn complex, non-linear relationships between observed galaxy images and shear, potentially outperforming traditional methods, especially in cases with significant noise and PSF distortions (Ribli et al., 2019; Tewes et al., 2019; Zhang et al., 2024). MetaCalibration is a recent method that calibrates shear measurements by applying artificial shear to the galaxy images and measuring the response. This technique corrects for multiplicative bias without requiring simulations, making it highly efficient and accurate for shear calibration (Huff and Mandelbaum, 2017; Sheldon and Huff, 2017; Sheldon et al., 2023).

Although we chose HSM measurement for the reasons mentioned above, we recognize the potential advantages of other methodologies. In future work, we plan to explore these advanced methods to assess their performance and potential benefits for shear measurement in galaxy cluster studies. Incorporating these techniques could provide additional insights and improve the accuracy and robustness of our shear calibration.

4.5 Mass estimate

Based on the shear measurements, we also utilize the LSST Science Pipelines src catalogs obtained from the cluster simulations to reconstruct and estimate the cluster mass. This is accomplished using the `pzmassfitter` code[8] specifically developed to perform the various stages of individual cluster mass reconstruction, starting with the LSST Science Pipelines outputs. This code includes magnitude correction from Galactic extinction, estimation of the photometric redshifts (photo-z), and corresponding probability density function $P(z)$ of each galaxy, background galaxy selection, and finally, mass map and cluster mass reconstruction. Given that this work involves simulations where all galaxies are background galaxies located at known redshifts, most of these steps are bypassed. A detailed description of software will be given elsewhere, but for the purpose of this work, it is only relevant to mention the following:

- For the cluster simulations, we plot the convergence map as a quality and validation test. It could also be useful to study the bias in the shear estimate due to the presence of detailed substructures.
- The mass estimate relies on the pzmassfitter code developed for the Weighing the Giants project (e.g., Applegate et al., 2014). The algorithm is based on a Bayesian statistical model using a likelihood function built from individual galaxy shapes (output by the LSST Science Pipelines), a photometric redshift $P(z)$, and a shear scatter parameterized by a Voigt profile (refer to Applegate et al., 2014 for a detailed description). The posterior distributions of the model parameters (cluster mass, concentration, and shear scatter parameters) are sampled using a Markov Chain Monte Carlo (MCMC) algorithm.
- This method has been demonstrated to accurately recover the mass of the cluster sample given good photo-z posterior probability distributions, as shown by Applegate et al. (2014). In our simulations, the redshift information is already known. Therefore, the pzmassfitter code can provide excellent performance on cluster mass estimation.

The `pzmassfitter` code requires WCS information inherited from the original image to process the datasets. To simplify this process, we add flat WCS coordinates in the headers with the LSST pixel scale, as described in Section 4.2.

5 Grid simulation results

The grid-layout simulations yield shear calibration measurements across weak to moderately strong lensing regimes, free from systematics such as deblending. We utilize these simulations to establish the relationship between the measured and true reduced shear of field galaxies.

5.1 Shape measurements in grid simulations

Throughout one grid simulation, all the galaxies share the same reduced shear g, which is a known value. When generated, the projected distance (*i.e.*, `grid_radius`) and azimuthal angle (*i.e.*, `grid_angle`) between the background galaxy and cluster center are already determined. Hence, it is straightforward to calculate the tangential ellipticity $e_{\tan}$ from the measured (e_1, e_2), similar to the case in cluster simulations. Again, to eliminate some irregular measurements, we apply a filter of $|$`ext_shapeHSM_HsmShapeRegauss_e1`$| < 1.5$ and $|$`ext_shapeHSM_HsmShapeRegauss_e2`$| < 1.5$.

Analogously, PSF stars are required for CCD processing in grid simulations. Given the size of each single simulation (1900×1900 pixels), we add 50 PSF stars on the background and avoid any blending with galaxies such that no extra measurement bias is introduced by the deblender.

To diminish statistical uncertainties, multiple simulations with the same reduced shear are measured and combined at the catalog level. In addition, each galaxy is rotated by 90° to form a

8 https://github.com/nicolaschotard/Clusters

parallel simulation such that the intrinsic shape uncertainty can be reduced (Massey et al., 2007).

For each set of the grid simulations generated with the same g, we plot the measured reduced shear against the corresponding true reduced shear and analyze the trend as shear increases. Furthermore, we can compare the plot with the empirical equations derived from the shape measurement challenges mentioned in Section 1.

5.2 Shear calibration

A key assumption in weak lensing is that the distortions of the galaxies caused by the mass distributions are small. In this limit, the information on the lensing is entirely encoded in the ellipticity-shaped moments of the galaxies. This approach is effective for measuring large-scale shear correlations, where the typical distortions are less than 12%, as demonstrated by the STEP (Massey et al., 2007) and the GREAT (Mandelbaum et al., 2015) simulations. However, the assumption becomes invalid as the dark matter surface density increases toward the center of galaxy clusters, where the images are more distorted. In individual cluster studies, this is managed by including higher-order shape moments, such as octopole moments, or separately fitting the strong lensing signal. However, recalculating higher-order moments for billions of galaxies is computationally infeasible for surveys like LSST. Instead, we investigate the calibration of the elliptical shear signal beyond the low-shear regime to derive a nonlinear normalization of the shear signal as an alternative.

To understand how the measured shear varies from a weak to a strong lensing regime and evaluate the performance of shear measurement in the LSST Science Pipelines, we measure and calculate tangential shear signals in the grid simulations. Given the absence of blending phenomena in these simulation images, we can eliminate biases due to the deblender. As mentioned in Section 4.4, 410 simulations (with 300–1000 galaxies in each) are included to constrain the error bars and reduce the "shape noise." Each simulation has a known *true tangential reduced shear* when generated as well as a *measured tangential reduced shear* that is derived from the shear measurements. Therefore, the comparison between the measured tangential reduced shear $g_{\rm tan}^{\rm meas}$ and the true tangential reduced shear $g_{\rm tan}^{\rm true}$ is shown in Figure 5.

The true tangential reduced shear values are set as 30 discrete values between 0.02 and 0.60, and the measured reduced shear is expected to accord with $g_{\rm tan}^{\rm true}$ in the weak lensing regime. As the shear increases, the shear measurement is impacted by the strong lensing signals, and there is evident bias in $g_{\rm tan}^{\rm meas}$. Shear calibration biases are measured as two components: a multiplicative calibration bias m_i and an additive residual shear offset c_i, such that the function relating $\gamma^{\rm meas}$ to $\gamma^{\rm true}$ is expressed as Eq. 29

$$\langle \gamma^{\rm meas} \rangle = (1 + m_i)\,\gamma^{\rm true} + c_i. \tag{29}$$

In Shear Testing Program 2 (STEP2), the HSM algorithm is implemented as an approach to shear measurement. It has the results of multiplicative and additive biases as $m_i = -0.019 \pm 0.01$ and $c_i = 0.002 \pm 0.0$ (Massey et al., 2007). Therefore, we can plot $g_{\rm tan}^{\rm meas}$ as a linear function of $g_{\rm tan}^{\rm true}$ (represented by the dashed line in Figure 5, with a linear extrapolation to cover larger shear) denoted by Eq. 30:

$$g_{\rm tan,HSM}^{\rm meas} = (1 - 0.019 \pm 0.010)\, g_{\rm tan}^{\rm true} + 0.002, \tag{30}$$

as a reference for our shear measurements. As indicated in the figure, the true value of g is within the error bar of our normalization up to $g_{\rm tan}^{\rm true} \lesssim 0.05$, which means that the shear measurement in the LSST Science Pipelines shows high fidelity on sources with reduced shear smaller than 0.05.

For small shears, we recover a linear relationship between the input distortion and measured shear, which is expected because the non-linear effects are minimized at low shears. Because the reduced shear values included in STEP2 are typically smaller than 0.05 and the results of multiplicative and additive biases are derived from these data, it can explain the phenomenon that our normalization behaves differently with the STEP2 HSM implementation in the range where $g_{\rm tan} \gtrsim 0.05$. However, even at $g_{\rm tan}^{\rm true} = 0.1$, there is a noticeable deviation from linearity. However, there exists a monotonic relationship between the distortion and the measured shear that can be characterized up to relatively high shear values. If the tangential reduced shear increases to 0.2, it is possible to have a measurement error up to ~25% and even more significant for a higher shear.

We fit the values of $g_{\rm tan}^{\rm meas}$ up to $g_{\rm tan}^{\rm true} = 0.4$ with a second-order polynomial given by Eq. 31

$$g_{\rm tan}^{\rm meas} = -1.046 (g_{\rm tan}^{\rm true})^2 + 0.9474 g_{\rm tan}^{\rm true} + 0.0008445, \tag{31}$$

and a third-order polynomial

$$g_{\rm tan}^{\rm meas} = 0.007023 (g_{\rm tan}^{\rm true})^3 - 1.089 (g_{\rm tan}^{\rm true})^2 + 0.9548 g_{\rm tan}^{\rm true} + 0.0005537. \tag{32}$$

To evaluate the goodness of fitting, we calculate the chi-square per degree of freedom χ^2 in both cases. The quadratic fitting has $\chi^2 = 1.365$, and the cubic fitting has $\chi^2 = 0.913$.

The normalization of the shear measurements allows us to obtain calibrated mass estimates for the innermost region of a cluster. These results demonstrate that the LSST Science Pipelines can be used to probe the lensing signal in clusters into $r \sim 200$kpc from the center, increasing the sample of clusters for which individual lensing signals can be measured dramatically.

6 Cluster simulation results

While the grid simulations are utilized to determine the normalization of shear measurements, we also generate more realistic cluster simulations. These cluster simulations demonstrate how applying this normalization enhances shape measurements in the complex environment of galaxy clusters, thereby improving the accuracy of mass estimates.

6.1 Shape measurements in cluster simulations

The strongest cosmological constraint on dark energy that will emerge from LSST's study of galaxy clusters comes from the evolution of the cluster mass function. To investigate the mass dependence of the mass bias in the reconstruction, we use our cluster simulations to measure the mass and mass profile of the simulated galaxy clusters.

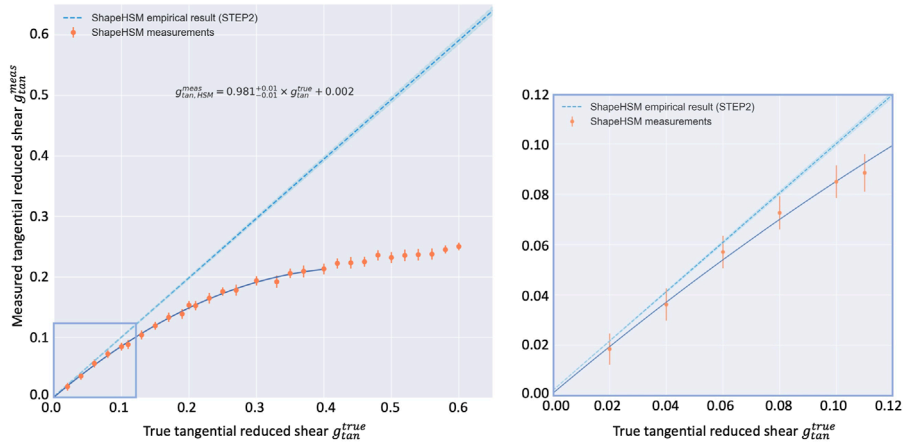

FIGURE 5
Left: measured tangential reduced shear plot against the true tangential reduced shear with data points from 410 grid simulations with no deblending. The value of g^{true}_{tan} ranges from 0.02 to 0.60 as input of the simulations. The dashed line shows the empirical results of multiplicative and additive biases using the HSM algorithm in STEP2. The solid curve is the quadratic fitting up to $g^{true}_{tan} = 0.40$. *Right*: close-up view of the fitting within $g^{true}_{tan} < 0.10$.

As discussed in Section 3.4 and Section 4.1, the cluster simulations can be considered deeply coadded r-band images of LSST. To retain only the background galaxies with reasonable measurements, we apply a filter with criteria `|ext_shapeHSM_HsmShapeRegauss_e1| < 1.5` and `|ext_shapeHSM_HsmShapeRegauss_e2| < 1.5`. In a cluster simulation, the center of the foreground cluster is located at the center of the output image (x_c, y_c). As introduced in Section 2.1, from Eq. 8, we can calculate the tangential ellipticity for each galaxy as Eqs 33, 34

$$e_{\rm tan} = -e_1 \cos(2\phi) - e_2 \sin(2\phi) \tag{33}$$

$$= -e_1 \cos\left(2\tan^{-1}\left(\frac{y-y_c}{x-x_c}\right)\right) - e_2 \sin\left(2\tan^{-1}\left(\frac{y-y_c}{x-x_c}\right)\right), \tag{34}$$

where (x, y) is the HSM centroid position of each galaxy in pixel coordinates (*i.e.*, `ext_shapeHSM_HsmSourceMoments_x` and `ext_shapeHSM_HsmSourceMoments_y`). The notation of ellipticity tensor (e_1, e_2) is equivalent to $(\chi_+, \chi_\times)$ or $(e_+, e_\times)$ in coordinates with object pairs.

With the calculated tangential ellipticities, the shear profile is plotted for each cluster simulation. Furthermore, we consider a fixed aperture in each simulation image with different cluster mass values and check the proportionality of mean tangential ellipticity $\langle e_{\rm tan}\rangle$.

The final image of each cluster simulation has the size of $3,542 \times 3542$ pixels at the LSST resolution, which corresponds to 3.25×3.25 Mpc^2 on the lens plane. The cluster mass values are $M_{200} = 5, 10, 15, and 20 \times 10^{14} M_\odot$, respectively. We calculate the azimuthally averaged tangential shear values for background galaxies in eight annular bins around the center of the cluster and plot against the radii of annulus up to 1.0 Mpc, as shown in Figure 6. For a randomly oriented population of background galaxies, an estimate of reduced shear can be related to the average ellipticity $\langle e\rangle$ denoted by Eq. 35:

$$\langle g\rangle \simeq \frac{\langle\chi\rangle}{2} = \frac{\langle e\rangle}{2}, \tag{35}$$

and further details on shear and ellipticity can be found in Schneider (2006) and Bernstein and Jarvis (2002b). Therefore, in the analysis

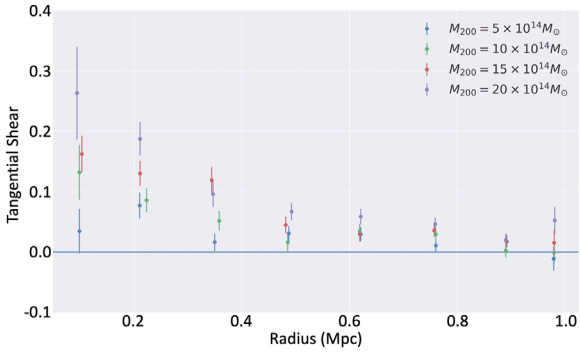

FIGURE 6
Azimuthally averaged tangential shear in different annular bins (eight bins ranging from 0 to 1.0 Mpc). Shear is descending following the corresponding NFW profile. At a given radius of the annulus, a higher cluster virial mass produces a larger tangential shear.

of the cluster simulations, we convert the measured tangential ellipticities to tangential shears by $\langle g_{\rm tan}\rangle \simeq \langle e_{\rm tan}\rangle/2$, if not specified. We expect to observe a distribution of $g_{\rm tan}$ in a similar shape as the shear plot from the corresponding NFW profile. The figure confirms a general descending trend as the radius increases and a larger $\langle g_{\rm tan}\rangle$ value for a higher virial mass.

If we take the average tangential ellipticity within a fixed aperture, the value of $\langle e_{\rm tan}\rangle$ is expected to be approximately proportional to the cluster virial mass at the weak lensing limit. Hence, we plot $\langle e_{\rm tan}\rangle$ measured within apertures of 0.25 Mpc, 0.5 Mpc, and 1.0 Mpc for different cluster mass values, as shown in Figure 7. The 1.0-Mpc aperture plot presents a linear relation between $\langle e_{\rm tan}\rangle$ and all four mass values, while for 0.25 and 0.5 Mpc apertures the linearity breaks for larger M_{200} (15 *and* $20 \times 10^{14} M_\odot$). The figure is consistent with the expectation that the shape measurement is biased by strong lensing signals at a small aperture that covers the central sky area of the foreground

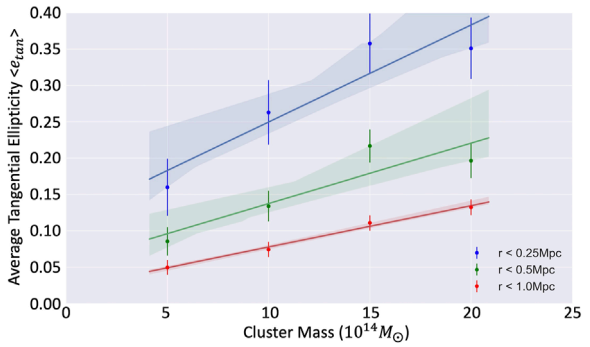

FIGURE 7
Average tangential ellipticities measured within given apertures (0.25, 0.5, and 1.0 Mpc) for different cluster masses. The linearity between $\langle e_{\tan} \rangle$ and M_{200} is true for the largest aperture but unavailable in smaller apertures with larger cluster mass. The solid lines are linearly fitting for data points corresponding to each aperture. The shaded bands represent the uncertainties.

galaxy cluster. In a realistic host dark matter halo, a larger mass can cause more distorted arcs due to strong lensing around the cluster center, which is also a factor affecting shear measurements. In the shear calibration using grid simulations, this factor contributes to the non-linearity and needs to be taken into account when calibrating the measured tangential reduced shear.

The shear at the innermost radius shows the characteristic saturation of the ellipticity demonstrated in Figure 5, whereas at larger radii, the average shear scales linearly with mass. This suggests a strategy in which cluster masses are calibrated using the signal outside of 250 kpc, corresponding to reduced shear $g_{\tan} = 0.3$, which is very similar to the conclusion from the grid simulations.

From the cluster simulations, the shear measurement in the LSST Science Pipelines provides a promising trend in the weak lensing regime, taking deblending and PSF modeling into account. On the other hand, if the sky area being used for measurement contains strong lensing signals, the measured shear can be biased because the strong lensed galaxies can be measured as a more circular source with a much lower tangential ellipticity than the true values. Other possible uncertainty sources in processing and analyzing procedures are discussed in Section 7.

6.2 Mass estimates

Using the pzmassfitter code, we reconstruct the convergence map and estimate the mass for the cluster, as introduced in Section 4.5. Figure 8 displays the reconstructed convergence maps of the cluster simulation shown in Figure 3. No *a priori* fiducial position of the foreground cluster is required. In the E-mode signal-to-noise (S/N) map shown in the left panel, the primary peak saturates at $(x, y) = (1786, 1786)$. Given that the full field of view has $3,542 \times 3,542$ pixels, the primary peak is in good agreement with the actual cluster center, which is located at $(x, y) = (1771, 1771)$. Because the weak lensing distortion is always in the tangential direction with respect to the galaxy cluster center, theoretically, it creates no net B-mode signal in the environment setup of our simulations. The B-mode map, shown in the right panel, may therefore be used as a null test to track potential systematic errors. Some minor clumps present in the northeast and southwest corners are likely due to measurement fluctuations and random noise. In practice, these signals are too far from the cluster center to affect the measurements.

In the design of the cluster simulations, foreground galaxy clusters are placed at $z = 0.3$, and all the background galaxies share the same redshift at $z = 1.5$. To estimate the cluster mass, we first generate a Dirac-like $P(z)$ for each galaxy in the catalog. Coupled with the individual shapes measured by the LSST Science Pipelines and the known location and redshift of the cluster, the output measurement data are processed by `pzmassfitter`. To reduce the shape noise, the galaxy postage stamps are rotated by 90° individually at the beginning of the simulation to generate a parallel set of images. The measurements of the "original images" and "90-degree images" are combined at the level of src catalog as a separate input sample. For each group of an input M_{200} value, we generate 10 cluster simulations together with their 90-degree pairs. We take the average of the mass estimates from the simulations in each group.

To illustrate the improvements from our shear calibration results, as shown in Section 5, we apply the third-order calibration (Eq. 32) to the shape measurement results and compare mass estimates with and without shear calibration.

Results are summarized in Table 2 and shown in Figure 9, for 5×10^{14} $M_\odot$ (first row), 10×10^{14} $M_\odot$ (second row), 15×10^{14} $M_\odot$ (third row), and 20×10^{14} $M_\odot$ (last row) cluster simulations. Histograms correspond to the dispersion of the posterior distribution of the reconstructed cluster mass M_{200}. The ground truth of cluster mass is represented by the gray vertical line, while the red vertical line gives the average of the maximum-likelihood mass estimates over the 10 simulations. The left column shows mass estimates in the absence of shear calibration, while the right column indicates results with calibrated shape measurements.

Since the fitted calibration relation covers up to $g = 0.4$, which approximately corresponds to a radius of 200 to 1000 kpc in our simulations, a radial cutoff of 250 kpc is applied to all mass estimations. Discussions regarding the radial cut can be found in Section 7 and Applegate et al. (2014).

As shown in Table 2 and the right four panels of Figure 9, the true mass values after calibration in all cases are close to the average maximum-likelihood mass estimates. The probability distributions also show good concentration for the true mass values. Given the fact that each cluster simulation has a finite number of background galaxies, it is possible to observe some outliers in the mass distributions. Hence, there may be some fluctuations in the peaks of the probability distributions, which is acceptable and reasonable.

The results in the left four panels of Figure 9 have significant underestimates in cluster mass. As a reference, the average maximum-likelihood mass estimate from 10 simulation realizations is compared with the corresponding true mass value in each panel. We notice that the difference between these two values increases with the true mass. The explanation is that, given a radial cutoff of 250 kpc, a stronger gravitational lensing signal is included as the cluster mass goes up to 20×10^{14} $M_\odot$. Therefore, the measured shear is underestimated in the simulations with a more massive cluster, as shown in Figure 5. These probability distributions show good agreement with our results from Section 5, and the underestimates are remarkably improved by shear calibration.

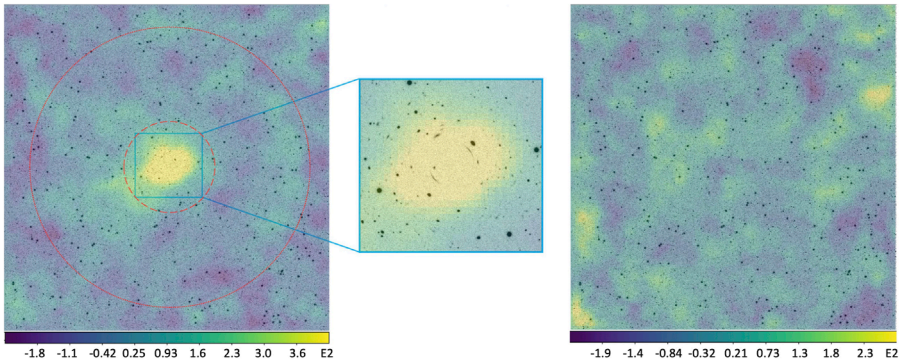

FIGURE 8
Reconstructed gravitational lensing convergence maps for one cluster simulation with $M_{200} = 20 \times 10^{14} M_{\odot}$ in 10-year depth. *Left*: E-mode S/N map of the full $12.2' \times 12.2'$ field of view, with a zoomed-in $2.3' \times 2.3'$ area. The map peaks at the center of the image, which is consistent with the actual cluster center. The red dashed and dotted circles represent the inner and outer radii of the effective region for choosing galaxies, respectively. *Right*: B-mode S/N map of the same sky area.

TABLE 2 Comparison between true virial masses of cluster simulations and average mass estimates with maximum-likelihood. The third column is the mass estimate after applying calibration on the shape measurement, while the fourth column is before calibration.

Simulation group	$M_{200}^{\rm true}/10^{14} M_{\odot}$	$\langle M_{200}^{\rm ML,Calibrated} \rangle / 10^{14} M_{\odot}$	$\langle M_{200}^{\rm ML,Uncalibrated} \rangle / 10^{14} M_{\odot}$
Group 1	5.0	5.192 ± 0.123	2.776 ± 0.336
Group 2	10.0	10.507 ± 0.498	4.954 ± 0.504
Group 3	15.0	14.689 ± 0.390	7.678 ± 0.564
Group 4	20.0	19.636 ± 0.637	9.496 ± 0.650

Based on these comparisons of results before and after shear calibration, we claim that the third-order calibration proves the expected improvements in the mass estimate results. More discussion regarding the uncertainties is included in Section 7.

7 Discussions on systematics

During the process of generating simulations and measuring shapes, we aim to recover factors close to realistic situations (*e.g.*, galaxy postage stamps, lensing algorithm, PSF, and sky noise). However, there are different types of systematics introduced that we expect to understand:

- **Sample size:** In jedisim, for now, we have 738 galaxy postage stamps as the input database. We select these galaxies from HST UDF and CANDELS by visual inspection to ensure a variety of shapes. In the simulation procedure, the galaxy postage stamps are assigned different parameters. In addition, the shape noise is suppressed by incorporating the 90°-rotated pairs. However, it is still necessary and helpful to add more galaxy postage stamps to the database.
- **PSF:** The simulated images are convolved with a uniform PSF kernel which is produced by PhoSim and characterized with parameters of LSST. In this way, the measurement biases due to PSF anisotropy and varying seeing are artificially removed. Ideally, the LSST Science Pipelines can conduct PSF correction accurately so that the shape measurements are effectively similar to our simulations. It is practical to make the PSF more realistic by feeding the simulated images into PhoSim directly instead of convolution.
- **Deblending:** The procedure of deblending is also simplified, given the fact that an NFW halo of pure dark matter is employed as the foreground cluster. On one hand, the absence of blending in grid simulations eliminates the systematics caused by the deblender in the LSST Science Pipelines. On the other hand, although the shape measurement in cluster simulations shows the expected trend, it is not realistic to exclude foreground–background blendings. We are making efforts to interpret the bias due to blending on lensed background sources.
- **Sample characteristics:** The simulations place the lens and source planes at fixed redshifts of $z = 0.3$ and 1.5, respectively. In practice, jedisim is capable of assigning and producing planes at different redshifts, which enables us to evaluate the same pipeline with a more realistic galaxy redshift distribution. In addition, the images are in a single band for now such that the LSST Science Pipelines is not able to determine the photometric redshift for each source. An improvement can be implemented in the near future by generating multi-band simulations.

In our simulations, the magnitude obeys a single power-law function for simplification, which is not the most accurate description of the magnitude according to the shear calibration results from the Kilo-Degree Survey (KiDS) (Conti et al., 2016). Although this factor does not have a dramatic impact on the shape

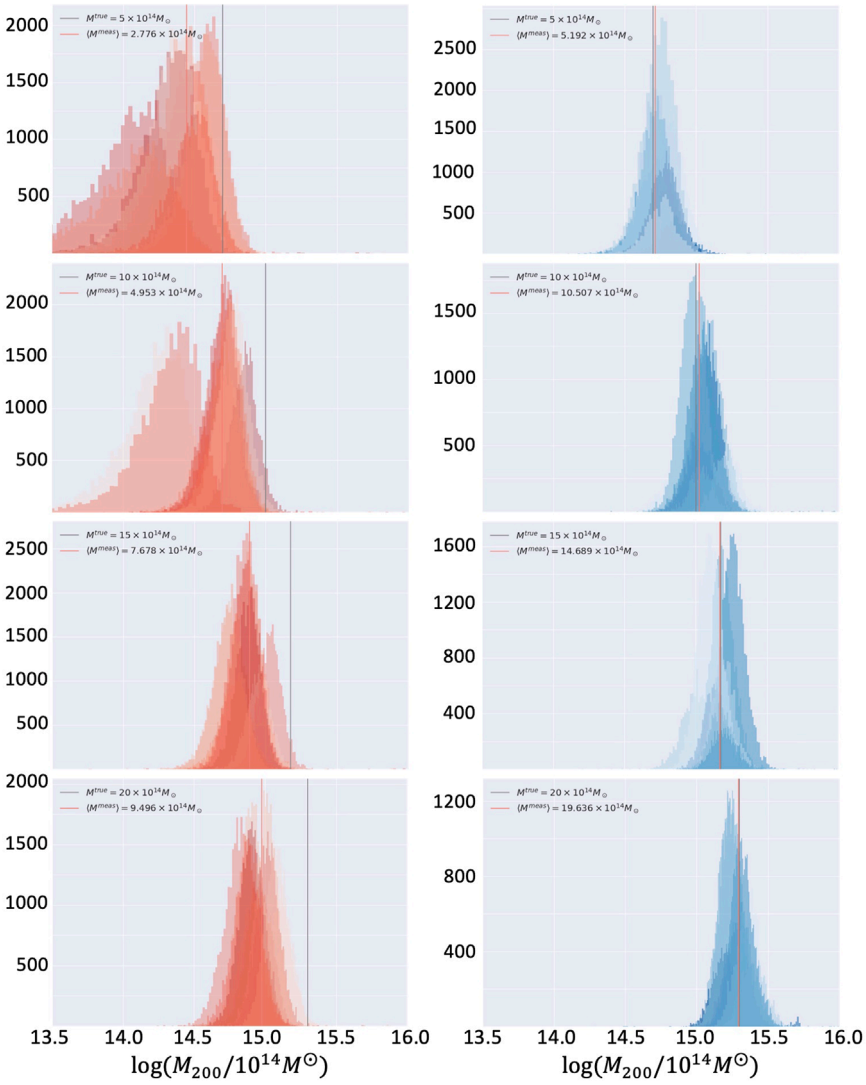

FIGURE 9
Likelihood distributions of mass estimates for cluster simulations, whose true virial mass values are 5,10,15,*and*$20 \times 10^{14} M_\odot$, respectively. These true mass values are indicated by the gray vertical solid lines. Each histogram (with a *y*-axis unit of counts) shows the dispersion of the maximum-likelihood over samples of 90° pair combined at the catalog level. The red vertical solid lines are the average of maximum-likelihood mass estimates of all samples within each panel. The left column shows results without shear calibration. The right column indicates the mass estimates after shear calibration.

measurement, it is reasonable to adopt more accurate functions to describe the magnitude distribution in the future.

The accuracy of the concentration parameter in the NFW profile is crucial for precise modeling of the mass distribution in galaxy clusters. The concentration parameter in this work is simplified when constructing the simulations. Systematic errors, such as PSF distortions, noise, and intrinsic shape noise, can propagate into shear calibration and subsequently affect the accuracy of the concentration parameter. We acknowledge that inaccuracies in shape measurements can introduce biases in the estimation of the concentration parameter. To mitigate these effects, more advanced shape measurement algorithms and rigorous shear calibration should be studied and employed in the future.

- **Single-lens-plane assumption:** In this work, we adopt the single-lens-plane assumption for our lensing simulations. This simplification allows us to focus on the lensing effects of the primary galaxy cluster while maintaining computational efficiency. However, it is important to acknowledge that this assumption does not account for the impact of additional structures along the line of sight, where these line-of-sight structures can boost the lensing cross-section (Li et al., 2019, 2021). Consequently, our results may underestimate the true lensing effects, particularly in scenarios where significant mass is distributed along the line of sight. This limitation should be considered when interpreting the results presented in this paper.

In future work, we plan to address the limitations of the single-lens-plane assumption by incorporating the effects of line-of-sight structures into our lensing simulations. This will involve the development of multi-plane lensing models that account for

additional mass distributions along the line of sight. By doing so, we aim to achieve a more accurate representation of the lensing cross-section and improve the precision of our shear calibration and shape measurement results. These efforts will enhance our understanding of the mass distribution in galaxy clusters and the contribution of line-of-sight structures to the overall lensing signal.

- **Mass estimate:** Parameters in the pzmassfitter code are set to default, where an inner radial cut is applied on the catalogs to exclude strong lensing signals around the cluster center. We set the radial cutoff to 250 kpc, and more discussions can be found in the *Weighing the Giants* project (Applegate et al., 2014). It is necessary to adjust and optimize these configurations as the next step. Meanwhile, the convergence map in Figure 8 shows fluctuations in the simulated images, which are unavoidable. As the virial mass drops to $5\times10^{14}M_{\odot}$, the signal-to-noise can be lower and rendered by the noise level. Given the fact that each sub-panel in Figure 9 is based on one pair of cluster simulations, it is logical to observe a skewness to low mass for the smallest cluster and high accuracy for the most massive cluster. A promising solution is to stack measurement catalogs for multiple simulations with the same cluster mass so that a larger sample can be analyzed by the MCMC algorithm to obtain more concentrated mass estimate distributions.

8 Conclusion and future work

We introduce the image simulation pipeline jedisim and generate simulation images of gravitational lensing at the scale of galaxy clusters. jedisim uses galaxy postage stamps extracted and cleaned from HDF/UDF and GOODS in CANDELS. The postage stamps are scaled to the assigned magnitude and half-light radius of each one, matching observations in HDF/GOODS, and rotated randomly before being traced through a mass distribution to construct full distortion, including both weak and strong lensing instances. Then, the lensed galaxies are convolved with a PSF kernel characterized by LSST parameters generated by PhoSim.

Cluster simulations with a size of $12.2'\times12.2'$ ($3,542\times3,542$ pixels at the LSST resolution) are created and rendered with noise in both 1-year and 10-year survey depths. The virial mass of each cluster is $5, 10, 15, and 20\times10^{14}M_{\odot}$, respectively, and the concentration is 4.0. In addition, 410 grid-layout simulations are generated, each of which has a given reduced shear g throughout all galaxies in it. The value of g ranges from 0.02 to 0.60.

Both the cluster and grid simulations are processed and measured using LSP software stack with the obs_file package. After processing the images, the adaptive moments and ellipticities are measured for background sources using the HSM algorithm. Given the fiducial position of the cluster center, the tangential reduced shear can be calculated for background galaxies.

In the grid simulations, biases due to PSF correction and deblender of the LSST Science Pipelines are artificially constrained so that shape measurements are relatively purified. We compare and plot the measured reduced shear $g_{\rm tan}^{\rm meas}$ against the true reduced shear $g_{\rm tan}^{\rm true}$ in Figure 5. Therefore, we derive the shear calibration from the second-order and third-order polynomial fitting. The multiplicative and additive shear calibration biases of the HSM algorithm in STEP2 are adopted to construct an empirical formula as a reference. The results are consistent with the empirical formula up to $g_{\rm tan}^{\rm true}\lesssim 0.06$, followed by an increasing discrepancy as shear ascends. This phenomenon can be explained by the biased shape measurement for strong lensed galaxies. Meanwhile, the LSST Science Pipelines provide expected performance on shape measurement for weak lensing signals.

In the cluster simulations, by choosing different M_{200} values and varying measurement apertures, the measured reduced shear shows proportionality with M_{200} for an aperture dominated by the weak lensing signal. The linearity breaks as the aperture shrinks to the strong lensing regime as expected.

We plot convergence maps for the cluster simulations. The E-mode convergence map shows a reasonable mass distribution and locates the primary peak in agreement with the actual cluster center. The B-mode map plots more randomly distributed voids in the same sky area, as expected.

The output source catalogs from the LSST Science Pipelines are processed by the pzmassfitter code to estimate the maximum-likelihood cluster mass. The distributions of mass estimates from the MCMC realizations of the shear field for our simulated galaxy clusters demonstrate how the LSST Science Pipelines measurements can reliably recover cluster masses. The comparison between mass estimates before and after applying the shear calibration results from the grid simulations proves the improvement. It demonstrates that the LSST Science Pipelines can be used to probe the lensing signal in a cluster at 250 kpc from the center, increasing the sample of clusters for which individual lensing signals can be measured dramatically.

In general, to produce more realistic cluster simulations, we plan to build a larger repository of galaxy postage stamps, which is in accordance with the morphology and magnitude distribution of observations. Meanwhile, multi-band images are necessary for evaluating photometric redshift calibration and forced photometry components in the LSST Science Pipelines. In the near future, we plan to double the current sample size of galaxy postage stamps in the F450W, F606W, and F814W bands. The source galaxies are supposed to be placed at different redshifts, and a more sophisticated PSF model can be constructed by feeding the simulated images at HST resolution directly into PhoSim instead of the current convolution algorithm.

The cluster galaxies are also to be added so that the corresponding effects due to deblending can be studied. As described by Fu et al. (2019), we adopt a semi-analytic halo model to distribute foreground galaxies. As the next step, we plan to construct a more realistic lensing plane from the smoothed particle hydrodynamics simulations (Aardwolf et al., 2019) and simulate the cluster galaxies according to the CosmoDC2 extra-galactic catalogs (Korytov et al., 2019).

We hope that this work will be helpful in the shear calibration of cluster gravitational lensing and provide feedback on relevant component developments in the LSST Science Pipelines. The upcoming LSST will measure strong and weak lensing signals in the largest and most uniform sample to date of thousands of galaxy clusters. Given the requirement of high accuracy on shear measurements, it is important to determine a feasible scope and calibrate the shear measurement. Furthermore, these measurements

are combined to constrain mass profiles and mass distribution in galaxy clusters and also provide a powerful probe of cosmology.

Data availability statement

The datasets presented in this study can be found in online repositories. The names of the repository/repositories and accession number(s) can be found in the article/Supplementary Material.

Author contributions

BL: writing–original draft, writing–review and editing, conceptualization, data curation, formal analysis, methodology, software, validation, and visualization. ID: writing–original draft, writing–review and editing, conceptualization, data curation, formal analysis, funding acquisition, investigation, methodology, project administration, resources, software, and supervision. NC: validation, writing–review and editing, software, methodology, and writing–original draft. DC: methodology, supervision, project administration, conceptualization, investigation, resources, writing–original draft, and writing–review and editing.

Funding

The author(s) declare that financial support was received for the research, authorship, and/or publication of this article. This work was supported by the DOE grant DE-AC02-76SF00515. This research was conducted using computational resources and services at the Center for Computation and Visualization, Brown University. This work is based on observations taken by the CANDELS Multi-Cycle Treasury Program with the NASA/ESA HST, which is operated by the Association of Universities for Research in Astronomy, Inc., under NASA contract NAS5-26555.

Acknowledgments

The authors thank the referees for their comments on this paper. They thank Daniel Parker for his fundamental contribution to the development of the first version of jedisim and Céline Combet for her substantial guidance in the usage of pzmassfitter. They express their gratitude to the LSST Data Management team for their guidance in utilizing software. BL expresses gratitude to Simon Krughoff, Dominique Boutigny, James Bosch, and Robert Lupton for their helpful comments and discussions. BL expresses gratitude to the members of the Observational Cosmology, Gravitational Lensing, and Astrophysics Research Group at Brown University for their support.

Conflict of interest

The authors declare that the research was conducted in the absence of any commercial or financial relationships that could be construed as a potential conflict of interest.

Publisher's note

All claims expressed in this article are solely those of the authors and do not necessarily represent those of their affiliated organizations, or those of the publisher, the editors, and the reviewers. Any product that may be evaluated in this article, or claim that may be made by its manufacturer, is not guaranteed or endorsed by the publisher.

Supplementary Material

The Supplementary Material for this article can be found online at: https://www.frontiersin.org/articles/10.3389/fspas.2024.1411810/full#supplementary-material

References

Aardwolf, A., Boutigny, D., Daniel, S., Heitmann, K., Kovacs, E., Mao, Y., et al. (2019). The lsst desc dc2 simulated sky survey. *Astrophysical J. Suppl.* doi:10.3847/1538-4365/abd62c

Albrecht, A., Bernstein, G., Cahn, R., Freedman, W. L., Hewitt, J., Hu, W., et al. (2006). *Report of the dark energy task force. arXiv:astro-ph/0609591* ArXiv: astro-ph/0609591.

Applegate, D. E., von der Linden, A., Kelly, P. L., Allen, M. T., Allen, S. W., Burchat, P. R., et al. (2014). Weighing the giants - iii. methods and measurements of accurate galaxy cluster weak-lensing masses. *Mon. Notices R. Astronomical Soc.* 439, 48–72. doi:10.1093/mnras/stt2129

Beckwith, S. V. W., Stiavelli, M., Koekemoer, A. M., Caldwell, J. A. R., Ferguson, H. C., Hook, R., et al. (2006). The hubble ultra deep field. *Astronomical J.* 132, 1729–1755. doi:10.1086/507302

Benitez, N., Ford, H., Bouwens, R., Menanteau, F., Blakeslee, J., Gronwall, C., et al. (2004). Faint galaxies in deep advanced Camera for surveys observations. *Astrophysical J. Suppl. Ser.* 150, 1–18. doi:10.1086/380120

Bernstein, G. M., and Jarvis, M. (2002a). Shapes and shears, stars and smears: optimal measurements for weak lensing. *Astronomical J.* 123, 583–618. doi:10.1086/338085

Bernstein, G. M., and Jarvis, M. (2002b). Shapes and shears, stars and smears: optimal measurements for weak lensing. *Astronomical J.* 123, 583–618. doi:10.1086/338085

Bertin, E. (2013). Psfex: point spread function extractor. *Astrophys. Source Code Libr. , ascl* 1301, 001.

Bosch, J., Armstrong, R., Bickerton, S., Furusawa, H., Ikeda, H., Koike, M., et al. (2017). *The hyper suprime-cam software pipeline.* arXiv:1705.06766 [astro-ph] ArXiv: 1705.06766.

Bridle, S., Balan, S. T., Bethge, M., Gentile, M., Harmeling, S., Heymans, C., et al. (2010). Results of the great08 challenge: an image analysis competition for cosmological lensing. *Mon. Notices R. Astronomical Soc.* 405, 2044–2061. doi:10.1111/j.1365-2966.2010.16598.x

Bridle, S., Shawe-Taylor, J., Amara, A., Applegate, D., Balan, S. T., Berge, J., et al. (2009). Handbook for the great08 challenge: an image analysis competition for cosmological lensing. *Ann. Appl. Statistics* 3, 6–37. doi:10.1214/08-aoas222

Coe, D., Benitez, N., Sanchez, S. F., Jee, M., Bouwens, R., and Ford, H. (2006). Galaxies in the hubble ultra deep field: I. detection, multiband photometry, photometric redshifts, and morphology. *Astronomical J.* 132, 926–959. doi:10.1086/505530

Collaboration, P., Aghanim, N., Akrami, Y., Alves, M., Ashdown, M., Aumont, J., et al. (2020). Planck 2018 results. *A&A* 641, A7. doi:10.1051/0004-6361/201935201

Conti, I. F., Herbonnet, R., Hoekstra, H., Merten, J., Miller, L., and Viola, M. (2016). Calibration of weak-lensing shear in the kilo-degree survey. *Mon. Notices R. Astronomical Soc.*, stx200. doi:10.1093/mnras/stx200

Fahlman, G. G., Kaiser, N., Squires, G., and Woods, D. (1994). Dark matter in ms1224 from distortion of background galaxies. *Astrophysical J.* 437, 56. doi:10.1086/174974

Fischer, P., and Tyson, J. A. (1997). The mass distribution of the most luminous x-ray cluster rxj1347.5-1145 from gravitational lensing. *Astronomical J.* 114, 14. doi:10.1086/118447

Fu, S., Liu, B., Parker, D., and Dell'Antonio, I. (2019). Effects of blending on cluster shear profiles. *Review*.

Grogin, N. A., Kocevski, D. D., Faber, S. M., Ferguson, H. C., Koekemoer, A. M., Riess, A. G., et al. (2011). enCandels: the cosmic assembly near-infrared deep extragalactic legacy survey. *Astrophysical J. Suppl. Ser.* 197, 35. doi:10.1088/0067-0049/197/2/35

Heymans, C., Van Waerbeke, L., Bacon, D., Berge, J., Bernstein, G., Bertin, E., et al. (2006). The shear testing programme - i. weak lensing analysis of simulated ground-based observations. *Mon. Notices R. Astronomical Soc.* 368, 1323–1339. doi:10.1111/j.1365-2966.2006.10198.x

Hirata, C., and Seljak, U. (2003). Shear calibration biases in weak-lensing surveys. *Mon. Notices R. Astronomical Soc.* 343, 459–480. doi:10.1046/j.1365-8711.2003.06683.x

Huff, E., and Mandelbaum, R. (2017). *Metacalibration: direct self-calibration of biases in shear measurement. arXiv:1702.02600 [astro-ph]* ArXiv: 1702.02600.

Iovino, A., Cucciati, O., Scodeggio, M., Knobel, C., Kovač, K., Lilly, S., et al. (2010). The zcosmos redshift survey: how group environment alters global downsizing trends. *Astronomy Astrophysics* 509, A40. doi:10.1051/0004-6361/200912558

Jarvis, M., Bernstein, G. M., Fischer, P., Smith, D., Jain, B., Tyson, J. A., et al. (2003). Weak-lensing results from the 75 square degree cerro tololo inter-american observatory survey. *Astronomical J.* 125, 1014–1032. doi:10.1086/367799

Joudaki, S., Cooray, A., and Holz, D. E. (2009). Weak lensing and dark energy: the impact of dark energy on nonlinear dark matter clustering. *Phys. Rev. D.* 80, 023003. doi:10.1103/physrevd.80.023003

Jurić, M., Kantor, J., Lim, K.-T., Lupton, R. H., Dubois-Felsmann, G., Jenness, T., et al. (2015). *The lsst data management system. arXiv:1512.07914 [astro-ph]* ArXiv: 1512.07914.

Kaiser, N., and Squires, G. (1993). Mapping the dark matter with weak gravitational lensing. *Astrophysical J.* 404, 441–450. doi:10.1086/172297

Kaiser, N., Squires, G., and Broadhurst, T. (1995). A method for weak lensing observations. *Astrophysical J.* 449, 460. doi:10.1086/176071

Koekemoer, A. M., Faber, S. M., Ferguson, H. C., Grogin, N. A., Kocevski, D. D., Koo, D. C., et al. (2011). Candels: the cosmic assembly near-infrared deep extragalactic legacy survey—the *hubble space telescope* observations, imaging data products, and mosaics. *Astrophysical J. Suppl. Ser.* 197, 36. doi:10.1088/0067-0049/197/2/36

Korytov, D., Hearin, A., Kovacs, E., Larsen, P., Rangel, E., Hollowed, J., et al. (2019). Cosmodc2: a synthetic sky catalog for dark energy science with lsst. *Astrophysical J. Suppl. Ser.* 245, 26. ArXiv:1907.06530 [astro-ph]. doi:10.3847/1538-4365/ab510c

Kubo, J. M., and Dell'Antonio, I. P. (2008). A method to search for strong galaxy-galaxy lenses in optical imaging surveys. *Mon. Notices R. Astronomical Soc.* 385, 918–928. doi:10.1111/j.1365-2966.2008.12880.x

Laureijs, R., Amiaux, J., Arduini, S., Augueres, J.-L., Brinchmann, J., Cole, R., et al. (2011). *Euclid definition study report. arXiv preprint arXiv:1110.3193*.

Li, N., Gladders, M. D., Rangel, E. M., Florian, M. K., Bleem, L. E., Heitmann, K., et al. (2016). Pics: simulations of strong gravitational lensing in galaxy clusters. *Astrophysical J.* 828, 54. doi:10.3847/0004-637x/828/1/54

Li, N., Gladders, M. D., Heitmann, K., Rangel, E. M., Child, H. L., Florian, M. K., et al. (2019). The importance of secondary halos for strong lensing in massive galaxy clusters across redshift. *Astrophysical J.* 828, 122. doi:10.3847/1538-4357/ab1f74

Li, N., Becker, C., and Dye, S. (2021). The impact of line-of-sight structures on measuring H_0 with strong lensing time delays. *MNRAS* 504, 2224–2234. doi:10.1093/mnras/stab984

LSST Science Collaboration (2009). *Lsst science book, version 2.0*. arXiv:0912.0201 *[astro-ph]* ArXiv: 0912.0201.

Mandelbaum, R., Lanusse, F., Leauthaud, A., Armstrong, R., Simet, M., Miyatake, H., et al. (2017). *Weak lensing shear calibration with simulations of the hsc survey*. arXiv:1710.*00885 [astro-ph]* ArXiv: 1710.00885.

Mandelbaum, R., Miyatake, H., Hamana, T., Oguri, M., Simet, M., Armstrong, R., et al. (2018). The first-year shear catalog of the subaru hyper suprime-cam subaru strategic program survey. *Publ. Astronomical Soc. Jpn.* 70, S25. doi:10.1093/pasj/psx130

Mandelbaum, R., Rowe, B., Armstrong, R., Bard, D., Bertin, E., Bosch, J., et al. (2015). Great3 results i: systematic errors in shear estimation and the impact of real galaxy morphology. *Mon. Notices R. Astronomical Soc.* 450, 2963–3007. doi:10.1093/mnras/stv781

Massey, R., Heymans, C., Bergé, J., Bernstein, G., Bridle, S., Clowe, D., et al. (2007). The shear testing programme 2: factors affecting high-precision weak-lensing analyses. *Mon. Notices R. Astronomical Soc.* 376, 13–38. doi:10.1111/j.1365-2966.2006.11315.x

McCleary, J., dell'Antonio, I., and Huwe, P. (2015). Mass substructure in abell 3128. *Astrophysical J.* 805, 40. doi:10.1088/0004-637x/805/1/40

Meneghetti, M., Natarajan, P., Coe, D., Contini, E., De Lucia, G., Giocoli, C., et al. (2016). The Frontier Fields lens modelling comparison project. *Mon. Notices R. Astronomical Soc.* 472, 3177–3216. doi:10.1093/mnras/stx2064

Miller, L., Heymans, C., Kitching, T. D., van Waerbeke, L., Erben, T., Hildebrandt, H., et al. (2013). Bayesian galaxy shape measurement for weak lensing surveys - iii. application to the Canada-france-Hawaii telescope lensing survey. *Mon. Notices R. Astronomical Soc.* 429, 2858–2880. doi:10.1093/mnras/sts454

Miller, L., Kitching, T. D., Heymans, C., Heavens, A. F., and van Waerbeke, L. (2007). Bayesian galaxy shape measurement for weak lensing surveys - i. methodology and a fast-fitting algorithm. *Mon. Notices R. Astronomical Soc.* 382, 315–324. doi:10.1111/j.1365-2966.2007.12363.x

Narayan, R., and Bartelmann, M. (1996). *Lectures on gravitational lensing. arXiv preprint astro-ph/9606001*.

Navarro, J. F., Frenk, C. S., and White, S. D. M. (1996). The structure of cold dark matter halos. *Astrophysical J.* 462, 563. doi:10.1086/177173

Navarro, J. F., Frenk, C. S., and White, S. D. M. (1997). A universal density profile from hierarchical clustering. *Astrophysical J.* 490, 493–508. doi:10.1086/304888

Peterson, J. R., Jernigan, J. G., Kahn, S. M., Rasmussen, A. P., Peng, E., Ahmad, Z., et al. (2015). Simulation of astronomical images from optical survey telescopes using a comprehensive photon Monte Carlo approach. *Astrophysical J. Suppl. Ser.* 218, 14. doi:10.1088/0067-0049/218/1/14

Plazas, A. A., Meneghetti, M., Maturi, M., and Rhodes, J. (2019). Image simulations for gravitational lensing with skylens. *Mon. Notices R. Astronomical Soc.* 482, 2823–2832. doi:10.1093/mnras/sty2737

Ribli, D., Dobos, L., and Csabai, I. (2019). Galaxy shape measurement with convolutional neural networks. *Mon. Notices R. Astronomical Soc.* 489, 4847–4859. doi:10.1093/mnras/stz2374

Rowe, B. T., Jarvis, M., Mandelbaum, R., Bernstein, G. M., Bosch, J., Simet, M., et al. (2015). Galsim: the modular galaxy image simulation toolkit. *Astronomy Comput.* 10, 121–150. doi:10.1016/j.ascom.2015.02.002

Schneider, P. (2006). Weak gravitational lensing. , arXiv:astro-ph/0509252 33, 269–451. doi:10.1007/978-3-540-30310-7_3

Schneider, P., King, L., and Erben, T. (2000). Cluster mass profiles from weak lensing: constraints from shear and magnification information. *Astronomy Astrophysics* 353, 41–56.

Sheldon, E. S., Becker, M. R., Jarvis, M., Armstrong, R., and Collaboration, T. L. D. E. S. (2023). Metadetection weak lensing for the vera c. *rubin Obs.* ArXiv:2303.03947 [astro-ph]. doi:10.48550/arXiv.2303.03947

Sheldon, E. S., and Huff, E. M. (2017). Practical weak-lensing shear measurement with metacalibration. *Astrophysical J.* 841, 24. doi:10.3847/1538-4357/aa704b

Spergel, D., Gehrels, N., Baltay, C., Bennett, D., Breckinridge, J., Donahue, M., et al. (2015). *Wide-field infrarred survey telescope-astrophysics focused telescope assets wfirst-afta 2015 report*. arXiv e-prints , arXiv–1503.

Tewes, M., Kuntzer, T., Nakajima, R., Courbin, F., Hildebrandt, H., and Schrabback, T. (2019). enWeak-lensing shear measurement with machine learning: teaching artificial neural networks about feature noise. *Astronomy Astrophysics* 621, A36. ArXiv:1807.02120 [astro-ph, stat]. doi:10.1051/0004-6361/201833775

Van Waerbeke, L., and Mellier, Y. (2003). *Gravitational lensing by large scale structures: a review. arXiv:astro-ph/0305089* ArXiv: astro-ph/0305089.

Voigt, L. M., and Bridle, S. L. (2010). Limitations of model-fitting methods for lensing shear estimation. *Mon. Notices R. Astronomical Soc.* 404, 458–467. doi:10.1111/j.1365-2966.2010.16300.x

Wright, C. O., and Brainerd, T. G. (2000). Gravitational lensing by nfw halos. *Astrophysical J.* 534, 34–40. doi:10.1086/308744

Zhang, Z., Shan, H., Li, N., Wei, C., Yao, J., Ban, Z., et al. (2024). FORKLENS: accurate weak-lensing shear measurement with deep learning. *Astronomy Astrophysics* 683, A209. ArXiv:2301.02986 [astro-ph]. doi:10.1051/0004-6361/202345903

frontiers | Frontiers in Astronomy and Space Sciences

TYPE Original Research
PUBLISHED 01 September 2025
DOI 10.3389/fspas.2025.1441984

OPEN ACCESS

EDITED BY
Hairen Wang,
Chinese Academy of Sciences (CAS), China

REVIEWED BY
Jonathan W. Arenberg,
Northrop Grumman, United States
Su Wang,
Chinese Academy of Sciences (CAS), China

*CORRESPONDENCE
Heidi Jo Newberg,
newbeh@rpi.edu

RECEIVED 31 May 2024
ACCEPTED 30 June 2025
PUBLISHED 01 September 2025

CITATION
Newberg HJ, Swordy L, Barry RK, Cousins M, Nish K, Rickborn S and Todeasa S (2025) The case for a rectangular format space telescope for finding exoplanets.
Front. Astron. Space Sci. 12:1441984.
doi: 10.3389/fspas.2025.1441984

The case for a rectangular format space telescope for finding exoplanets

Heidi Jo Newberg[1]*, Leaf Swordy[1], Richard K. Barry[2], Marina Cousins[1,3], Kerrigan Nish[1], Sarah Rickborn[1,3] and Sebastian Todeasa[1]

[1]Department of Physics, Applied Physics and Astronomy, Rensselaer Polytechnic Institute, Troy, NY, United States, [2]Laboratory for Exoplanets and Stellar Astrophysics, NASA/GSFC, Greenbelt, MD, United States, [3]Department of Mechanical, Aerospace, and Nuclear Engineering, Rensselaer Polytechnic Institute, Troy, NY, United States

We suggest that rectangular primary-mirror telescopes provide a clearer path to discovering habitable worlds than other designs currently being pursued. We show that a simple infrared (λ ~10 μm) telescope design with a rectangular mirror 20 m in length and 1 m in width, combined with technology already developed for JWST, can discover ~11 habitable exoplanets and measure ozone in their atmospheres in a mission of ~1 year. A mission of ~3.5 years could plausibly discover ~27 habitable exoplanets closer than 10 pc to the Earth, and determine whether there is ozone in their atmospheres. A square primary mirror with the same collecting area cannot resolve exoplanets that are within 0.23″ of the host star, making it impossible to detect most of the nearby Earth-like exoplanets. The idea of collecting light with a high aspect ratio rectangular mirror could be used at any wavelength. It is particularly useful for measuring point sources with very small angular separations, as is required for exoplanet observation.

KEYWORDS

exoplanet detection, habitable worlds, space optics, telescopes, dittoscopes, exoplanet atmospheres

1 Introduction

One of the most exciting scientific endeavors of this century is the quest to find a habitable, Earth-like exoplanet. It would be most exciting to find a habitable exoplanet that is close enough to the Earth that one could imagine sending a probe to explore it, or maybe one day sending human explorers. Even more exciting would be the discovery of a planet that has oxygen in its atmosphere, which would make it potentially habitable for us and also likely to support life of its own. Direct imaging of at least 25 habitable exoplanets and finding biosignatures such as oxygen and methane in their atmospheres is in fact the primary science driver for the Habitable Worlds Observatory (HWO), a conceptual future NASA flagship mission that is thought to require a significant technology maturation process (National Academies of Sciences, Engineering, and Medicine, 2021) before it can be selected.

Most current and planned exoplanet discovery missions use the transit method, which relies on the small decrease in starlight observed when an exoplanet passes

in front of a star, to find exoplanets. TESS (Ricker et al., 2014) is the current NASA transit mission, following the highly successful Kepler mission (Borucki et al., 2003), which discovered 2,806 of the 5,638 currently known exoplanets according to the NASA Exoplanet Archive (Akeson et al., 2013; NASA Exoplanet Archive, 2024). Both ESA (PLATO, Rauer et al., 2014) and China (Earth 2.0, Ye, 2022) are building new missions to detect Earth-like planets using the transit method and aim to launch in 2026 and 2027 (Zang et al., 2024), respectively. However, only a small fraction of exoplanet orbits are edge-on as observed from the Solar System, so a large volume of the local Galactic neighborhood must be searched to have a high probability of finding an Earth-like planet.

Instruments such as ESPRESSO (Pepe et al., 2021), EXPRES (Jurgenson et al., 2016), and NEID (Schwab et al., 2016) could reach a radial velocity precision of 10 cm/s (compare with the Sun's speed of 9 cm/s around the Earth-Sun center of mass), if difficulties with velocity variation of the material on the surface of the host star can be overcome. This raises the possibility that habitable exoplanets with a wider range of orbital inclinations could be identified. Even so, the radial velocity method misses planets that orbit face-on.

The only way to find all of the local Earth-like exoplanets is to resolve exoplanets from their host stars, for example, by direct imaging. Resolving exoplanets from their host stars also vastly improves the signal-to-noise for spectroscopy of exoplanet atmospheres. However, to detect Earth, which is 1 AU from the Sun, from a distance of 10 pc requires an angular resolution of 0.1 arcseconds (0.1″). The Sun is more than ten billion times brighter than the Earth in visible (reflected) light, but the luminosity contrast can be reduced by observing in the infrared (optimally ~10 μm) where the Earth peaks in emission and the Sun is only a million times brighter than the Earth. To separate two objects that are 0.1″ apart at a wavelength of 10 μm, the diffraction limit ($\theta \sim \lambda/D$) requires optics with a physical length scale of at least 21 m. Even then, coronagraphic techniques are required to reduce the light from the host star enough that the exoplanet can be detected. The National Academy of Sciences (NAS) Exoplanet Science Strategy (National Academies of Sciences, Engineering, and Medicine, 2018) document recognized the desire to resolve Earth-like exoplanets from their host stars in the infrared, where habitable planets are brightest. However, they concluded that: "Constructing a diffraction-limited 20 m class space telescope that would be cold enough to operate at 10 microns is considered exceptionally difficult."

Two recent proposals for NASA Great Observatories that could find habitable exoplanets were the Habitable Exoplanet Observatory (HabEx, Gaudi et al., 2020) and the Large UV/Optical/IR Surveyor (LUVOIR, The LUVOIR Team, 2019). HabEx combined a 4 m telescope with a separate starshade flying ~10^5 km away. LUVOIR explored the deployment of an 8 m or 15 m mirror paired with a coronagraph with a contrast of order 10^{-10}. Neither design planned to detect the infrared (~10 μm) emission spectrum from an Earth-like planet, so high resolution and extreme coronagraphy in visible/ultraviolet were required. Because of the difficulty in developing and launching the James Webb space telescope (JWST, Gardner et al., 2006), the NAS review recommended that while "Pathways to Habitable Worlds" was a top priority, it would require significant technology maturation (National Academies of Sciences, Engineering, and Medicine, 2021) before a final design could be chosen. A scaled-back Great Observatory consisting of a "~6 m diameter Infrared/Optical/Ultraviolet space telescope with high-contrast imaging and spectroscopy," and that combined elements of HabEx and LUVOIR, is currently under consideration; NASA has established the HWO Technology Maturation Project Office (HTMPO) to address critical technical hurdles to the success of the HWO.

Our calculations suggest that local exoplanets could be identified and characterized in the infrared using a telescope that has a similar collecting area to JWST (and the proposed HWO), and using Achromatic Interfero Coronagraph (AIC, Rabbia et al., 2007) technology that is already mature, as long as the primary mirror is rectangular rather than roughly circular. The rectangular mirror should be ~20 m long in one direction, which makes it possible to resolve the Earth and the Sun (1 AU apart) from a distance of 10 pc, as long as the long axis of the telescope is aligned with the line from the Sun to the Earth. To detect exoplanets at all orientations, the telescope must take (at least) two images of the sky; one should be taken with the primary mirror rotated 90° from the other. High-aspect-ratio rectangular mirrors require more observation time, but a much smaller telescope mirror to reach a given resolution.

A less ambitious mission based on an infrared rectangular mirror concept could provide a much more efficient pathway to identifying habitable planets that have promising aspects, in anticipation of more complex missions that have enhanced characterization capabilities.

2 Methods

We describe here our suggestion that current technology could achieve the HWO primary goals if a rectangular telescope design is adopted. This discovery has arisen from our work in understanding the properties of Dittoscopes (Ditto, 2003), which collect light with a large Primary Objective Grating (POG); the grating is then "observed" at grazing exodus with a focusing element akin to a conventional telescope. The grazing exodus is required for the secondary telescope to collect light from the entire surface of the grating. As shown in our previous work (Swordy et al., 2023), the rate of photon collection from this system is determined primarily by the secondary telescope, but the diffraction limit (in one direction) is set by the length of the grating. The fact that Dittoscopes could achieve high angular resolution inspired us to use them for exoplanet detection and spectroscopy of their atmospheres. We attempted to design a large space telescope for direct detection of habitable exoplanets using a primary objective diffraction grating design.

In Swordy et al. (2025), we outline the concept of the Dispersion Leverage Coronagraph (DLC) and the application for which DLC was originally designed: the Diffractive Interfero Coronagraph Exoplanet Resolver (DICER), a notional space-based Dittoscope designed to detect Earth-like planets orbiting Sun-like stars within 10 parsecs from Earth and identify ozone (O_3) in their atmosphere. DICER collects infrared (~10 μm) light with two large primary objective gratings that are each 10 m by 1 m in size, and uses DLC interferometry to extinguish the light from the exoplanet's host star. We showed that this optical design is capable of resolving

Earth-like exoplanets from Sun-like stars. However, it has difficulty resolving the exoplanet from the background zodiacal light in our solar system and also any zodiacal light around the host star. This problem was partially solved by adding a technically challenging, high resolution spectrograph to the optical train. With this component, we showed that DICER could plausibly find and characterize ~4 nearby, habitable exoplanets around Sun-like stars in a 7 year mission. This represents about 30% of the habitable exoplanets within 8 pc that were in our simulation.

In this paper, we show that if we instead collect the light with mirrors that are the same size and shape as the primary objective gratings that were imagined for DICER, a larger number of exoplanets could be discovered. In addition, the optical design is much less complicated because we would not require a high resolution spectrograph. This suggests that the important innovation for finding exoplanets was not the grating, but the shape of the light-collecting optical element.

First, we describe the proposed rectangular infrared telescope and coronagraph. We then identify stars closer than 10 pc to the Earth, and run a simulation to generate mock habitable exoplanets around those stars in 1,000 universes. Considering the properties of the stars and the simulated exoplanets, we estimate how many of these would be discovered with the rectangular infrared telescope, and how much exposure time would be required. We then determine the amount of time required to detect the 9.6μm absorption band of ozone; the calculation assumes we need a five sigma detection of the dip in the spectrum.

We show that using technology that has already been developed for JWST, we could plausibly build an infrared telescope that could achieve the HWO goal of detecting 25 habitable, Earth-like exoplanets and determine whether there is ozone in their atmospheres within a 3.5 year mission. There are many assumptions in our calculations, and many design choices that could increase or decrease this yield and the time-to-completion.

3 Telescope design

Our goal is a telescope design that could detect all of the habitable, Earth-like planets around Sun-like stars that are closer than 10 pc. Because planets with habitable temperatures have a peak blackbody emission wavelength near 10 µm, we start with a telescope design that is optimized in the infrared. At 10 µm, the diffraction limit requires that at least one dimension of the primary collector be about 20 m across to achieve 0.1″ resolution; and that dimension must be aligned with the direction in the sky from the host star to the exoplanet. Because a round mirror of diameter 20 m is not feasible, we suggest making a rectangular mirror that has a long dimension of 20 m.

If we do not know the position angle of a planet around its host star (the normal situation when attempting to discover an exoplanet), then for optimal resolution the long axis of the mirror needs to be rotated, while staring straight at the host star, to try all possible exoplanet position angles. However, most of the exoplanets can be identified from two images taken with the primary mirror rotated by 90° between exposures. The technique for finding exoplanets and the implications for the observation time will be covered in the next section.

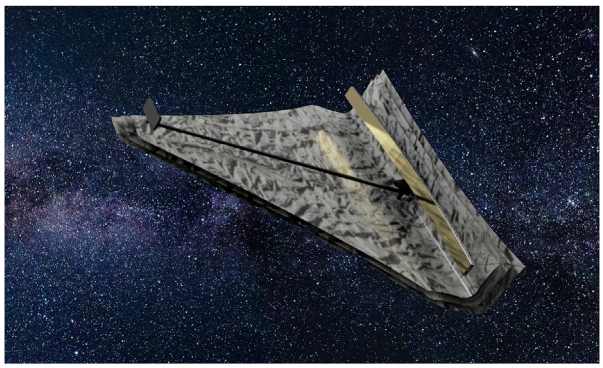

FIGURE 1
Concept design for a rectangular space telescope, modeled after DICER and JWST. The primary mirror is made of twenty 1 m × 1 m beryllium mirror segments. Scaling from JWST, the secondary mirror is 1 m × 2.3 m and deployed about 23 m away and offset from the primary mirror. The sunshield is meant to allow observations in all sky directions, though mirror position angles will be limited in directions that are at large angles from the antisolar point. During launch, two 10 m sections of mirrors can be folded with the reflective sides together, next to the secondary mirror support and a folded sunshade. After the two mirrors unfold, the secondary mirror beam extends out, dragging the triangular portion of the sunshade with it. The folded payload could reasonably fit in a space that is 11 m × 2.5 m × 2.5m, plausibly fitting in a Falcon Heavy launch vehicle.

In this paper, we imagine the capabilities of a 20 m × 1 m version of JWST, equipped with a modern coronagraph that is optimized for discovery of nearby exoplanets and a mid-infrared instrument with a fraction of the capabilities of JWST's Mid-Infrared Instrument (MIRI, Rieke et al., 2015). The mirror would most likely be made in segments, as shown in Figure 1. For calculation purposes, we imagine an optical design that is a 1 m-wide slice of JWST that has been scaled up by a factor of 20/6.5. In this system, the secondary mirror is ~2.3 m × 1 m, and is placed to the side of the primary mirror so that it does not obscure the primary mirror. The expectation is that, like JWST, this telescope would be deployed at L2, and the mirrors would be passively cooled with the aid of a sunshield. Also like JWST, the primary mirror segments would be actively aligned to achieve an optimal point spread function in the focal plane.

The sunshield concept presented in Figure 1 extends 2 m past the ends of the primary mirror, and curls behind the secondary support and up to the secondary mirror. When pointed within 25° of the antisolar point (away from the Sun), the portion of the sunshade behind the mirror will shield all of the optical elements at all rotation angles of the primary mirror. When pointed perpendicular to the plane of the ecliptic (the worst case), the triangular portion will shield the optical elements for 120° of primary mirror position angle, which would easily allow the spacecraft to obtain two images separated by a 90°, as required for our baseline exoplanet search. For launch, we imagine that two 10 m portions of the primary mirror are folded with their reflective surfaces towards each other, the secondary mirror support is compressed to about the same length of 10 m, and the triangular portion of the sunshield is folded up. Note that both the primary mirror and the sunshield would require far less folding than JWST to fit in a launch vehicle, and

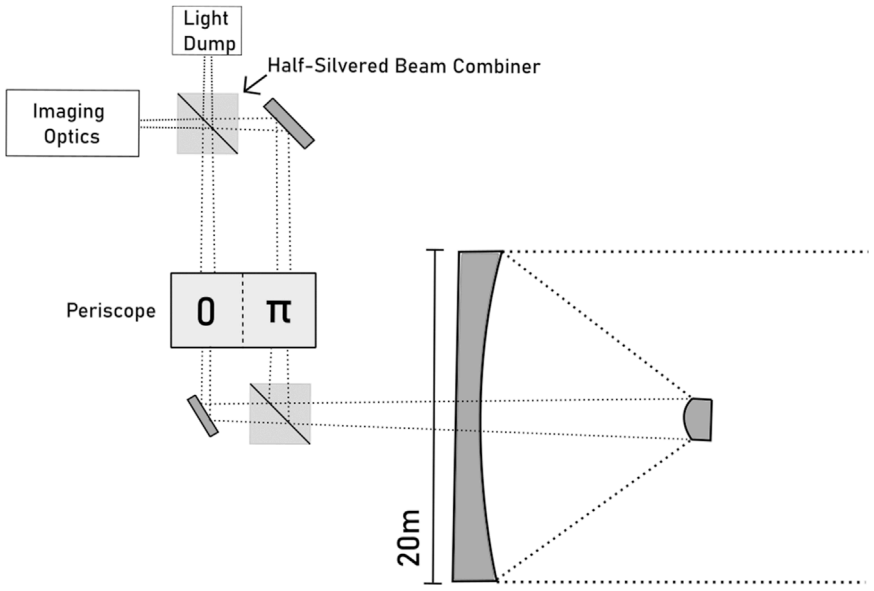

FIGURE 2
Schematic diagram for a rectangular space telescope with conventional mirror design (not to scale). The 20 m primary mirror is shown edge-on. The secondary mirror is 1 m × 2.3 m and deployed about 23 m away. Light is focused to an AIC coronagraph; half of the beam goes through a pi phase shift and the other does not. The phase shift can be accomplished with periscope optics, or by sending one of the beams through focus. The beams are then recombined with a loss of all of the coherent light. Since the path length of the light from the host star is the same in both paths, it will be removed as coherent light.

require far fewer steps to unfold after launch. We estimate the size of the folded spacecraft as 11 m long (10 m of mirrors plus the thickness of the secondary mirror, the thickness of the sunshield, and possibly additional room for power, communications, and instrument packages), 2.5 m wide (slightly larger than the width of the secondary mirror), and 2.5 m deep (the thickness of two primary mirror segments folded together, plus the sunshield behind them, and imagining the power, communications and instrument packages will also need some space). This is of course a very rough estimate.

Although there are many coronagraph designs that work with conventional telescopes, we have assumed a coronagraph of type AIC. With AIC, the focal plane contains two images of the exoplanet, separated by twice the angular separation of the exoplanet and the host star. The PSF of each exoplanet image has an elongated profile determined by the diffraction limit of the rectangular mirror: $0.1'' \times 2''$. AIC is capable of nulling over a 25% bandwidth (Gappinger et al., 2009), which covers the 1.8 μm range of the MIRI F1000W filter we are assuming for our observations, but it can be tuned to other wavelength ranges. The coronagraph would need both active cooling and active correction of the path length. An optical schematic is given in Figure 2.

We are also assuming that the detectors are state-of-the-art single photon detectors: transition edge sensors (TES, Nagler et al., 2018; Höpker et al., 2019; Nagler et al., 2021), superconducting nanowire single-photon detectors (SNSPD, Wollman et al., 2021; Verma et al., 2021; Lita et al., 2022), or mid-infrared kinetic inductance detectors (MKID, Ras et al., 2024). With these detectors, all photons are collected without the introduction of noise; the only noise comes from zodiacal light in the Solar System and the exoplanet host system.

4 Feasibility study

The development of an optimal survey strategy and detailed throughput information for each observation is beyond the scope of this work. For example, it would require determining the best strategy to observe each known star so that the local zodiacal light is a minimum. Here, we present only a simple calculation to elucidate the capabilities of this system. Note that this study closely follows the feasibility simulation done by Swordy et al. (2025) for DICER, but we repeat the steps here for clarity.

4.1 Simulated exoplanets

We generated a simulated set of habitable exoplanets around actual Sun-like stars in the solar neighborhood. Compiling a list of Sun-like stars within 10 pc of the Earth, and meeting the needs of a particular survey, is a surprisingly complex endeavor. This is in part because information about each star is constantly being updated, and in part because the nomenclature and tabulated information for binary stars is confusing, incomplete, and often contradictory. We have attempted here to generate a reasonable set of target stars for demonstration purposes, but more work would be required to mount an actual survey.

We started with the list of 2,398 stars from the Exoplanet Direct Imaging Mission Planning Catalog (ExoCat) of stars within 30 pc compiled by M. Turnbull (Turnbull, 2015). We then restricted the dataset to the 185 stars within 10 pc, using the ExoCat distances. We then restricted the dataset to the 68 of those stars that had F, G, or K spectra as determined by ExoCat. We then modified

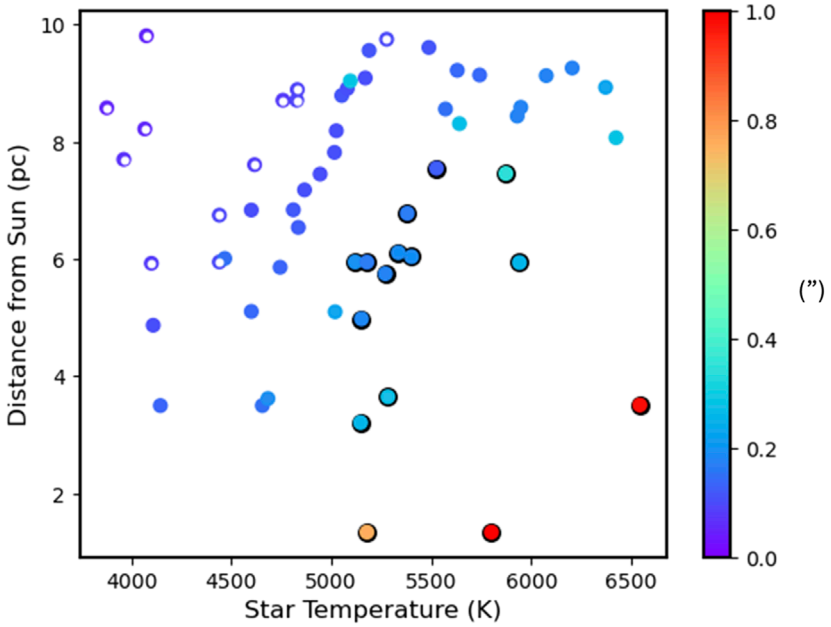

FIGURE 3
Target stars. We show the distances and temperatures of the 58 F/G/K stars within 10 pc of the Sun. The points are colored by the angular distance from the host star to the middle of the habitable zone, as observed from the Sun, in arcseconds. Typically, closer, hotter host stars have a larger angular distance to the habitable zone, but there is some variation due to stellar radius. Twelve stars with a calculated angular distance to the center of the habitable zone, as described in the text, that is smaller than 1″ are indicated by rings instead of filled circles and are excluded from our sample. The fifteen stars in the nearby sample are encircled by a black ring.

this original list based on more modern measurements. Six of the stars had distances determined by Gaia EDR3 (Gaia Collaboration, 2020) that were much larger than 10 pc, so they were removed. Ten stars were removed because their spectral types, as compiled in the SIMBAD astronomical database (Wenger et al., 2000) were not F, G, or K. Five stars were removed because they were closer than 1″ to another star in their binary system, according to the Sixth Catalog of Orbits of Visual Binary Stars (WDS-ORB6, an updated version of the Fifth Catalog, Hartkopf et al., 2001). This leaves 47 stars from the original ExoCat list that fit all of our criteria and were used for our exoplanet detection simulations.

We then searched through SIMBAD and found 11 additional stars to include in the list. In some cases, they are stars for which the distance from the Sun decreased in Gaia EDR3 compared to the original measurements included in ExoCat. Some of the added stars are the fainter stars in binary systems. The list of stars thus increased to 58 Sun-like stars within 10 pc of the Sun, that are at least 1″ from any binary companion. The temperatures and distances to these stars are shown in Figure 3.

When simulating exoplanets around these 58 stars, we noticed that some of the habitable exoplanets were inside our coronagraph inner working angle of 0.05″. To eliminate these, we removed K stars if the average of the minimum and maximum radius of the habitable zone was less than 0.1″, as determined from (Kopparapu et al., 2013); the inner HZ was calculated using the Moist Greenhouse parameters and the outer HZ was calculated using the Maximum Greenhouse parameters from that paper, using the temperature and luminosity of each star from ExoCat. The center of the HZ was calculated as the average of these two values. If the angular distance between the star and the center of the HZ, as observed from the Sun, was less than 0.1″, then the star was removed from the sample. This removed some of the cooler K stars, particularly those that are further from the Sun. The 12 stars removed (rings in Figure 3) were: HD 4614B, HD 131156B, HIP 113283, HIP 85295, HIP 113576, HD 32450A, HIP 32984, HIP 23311, HD 38392, HIP 81300, HIP 82003 and HIP 84478, leaving us a sample of 46 target stars.

Since compiling our list, a list of HWO ExEP Precursor Science Stars (Mamajek and Stapelfeldt, 2024) was published. This list includes 51 stars closer than 10 pc. There are six stars that we selected that they do not have (HIP 5336, HIP 12114, HIP 37297, HIP 86974, HD 156384A, and HD 156384B). There are eleven stars on their list that we did not include: three stars (HIP 54035, HIP 114046, and HIP 105090) were not included because SIMBAD lists them as spectral type M, one was eliminated because it is a close binary (HIP 7981), and seven were eliminated because the calculated center of the HZ was within 0.1″ of the host star (HIP 32984, HIP 81300, HIP 84478, HIP 113283, HD 38392, HD 131156B, and HIP 23311). Although one could make different choices in the selection of the input star list, there are no additional stars in the HWO ExEP Recursor Sceince Stars list that we have not considered.

We also selected a subset of 15 of these stars that are within 8 pc of the Sun and have temperatures of $5100 < T_{\rm eff} < 6600$ K. The 15-star list is the same one used by Swordy et al. (2025) to evaluate DICER. They represent a set of stars that are slightly closer and have temperatures that are more similar to the Sun.

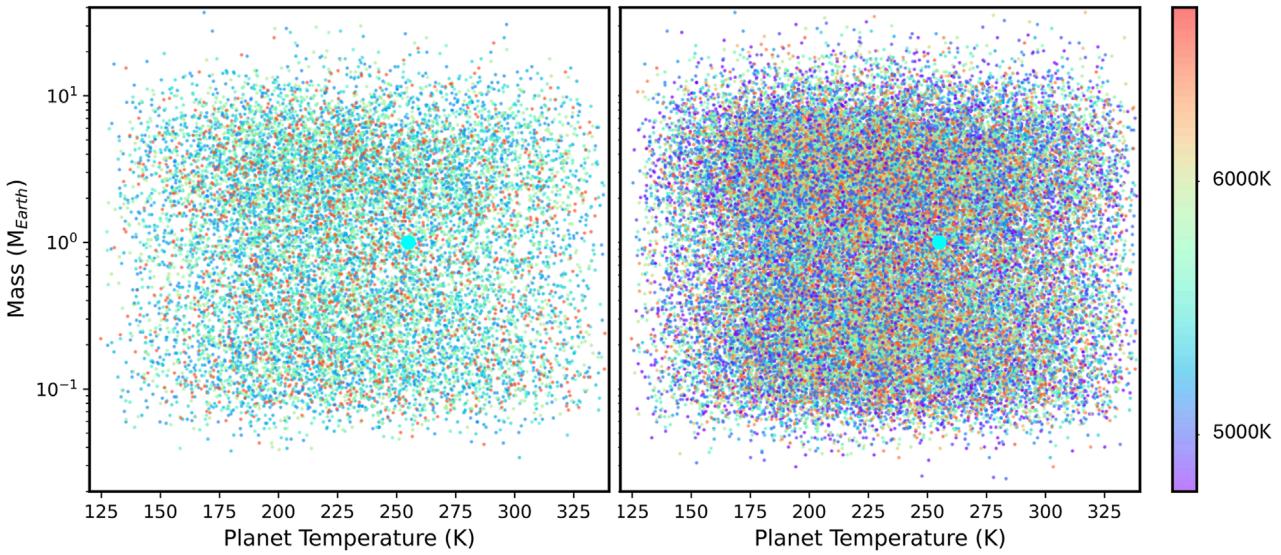

FIGURE 4
Simulated exoplanets. The left panel shows the mass, temperature, and host star temperatures (color bar) for 13,624 simulated habitable exoplanets orbiting 15 Sun-like stars closer than 8 pc. The simulation was done for 1,000 universes, so in our Universe we expect about 1,000 times fewer exoplanets than were simulated, or about one habitable exoplanet per host star. The right panel shows the same information for 45,652 simulated habitable exoplanets orbiting 46 F, G, K stars closer than 10 pc. Note that the larger sample of host stars includes not only more distant target stars but also a wider range of host star temperatures; in particular there are a larger number of cooler host stars. The blue cyan dot in each panel shows the mass and effective blackbody temperature of the Earth (255 K, assuming and albedo of 0.3).

Clearly, we have not heavily optimized the target list for a comprehensive exoplanet discovery mission; the temperature range of host stars could be wider, and wider separation planets could be identified around more distant stars. However, this set will give us a sense of the sensitivity of our proposed telescope to the most valuable targets.

To generate simulated exoplanets, we used the lower yield Bryson et al. (2021) model, as implemented in the P-pop exoplanet simulation tool (Kammerer et al., 2022), to simulate habitable exoplanets orbiting each of the stars. Only habitable exoplanets on circular orbits are simulated. Using the Kepler DR25 dataset, the model estimates through Approximate Bayesian Computation (Hsu et al., 2019) that, on average, each Sun-like star hosts about one planet in the habitable zone. Of our 46 target stars, 42 were included in the P-pop ExoCat_1 input catalog that is distributed with the P-pop code. Of those 42 stars, we only changed the spectral types of HIP 84720 and HD 156384A, which were originally listed as M0V and M1.5V, respectively, to the SIMBAD values of G9V (Corbally, 1984) and K3 (Bidelman, 1985). The P-pop input data for HD 10360, HIP 88601B, HD 155885, and HD 156384B came from the HWO ExEP Precursor Science Stars; these stars did not have 2MASS magnitudes because they were not resolved by 2MASS.

To achieve better statistics, the simulation was run 1,000 times, simulating 1,000 universes. Using this tool, 13,624 habitable zone planets were generated (about one planet per star per universe) around the list of 15 stars closer than 8pc, and 45,652 habitable zone planets were generated around the list of 46 stars closer than 10pc. The masses and surface temperatures of the simulated planets, as well as the temperatures of the host stars, are shown in Figure 4.

4.2 Exoplanet discovery

Since we imagine using this telescope to search for previously unknown exoplanets, we will not know in advance where the exoplanet is in relation to the host star. Because a rectangular telescope has a higher resolution in the direction of the long dimension of the mirror, we need to take two images with the telescope's primary mirror rotated by 90° between the two images. This way, we can discover exoplanets outside of a 0.1″ square, centered on the host star. One could instead rotate through a set of smaller (or continuous) angles to instead exclude a circular region inscribed in the square; while there might be engineering design reasons for a continuously rotating telescope, there is very little advantage in terms of exoplanet detection. If the exoplanet has already been identified, the telescope can be rotated so that its position with respect to the host star is aligned with the long axis of the mirror so that it can be most efficiently detected.

For a telescope that is 20 m by 1 m, all exoplanets further than 1″ from the host star will be distinguishable, regardless of the angle at which the telescope is rotated. All exoplanets closer than 0.05″ to the host star will not be detected, regardless of mirror rotation. For exoplanets with a separation of $0.05 < \theta < 1$, the detectability will depend on the orientation of the telescope and the brightness of the host star, exoplanet, and background. The larger the angular separation, the more likely the exoplanet will be detected, assuming a random telescope orientation.

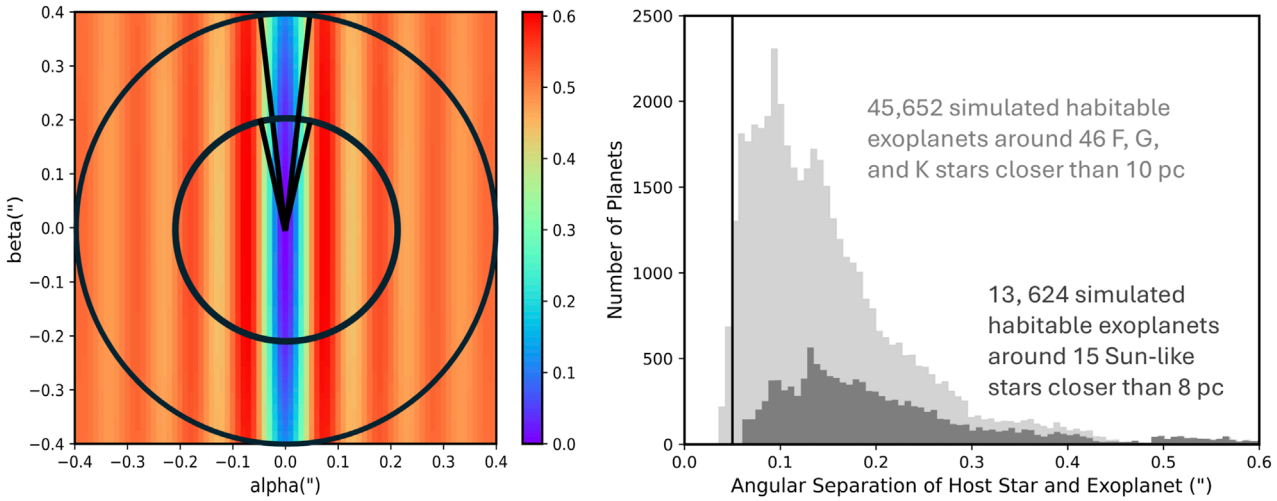

FIGURE 5
The effect of exoplanet position on planet detection. The left panel shows the AIC transmission fraction (The maximum AIC transmission is ~0.5 because half of the light is lost in combining the two beams) as a function of the relative sky position of the planet with respect to the star. Here, α is the angle in the sky that is aligned with the long axis of the mirror, and β is the angle in the sky that is perpendicular to that. If the telescope rotates while staring at the host star, the planet traverses the transmission plane in a circle with a radius given by the angular separation between the star and the planet. The two circles shown in the panel correspond to star-exoplanet separations of 0.2″ and 0.4″. For smaller angular separations, the planet spends a larger fraction of the time in the low transmission (blue) region of the focal plane where it cannot be detected. The histograms in the right panel show the distribution of angular distance from the host star for 45,652 simulated habitable exoplanets orbiting 46 F, G, K stars closer than 10 pc (light gray), and also for the 13,624 simulated exoplanets orbiting 15 Sun-like stars closer than 8 pc (dark gray). The simulation was done for 1,000 universes, so in our Universe we expect about 1,000 times fewer exoplanets than were simulated, or about one habitable exoplanet per host star. The simulation creates only circular planet orbits, which we view at any orientation, so the angular separation represents the largest angular separation that the planet will have on its orbit. Simulated exoplanets that have a maximum separation of less than 0.05″ are not detectable; note that the target host stars were selected in temperature and distance so that their habitable zones are nearly completely detectable.

The left panel of Figure 5 shows in red and orange the angular positions at which light from an exoplanet would be transmitted, and not nulled by AIC. The transmission function for this optical design is given by:

$$T = \frac{1}{2} I_0 L W \left(1 - \frac{\sin(2\pi W\beta/\lambda)}{2\pi W\beta/\lambda} \frac{\sin(2\pi L\alpha/\lambda)}{2\pi L\alpha/\lambda} \right),$$

where α is the angular sky position of the exoplanet in the direction aligned with the long axis of the telescope, β is the angular sky position perpendicular to that direction, L and W are the length and width of the primary mirror (in this case 20 m and 1 m, respectively), and the observed wavelength (λ) is 10 μm. The leading factor of a half is included because AIC detects at most half of the photons that are incident to the system. Because the AIC papers derive transmission functions only for circularly symmetric apertures, we derived the transmission function following the derivation in Sections 3, 4 of Swordy et al. (2025). Because the design of DLC is parallel to the design of AIC, the transmission function math is very analogous. The only difference between the mathematics of our transmission function derivation and that of DLC is that the integration is over an $L \times W$ rectangle instead of a square with sides D. Since the integrals are all separable in the X, Y plane, the math is identical, except that in the part of the integration associated with the X-direction, D is replaced by L, and in the part of the integration associated with the Y-direction, D is replaced by W. If X is along the long axis of the primary mirror, then $\alpha = (\delta_{0x} - \delta_{1x})/f$ and $\beta = \delta_{0y}/f$. Using these substitutions, our derived transmission function is similar to the rectangular transmission function corresponding to Equation 9 of Swordy et al. (2025).

The right panel of Figure 5 shows the maximum angular separation between the simulated exoplanets and their host stars. Because the exoplanet simulator only models circular orbits, the projected path of the exoplanet on the sky is an ellipse with a semimajor axis that is set by the radius of the exoplanet's orbit and the distance from us to the host star, and an eccentricity that is set by the inclination of the orbit. The figure shows that the inner working angle (0.05″) for the AIC coronagraph and a 20 m mirror is small enough that almost all of the simulated habitable exoplanets are observable. However, exoplanets with orbital planes that are inclined to our line-of-sight might not be visible at all points in their orbits. Repeat observations, at times when the exoplanets are at different positions in their orbital paths, would allow us to trace planetary orbits and identify planets in edge-on or eccentric systems that are sometimes too close to the host star to detect.

Planets that are too close to the host star (hot) will not be resolved, and planets that are too far away (cold) will not emit significant light at 10 μm; because of this, this rectangular infrared space telescope preferentially finds only habitable zone planets.

4.3 Simulated exoplanet yield

We calculated the number of simulated exoplanets that we would detect with a rectangular infrared telescope. Given the simulated exoplanet temperatures and radii, we calculated the angular distance

from the host star, the blackbody flux at 10 μm, the subtended solid angle of the host star, and the planet flux as observed from the Earth. We then compared this planet signal with the background noise from stellar leakage and zodiacal light. For example, we calculate that a 256 K blackbody planet with the radius of the Earth, at a distance of 7.5 pc, would produce ~17,000 photons per hour. (Though note that the actual Earth emission is somewhat higher at 10 μm than the blackbody emission for an equivalent total emission object with a temperature of 256 K.) In this section, all calculations were done assuming that the bandwidth of the observations is 1.8 μm, similar to the MIRI F1000W filter. The central wavelength of the observations was assumed to be 10 μm. We multiplied the planet flux by the transmission function (Figure 5) and by the fraction of the planet's light that would be within the diffraction-limited resolution of the telescope, which in this case is 0.737.

The optimal transmission function for the system was assumed to be 25%, including 50% from loss in the AIC beamsplitter and another 50% due to other optical elements (equal to the overall throughput of JWST; Giardino et al., 2022). Note that transmission might be improved by using detector efficiency from TESs, SNSPDs, or MKIDs.

The main source of background is zodiacal light from the Solar System or from the exoplanet's host solar system. The local zodiacal cloud varies in brightness as a function of position in the sky, and depends on the relative position of the Sun and Earth (and therefore the time of year). It is typically brighter towards the Sun (where the dust is hotter) and near the plane of the ecliptic. Using IRAS data (Schlegel et al., 1998) and the NASA Euclid background model tool (Euclid Background Model, 2017), we estimated that when observing from L2, the local zodiacal light background varies between 10 and 20 MJy/sr. Unless the exoplanet system is located very near the Celestial Equator, there is an optimal time of year when it can be observed with ~10 MJy/sr of local zodiacal light background, which is what we assumed in the signal-to-noise calculation.

It is difficult to estimate the zodiacal dust background that comes from the exoplanet system itself, because habitable zone zodiacal dust has been observed in very few systems. While there are dozens of systems that have zodiacal light that is known to be orders of magnitude brighter than in the Solar System (di Folco et al., 2007), it is possible that these are unusual systems for which the zodiacal dust has been detected because it is so bright. Adding to the uncertainty, it matters how the exozodiacal dust is distributed in the host system. If it is concentrated close to the host star, it will be nulled. If it is preferentially in the same plane as the exoplanet, it would be preferentially located near the exoplanet, especially in edge-on systems. The Large Binocular Telescope Interferometer (LBTI) Hunt for Observable Signatures of Terrestrial Systems (HOSTS, Ertel et al., 2020) survey found zodiacal dust in four out of 25 Sun-like stars observed. By fitting the luminosity function of the observed light, they estimate that the typical Sun-like star has a zodiacal dust emission similar to our own Solar System, with a median habitable zone zodiacal dust level of three times that of the Solar System. With one sigma error bars, the median habitable zone zodiacal dust level is less than 9 times that of the Solar System.

In our signal-to-noise estimates, we assumed that the exozodiacal light in the region around the exoplanet has twice the surface brightness as the minimum local zodiacal light. This estimate is very uncertain, but is justified by the following argument. The whole range of surface brightness from the local zodiacal dust is 10 – 20 MJy/sr, including towards the Sun, towards the plane of the ecliptic, and looking out of the plane. If the surface brightness of dust looking through a disk is twice as high as looking out of a disk from the midplane (where the zodiacal light background is low), then the surface brightness looking through a disk is about the same as the highest zodiacal backgrounds in the Solar System. Since surface brightness is independent of distance, the exozodiacal light background is also independent of distance to the host system, as long as the planet is located within a disk of zodiacal dust. The estimate of 20 MJy/sr for exozodiacal dust could be optimistic or pessimistic, since the amount and distribution of exozodiacal dust in each system is not known; it is possible that much of the exozodiacal dust (including much of the brighter, hotter dust near the star) could be nulled along with the host star light.

We used 30 MJy/sr for the total zodiacal light background for all of the simulated exoplanets. This amounts to ~15,000,000 photons per hour in a $2 \times 0.1'' \times 2''$ region. The first factor of 2 comes from the two exoplanet images in the focal plane, that in AIC often do not overlap). The angular resolution in the long direction of the mirror is 0.1, and the resolution in the short direction of the mirror is 2. At a particular sky position, the total zodiacal light background is multiplied by the transmission function (Figure 5); zodiacal light close to the host star is nulled along with the host star light.

Background can also be contributed by the host star itself from stellar leakage, pointing jitter, or residual optical path difference. The stellar leakage was calculated using:

$$I_0 L W \pi^2 r_*^2 \left[L^2 + W^2\right] / 12\lambda^2.$$

This was computed using the small angle approximation of our transmission function:

$$T(\alpha,\beta) = I_0 L W \pi^2 \left(L^2\alpha^2 + W^2\beta^2\right) / 12\lambda^2,$$

which includes a factor of 1/2 for the transmission loss in beam combining. The star was assumed to emit I_0 uniformly over a disk of angular radius r_*, so the leakage is the integral of the transmission function over the stellar disk divided by $I_0 \pi r_0^2$. A G star at a distance of 7.5pc would produce 1.0×10^{11} photons per hour. The stellar leakage is only 3,200,000 photons per hour (a factor of 3.2×10^{-5} suppression of the starlight).

If the planet is located inside of half of the diffraction limit of the telescope, then it will be impossible for us to determine the background level from stellar leakage, and the planet is assumed to be impossible to observe. If the planet is outside of half of the diffraction limit, then it is assumed that the background can be determined with very little error. The amount of light in the pixel(s) in which the planet light is captured is found by integrating a normalized Gaussian with sigma of 0.34 times the diffraction-limited resolution:

$$L_{frac} = 2\int_{X-\theta_L/2}^{X+\theta_L/2} G\left(X', 0.34\lambda/L\right) dX' \int_{Y-\theta_W/2}^{Y+\theta_W/2} G\left(Y', 0.34\lambda/W\right) dY'.$$

Here, L_{frac} is the fraction of leaked light that overlaps with the planet. The factor of 2 is there because there will be two images of the planet in the focal plane. The primary mirror has length L and width W. The angular position of the exoplanet with respect to the host star is (X, Y), where X is in the direction of the long axis of the primary mirror and Y is in the direction of the short axis of the primary

mirror. $G(X,\sigma)$ is a normalized Gaussian centered on zero with a width given by σ. The σ of the Gaussian in each direction is calculated as 0.34 times the diffraction limit in the direction being integrated over; the factor of 0.34 is a standard assumption for the fit of a Gaussian to the Airy function.

We did not include star background from pointing jitter or residual optical path difference, because we expect these to be much smaller than either the zodiacal light background or the stellar leakage; it is not expected that this approximation will significantly affect our results.

For the case of an Earth-like planet orbiting a Sun-like star at a distance of 7.5 pc, and with the position angle of the planet aligned with the long axis of the telescope, the estimated flux for the exoplanet, zodiacal light and star are 15,000, 18,000,000 and 1,900,000 photons per hour. The primary source of noise is zodiacal light. For different stars, exoplanets, and telescope position angle, the stellar leakage can vary widely. The signal-to-noise ratio (SNR) is calculated as:

$$SNR = R_p t / \sqrt{\left(R_p + R_z + R_s\right) t},$$

where R_p, R_z, and R_s are the rates at which photons are collected from the planet, zodiacal light, and stellar leakage, respectively. t is the exposure time of the observation. In this case, for an exposure of 1 day, the SNR is seventeen.

We estimated the output of a very simple survey strategy, in which each star is observed for the same amount of time. In practice, we expect the time to completion (or alternatively the number of identified exoplanets) could be significantly improved with an adaptive approach that uses different exposure times based on the host star's distance and temperature, and that uses the results of previous observations of each star to inform future observations.

We first imagine searching for the 13,624 simulated exoplanets simulated around 15 nearby Sun-like stars, trying a range of different exposure times up to 40 days. With longer exposure times, fainter (lower mass and lower temperature) exoplanets can be discovered. Each planet was assumed to have a circular orbit. A random angle between 0 and 2π was selected to represent the position of the planet on the orbit. A random angle between 0 and $\pi/2$, weighted by $\sin(i)$, was generated to indicate the inclination of the orbit to our line of sight. A random angle between 0 and π was generated to indicate the angle between the long angle of the ellipse that the planet traces on the sky and the long axis of the telescope mirror. For each planet, a particular (α,β) was calculated from these three random angles, where the angles are measured from the host star. α is the angle in the direction of the long axis of the telescope mirror, and β is in the direction of the short axis of the telescope mirror, as pictured in the left panel of Figure 5.

From these (α,β) values, the properties of the host star, and the properties of the simulated exoplanets, we calculated a SNR for each exoplanet, as outlined above. For each exposure time listed, the sky is exposed for half of that time in one random position angle of the primary mirror, and then the other half of the time it is exposed with the primary mirror rotated by 90°. The SNR is calculated by adding together the photons from the planet as calculated from each of the two exposures, and then dividing by the square root of the sum of the photons from the planet, zodiacal light, and stellar leakage from the two exposures.

Figure 6 shows the calculated SNR as a function of the maximum angle between the exoplanet and the host star for both of the star samples. The left panel shows 10 days of observation for each of the fifteen closer stars, and the right panel shows 10 days of observation for each of the stars in the larger sample of 46 stars that extends out to distances of 10 pc. There is a maximum and minimum angular distance from the host star that depends on the temperature of the host star (and therefore the range of orbital radius in the habitable zone) and the distance (which determines the angular separation). The exoplanets that are closer to the host star are hotter and therefore brighter; if the closer exoplanets are far enough from the host star that they can be resolved, then they have a higher SNR. Many of the exoplanets are detected with extremely high SNR.

Figure 7 (left panel) shows the exoplanets detected at a 7 sigma level given the exposure time, the randomized position of the exoplanet with respect to the host star, the properties of the host star and simulated exoplanet, and their distance. Of the 13,624 simulated planets, 8,883 were found with a 2 day integration time on each host star (red), 9,658 were found in 4 days of integration (orange), 10,093 were found with 6 days (green), 10,394 were found with 8 days (blue), and 10,511 were found with 10 days (light gray). Each of these exoplanet yields must be divided by 1,000 (number of simulated universes) in order to estimate the actual yield. This panel can be compared with the 80 day exposure DICER detections in the right panel of Figure 16 of Swordy et al. (2025); note that the mirrored telescope finds more than twice as many exoplanets, including lower mass, cooler exoplanets, and exoplanets with a smaller exoplanet-host star separation, in a fraction of the time. Because the exoplanet phase, inclination, and position angle are chosen randomly, the exact number of exoplanets discovered is slightly different each time the selection program is run.

This calculation shows that in 10 days of exposure time on each of 15 Sun-like stars (0.4 years of exposure time), we expect to find 11 habitable exoplanets. About 83% (66 out of 80) of the simulated exoplanets with radii, masses and temperatures similar to the Earth ($0.9 < R_p/R_\oplus < 1.1$, $0.9 < M_p/M_\oplus < 1.1$, and $250\ \mathrm{K} < T_p < 300\ \mathrm{K}$) were detected. The number of detected planets as a function of the planet's angular separation from the host star is shown in the left panel of Figure 8.

We then imagined searching for the 45,652 exoplanets simulated around 46 F, G, or K stars within 10 pc. Figure 7 (right panel) shows the exoplanets detected at a 7 sigma level given a range of exposure times between 2 days and 10 days. Of the simulated exoplanets, 20,492 were found with a 2 day integration time on each host star (red), 23,306 were found in 4 days of integration (orange), 24,908 were found with 6 days (green), 26,019 were found with 8 days (blue), and 26,682 (light gray) were found with 10 days.

This calculation shows that in 10 days of exposure time on each of 46 selected stars closer than 10 pc (1.3 years of exposure time), we expect to find 27 habitable exoplanets. About 71% (198 of 278) of the simulated exoplanets with radii, masses and temperatures similar to the Earth ($0.9 < R_p/R_\oplus < 1.1$, $0.9 < M_p/M_\oplus < 1.1$, and $250\ \mathrm{K} < T_p < 300\ \mathrm{K}$) were detected. Note that many of the detections (right panel of Figure 8) are closer than $0.1''$ from the host star.

Because the exozodiacal light is so poorly understood, we explored how a much brighter exozodiacal light background would affect the results. Previously, we assumed that the amount of zodiacal dust in the host exoplanet system was the same as in the Solar System. For

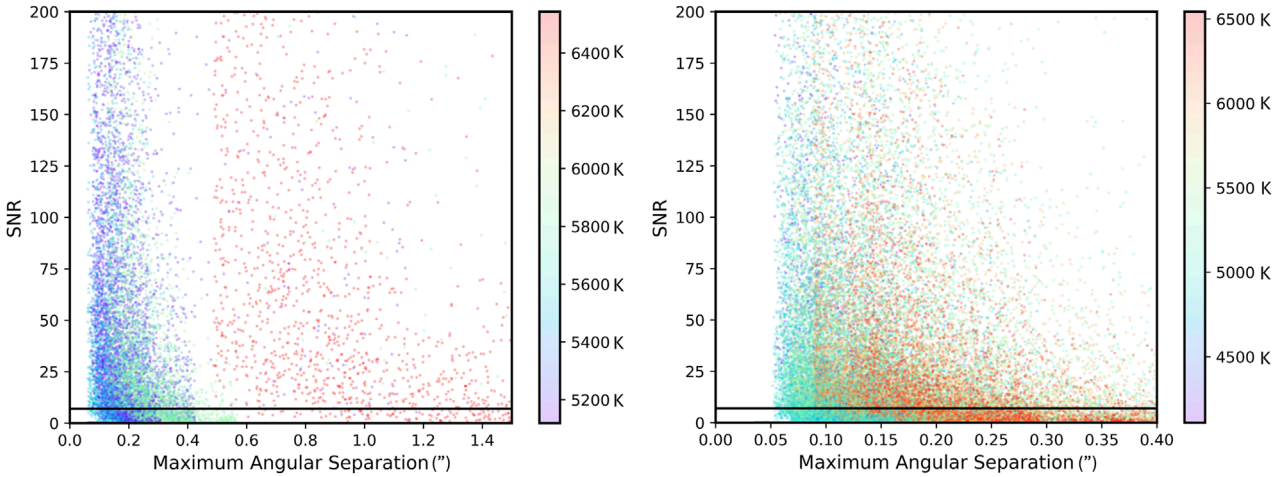

FIGURE 6
SNR as a function of the maximum angular separation (in arcseconds) for a 10 day exposure time. We use a SNR of 7 (horizontal line) as a detection limit. For each of the 13,624 exoplanets simulated around 15 nearby Sun-like stars, we calculated the SNR ratio when the planet was in a random orbital phase, at a random inclination, and viewed at a random position angle. Note that if the planet happens to be closer than 0.05″ to the host star at this particular place on its orbit, it will be unresolved and the SNR will be zero. The left panel shows the calculated SNR for a 10 day exposure time, with the points color-coded by the surface temperature of the host star. For example, the red points in the left panel represent all of the exoplanets simulated in ~1,000 universes that are orbiting one star. Because the simulation only generates planets in the habitable zone, there are no simulated exoplanets within ~0.5″ of the host star. The exoplanets that are closer to the host star are generally hotter and therefore brighter than the more distant exoplanets, so they have a higher SNR. Smaller exoplanets that are in the outer part of the habitable zone are more difficult to find. The right panel shows the SNR versus maximum angular separation for the 45,652 simulated exoplanets orbiting 46 stars closer than 10 pc from the Sun. This simulation includes all of the stars in the smaller sample, but also includes more distant stars with habitable zones that have a smaller angular separation. We chose to show only the simulated planets in the inner 0.4″ for this panel so that more of the closer exoplanets could be distinguished. Note that the color bars of the two plots are different because the temperature range of the stars in the two samples are different.

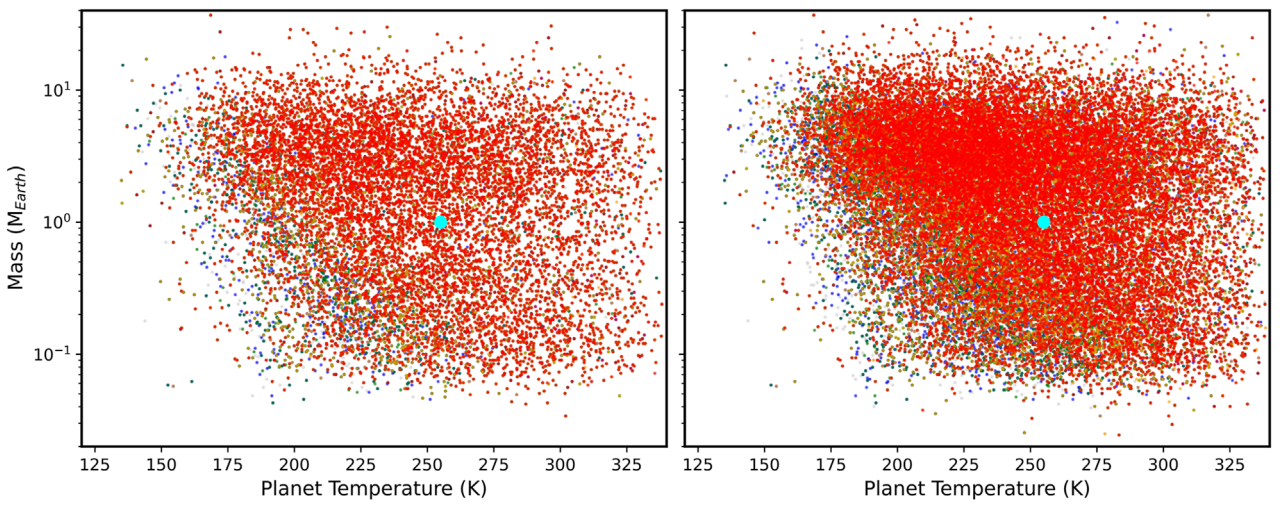

FIGURE 7
Exoplanets detected at the 7 sigma level with the rectangular mirror space telescope. On the left, we show exoplanet detections in 10 days of exposure time for 15 nearby Sun-like stars (closer than 8 pc), simulated 1,000 times each. Of the 13,624 simulated planets, 8,883 were found with a 2 day integration time on each host star (red), 9,658 were found in 4 days of integration (orange), 10,093 were found with 6 days (green), 10,394 were found with 8 days (blue), and 10,511 were found with 10 days (light gray). On the right, we show exoplanet detections in 10 days of exposure time for 46 F, G, or K stars within 10 pc, simulated 1,000 times. Of the 45,652 simulated exoplanets, 20,492 were found with a 2 day integration time on each host star (red), 23,306 were found in 4 days of integration (orange), 24,908 were found with 6 days (green), 26,019 were found with 8 days (blue), and 26,682 (light gray) were found with 10 days. With the larger sample of nearby stars (where 27 exoplants are found in one universe), we show that the rectangular infrared telescope can feasibly meet the HWO goal of finding ~25 nearby, habitable exoplanets.

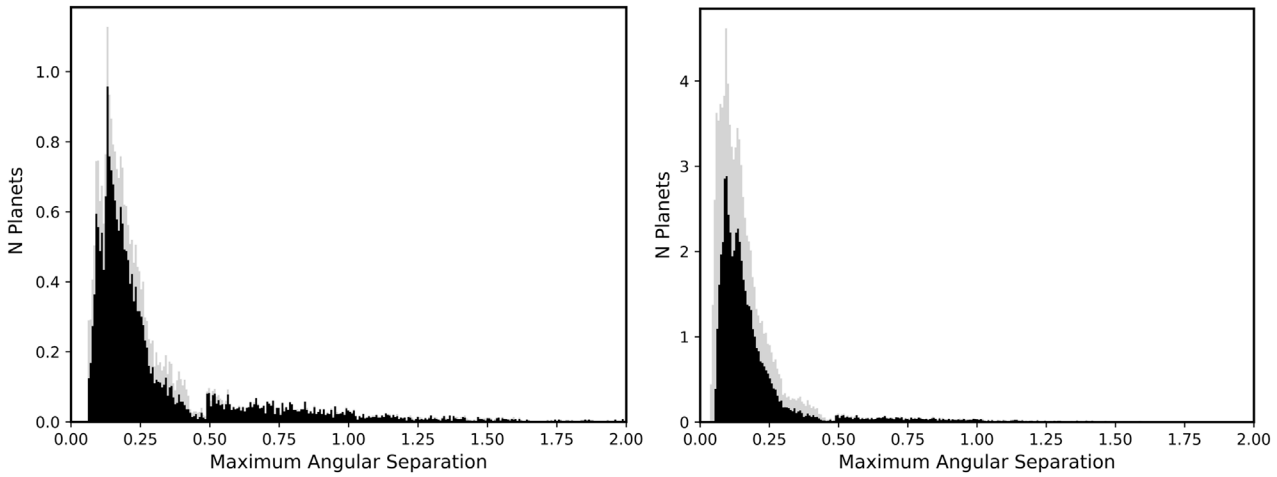

FIGURE 8
Efficiency for finding exoplanets as a function of separation from the host star in arcseconds. In the left panel we show in gray the distribution of maximum angular separation for the 13,624 simulated planets orbiting 15 nearby, Sun-like stars. In black, the distribution of exoplanets that are above a 7-sigma detection limit with 10 days of exposure on each star is shown for comparison. The right panel shows the distribution of maximum angular separation for the 45,652 simulated planets orbiting 46 nearby stars (gray), along with the distribution of exoplanets that are above a 7-sigma detection limit with 10 days of exposure. Note that in both cases we can find exoplanets all the way in to the diffraction-limited resolution of 0.05″.

comparison, we will now assume that the exozodiacal light is ten times as large as in the Solar System, so that the total zodiacal light background is 210 MJy/sr. In this high exozodiacal light regime, instead of finding 27 exoplanets around 46 nearby stars with 10 days of exposure each, we would find 20 planets. If we increased the exposure time by a factor of 6 (60 days each), we would recover the original 27 exoplanets. From this, we conclude that the exozodiacal dust significantly affects the detection of habitable, Earth-like worlds; but within current expectations for the amount of exozodiacal dust, a rectangular telescope of this design would still be successful.

4.4 Measuring biomarkers

Once habitable exoplanets are identified, it is important to then be able to obtain information about their planetary atmospheres in order to identify biomarkers. While it is possible for exoplanets to contain oxygen in their atmospheres without the presence life, abiotic mechanisms are not expected to sustain oxygen in atmospheres of Earth-like habitable planets orbiting Sun-like stars for a sustained period of time (Meadows, 2017). In the case of the Earth, the ozone in the Earth's atmosphere was created from oxygen that was released through photosynthesis. Therefore, finding ozone in the atmosphere of a habitable planet would be a strong indicator of life and in particular of life that uses and stores energy from the host star through photosynthesis (on Earth photosynthesis occurs in vegetation and micro-organisms).

Because the AIC can only null over a 25% bandwidth, we assume that in each exposure we will only be able to obtain spectra over a wavelength range of 2.5μm in the infrared. For our simple calculations, we are assuming we wish to only identify the O_3 absorption band at 9.6μm; the entire width of this band, including some continuum on each side, can easily be obtained within the spectral bandwidth of one observation with a simple mid-infrared spectrograph. Since spectroscopy would only be done once exoplanets are detected, we could rotate the telescope mirror so that the long axis of the mirror points along the direction from the star to the exoplanet, for maximal separation of the two objects, and we could transmit to the spectrograph only the photons within the resolution of the habitable exoplanet. We note that like JWST, it would be possible to include multiple instruments that cover a wider range of infrared wavelengths. However, that is not necessary to achieve our stated science goal.

We imagined obtaining spectra of the O_3 absorption line for the 10,511 habitable exoplanets detected from the 15 stars closer than 8pc in 1,000 realizations of the Universe with an effective observation time of 10 days per host star. While it is easy to design a spectrograph with higher resolution, the photon flux from exoplanets is so low that we expect to look just for a detection of a lower number of counts in the 0.6μm-wide absorption line. We aimed to detect a flux that is half of the blackbody signal at 10μm, in a bandwidth of 0.6μm (the width of the line), with a signal-to-noise ratio (SNR) of 5. In most other respects, the calculation is the same as the calculations of SNR for the photometry. The average exposure time to get a 5σ detection of the O_3 absorption line is 4 days; the SNR for the continuum on either side of the line will have much higher signal-to-noise. For the expected 11 exoplanets that would be identified in one universe, it would take 0.12 years of exposure time to search for O_3. Including the 0.4 years of exposure time required to detect these exoplanets, 0.5 years of exposure are required; this might be accomplished within a ~1 year mission.

For the larger sample of 46 stars, observing each star for a total of 10 days, we expect to find 27 habitable zone exoplanets within 10 pc in 1.3 years of exposure time. These discoveries could then be searched for ozone with an average of 6 days of exposure time each, requiring an additional 0.4 years of exposure time. If we could operate the telescope long enough to obtain 1.7 years of exposure time, we would achieve the HWO goal of finding at least 25 habitable exoplanets and searching them for an O_3 biosignature.

Depending on the duty cycle, this could require about a three and a half year mission.

5 The equivalent area square telescope

For comparison, we evaluated the exoplanet-finding capability of a square telescope with an equivalent collecting area. This telescope has a "diameter" of 4.47 m. The results for the square telescope will be similar to the typical circular footprint for a telescope collecting area, and have the advantage that we can run exactly the same code with only two numbers (the length and width of the telescope) changed.

The PSF is spread over the same number of pixels either way; one resolution element in the rectangular case is $\lambda^2/(LW)$ and in the square case is $\lambda^2/(\sqrt{LW})^2$. Therefore, the detection of isolated point sources is about the same in either case. If the goal is to measure the detailed shape of an extended object, the rectangular telescope would require multiple pointings at different rotation angles, and a much more complex data analysis pipeline. Where the rectangular telescope design really shines is in the detection of point sources that are closer to each other than can be detected with the equivalent circular telescope. Note, however, that engineering capabilities such as mirror alignment, pointing and jitter, residual optical path length, etc., will need to be at the level (at least in one dimension) that is required for a circular telescope of diameter L.

With a diameter of 4.47 m, the diffraction limit is $0.46''$, which means we will not be able to resolve planets that are closer than $0.23''$ to the host star. This restriction makes it impossible to find most of the habitable planets we are trying to identify. For the 46 stars with 45,652 simulated exoplanets, we found 2,563 exoplanets with an exposure time of 2 days, 2,795 exoplanets with an exposure time of 4 days, 2,903 exoplanets with an exposure time of 6 days, 3,044 exoplanets with an exposure time of 8 days, and 3,144 with an exposure time of 10 days. Increasing the exposure time will not allow us to reach our goal for finding Earth-like habitable exoplanets, because most of the exoplanets we wish to find cannot be resolved from the host star with the square design and are therefore not possible to detect.

The left panel of Figure 9 shows the exoplanet temperatures and radii that we can find with the equivalent area square telescope. Note that we are preferentially losing the lower mass and warmer exoplanets, including those that are most similar to the Earth. Only 5% (14 of 278) of the simulated exoplanets with radii, masses and temperatures similar to the Earth ($0.9 < R_p/R_\oplus < 1.1$, $0.9 < M_p/M_\oplus < 1.1$, and $250\ \mathrm{K} < T_p < 300\ \mathrm{K}$) were detected. The right panel of Figure 9 shows the distribution of angular separation between the host star and the detected exoplanets, highlighting the much larger inner working angle of this telescope footprint.

6 Discussion

There is nothing about the idea of making a rectangular mirror, or the AIC coronagraph, that precludes its use at any wavelength. Any current design for HWO or any other flagship mission could be adapted to work with a rectangular primary optical element. For example, if the 20 m × 1 m mirror proposed here was used in the visible at 500 nm, the images could in principle be $0.005'' \times 0.05''$. This would allow for the detection of Earth-like exoplanets to distances of about 200 pc (twenty times farther, because the wavelength of the light is 20 times shorter). We note, however, that there would be considerably more stellar leakage, and the constraints on pointing and stability would make construction much more difficult.

We also point out that the proposed infrared survey for exoplanets favors the detection of habitable exoplanets, with only modest coronagraph performance. Planets that are much cooler than the Earth will be very faint at 10 μm, and therefore much more difficult to detect. Planets that are much warmer than the Earth will be closer to the host stars, and therefore less likely to be resolved. The extremely faint, habitable exoplanets are detected at their most luminous wavelength.

In general the design of a rectangular telescope can be adapted to favor discovery of any particular exoplanet type, at any distance. It can also be designed to enable detailed followup for discovered exoplanets, in which case one would be able to orient the long axis of the mirror in the direction of the current position angle of the exoplanet for maximum resolution. Resolving an exoplanet from its host star is the first step to any exoplanet observation, and for fixed mirror area the highest resolution can be obtained with a rectangular shape. It is instructive to compare the rectangular mirror infrared telescope with other concepts that are being considered for habitable exoplanet discovery.

The Large Interferometer For Exoplanets (LIFE, Quanz et al., 2022; Dannert et al., 2022) collaboration is exploring the use of an array of smaller space telescopes that fly in formation to very high precision. LIFE benefits from two past interferometric, planet-finding mission concepts, ESA's Darwin (Cockell et al., 2009) and the NASA's Terrestrial Planet Finder Interferometer (TPF-I, Beichman et al., 1999), that were canceled due to limitations of our technology and knowledge of exoplanets. Conceptually, LIFE includes four collector spacecraft that formation-fly in a rectangular array, sending light to a beam combiner spacecraft in the center. The whole array rotates to modulate the signal from an exoplanet. LIFE uses a Bracewell interferometer that is enormously expensive in terms of conops; changing the boresight direction is prohibitively expensive for use as a survey instrument. Because of this, it is better utilized for assaying promising planets that have already been detected. Our concept is more feasible because the fixed 20 m long mirror alleviates the need for formation flying, but it does not allow for baselines in the 25–250 m range imagined by LIFE.

The LUVOIR Decadal Survey Mission Concept Study (The LUVOIR Team, 2019) imagined finding and characterizing exoplanets with an 8–15 m space telescope with a coronagraph that is capable of extremely high contrast nulling. The HabEx Decadal Survey Mission Concept Study (Gaudi et al., 2020) also aimed to study exoplanets, but with a 4 m diameter telescope and a 52 m starshade that flew 76,600 km away from the telescope to enable a $0.07''$ inner working angle coronagraph. These ideas are the basis of the technology development for HWO.

The Chinese Academy of Sciences (CAS) has funded a concept study for the Tianlin mission (Wang et al., 2023), a ~6 m UV/Opt/NIR space telescope that is primarily designed to discover and measure biosignatures for nearby G/K stars with the direct imaging method. They aim to start operation of this 5+ year survey within the next 10–15 years. They imagine looking for water, O_3, O_2,

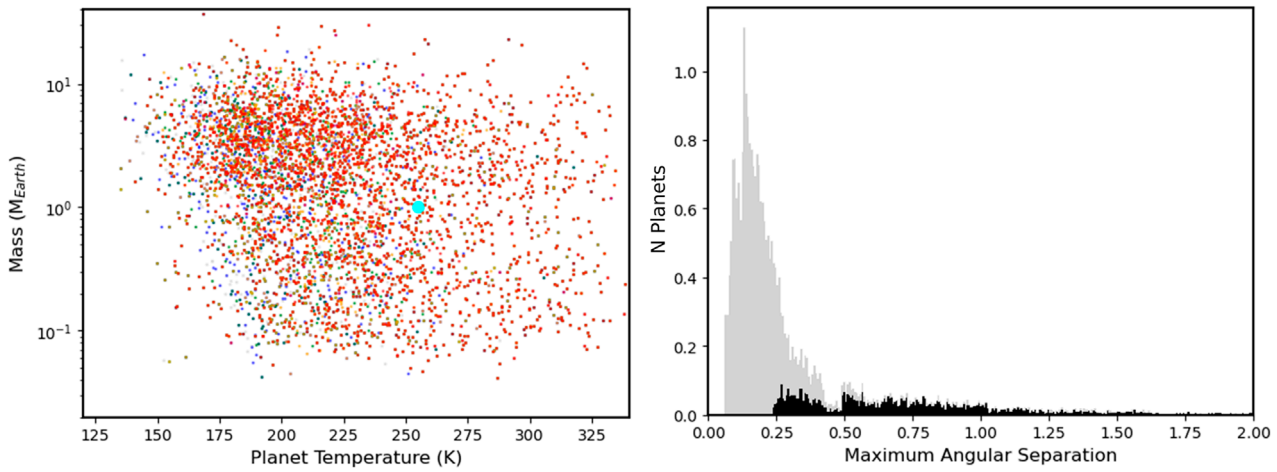

FIGURE 9
Exoplanet detections with an equivalent area square telescope. We consider the number of exoplanets we can discover around the 45,652 simulated planets orbiting 46 nearby stars, changing only the length of the telescope from 20m to 4.47 m and the width of the telescope from 1m to 4.47 m. We show here the equivalent area square telescope detections by reproducing the information in the right panel of Figure 7 and the right panel of Figure 8 for this primary shape. Notice that all of the exoplanets with angular separations smaller than 0.23″ can no longer be detected. That eliminates most of the habitable exoplanets that we aim to find.

CH_4 and chlorophyll in the planetary atmospheres. For example, a 6 m telescope fitted with a coronagraph that can suppress starlight by a factor of 10^9 can detect water vapor in a nearby Earth-like planet orbiting a Sun-like star with about 40 days of exposure time.

The LUVOIR, HabEx, Tianlin and LIFE concepts grew out of the strong need for an exoplanet observatory with a large baseline and an efficient coronagraph with small inner working angles. The rectangular mirror design proposed in this paper would be easier to launch into space and requires a dramatically lower contrast coronagraph than LUVOIR or Tianlin. It does not require a starshade to fly thousands of miles to point from one host star to another like HabEx, and does not require formation flying like LIFE. It has somewhat more modest goals in that it targets a smaller list of nearby exoplanets and as proposed here does not really deliver spectra. However, discovering habitable planets around the closest stars to Earth arguably promises the highest reward. Our proposed design might be a simpler way to identify interesting habitable planets for later follow-up with HWO or LIFE.

The rectangular mirror telescope is not without its own engineering challenges. One such challenge that requires further study is the structural stability of the rectangular primary mirror. Thermal stability will also need to be considered. While we did not specifically address structural and thermal stability of the optics, they are design concerns because vibration in the mirrors and their support structure will cause the mirror to bend and contribute to jitter (Hyde et al., 2004) and optical thermal stability is required to control distortion. Infrared observing in particular requires a high degree of temperature control to reduce thermal backgrounds. However, it seems plausible that careful design, informed by structural models and confirmed by environmental testing (Kimble et al., 2018), will ameliorate any concern about launch loads or geometric changes in the primary mirror due to thermal gradients (Arenberg et al., 2006). We note the extensive modeling and design effort conducted by NASA to assure that JWST's 18 hexagonal beryllium mirrors, mounted on individual hexapods, were capable of maintaining their shape in the presence of launch loads and, during operations, external thermal variability. The design we propose for the primary grating is well within NASA's high-fidelity modeling and environmental test (cryovac and vibration) capabilities (Feinberg et al., 2024).

Although we arrived at the idea of a high aspect ratio mirror independently, we point out that we were not the first to suggest this. The Terrestrial Planet Finder (TPF) project considered two space mission design concepts: an infrared astronomical interferometer (TPF-I; Lawson et al., 2006), which imagined several small telescopes flying in formation, and a visible light coronagraph (TPF-C; Traub et al., 2006), which studied a design with a large oval telescope with a major axis of 8 m and a minor axis of 3.5 m. The oblong mirror design was proposed to reach small inner working angles while keeping the mirror small enough to be easily deployed in space. A variation of TPF-C that used a 50 m diameter disk called an occulter (Cash, 2006), flying in formation with TPF-C at a distance of 50,000 to 70,000 km, was called TPF-O, and predated the HabEx starshade. Our simple design uses a mirror that is more elongated than that of TPF-C, but operates in the infrared like TPF-I. By operating in the infrared, the requirements on the coronagraph are more relaxed, eliminating the need for an occulter.

TPF-C concentrated much more on exoplanet spectroscopy and the identification of biosignatures than we have. However, our proposed mission operations could be enhanced to include identification of other biosignature molecules (for example, Levine et al., 2006, Appendix 1.A), most notably carbon dioxide (15.0 μm, 10.4 μm, and 9.3 μm), methane (7.7 μm and 8.0 μm), and water (7.0 μm and 20.5 μm). Because AIC only nulls over a 25% bandwidth, we are limited to a spectral bandwith of ~1 – 5 μm in the mid-infrared. While a few of these absorption bands could be probed in one pointing, others would require a pointing just for that line. Details of the science case might also require measurements of the continuum, for instance to determine the temperature of the exoplanet. Alternatively, this mission could be

viewed as a less expensive way to identify the most promising targets for future spectroscopic missions such as HWO and LIFE. Slewing HWO or LIFE from one pointing to the next will be enormously expensive; certainly, the LIFE conops is such that moving the rotating constellation will be very complex and require a significant expenditure of propellant.

Refinements of the science plan should also include varying the exposure time for each star, based on the star's distance and temperature; closer, hotter stars will need less exposure time to observe exoplanets in the habitable zone. The required exposure time will also evolve as more information on exozodiacal dust, including exozodiacal dust around these stars in particular, becomes available.

In our proof-of-concept calculations, we have not considered repeat observations of exoplanets to determine their orbits. It takes observations of at least three orbital positions to determine an elliptical path of the planet in the sky, but more could be required depending on the positional accuracy of the measurements.

Figure 10 of Stark et al. (2019) shows the number of exoplanets that could be discovered in 2 years of telescope time (1 year of exposure time) as a function of telescope diameter for several popular exoplanet telescope/coronagraph/starshade designs. While our calculation uses different assumptions and is in many aspects less rigorous, it is interesting to note that our estimate of three discovered exoplanets with 1.3 years of telescope exposure with a ~4.5 m telescope is similar to the number of exoplanets that Stark et al. (2019) estimated for a segmented on-axis telescope of the same diameter with an apodized pupil Lyot coronagraph. Looking at the curves for yield as a function of diameter, our yield for a 20 m × 1 m telescope is roughly equivalent to the yield for a 10 m diameter telescope. This suggests that if building, deploying, and operating a 20 m × 1 m telescope is easier and less costly than a 10 m diameter telescope, the rectangular design is preferred.

Our proof-of-concept calculations consider only optics and not the very real engineering considerations for operating a space telescope. For example, we calculated the throughput for two images taken with the mirror rotated 90° between the two observations. In practice, rotating a telescope–and in particular a telescope with mass distributed to large radii–could consume a considerable amount of fuel. It might be more advantageous to continuously rotate the telescope through 90°. This will cause smearing over the distance that a point source moves in the image plane during the length of an observation. The rate at which an exoplanet will move is $v = 2\pi r/T$, where r is the angular distance from the host star to the exoplanet and T is the rotation period, which is four times the exposure time. For a 10 day exposure time, and a large separation angle of 2″, the exoplanet moves 0.013″ per hour. If the image is read out every hour, or even every few hours, the smearing from rotation will be considerably smaller than the point spread function. This does complicate the data analysis, but if anything increases exoplanet detectability; exoplanets will be excluded inside a circular region with radius equal to half of the diffraction limit for the long axis of the telescope rather than a square with a side length of the diffraction limit for the long axis of the telescope. Exoplanets that would have landed in a place with unfavorable transmission function in one of two images will instead have a much longer effective exposure time because they will be excluded less than half of the time; in exchange, many more exoplanets will fall in the unfavorable region for a small fraction of their exposure.

7 Conclusion

In this paper, we suggest that the search for exoplanets would benefit from changing the shape of the primary collecting element to a rectangle. We show that using technology that has already been developed for JWST, we could plausibly build an infrared telescope that could achieve the HWO goal of detecting 25 habitable, Earth-like exoplanets and determine whether there is ozone in their atmospheres. Since HWO does not aim to image exoplanets in the mid-infrared, the proposed mission would not only be a precursor mission, but would also provide complementary data for future HWO observations.

The rectangular mirror telescope outlined here is an infrared space observatory with a 20 m × 1 m primary mirror and an AIC coronagraph. This observatory can find an estimated 11 habitable exoplanets orbiting the closest 15 stars with 5100 K < $T_{\rm eff}$ < 6600 K, and determine whether they have ozone in their atmospheres, in a mission of 1 year. If the mission is extended to ~3.5 years, an estimated 27 habitable exoplanets are expected from a sample of 46 F, G, and K stars within 10 pc.

These nearby exoplanets are the most precious planets to find because we will be able to study them in the most detail. The closer the exoplanet is, the more likely we could send a probe to investigate, establish communication with its residents, or possibly one day visit.

A fixed rectangular mirror allows for high resolution measurements only along the long axis of the rectangle. By taking half of the exposure time at one mirror position and half of the exposure time with the mirror rotated by 90° (or alternatively by smoothly rotating the telescope through 90° during the exposure), we can achieve most of the resolution for finding exoplanets that a more conventional circular telescope with a diameter equal to the long axis of the rectangular mirror does. A wider rectangular mirror will increase the light collecting area of the rectangular telescope, but does not change the inner working angle of the system.

The calculations presented in this paper are intended as proof-of-concept only. There are an enormous number of parameters that can be optimized in the design of such a telescope. The total required exposure time can be reduced by making the mirror slightly wider. The wavelengths at which the planet's spectrum is observed can be changed. The central wavelength of the observations could be adjusted. The number of habitable exoplanets that were used in our simulation or the zodiacal light estimates could be adjusted, leading to a different yield than was calculated here. Additional instrumentation can be added to enable additional science programs. We suggest here only the idea that a smaller, simpler, and therefore less expensive telescope could be deployed to achieve the primary science driver of the Habitable Worlds Observatory. A more careful mission design would certainly use different exposure times for each target star and a more nuanced plan for identifying biomarkers in the identified exoplanet spectra.

We suggest that a rectangular mirror infrared telescope could identify the most interesting nearby habitable planets for follow-up with HWO or LIFE. But the concept of a rectangular mirror is adaptable to any mission concept that requires high resolution, particularly the ability to distinguish between two point sources. For this purpose, we trade longer exposure times (due to a smaller primary mirror) and more complicated data analysis (the telescope must be rotated through different position angles on the sky

if the position angle of the second source is not known) for the ease and lower cost of deploying a much smaller primary mirror. The rectangular mirror concept can be implemented at any wavelength range and in combination with any standard astronomical instrument.

Data availability statement

Publicly available datasets were analyzed in this study. This data can be found here: https://exoplanetarchive.ipac.caltech.edu/cgi-bin/TblView/nph-tblView?app=ExoTbls&config=mission_exocat ExoCat-1; http://simbad.cds.unistra.fr/simbad/ SIMBAD.

Author contributions

HN: Conceptualization, Formal Analysis, Funding acquisition, Investigation, Methodology, Project administration, Resources, Software, Supervision, Validation, Writing – original draft, Writing – review and editing. LS: Conceptualization, Formal Analysis, Investigation, Methodology, Software, Validation, Visualization, Writing – original draft, Writing – review and editing. RB: Writing – original draft, Writing – review and editing. MC: Investigation, Writing – original draft, Writing – review and editing. KN: Software, Writing – original draft, Writing – review and editing. SR: Investigation, Writing – original draft, Writing – review and editing. ST: Methodology, Validation, Writing – review and editing.

Funding

The author(s) declare that financial support was received for the research and/or publication of this article. This paper is supported by Phase I grant 80NSSC23K0588 from NASA Innovative Advanced Concepts (NIAC). LS was partially supported by a NASA/NY Space Grant fellowship.

Acknowledgments

We thank L. Drake Deming, Thomas D. Ditto, Frank Ravizza, and Ivars Vilums for their contributions to helping us imagine this new technology and assess its suitability to discovering exoplanets. This research has made use of the NASA Exoplanet Archive, which is operated by the California Institute of Technology, under contract with the National Aeronautics and Space Administration under the Exoplanet Exploration Program. This research has made use of the SIMBAD database, operated at CDS, Strasbourg, France. HJN thanks the CCA at Flatiron Institute for hospitality while (a portion of) this research was carried out; the Flatiron Institute is a division of the Simons Foundation.

Conflict of interest

The authors declare that the research was conducted in the absence of any commercial or financial relationships that could be construed as a potential conflict of interest.

Publisher's note

All claims expressed in this article are solely those of the authors and do not necessarily represent those of their affiliated organizations, or those of the publisher, the editors and the reviewers. Any product that may be evaluated in this article, or claim that may be made by its manufacturer, is not guaranteed or endorsed by the publisher.

References

Akeson, R. L., Chen, X., Ciardi, D., Crane, M., Good, J., Harbut, M., et al. (2013). The NASA exoplanet archive: data and tools for exoplanet research. *Publ. Astronomical Soc. Pac.* 125, 989–999. doi:10.1086/672273

Arenberg, J., Gilman, L., Abbruzze, N., Reuter, J., Anderson, K., Jahic, J., et al. (2006). "The JWST backplane stability test article: a critical technology demonstration," in *Space telescopes and instrumentation I: optical, infrared, and millimeter*. doi:10.1117/12.671714

Beichman, C., Woolf, N. J., Lindensmith, C. A. (Editors) (1999). The terrestrial planet finder (TPF): a NASA origins program to search for habitable planets. *JPL publication*. Pasadena, CA: *Cal. Inst. Tech.* 99–3.

Bidelman, W. P. (1985). G.P. Kuiper's spectral classifications of proper-motion stars. *Astrophys. J. Suppl. Ser.* 59, 197–227. doi:10.1086/191069

Borucki, W. J., Koch, D., Basri, G., Brown, T., Caldwell, D., Devore, E., et al. (2003). "Kepler Mission: a mission to find Earth-size planets in the habitable zone," Proceedings of the Conference on Towards Other Earths: DARWIN/TPF and the Search for Extrasolar Terrestrial Planets, April 22-25, 2003, Heidelberg, Germany. Editors M. Fridlund, T. Henning, and H. Lacoste (Netherlands: ESA Special Publication), 69–81.

Bryson, S., Kunimoto, M., Kopparapu, R. K., Coughlin, J. L., Borucki, W. J., Koch, D., et al. (2021). The occurrence of rocky habitable-zone planets around solar-like stars from Kepler data. *Astronomical J.* 161, 36. doi:10.3847/1538-3881/abc418

Cash, W. (2006). Detection of Earth-like planets around nearby stars using a petal-shaped occulter. *Nature* 442, 51–53. doi:10.1038/nature04930

Cockell, C. S., Herbst, T., Léger, A., Absil, O., Beichman, C., Benz, W., et al. (2009). Darwin—an experimental astronomy mission to search for extrasolar planets. *Exp. Astron.* 23, 435–461. doi:10.1007/s10686-008-9121-x

Corbally, C. J. (1984). Close visual binaries. I - MK classifications. *Astrophysical Journal Suppl. Ser.* 55, 657–677. doi:10.1086/190973

Dannert, F. A., Ottiger, M., Quanz, S. P., Laugier, R., Fontanet, E., Gheorghe, A., et al. (2022). Large Interferometer for Exoplanets (LIFE). II. Signal simulation, signal extraction, and fundamental exoplanet parameters from single-epoch observations. *Astronomy Astrophysics* 664, A22. doi:10.1051/0004-6361/202141958

[Dataset] Gaia Collaboration (2020). VizieR online data catalog: Gaia EDR3 (Gaia collaboration, 2020). *VizieR On-line Data Cat. I/350*. doi:10.26093/cds/vizier.1350

di Folco, E., Absil, O., Augereau, J. C., Mérand, A., Coudé du Foresto, V., Thévenin, F., et al. (2007). A near-infrared interferometric survey of debris disk stars. I. Probing the hot dust content around Eridani and τ Ceti with CHARA/FLUOR. *Astronomy Astrophysics* 475, 243–250. doi:10.1051/0004-6361:20077625

Ditto, T. (2003). The Dittoscope in future giant telescopes. *Proc. of the SPIE*. Editor J. Angel, P. Roger, and R. Gilmozzi 4840, 586–597. doi:10.1117/12.459878

Ertel, S., Defrère, D., Hinz, P., Mennesson, B., Kennedy, G. M., Danchi, W. C., et al. (2020). The HOSTS survey for exozodiacal dust: observational results from the complete survey. *Astronomical J.* 159, 177. doi:10.3847/1538-3881/ab7817

Euclid Background Model (2017). Available online at: https://irsa.ipac.caltech.edu/applications/BackgroundModel/ (Accessed February 4, 2024).

Feinberg, L. D., McElwain, M. W., Bowers, C. W., Johnston, J. D., Mosier, G. E., Kimble, R. A., et al. (2024). James Webb Space Telescope optical stability lessons learned for future great observatories. *J. Astronomical Telesc. Instrum. Syst.* 10, 011204. doi:10.1117/1.JATIS.10.1.011204

Gappinger, R. O., Diaz, R. T., Ksendzov, A., Lawson, P. R., Lay, O. P., Liewer, K. M., et al. (2009). Experimental evaluation of achromatic phase shifters for mid-infrared starlight suppression. *Appl. Opt.* 48, 868–880. doi:10.1364/AO.48.000868

Gardner, J. P., Mather, J. C., Clampin, M., Doyon, R., Greenhouse, M. A., Hammel, H. B., et al. (2006). The James Webb space telescope. *Space Sci. Rev.* 123, 485–606. doi:10.1007/s11214-006-8315-7

Gaudi, B. S., Seager, S., Mennesson, B., Kiessling, A., Warfield, K., Cahoy, K., et al. (2020). The habitable exoplanet observatory (HabEx) mission concept study final report. *arXiv e-prints*, arXiv:2001.06683. doi:10.48550/arXiv.2001.06683

Giardino, G., Bhatawdekar, R., Birkmann, S. M., Ferruit, P., Rawle, T., Alves de Oliveira, C., et al. (2022). Optical throughput and sensitivity of JWST NIRSpec, in Space telescopes and instrumentation 2022: Optical, Infrared, and Millimeter Wave. *Society of Photo-Optical Instrumentation Engineers (SPIE) Conference Series*. Editor L. E. Coyle, S. Matsuura, and M. D. Perrin 12180, 121800X. doi:10.1117/12.2628980

Hartkopf, W. I., Mason, B. D., and Worley, C. E. (2001). The 2001 US naval observatory double star CD-ROM. II. The Fifth catalog of orbits of visual binary stars. *The Astronomical Journal*, 122, 3472–3479. doi:10.1086/323921

Höpker, J. P., Gerrits, T., Lita, A., Krapick, S., Herrmann, H., Ricken, R., et al. (2019). Integrated transition edge sensors on titanium in-diffused lithium niobate waveguides. *Apl. Photonics* 4, 056103. doi:10.1063/1.5086276

Hsu, D. C., Ford, E. B., Ragozzine, D., and Ashby, K. (2019). Occurrence rates of planets orbiting FGK stars: combining Kepler DR25, Gaia DR2, and Bayesian inference. *Astronomical J.* 158, 109. doi:10.3847/1538-3881/ab31ab

Hyde, T. T., Ha, K. Q., Johnston, J. D., Howard, J. M., and Mosier, G. E. (2004). Integrated modeling activities for the James Webb Space Telescope: optical jitter analysis, in Optical, infrared, and millimeter space telescopes. *Proc. of the SPIE*. Editor J. C. Ed Mather 5487, 588–599. doi:10.1117/12.551806

Jurgenson, C., Fischer, D., McCracken, T., Sawyer, D., Szymkowiak, A., Davis, A., et al. (2016). EXPRES: a next generation RV spectrograph in the search for earth-like worlds. *Proc. of the SPIE* 9908, 99086T. doi:10.1117/12.2233002

Kammerer, J., Quanz, S. P., and Dannert, F. (2022). Large Interferometer for Exoplanets (LIFE). VI. Detecting rocky exoplanets in the habitable zones of Sun-like stars. *Astronomy Astrophysics* 668, A52. doi:10.1051/0004-6361/202243846

Kimble, R. A., Feinberg, L. D., Voyton, M. F., Lander, J. A., Knight, J. S., Waldman, M., et al. (2018). James Webb Space Telescope (JWST) optical telescope element and integrated science instrument module (OTIS) cryogenic test program and results. *Proc. SPIE* 10698, 1069805. doi:10.1117/12.2309664

Kopparapu, R. K., Ramirez, R., Kasting, J. F., Eymet, V., Robinson, T. D., Mahadevan, S., et al. (2013). Habitable zones around main-sequence stars: new estimates. *Astrophysical J.* 765, 131. doi:10.1088/0004-637X/765/2/131

Lawson, P. R., Ahmed, A., Gappinger, R. O., Ksendzov, A., Lay, O. P., Martin, S. R., et al. (2006). Terrestrial planet finder interferometer technology status and plans. *Proceedings of the SPIE*. Editor J. D. Monnier, M. Schöller, and W. C. Danchi (Advances in Stellar Interferometry) 6268, 626828. doi:10.1117/12.670318

Levine, H., Shaklan, S., and Kasting, J. (2006). *Terrestrial planet finder coronagraph Science and technology definition Team (STDT) report. Tech. Rep. D-34923*. Pasadena, CA: California Institute of Technology.

Lita, A. E., Reddy, D. V., Verma, V. B., Mirin, R. P., and Nam, S. W. (2022). Development of superconducting single-photon and photon-number resolving detectors for quantum applications. *J. Light. Technol.* 40, 7578–7597. doi:10.1109/JLT.2022.3195000

Mamajek, E., and Stapelfeldt, K. (2024). NASA exoplanet exploration program (ExEP) mission star list for the habitable worlds observatory (2023). *arXiv e-prints* doi:10.48550/arXiv.2402.12414

Meadows, V. S. (2017). Reflections on O_2 as a biosignature in exoplanetary atmospheres. *Astrobiology* 17, 1022–1052. doi:10.1089/ast.2016.1578

Nagler, P. C., Greenhouse, M. A., Moseley, S. H., Rauscher, B. J., and Sadleir, J. E. (2018). Development of transition edge sensor detectors optimized for single-photon spectroscopy in the optical and near-infrared. *Proc. of the SPIE* 10709, 1070931. doi:10.1117/12.2313730

Nagler, P. C., Sadleir, J. E., and Wollack, E. J. (2021). Transition-edge sensor detectors for the origins space telescope. *J. Astronomical Telesc. Instrum. Syst.* 7, 011005. doi:10.1117/1.JATIS.7.1.011005

NASA Exoplanet Archive (2024). Available online at: https://exoplanetarchive.ipac.caltech.edu/ (Accessed May 31, 2024).

National Academies of Sciences, Engineering, and Medicine (2021). *Pathways to discovery in astronomy and astrophysics for the 2020s*. Washington, DC: The National Academies Press. doi:10.17226/26141

National Academies of Sciences, Engineering, and Medicine (2018). *Exoplanet science strategy*. Washington, DC: The National Academies Press. doi:10.17226/25187

Pepe, F., Cristiani, S., Rebolo, R., Santos, N. C., Dekker, H., Cabral, A., et al. (2021). ESPRESSO at VLT. On-sky performance and first results. *Astronomy Astrophysics* 645, A96. doi:10.1051/0004-6361/202038306

Quanz, S. P., Ottiger, M., Fontanet, E., Kammerer, J., Menti, F., Dannert, F., et al. (2022). Large Interferometer for Exoplanets (LIFE). I. Improved exoplanet detection yield estimates for a large mid-infrared space-interferometer mission. *Astronomy Astrophysics* 664, A21. doi:10.1051/0004-6361/202140366

Rabbia, Y., Gay, J., and Rivet, J.-P. (2007). The achromatic Interfero coronagraph. *Comptes Rendus Phys.* 8, 385–395. doi:10.1016/j.crhy.2007.04.003

Ras, W. G., Kouwenhoven, K., Thoen, D. J., Murugesan, V., Baselmans, J. J. A., and De Visser, P. J. (2024). Experimental demonstration of photon counting with kinetic inductance detectors at mid-infrared wavelengths. *Proc. SPIE* PC13103, PC1310305. doi:10.1117/12.3018412

Rauer, H., Catala, C., Aerts, C., Appourchaux, T., Benz, W., Brandeker, A., et al. (2014). The PLATO 2.0 mission. *Exp. Astron.* 38, 249–330. doi:10.1007/s10686-014-9383-4

Ricker, G. R., Winn, J. N., Vanderspek, R., Latham, D. W., Bakos, G. Á., Bean, J. L., et al. (2014). Transiting exoplanet survey satellite (TESS). *Proc. SPIE* 9143, 914320. doi:10.1117/12.2063489

Rieke, G. H., Wright, G. S., Böker, T., Bouwman, J., Colina, L., Glasse, A., et al. (2015). The mid-infrared instrument for the James Webb space telescope, I: introduction. *Publ. Astronomical Soc. Pac.* 127, 584–594. doi:10.1086/682252

Schlegel, D. J., Finkbeiner, D. P., and Davis, M. (1998). Maps of dust infrared emission for use in estimation of reddening and cosmic microwave background radiation foregrounds. *Astrophysical J.* 500, 525–553. doi:10.1086/305772

Schwab, C., Rakich, A., Gong, Q., Mahadevan, S., Halverson, S. P., Roy, A., et al. (2016). Design of NEID, an extreme precision Doppler spectrograph for WIYN. *Proc. of the SPIE* 9908, 99087H. doi:10.1117/12.2234411

Stark, C. C., Belikov, R., Bolcar, M. R., Crill, B. P., Groff, T., Krist, J., et al. (2019). The exoplanet yield landscape for future direct imaging space telescopes. *LPI Contrib.* Editors J. E. Moores, P. L. King, C. L. Smith, G. M. Martinez, C. E. Newman, and S. D. Guzewich (The space astrophysics landscape for the 2020s and beyond) 2135, 5001.

Swordy, L., Newberg, H. J., and Ditto, T. (2023). Primary objective grating telescopy: optical properties and feasibility of applications. *J. Astronomical Telesc. Instrum. Syst.* 9, 024001. doi:10.1117/1.JATIS.9.2.024001

Swordy, L., Newberg, H. J., Hill, B., Barry, R. K., Cousins, M., Nish, K., et al. (2025). The Dispersion Leverage Coronagraph (DLC): an achromatic nulling coronagraph for use on primary objective grating telescopes. *J. Astronomical Telesc. Instrum. Syst. Submitt*. Available online at: https://arxiv.org/pdf/2507.11745.

The LUVOIR Team (2019). The LUVOIR mission concept study final report. *arXiv e-prints,* doi:10.48550/arXiv.1912.06219

Traub, W. A., Levine, M., Shaklan, S., Kasting, J., Angel, J. R., Brown, M. E., et al. (2006). TPF-C: status and recent progress. *Proc. SPIE* 6268, 62680T. doi:10.1117/12.673608

Turnbull, M. C. (2015). ExoCat-1: the nearby stellar systems catalog for exoplanet imaging missions. *arXiv e-prints*. doi:10.48550/arXiv.1510.01731

Verma, V. B., Korzh, B., Walter, A. B., Lita, A. E., Briggs, R. M., Colangelo, M., et al. (2021). Single-photon detection in the mid-infrared up to 10 μm wavelength using tungsten silicide superconducting nanowire detectors. *Apl. Photonics* 6, 056101. doi:10.1063/5.0048049

Wang, W., Zhai, M., Zhao, G., Wang, S., Liu, J., Chang, J., et al. (2023). The Tianlin mission: a 6 m UV/Opt/IR space telescope to explore habitable worlds and the universe. *Res. Astronomy Astrophysics* 23, 095028. doi:10.1088/1674-4527/ace90f

Wenger, M., Ochsenbein, F., Egret, D., Dubois, P., Bonnarel, F., Borde, S., et al. (2000). The SIMBAD astronomical database. The CDS reference database for astronomical objects. *Astronomy and Astrophysics Supplement*, 143, 9–22. doi:10.1051/aas:2000332

Wollman, E. E., Verma, V. B., Walter, A. B., Chiles, J., Korzh, B., Allmaras, J. P., et al. (2021). Recent advances in superconducting nanowire single-photon detector technology for exoplanet transit spectroscopy in the mid-infrared. *J. Astronomical Telesc. Instrum. Syst.* 7, 011004. doi:10.1117/1.JATIS.7.1.011004

Ye, Y. (2022). China is hatching a plan to find Earth 2.0. *Nature* 604, 415. doi:10.1038/d41586-022-01025-2

Zang, W., Mao, S., Ge, J., Gould, A., and Yee, J. (2024). The Earth 2.0 microlensing space telescope. *Bull. Am. Astron. Soc.* 56, 231.01.

Frontiers in
Astronomy and Space Sciences

Explores planetary science and extragalactic astronomy in all wavelengths

Advances the understanding of our universe - from planetary science to extragalactic astronomy, to high-energy and astroparticle physics.

Discover the latest Research Topics

See more →

Frontiers

Avenue du Tribunal-Fédéral 34
1005 Lausanne, Switzerland
frontiersin.org

Contact us

+41 (0)21 510 17 00
frontiersin.org/about/contact